



**HAL**  
open science

# Contribution to the development of 4D-printed Hydromorph Biocomposites for marine restoration

Thomas Fruleux

► **To cite this version:**

Thomas Fruleux. Contribution to the development of 4D-printed Hydromorph Biocomposites for marine restoration. Materials. Université de Bretagne Sud, 2023. English. NNT : 2023LORIS670 . tel-04624734

**HAL Id: tel-04624734**

**<https://theses.hal.science/tel-04624734>**

Submitted on 25 Jun 2024

**HAL** is a multi-disciplinary open access archive for the deposit and dissemination of scientific research documents, whether they are published or not. The documents may come from teaching and research institutions in France or abroad, or from public or private research centers.

L'archive ouverte pluridisciplinaire **HAL**, est destinée au dépôt et à la diffusion de documents scientifiques de niveau recherche, publiés ou non, émanant des établissements d'enseignement et de recherche français ou étrangers, des laboratoires publics ou privés.

# THESE DE DOCTORAT DE

L'UNIVERSITE BRETAGNE SUD

ECOLE DOCTORALE N° 647  
*Sciences pour l'Ingénieur*  
Spécialité : *Génie des Matériaux*

Par

**Fruleux Thomas**

## **Contribution to the development of 4D-printed Hydromorph Biocomposites for marine restoration**

Thèse présentée et soutenue à Lorient, le 12 Octobre 2023  
Unité de recherche : IRDL UMR CNRS 6027  
Thèse N° : 670

### **Rapporteurs avant soutenance :**

M. Fabrizio SCARPA Professeur des Universités, Department of Aerospace Engineering, Bristol, United Kingdom  
M. Benoit ROMAN Directeur de Recherche CNRS, ESPCI, Université de la Sorbonne, Paris, France

### **Composition du Jury :**

Examineur :	M. Joël BREARD	Professeur des Universités, UNICAEN, Caen, France
Examineur :	M. Ali ZOLFAGHARIAN	Maître de Conférences, Deakin University, Deakin, Australia
Examinatrice :	Mme. Fabienne TOUCHARD	Directrice de Recherche CNRS, ENSMA, Poitiers, France
Dir. de thèse :	M. Antoine LE DUIGOU	Professeur des Universités, IRDL, Université Bretagne Sud
Co-encadrant de thèse :	M. Mickaël CASTRO	Maître de Conférences, IRDL, Université Bretagne Sud
Co-encadrant de thèse :	M. Pierre SAULEAU	Maître de Conférences, LBCM, Université Bretagne Sud



« Le véritable voyage de découverte ne consiste pas à chercher de nouveaux paysages, mais à avoir de nouveaux yeux. »

Marcel Proust



## Acknowledgments - Remerciements

Il m'est essentiel de démarrer ce récit en adressant un sincère remerciement à toutes les personnes qui m'ont accompagné au cours de ces trois années de thèse, et bien plus. Bien qu'étant une aventure professionnelle plutôt solitaire, cette thèse m'a enseigné beaucoup de choses aussi bien scientifiquement qu'humainement.

Pour commencer, je souhaiterais remercier mon directeur de thèse, Antoine Le Duigou, qui m'a fait découvrir le monde de la recherche académique à travers un sujet de thèse pluridisciplinaire passionnant. Merci pour ton soutien et ton expertise qui m'ont fait grandir en tant que chercheur ainsi que pour la confiance que tu m'as accordée dès le début de l'aventure. Un grand merci pour ces nombreux instants enrichissants, de partage et parfois même insolites vécus en terre nippone ! J'estime avoir eu beaucoup de chances de vivre toutes ces aventures et tout cela ne serait pas arrivé sans toi.

Mes pensées s'adressent également à vous, mes co-directeurs de thèse, Mickaël Castro et Pierre Sauleau, pour votre aide et votre écoute. J'ai apprécié collaborer avec vous, ce qui m'a permis d'engranger beaucoup de connaissances dans plusieurs domaines scientifiques ; aussi bien en science des polymères, sur les biocomposites et l'impression 4D ou encore en biologie marine. L'opportunité de participer à des cours de plongée sous-marines dans le cadre de ce projet fut incroyable ! Merci encore pour tes enseignements Pierre. Je saurai désormais improviser si je tombe nez à nez avec un congre ou un homard !

Un énorme merci à Hervé, Antoine, Isabelle, Françoise, Anthony J. et Anthony M. pour votre patience. Merci de m'avoir formé sur ces nombreux appareils et instruments de laboratoire qui furent essentiels à l'avancement de ce projet.

Je souhaite également saluer nos différents collaborateurs internationaux, Ryosuke Matsuzaki, Masafumi Kurihara, David Correa et Simon Poppinga, dont les connaissances pointues en

architecture, impression 4D et biomimétisme ont accru la rigueur et la compréhension des études menées.

Un grand merci aux trois stagiaires, Juliette, Mathias et Laurianne, ayant contribué à la partie expérimentale de différentes études avec envie et détermination.

Je suis également très reconnaissant envers tous les copains/copines du laboratoire. Car mener un bon projet nécessite, avant tout, une ambiance pérenne et agréable. J'ai donc beaucoup de personnes à remercier ! Mes premières pensées se tournent vers les plus vieux copains du lab : Mathias alias la Grande Courge, Kiki, Quentin, Max, Cindy, Marion, Roxane, Kolja, Aïssata, Lise, Gabrielle, Delphine, Julien, Flore, Marie, Lata, Maïa, Elouan, Malik, Andréa, Delphin et Lulu et aux plus jeunes JB, Monia, Pierre-Louis, Melvin, Loren, Lilian, Léopold, Margot, Matheus, Elouan, Xavier, Wilfried et Adèle. J'embrasse aussi les copains/copines extra labo, notamment l'équipe de danse bretonne (Marie, Ewen, Juliette, Colette et bien d'autres), Vlad, Soso et Rebecca. J'espère n'avoir oublié personne ! Merci pour ces bons moments passés ensemble tout au long de ces trois années de thèse.

Enfin, il est difficile de trouver un ordre logique pour saluer mes proches. En effet, j'ai la chance d'avoir un entourage présent peu importe la distance qui m'en sépare. Pour commencer, j'aimerais remercier l'une des personnes les plus importantes dans ma vie, ma Maman ! Sur le chemin de la thèse mais surtout pendant ce périple de 26 ans arpenté depuis le 5 juillet 1997. Tu as toujours été là pour moi et, même si les polymères ne représentent pas une passion naturelle chez toi, tu as toujours regardé les choses avec clairvoyance. En effet, il est parfois plus simple de résoudre un problème avec le cœur qu'avec des articles scientifiques. Et ça, c'est une qualité que j'admire beaucoup chez toi. Je pense que beaucoup de fils aimeraient avoir une relation aussi fusionnelle avec leur mère. Ensuite, je souhaiterais embrasser mon petit frère chéri, Kiki, alias Yann. J'espère que tu n'hésiteras plus à me solliciter pour tes DMs de maths... Et puis mon Papa, dont les rencontres de plus en plus occasionnelles n'entravent pas

son rôle de pilier dans ma vie. Bien sûr, la famille ne s'arrête pas là. Je pense notamment à mes deux grands-mères, Mamy Bichou et Mamy Mizou (profitez, les remerciements ne sont pas en anglais !), ma Marraine et ma filleule d'amour, mon Parrain, Loulou et tous mes autres cousins, cousines, oncles, tantes et à ce cher Ryuk. Et enfin, à mes deux grands-pères, Papy Bernard et Papy Christian, qui sont sans doute, depuis les cieux, en train de se demander ce que je baragouine depuis 45 minutes.

Alors oui je suis très famille, mais je suis aussi très copains ! Et j'ai la chance d'avoir une belle bande de pichelourds autour de moi. A cette occasion, je voudrais embrasser toutes celles et ceux qui, n'étant pas de Lorient (ni même de Bretagne), ont parcouru ce chemin périlleux en terre morbihannaise afin de profiter : des fameux FIL 2023/2024, de Cochinchine éreintante, de randonnées cyclistes à Fort Bloqué (6h de trajet en Vélib, ça commence à faire), de démarchages de toutes les librairies locales, d'un appartement infesté, de semi-marathon sur le GR 34, de randonnées de 10km... pardon, 20 km ! Mais aussi de tournois 3vs3 avec une finale aux urgences du Scorff, de sessions de surf sans vagues, de parties de Poker des Cafards truquées, d'un nouvel an pluvieux mais heureux, d'un délicieux gratin de chou pour 15 personnes ou encore d'un show des Ramoneurs de Menhir en béquilles. Un gros bisous à Louise, Aline, Vand, Denoeu, JR, Moun, Clémiche, Aline, Thom, Clairette, Chloé, Gab, Eva, Baba, Coco, Dodo, Jojo, Cocol, SJ, Arthur, Jé, Alex, Sélena, Kiki, Loulou, Marceau, Simon et Mathou. Enfin, un grand merci à toutes celles et ceux que j'oublie et à qui je penserai, hélas, 30 secondes après l'impression de ce manuscrit.





# General introduction

## *Version française*

Les Biocomposites Hygromorphes et Hydromorphes (HBC) représentent une nouvelle gamme de matériaux intelligents (capables de changer de forme dans le temps) actionnés par un gradient d'humidité. Conçus à partir de ressources naturelles, ces actionneurs autonomes ne requièrent aucune énergie externe pour générer leur mouvement. De nos jours, une grande motivation est dédiée au développement des HBC et à l'exploration de leur potentiel dans le développement de solutions futures, écologiques et durables. Bien que développés depuis plusieurs décennies, leur champ d'amélioration, allant de leur formulation à leur architecture, reste important. Grâce à l'impression 4D, les HBC pourraient recouvrir une gamme de fonctions et d'applications plus large dans la société de demain. Dans cette idée, ce projet de thèse vise **à contribuer au développement des HBC fabriqués à partir de fibres continues de lin en investiguant leur mécanisme d'actionnement, leurs propriétés mécaniques et leurs interactions avec la nature**. Bien que ciblant ici des applications marines, les concepts de changement de forme proposés pourraient être utilisés dans plusieurs domaines scientifiques innovants.

Le **Chapitre 1** propose une étude bibliographique du **récent développement des HBC et évalue leur potentiel dans la sauvegarde des écosystèmes marins**.

Le **Chapitre 2** est un chapitre « **Matériaux et Méthodes** » présentant les **différents matériaux, techniques de fabrication et de caractérisation** utilisés dans le cadre du projet.

Abordé dans le **Chapitre 1**, le changement de forme (aussi appelé actionnement) des HBC relate du gonflement intrinsèque des fibres naturelles lorsqu'elles subissent un gradient hydrique. Bien qu'étant le déclencheur de l'actionnement des HBC, les fibres connaissent un

gonflement diminué quand une matrice polymère les enrobe. Le **Chapitre 3** est consacré à l'étude de **l'impact des matrices biopolymères sur le gonflement des fibres de lin, nécessaire pour repousser les limites des HBC.**

Les considérations architecturales sont aussi des paramètres importants pour maximiser l'amplitude et la complexité de l'actionnement des HBC. Dans la nature, plusieurs végétaux présentent une mésostructure (architecture locale située entre l'échelle microstructurale et macrostructurale) complexe facilitant les interactions avec l'eau. Cet échange est primordial pour la croissance et pour l'adaptation de ces plantes face aux phénomènes climatiques. En s'appuyant sur l'impression 4D, l'optimisation du design des HBC est aujourd'hui envisageable. En contrôlant la distribution de matière et l'anisotropie au sein d'HBC conçus par impression 4D, **des prototypes intelligents sont développés, donnant une meilleure compréhension de la relation entre leur mésostructure et leur mécanisme d'actionnement (Chapitre 4).**

Résultant de cette approche bioinspirée, des architectures plus complexes sont recherchées pour cibler des structures biologiques encore inconnues des HBC. Le **Chapitre 5** présente **les limitations géométriques existant dans la mise en forme d'HBC renforcés à partir de fibres continues de lin par impression 3D.** La complexité de l'impression hors plan (suivant l'axe z) y est mise en exergue.

Les porosités représentent des éléments constitutifs des matériaux composites. Dépendant grandement du procédé de fabrication, leur proportion varie et suit une distribution aléatoire au sein du matériau. Cependant, lorsqu'elles sont spécifiquement distribuées, ces entités poreuses peuvent agir comme promoteur du transport de l'eau et d'autres fonctionnalités. Puisque l'impression 4D permet le contrôle de l'anisotropie au sein des HBC, un intérêt existe à connecter ces porosités localisées (nommés canaux) à leur mécanisme d'actionnement.

**S’inspirant de l’architecture poreuse de systèmes biologiques, le contrôle du transport de l’eau et de l’actionnement des HBC est exploré grâce au design d’architecture à canaux par impression 4D (Chapitre 6).**

Enfin, s’éloignant des sujets de thèse purement théoriques, ce projet propose une réflexion sur le développement des HBC pour des applications marines. Se basant sur le concept de récif artificiel, des pensées sont données à l’immersion de prototypes HBC permettant de redynamiser les écosystèmes marins. Dans le **Chapitre 7, une étude est menée sur le potentiel de colonisation (biofouling) des microorganismes et macroorganismes marins sur des biocomposites**. De plus, **l’impact des produits de dégradation des biocomposites sur la croissance de deux modèles biologiques** est analysé.

### *English version*

Hydromorph and Hygromorph Biocomposites (HBC) represent a new range of sustainable shape-changing materials actuated by water gradient or humidity gradient. Made of local renewable resources, they are autonomous sensors and actuators that require no additional energy to generate motion. Nowadays, there is a huge motivation to explore what Hygromorph BioComposites could offer to green engineering and sustainable solutions. Although they have recently been deployed on an unprecedented scale, there is still plenty of scope for improving their formulation and architecture. Starting with the connection to 4D-printing, smarter and more functionalized HBC prototypes should be created soon. This entire project aims to **enhance the range of applications of continuous flax-fiber reinforced HBC by increasing their performances regarding their mechanical behavior, their actuation mechanisms and their interactions with nature**. Although there is a specific interest in developing HBC for marine applications, the proposed morphing concepts could be used for several innovative

topics. The two first chapters are dedicated to a consequent reminder of **the recent development of Hygromorph Biocomposites and potential for marine restoration (Chapter 1)** and the **materials/characterization techniques (Chapter 2)** used in this PhD project.

The shape-changing behavior of Hygromorph BioComposites relies on the inherent swelling of natural fibers triggered by water uptake. Though being the main promotor of actuation, the natural fiber does not swell the same way alone than surrounding by polymer matrix. Besides, flax fiber content is limited inside composites for adherence purposes. **A deeper understanding of the impact of biopolymer matrix on the fiber swelling is required to push the boundaries of HBC actuation. Material selection to fabricate stable or water-sensitive biocomposites depending on structural applications must be investigated (Chapter 3).**

Architectural considerations are also important to unlock the amplitude and complexity of HBC actuation. In nature, some plants exhibit a complex mesostructure to facilitate interactions with water allowing for plant growth and structural adaptation to climatic factors. Thanks to development of 4D-printing, design optimization of HBC should be envisioned. **By controlling matter distribution and anisotropy within 4D-printed HBC, constitutive smart prints will be manufactured to give a strong understanding of the relation between material mesostructure and shape-changing behavior (Chapter 4).**

Resulting from this biomimetic approach, more complex and controlled architectures are expected to tackle biological structures still unthought in 4D-printed HBC. **This third mission consists in upscaling the traditional in-plane printing of beams or 2D-patterns into 3D shapes. Working with continuous flax-fiber filament, an investigation needs to be conducted on its printability in the design of out-of-plane lattice structures (Chapter 5).**

Porosity is a constitutive element of biocomposites. Depending on the manufacturing process and fiber/matrix association, its proportion is highly variable and follows a random distribution inside the material. However, when specifically distributed, porous entities can act as promoters for water supply and functionalization (e.g. in plants). Because 4D-printing allows for the control of the anisotropy inside HBC, an interest arises from the nebulous connection between locally distributed porosity on the actuation performances. **Relying on plant architecture, the control of water transport and morphing inside HBC by using 4D-printed channel-induced architecture should be explored (Chapter 6).**

Instead of working on a purely theoretical project, potential applications of HBC are important to anticipate as the world is every day in needs of sustainable and energy-sparing inventions. Since HBC are promoted by humid environments, thoughts about developing immersed prototypes addressing the issue of marine depletion appeared. In the final section, a deep look will be given to the design of reconfigurable and biocompatible artificial reefs made of biopolymer matrix and continuous flax fibers. **The impact of released products from flax leachates or degradation of biopolymers on marine organisms as well as micro- and macrofouling potential will be tackled. (Chapter 7).**



# Scientific contributions

## I. Scientific papers

### I. 1. Accepted

A. Le Duigou, **T. Fruleux**, R. Matsuzaki, G. Chabaud, M. Ueda and M. Castro, “4D printing of continuous flax-fibre based shape-changing hygromorph biocomposites : Towards sustainable metamaterials”, *Materials & Design*, Volume 211, 2021

DOI : <https://doi.org/10.1016/j.matdes.2021.110158>

**T. Fruleux**, M. Castro, P. Sauleau, R. Matsuzaki and A. Le Duigou, “Matrix stiffness : A key parameter to control hydro-elasticity and morphing of 3D printed biocomposite “, *Composites Part A*, Volume 156, 2022

DOI : <https://doi.org/10.1016/j.compositesa.2022.106882>

**T. Fruleux**, M. Castro, D. Correa, K. Wang, R. Matsuzaki and A. Le Duigou, “Geometric limitations of 3D printed continuous flax-fiber reinforced biocomposites cellular lattice structures”, *Composites Part C*, Volume 9, 2022

DOI : <https://doi.org/10.1016/j.jcomc.2022.100313>

### I. 2. Under review

**T. Fruleux**, D. Correa, M. Castro, S. Poppinga, K. Wang and A. Le Duigou, “Toward control of water transport inside 4D-printed bioinspired Hydromorph Biocomposite actuators through tailored channel architecture“, *Advanced Functional Materials*.

M. Kurihara, **T. Fruleux**, A. Le Duigou, M. Ueda and R. Matsuzaki, “Bridging in 4D printing using continuous natural-fiber composites“

**T. Fruleux**, Q. Le Paih, D. Correa, S. Poppinga, M. Castro and A. Le Duigou, “Toward control of soft bifurcation inside 4D-printed bioinspired Hygromorph Biocomposite actuators through tailored architecture“, *Nature Sustainability*.



## II. Conferences

### II. 1. International conferences

**T. Fruleux**, M. Castro, P. Sauleau, R. Matsuzaki and A. Le Duigou, “Matrix stiffness : A key parameter to control hydro-elasticity and morphing of 3D printed biocomposite”, Conference on Biobased Composites in Marine Environment, March 2021

**T. Fruleux**, M. Castro, P. Sauleau, R. Matsuzaki and A. Le Duigou, “Matrix stiffness : A key parameter to control hydro-elasticity and morphing of 3D printed biocomposite”, 5<sup>th</sup> International Conference on Natural Fibers, May 2021

**T. Fruleux**, M. Castro, P. Sauleau, R. Matsuzaki and A. Le Duigou, “Matrix stiffness : A key parameter to control hydro-elasticity and morphing of 3D printed biocomposite”, 7<sup>th</sup> International Polysaccharide Conference of the European Polysaccharide Network of Excellence (EPNOE), October 2021

**T. Fruleux**, M. Castro, P. Sauleau, R. Matsuzaki and A. Le Duigou, “Matrix stiffness : A key parameter to control hydro-elasticity and morphing of 3D printed biocomposite”, 2<sup>nd</sup> International Conference on Additive Fabrication of Composites, November 2021

**T. Fruleux**, M. Castro, P. Sauleau, R. Matsuzaki and A. Le Duigou, “Controlling water transport inside 4D-printed biomimetic actuators”, 4D Materials Design and Additive Manufacturing Conference, September 2022

**T. Fruleux**, M. Castro, P. Sauleau, R. Matsuzaki and A. Le Duigou, “4D-printed Bistable Hygromorph Biocomposites : Tailoring the bifurcation behavior”, 3<sup>rd</sup> International Conference on Additive Fabrication of Composites, December 2022

### II. 2. National conferences

**T. Fruleux**, M. Castro, P. Sauleau, R. Matsuzaki and A. Le Duigou, “Impact de la rigidité de la matrice sur l’actionnement de biocomposites hygromorphes par impression 4D”, Journées Nationales des Composites, Juin 2021





# Table of contents

<b>ACKNOWLEDGMENTS - REMERCIEMENTS</b> .....	5
<b>GENERAL INTRODUCTION</b> .....	9
<b>SCIENTIFIC CONTRIBUTIONS</b> .....	15
<b>GLOSSARY</b> .....	23
<b>CHAPTER 1 : STATE-OF-THE-ART IN THE DEVELOPMENT OF BIOINSPIRED 4D-PRINTED HYGROMORPH BIOCOMPOSITES AND THEIR POTENTIAL FOR MARINE RESTORATION</b> .....	27
I. DEVELOPMENT OF HYGROMORPH BIOCOMPOSITES .....	29
I.1. GENERAL DEFINITION .....	29
<i>I.1.a. Overview of the natural reinforcements</i> .....	29
<i>I.1.b. Overview of the biopolymer matrices</i> .....	32
I.2. MECHANICAL PERFORMANCES .....	33
<i>I.2.a. Influence of the natural reinforcement</i> .....	34
<i>I.2.b. Influence of the biopolymer matrix</i> .....	36
I.3. HYGROSCOPIC PERFORMANCES.....	37
<i>I.3.a. Water sorption</i> .....	37
<i>I.3.b. Hygroexpansion</i> .....	43
<i>I.3.c. Hygroelastic properties</i> .....	49
I.4. HBC : A NEW RANGE OF SHAPE-CHANGING MATERIALS .....	51
<i>I.4.a. What triggers the actuation of HBC ?</i> .....	51
<i>I.4.b. Water ageing of HBC</i> .....	55
<i>I.4.c. Range of applications and development</i> .....	58
I.5. CURRENT LOCKS REGARDING THE ACTUATION OF HBC .....	59
<i>I.5.a. Limited reactivity</i> .....	59
<i>I.5.b. Limited shape-changing pattern and responsiveness</i> .....	60
II. THE REVOLUTIONARY ROLE OF ADDITIVE MANUFACTURING IN THE DESIGN OF HBC .....	61
II.1. FUSED FILAMENT FABRICATION (FFF) .....	61
<i>II.1.a. Filament production</i> .....	61
<i>II.1.b. 3D-printing of continuous fiber reinforced composites</i> .....	62
II.2. 4D-PRINTING .....	66
<i>II.2.a. Actuation based on material selection</i> .....	67
<i>II.2.b. Actuation based on matter distribution</i> .....	69
<i>II.2.c. The case of cellular structures</i> .....	72
III. RECONFIGURABLE WATER-INDUCED BIOLOGICAL MODELS.....	76
III.1. WATER TRANSPORT THROUGH PLANT TISSUE .....	77
III.2. HOW WATER SORPTION GENERATES MOTION.....	78
<i>III.2.a. Slow hydraulic movements</i> .....	79
<i>III.2.b. Mechanical instability</i> .....	81
III.3. EXAMPLE OF BIOLOGICAL HYDRAULIC ACTUATORS .....	83
<i>III.3.a. Reconfigurable biological models</i> .....	83
<i>III.3.b. Towards 4D-printed Hygromorph biomimetic prototypes</i> .....	88
IV. POTENTIAL ASSET FOR MARINE RESTORATION AND ARTIFICIAL REEFS.....	99

IV.1. MATERIAL SELECTION .....	101
IV.1.a. A promotor of marine biofouling .....	101
IV.1.b. Seawater ageing and controlled lifetime of biocomposites.....	107
IV.2. CHOICE OF THE ARCHITECTURE .....	108
<b>CHAPTER 2: MATERIALS &amp; METHODS .....</b>	<b>113</b>
I. INTRODUCTION.....	114
II. "MATERIAL AND DESIGN" SURVEY.....	115
II.1. Materials .....	115
II.2. Manufacturing process .....	116
II.3. Characterization techniques.....	118
III. "BIOLOGICAL" SURVEY.....	126
III.1. Materials.....	126
III.2. Manufacturing process.....	127
III.3. Characterization of substrates.....	127
III.4. Cultivation of the biological strains.....	128
III.5. Sample preparation .....	129
III.6. Microorganism and macroorganism adhesion .....	131
III.7. Influence of flax leachates on the growth of microorganisms.....	134
<b>CHAPTER 3: MATRIX SELECTION: A KEY TOWARDS WIDER ACTUATION ? .....</b>	<b>137</b>
I. INTRODUCTION.....	138
II. MICROSTRUCTURAL DESCRIPTION .....	141
III. HYGROSCOPIC BEHAVIOR.....	142
III.1. SORPTION ISOTHERM .....	142
III.2. HYDROSCOPIC EXPANSION .....	144
IV. HYGRO-/HYDROMECHANICAL BEHAVIOR .....	147
IV. 1. HYGRO-/HYDROMECHANICAL PROPERTIES .....	147
IV. 2. EVALUATION OF THE INTERNAL STRESS .....	149
V. MATRIX SELECTION AS A PROMOTOR OF HBC ACTUATION .....	149
VI. CONCLUSION.....	152
<b>CHAPTER 4 : HOW BIOINSPIRED DESIGN FOSTERS THE MORPHING BEHAVIOR OF HBC ? .....</b>	<b>155</b>
I. INTRODUCTION.....	156
II. RESULTS.....	159
II. 1. CONCEPTUALIZATION OF PINE CONE ARCHITECTURE AND GEOMETRY .....	159
II. 2. INFLUENCE OF THE LENGTH TO WIDTH (L/W) ASPECT RATIO OF HBC.....	163
II. 3. CROSS-SECTIONAL DISTRIBUTION OF TISSUE : INFLUENCE OF THE PASSIVE-TO-ACTIVE THICKNESS RATIO .....	165
II. 4. INFLUENCE OF PASSIVE-TO-ACTIVE STIFFNESS RATIO IN THE BIFURCATION BEHAVIOR .....	168
II.4.a. In-plane distribution of tissue : Influence of the Interfilament Distance in the passive layer (IDp).....	168
II.4.b. Impact of the selected material.....	169
III. RESHAPING 4D-PRINTED HBC WITH DUAL ACTUATION .....	171

IV. CONCLUSION.....	174
<b>CHAPTER 5 : TECHNICAL LIMITATIONS OF 3D-PRINTING IN THE DEPLOYMENT OF CONTINUOUS NATURAL-FIBER HBC.....</b>	<b>177</b>
I. INTRODUCTION.....	178
II. RESULTS.....	180
III. CONCLUSION.....	183
<b>CHAPTER 6 : HOW BIOINSPIRED DESIGNS SPEED UP THE ACTUATION OF HBC ? .....</b>	<b>187</b>
I. INTRODUCTION.....	188
II. RESULTS.....	190
II.1. Concept .....	190
II.2. Investigation of the active layer scale .....	191
II.2.a. Mesostructure qualification.....	191
II.2.b. Water sorption and transport during immersion.....	193
II.2.c. Hydroscopic expansion.....	195
II.2.d. Hydromechanical properties .....	197
III. DISCUSSION.....	199
III.1. 4D-printed HBCs with improved performance.....	199
III.2. 4D-printed HBCs with tailored performance .....	201
IV. CONCLUSION.....	202
<b>CHAPTER 7 : BIOCOMPOSITES, TOWARDS GREENER ARTIFICIAL REEFS ?.....</b>	<b>205</b>
I. INTRODUCTION.....	206
II. RESULTS AND INTERPRETATIONS.....	210
II.1. Influence of flax leachates on the growth of microorganisms .....	210
II.1.a. <i>Pseudoalteromonas sp. 3J6</i> .....	210
II.1.b. <i>Cylindrotheca closterium</i> .....	210
II.2. Influence of monomers on microorganism growth.....	211
II.2.a. <i>Pseudoalteromonas sp. 3J6</i> .....	211
II.2.b. <i>Cylindrotheca closterium</i> .....	212
II.3. Biofouling potential.....	213
II.3.a. <i>Microorganism adhesion</i> .....	213
II.3.b. <i>Biofilm formation</i> .....	216
II.2.c. <i>Macroorganism adhesion (in situ study)</i> .....	219
III. CONCLUSION.....	223
<b>GENERAL CONCLUSION AND PERSPECTIVES.....</b>	<b>226</b>
I. CONTEXT .....	226
II. ACHIEVEMENTS .....	227
III. PERSPECTIVES .....	228
<b>REFERENCES.....</b>	<b>230</b>



## Glossary

<b>3DP</b>	3D-printed
<b>4DP</b>	4D-printed
<b>ABS</b>	Acrylonitrile Butadiene Styren
<b>ASW</b>	Artificial SeaWater
<b><i>C. closterium</i></b>	<i>Cylindrotheca closterium</i>
<b>CD</b>	Calcium Diformate-based concrete formulation
<b>CE</b>	Cellulose Ether-based concrete formulation
<b>cFF</b>	continuous Flax Fiber
<b>cJF</b>	continuous Jute Fiber
<b>cKF</b>	continuous Kevlar Fiber
<b>EMC</b>	Equilibrium Moisture Content
<b>FFF</b>	Fused Filament Fabrication
<b>HBC</b>	Hygromorph/Hydromorph BioComposites
<b>HIPS</b>	High Impact PolyStyrene
<b>ID</b>	Interfilament Distance
<b>LH</b>	Layer Height
<b>LF</b>	Limestone Filler-based concrete formulation
<b>LN</b>	Layer Number
<b>MB</b>	Marine Broth medium
<b>MFR</b>	Melt Flow Rate
<b>MFI</b>	Melt Flow Index
<b>NFRC</b>	Natural Fiber Reinforced Composite
<b>NFRB</b>	Natural Fiber Reinforced Biocomposite
<b>PBS</b>	PolyButylene Succinate
<b>PBSA</b>	Poly(Butylene Succinate-co-butylene Adipate)
<b>PBAT</b>	PolyButylene Adipate Terephthalate
<b>PC</b>	Polycarbonate
<b>PEEK</b>	Poly-Ether-Ether-Ketone
<b>PHA</b>	PolyHydroxyAlkanoate
<b>PLA</b>	Polylactic acid
<b><i>P. sp. 3J6</i></b>	<i>Pseudoalteromonas sp. 3J6</i>
<b>sCF</b>	short Carbon Fiber

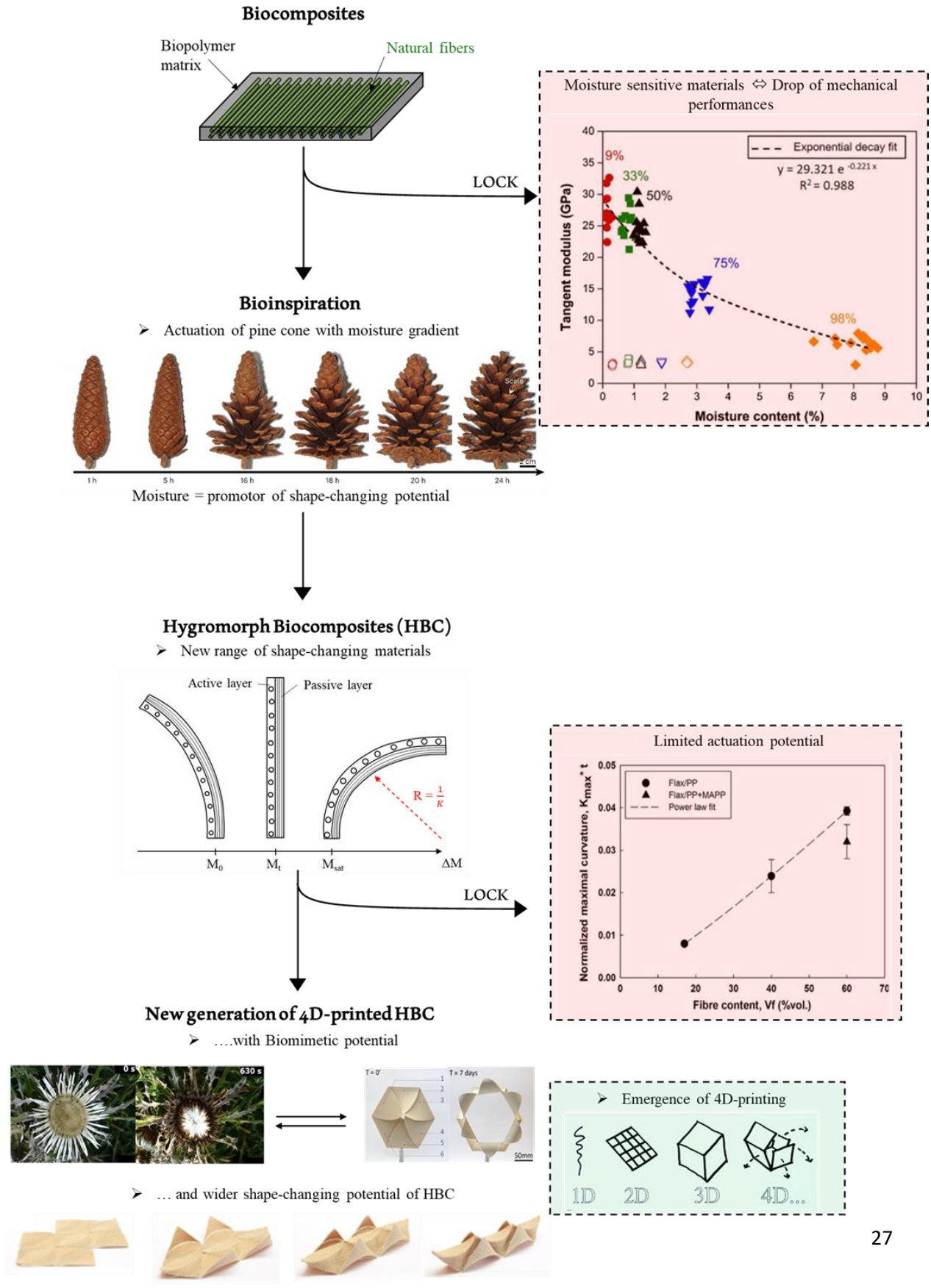


<b>sFF</b>	short Flax Fiber
<b>SMP</b>	Shape-Memory Polymer
<b>SFRPC</b>	Synthetic Fiber Reinforced Polymer Composite
<b>TGA</b>	ThermoGravimetric Analysis
<b>TPU</b>	ThermoPolyUrethane
<b>X</b>	Raw concrete formulation





# Chapter 1 : State-of-the-art in the development of bioinspired 4D-printed Hygromorph Biocomposites and their potential for marine restoration



**Chapter 1** discusses the development of Hygromorph BioComposites (HBC) that are able to shape-change due to a moisture absorption and propose a dedicated biologically inspired architecture. It aims to understand the continuous expansion of these smart materials and their current limitations over the past years. Hygromorph biocomposites (HBC) have been created from biological examples of which the structure is reconfigured by water gradient (e.g. pine cone scale). Categorized as water-induced shape-changing materials, their actuation is driven by natural reinforcements unlike smart conventional materials driven by polymer matrix. They are examined in terms of formulation and architecture. Made of natural fibers and biopolymer matrix, their biobased formulation is optimized to propose a predictable reconfigurable behavior. Their actuation performances are quantified by their amplitude of shape-changing pattern, called “responsiveness”, and their kinetic of actuation, called “reactivity”. However, some restrictions slower the development of HBC and their targeted applications. The role of 4D-printing in HBC design has generated a wide range of conforming structures with specific functions. In order to overcome these limitations, a deep insight is given to architectural and morphological features of several biological models through a bioinspired approach. Finally, the possibility of using HBC as a lever for marine rehabilitation, i.e. as novel artificial reef, is discussed.

# I. Development of Hygromorph Biocomposites

Natural fiber reinforced biocomposites (NFRB) are presented as a new opening and approach in load-bearing applications. Well-known for their eco-friendly characteristics, their development is still having a growing interest in the scientific community.

## I.1. General definition

Hygromorph Biocomposites (HBC) are composed of natural reinforcements and polymer matrix. Though coming mostly from petrochemical resources, biobased and/or biodegradable polymer matrix are today increasingly used in the formulation of HBC. In the following sections, a specific attention is given to the association of these polymer matrices, referred as biopolymer matrix, with natural reinforcements.

### I.1.a. Overview of the natural reinforcements

#### *I.1.a.i. Origins and applications*

The use of natural fibers for anthropogenic activities dates back to 40,000 years ago. Interests on these natural compounds started for textile applications [1] and medicine ([2], [3]). They continue to play a primordial role in our time: from traditional resources in the textile market [4] to new reinforcement for modern architecture [5].

Nowadays, the role of natural fibers has reached higher standards in the context of limiting carbon emissions and replacing petrochemical products. Indeed, there is a global wish to turn carbon, glass or aramid into flax, hemp or wood reinforcements for creating more environmentally friendly materials [6]. Besides being greener, natural fibers could promote the development of lightweight structure with biodegradable functions essential for life span control. This property is becoming essential for current manufactured materials as life cycle analysis is increasingly recommended for environmental purposes. Most of synthetic fiber reinforced polymer composites (SFRPC) are not able to reach these objectives. However,

serious challenges restrict the presence of natural fiber reinforced polymer composites (NFRPC) on the industrial market. One of the most important is the significant gap between the mechanical performances of SFRC and NFRC, even though scientific researches has increased their potential over the years [7].

The wide range of natural fibers opens up multiple possibilities of use. It is related to their morphology, biochemical composition and structural features. Two distinguishable families exist : non-wood natural fibers and wood fibers. Figure 1 classifies the provenance of the main natural fibers.

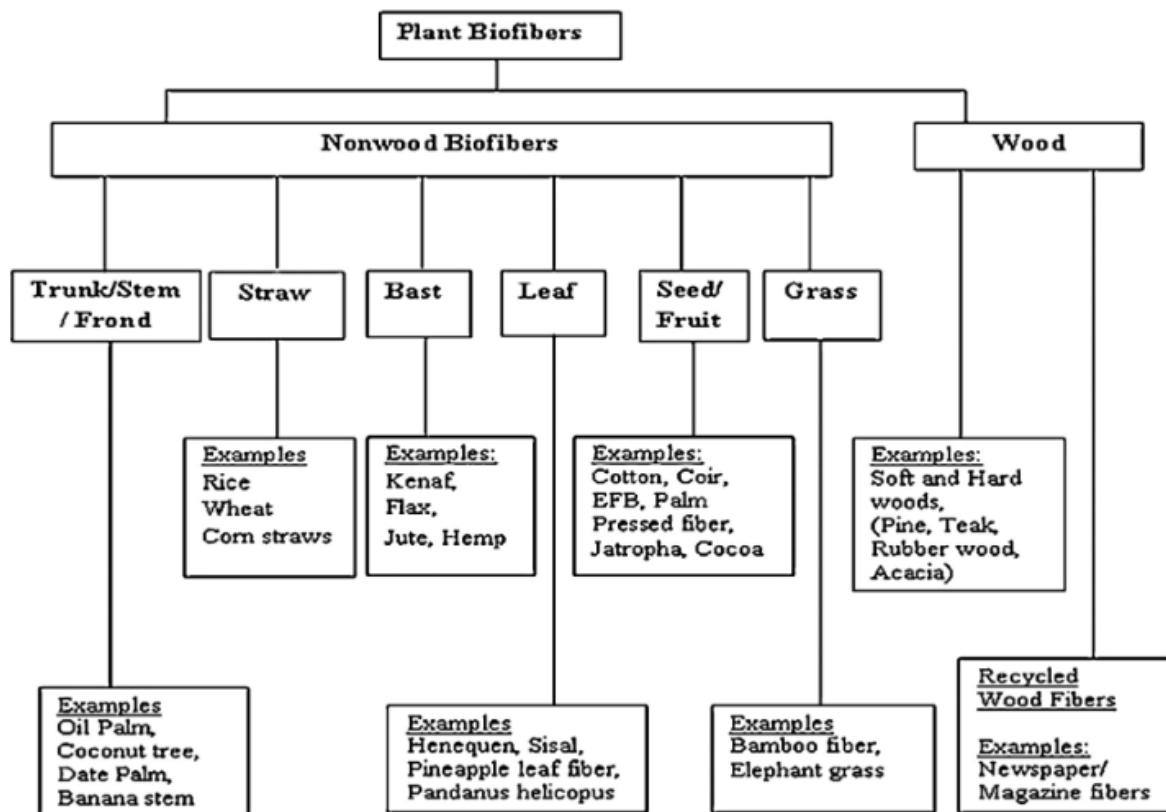


Figure 1: Overview of natural fibers used for anthropogenic purposes [8].

Origins of natural fibers as well as harvesting conditions and variety affect the fiber morphology and performance. This impact could even affect two successive yearly crops since the retting period, i.e. period required to degrade the flax stem and harvest individualized flax

bundles [9], is rarely identical [10]. The use of natural fibers in high-performance structures is therefore all the more critical and important to finely assess.

### *I.1.a.ii. Microstructure*

The overall structure of an elementary natural fiber is given in Figure 2. Fiber cell wall is built on two-stage structure: primary wall and secondary wall. Each layer presents an association of cellulosic microfibrils acting as reinforcement and a polysaccharide network of hemicellulose and lignin macromolecules. Following this schematic overview, elementary fibers can be considered as composite materials. Secondary layer can be divided into three entities S1, S2 and S3 whose dimension and composition ensure specific functions to the plant. Representing the predominant layer, S2 layer dictates the mechanical behavior of the fiber. Reaching 80% of the total fiber thickness, it acts as the main load bearing component inside the structure [11]. Furthermore, the presence of cellulosic microfibrils, their orientation and crystallinity of the embedding matrix affect the physico-chemical properties of natural fibers [5]. In particular, the orientation of cellulosic microfibrils symbolized by microfibrillar angle (MFA) regulates plant functionalities. MFA quantifies the existing angle between microfibrillar axis and cell wall axis. Fiber location in plant sharpens fiber architecture and its function. Depending on the fiber function, structural features (e.g. MFA, S2 thickness, biochemical composition, fiber dimension) will change [5]. Figure 2 displays a simplified scheme of plant fiber structure.

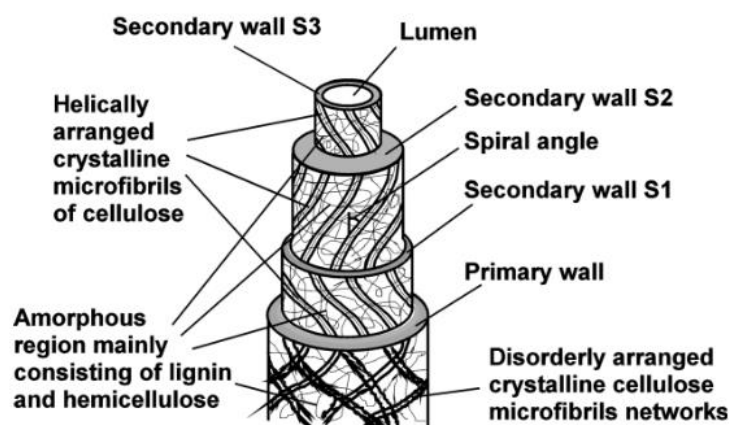


Figure 2: Schematic overview of elementary plant fiber structure [11].



Through plant tissue, elementary fibers are embedded in a polysaccharide matrix called middle lamellae. The association of elementary fibers within middle lamellae is defined as fiber bundle (i.e. technical fiber). The property of fiber bundle stems from the associative effect of elementary fibers. Impacts of the aforementioned parameters on mechanical performances, hygroscopic properties and sustainability of elementary plant fibers will be tackled in following sections.

#### I.1.b. Overview of the biopolymer matrices

Biopolymers are barely defined in an unanimous paradigm by scientists, designers and chemical engineers. The most uniting definition identifies biopolymers as polymers being (1) biobased i.e. extracted from natural entities, (2) biodegradable under aerobic conditions by microorganisms and enzymes or (3) biobased and biodegradable [12].

Biobased polymers may arise from plants, animals or bacteria. From these families, various natural substances are recovered to synthesize the final bioplastics. Among them, starch, lignocellulosic biomass or vegetable oils predominate biopolymer market. From the production of polylactic acid by corn to lignocellulosic fermentation to obtain biobased ethylene, an exhaustive list of biopolymers synthesized from ecological resources already exists in the literature ([13]–[15]). Even if the number and rate of use of biopolymers are still insignificant compared with synthetic polymers, their predicted growth could lead to the replacement of 30-90% of their synthetic counterparts in the future [16].

However, it is essential to remind that biobased polymers are not essentially biodegradable. Figure 3 elucidates this nuance by dividing biopolymer matrices into three different groups. The first group incorporates the naturally biodegradable polymers. Their synthesis relies on hydrolysis or microbial fermentation of raw polysaccharides without any structural changes. By this way, only biodegradable polymers are produced. It represents the best candidates for

environmental and ecological motivations. Then, some polymers are designed to become biodegradable. For example, chemical modifications can be applied on natural polysaccharides to rearrange the macromolecular structure of monomers. For instance, it is used to produce polylactic acid (PLA) or polybutylene succinate (PBS). In parallel, polymers synthesized with synthetic monomers can be biodegradable in industrial compost. Polybutylene adipate terephthalate (PBAT) belongs to this class of biopolymers. Then, the last family gathers the biobased polymers that are not biodegradable. It concerns many derivatives from synthetic polymers such as bio-polypropylene and bio-polyethylene whose ongoing investigations are conducted to reach completely green products.

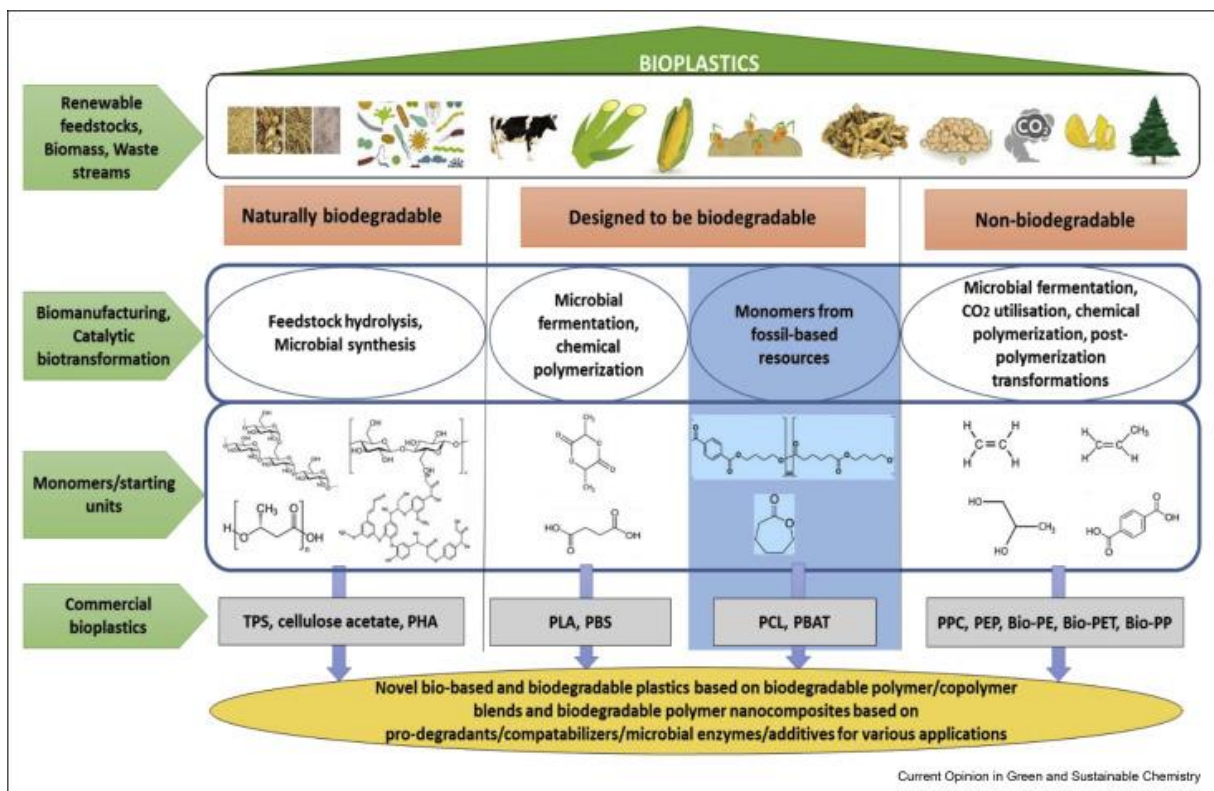


Figure 3: Schematic representation of existing biopolymers and their natural/synthetic provenance [17].

## I.2. Mechanical performances

A started mission aims to make the mechanical performance of natural fiber reinforced biocomposites competitive with those of conventional composites reinforced with synthetic fibers. Some of them are showing greater and greater rigidity over the carried investigations.

Depending on the used fiber and matrix, the interaction at the fiber/matrix interface and the manufacturing process, significant mechanical properties can be reached. A list of the various material design parameters that directly affect these properties is given in the next section.

### I.2.a. Influence of the natural reinforcement

As an evidence, natural fibers impact the mechanical behavior of biocomposites. Their mechanical performances overcome those of steel or concrete in some aspects such as strength to weight ratio [18]. Natural reinforcements exhibit a wide range of fibers whose inherent properties vary with the type and nature of fibers, production area, growing and harvest conditions. Nowadays, it exists several plant fibers of interest as reinforcements in NFRB such as flax, hemp, coir, bamboo, etc. Their degree of performance as reinforcement in NFRB will be determined by their biochemical composition and microstructure.

#### *I.2.a.i. The impact of fiber structure and morphology*

Starting with elementary fibers, the main structural parameter affecting their mechanical performances is the microfibrillar angle. Decreasing the MFA improves the tensile modulus of the fibers. Indeed, lower the MFA, better aligned the cellulose microfibrils with the loading axis, more resistant the fibers [19]. This point is highlighted by Figure 4.

At the scale of fiber bundle, Tanguy et al. [20] evaluated two types of natural reinforcements (flax and jute fibers) on mechanical properties of PP-based composites. Depending on the investigated property, both formulations report assets. Indeed, the transverse properties of jute/PP-MAPP exhibited a slightly higher stress at break ( $\sigma_{\text{break}} = 7.8 \pm 0.8$  GPa) than flax/PP-MAPP composites ( $\sigma_{\text{break}} = 6.7 \pm 0.5$  GPa) explained by the compact arrangement of jute fibers (in bundles) compared to flax fibers which are more individualized and give a lower cohesion in the transverse direction (Figure 5). However, flax fibers strengthen the longitudinal modulus by 50% compared with jute/PP-MAPP because of the higher length (i.e.  $L_{\text{flax}} = [15-80]$  mm,

$L_{\text{jute}} = [0.8-6]$  mm) and limited lignin content (i.e. 2% for flax fiber against 11.8% for jute fiber [8]) of flax fibers, improving the interactions with PP-MAPP matrix.

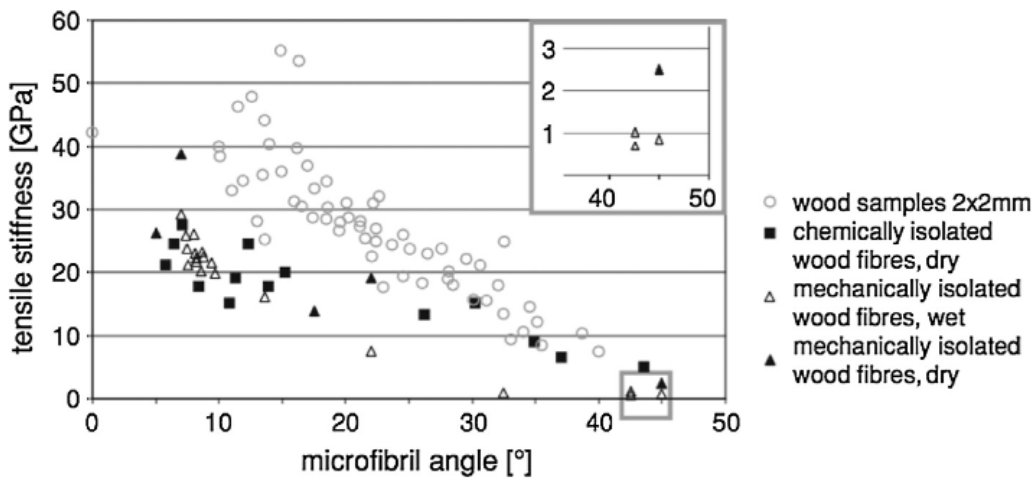


Figure 4: Influence of MFA on tensile stiffness of wood fibers and samples [21].

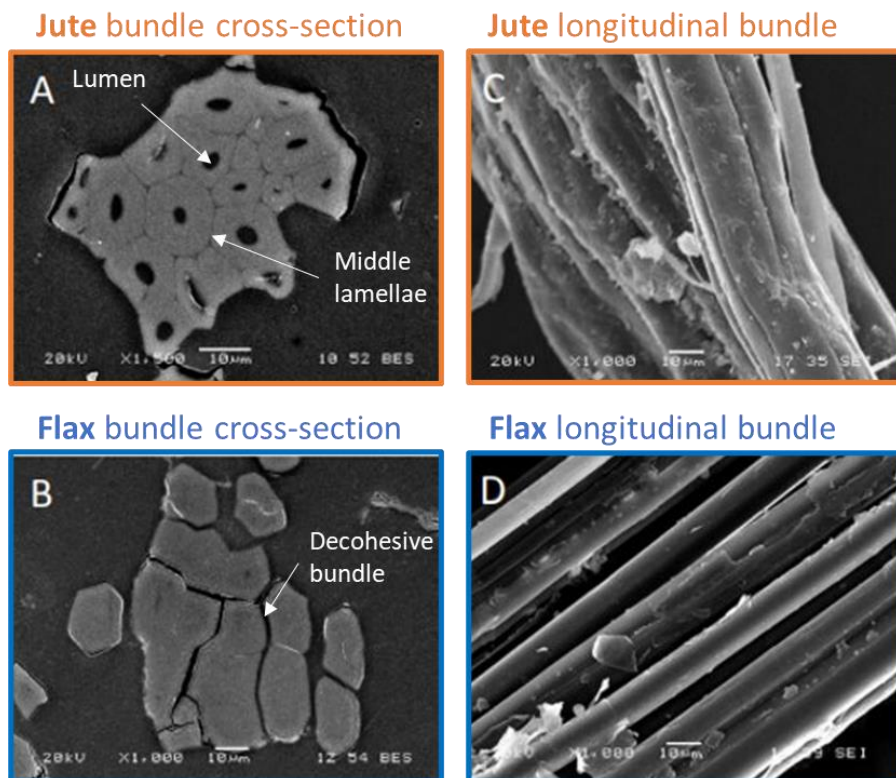


Figure 5: Structural organization of jute and flax fiber bundles. Cross-sectional images of A/ jute and B/ flax fiber bundles. Longitudinal aspect of C/ jute and D/ flax fiber bundles [20].

### I.2.a.ii. The impact of biochemical composition

Pectin, hemicellulose, lignin and cellulosic microfibrils content change the mechanical properties of plant fibers. For example, flax fiber exhibits a high-cellulosic content ([60-85]%

) and great tensile modulus ( $E_L = 68.9 \pm 24.6$  GPa) [5]. Then, the ratio between the coated hemicellulose located all around the microfibrils (EOH) and the encrusted pectin chains filling the inter-fibrillar space (EH) represents an influencing parameter too (Figure 6). Increasing EH content would widen the space between the fibrils leading to debonding [19].

The organization of cellulose microfibrils also enlarges the loading capacity of fibers. Similarly to polymer network, crystalline areas will bring more stiffness and toughness to fibers compared to amorphous regions. For example, comparisons between microcrystalline amorphous cellulose ( $I_c = 48.5 \pm 1.1\%$ ) and more crystalline fibers such as flax fiber ( $I_c = 64.3 \pm 1.1\%$ ) and hemp fiber ( $I_c = 59.7 \pm 2.0\%$ ) was investigated [22]. This approximate 30%-increase in crystallinity index led to a 44% and 60%-increase in elastic modulus of the aforementioned fibers.

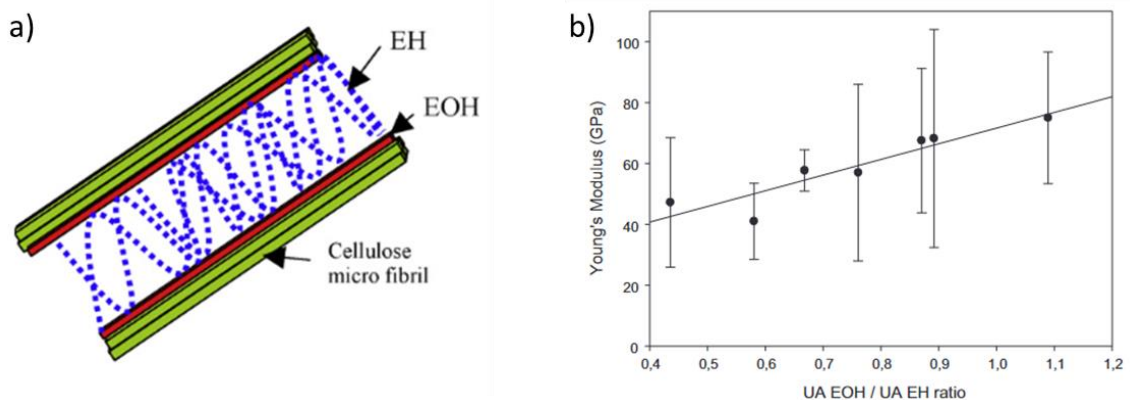


Figure 6: a) Schematic description of the biochemical components present in S2 layer of flax fiber and b) its impact on flax fiber Young's modulus [19]

### I.2.b. Influence of the biopolymer matrix

Intrinsic properties of the used matrix are also directly linked to the final mechanical properties of composites. With the aim of maximizing the mechanical performance of composites by selecting the best matrix with the optimum volume fraction, Badouard et al. [23] explored the use of fully compostable filaments for 3D printing applications, i.e. Flax/PLLA, Flax/PLLA-PBS and Flax/PBAT where flax was introduced in the form of shives or short fibers at 10wt%.

The results showed a longitudinal tensile modulus of 217 MPa and an elongation at break of 364% for PBAT-based 3D-printed specimens (more flexible). These values are clearly in opposition with those of PLA-based specimens having a longitudinal tensile modulus of 3968 MPa and a low elongation at break of 1.2%. The blend PLLA-PBS shows a mechanical performance close to PLA-printed parts with 2786 MPa in tensile modulus and 1.8% in elongation at break. Although associated with short fiber reinforcements, the matrix owns a significant influence on the mechanical properties of 3D-printed composites.

### I.3. Hygroscopic performances

A rising interest of using natural fiber reinforcements in composites relates to their ability to swell or shrink when subjected to a moisture gradient. As previously discussed, the biochemical composition of natural fibers is made of hydrophilic and hydrophobic compounds. The presence of hydrophilic polysaccharides (hemicellulose, pectin) facilitates the water sorption and moisture uptake of the plant. Those phenomena induce a swelling stage and consequently a reorganization of the local arrangement of polymer chains and a modification of dimensional properties. For this reason, the hydrophilic behavior of natural fibers represents a lock for designers targeting performing load bearing applications. However, it is also a source of inner restructuration that can lead to the conception of water-induced smart materials [24].

#### I.3.a. Water sorption

As old as the Earth plants have endured and crossed the ages for millions of years [25]. Main contributors of the fauna survival, all natural beings depend on their functionalities. The understanding of plant/water interactions have been guiding scientists towards the development of high performance water-sensitive materials. Controlling the water sorption and transport within cleverly manufactured structures allows today the control of their deployment. With this in mind, a closer look to the water sorption at fiber and composite scale is proposed.

### I.3.a.i. At the fiber scale

The multicomponent and multilayered architecture of natural fibers charts the inherent complexity of biological systems; helping them to target specific functions (e.g. shape-changing, water supply, stress release). Water sensitivity is emphasized by the physical bonds appearing between water molecules and a substrate [26]. In natural fibers, hydrogen bonds are created between water and polysaccharide macromolecules exhibiting polar groups (hemicellulose and pectin). Cellulosic region is also sensitive to water sorption although the crystallinity index can inhibit/accentuate this effect. For example, the disorganized nature of the amorphous phase promotes both water sorption and diffusion. In the opposite, crystalline regions are denser and exhibit a lower accessibility, i.e. fraction of reactive cellulose interacting with water molecules, that both prevent water uptake (Figure 7) [27].

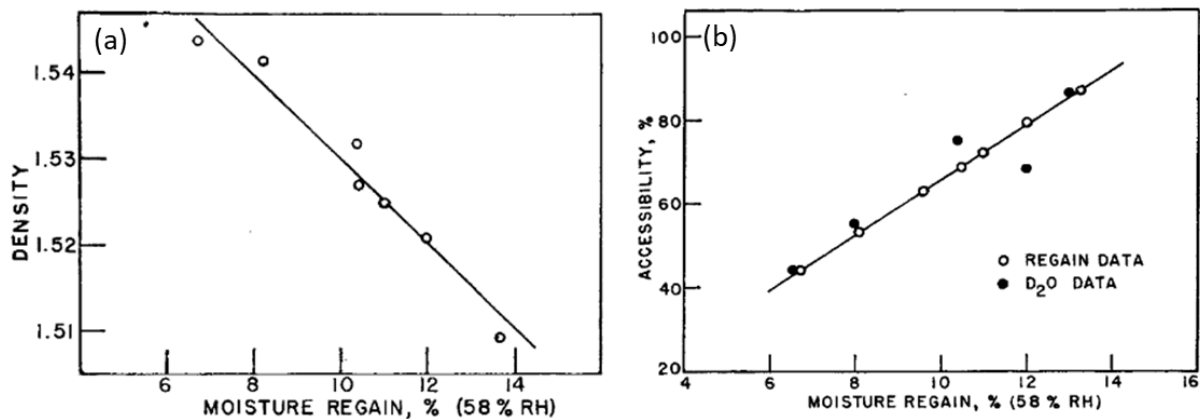


Figure 7: Impact of (a) density and (b) accessibility of cellulose fibers on water regain [27]

Besides, other parameters such as degree of crystallinity of microfibrils or availability of hydroxyl functions also impact the sorption mechanism of natural fibers [27], [28]. From these interactions, two types of water molecules are identified: bound water that create hydrogen bonds with polysaccharide and microfibrils chains and free water incorporating water molecules contained in microcavities (lumen) [28]. Sensitivity of natural fibers to water uptake is estimated by gathering both free and bound water inside their structure.

The isothermal sorption behavior of flax fiber is based on Park's model [29], describing a three-step sorption behavior with 1) water interacting with hydrophilic groups and microcavities at fiber surface, 2) water going-through specific sites inside the fiber and then 3) accumulation of water molecules forming clusters as RH increases.

Regarding technical flax fibers, the sorption mechanism follows a sigmoidal trend corresponding to Park's model as illustrated in Figure 8. However, the desorption slope does not take the same path. This decay is considered as structural damages caused by elementary fiber swelling (tackled in **Section I.3.b.i.**) at the fiber/fiber interface [30] and the removal of hydrophilic polysaccharide present in the middle lamellae.

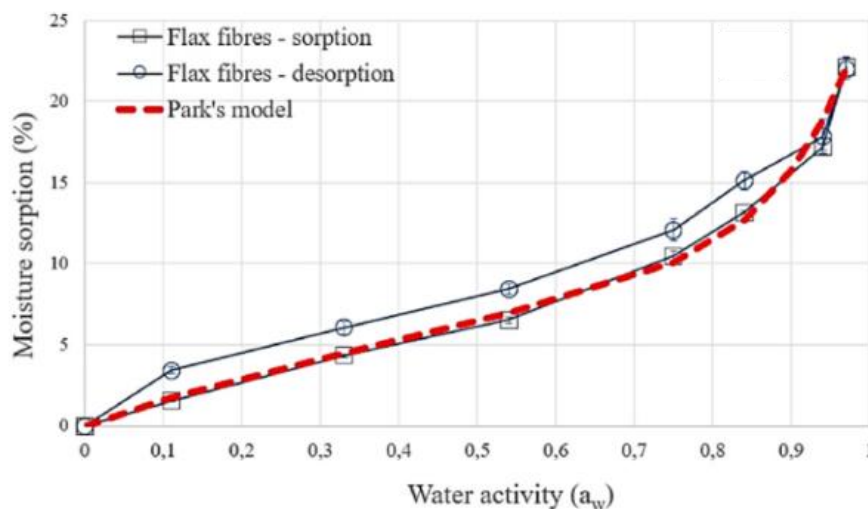


Figure 8: Sorption/Desorption cycle of flax fiber bundles and regression with Park's model [29]

Sorption and desorption are complexly related mechanisms in natural systems. The degree of the hysteresis between sorption and desorption gives information about the water accessibility to fiber cell wall and the most critical range of humidity for fiber integrity.

Figure 9a emphasizes the hysteresis evolution as a function of relative humidity. It appears that higher hysteresis is observed for low RH and thus major structural variations of fibers due to water uptake occur at low RH. Higher and more distinct hysteresis means less stable fiber that are more difficult for water molecules to penetrate. According to Okubayashi et al. [31], the



significant difference between hysteresis of lyocell (46.9%) and cotton (24.7%) fibers, illustrated in Figure 9a, is due to lower crystallinity, larger pore volume and inner surface area of lyocell that promote water wicking. This water wicking can appear at different areas such as fiber external surface, in the amorphous regions, in voids and crystallites (Figure 9b).

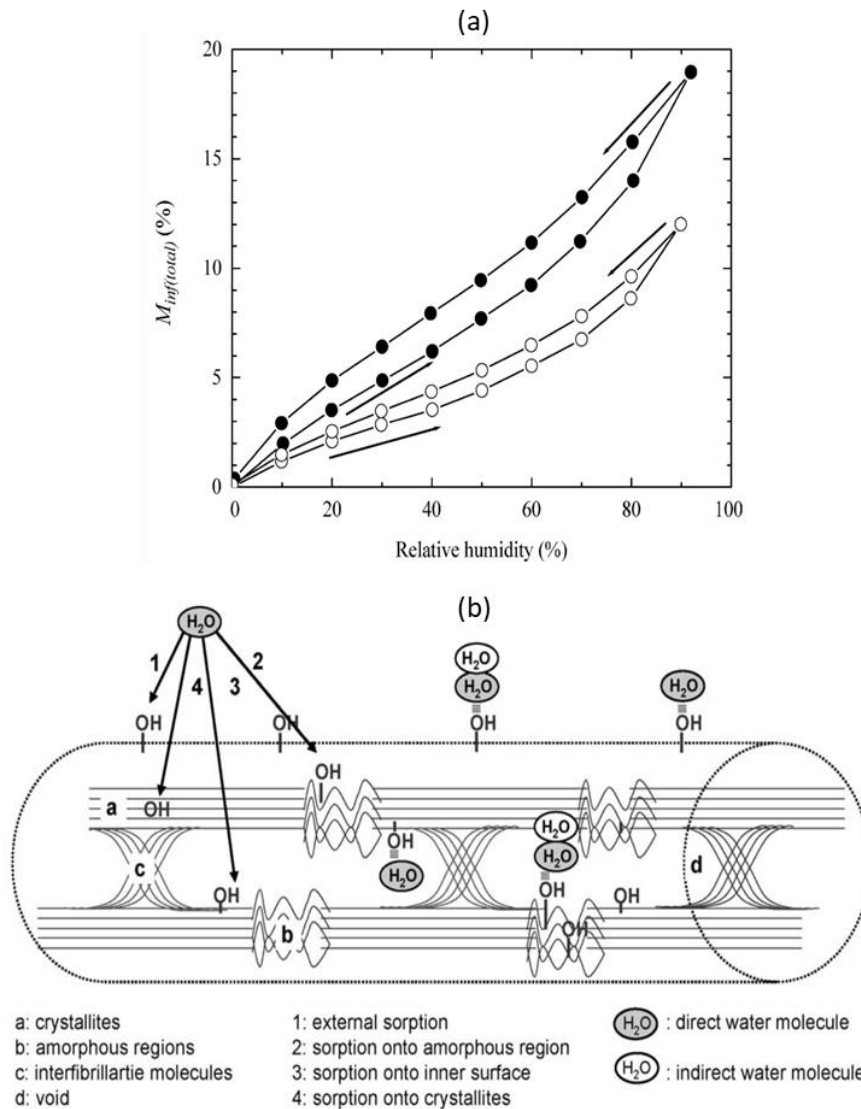


Figure 9: a) Hysteresis between sorption/desorption mechanisms of (●) lyocell and (○) cotton fibers. b) Areas of water sorption inside fiber cell wall [31]

### I.3.a.ii. At the composite scale

Water molecules have three possible options to permeate biocomposites : through fiber cell wall, through macromolecular network and/or at the fiber/matrix interface where microcavities are often observed [32].

Indeed, depending on the inherent fiber content, the sorption behavior of the material is affected (Figure 10). For high fiber volume fraction, water diffusion is promoted since natural fibers are highly hydrophilic and hygroscopic. From this specificity, a percolation mechanism has been proposed by Wang et al. [32] in 2006 inside natural fibers reinforced composites (NFRC). This phenomenon relies on the random distribution of fiber within the X-Y plan. Indeed, fiber clusters represent significant sinks for water sorption and their interconnections promote the water diffusion. However, not all fiber are involved in a continuous path of water. An insulated fiber will have an impact on water sorption, but not at all on conduction properties (Figure 11). For this reason, the apparent diffusion coefficient  $D$  takes into account the « infinite cluster » created by specific fiber loading [33]. The authors concluded that fiber content triggers the diffusion models. For high fiber content ( $V_f > 65\%$ ), accessible paths for water exist; the diffusion is predominant. For low fiber content ( $V_f < 40\%$ ), porous paths are lower and more tortuous which leads to a percolation mechanism.

However, this behavior is modified for continuous fiber reinforced composites where natural reinforcements follow a specific direction. Djellouli et al. [34] estimated the hygroscopic properties of 30% reinforced flax-epoxy composites. The water diffusion in such material is promoted by the flax fibers hydrophilicity and its lumen. They found a diffusion parameter in the longitudinal axis  $D_x$  ( $650\text{mm}^2/\text{s}$ ) 100 times higher than  $D_z$  ( $6\text{mm}^2/\text{s}$ ) and 2 times higher than  $D_y$  ( $290\text{mm}^2/\text{s}$ ). Besides, water sorption is the highest in the x direction (9.14%) since hydrophilic compounds of flax fibers are numerous and react by H-bondings with water molecules. This leads to a stress state at the fiber/matrix interface resulting into micro-cavities and more space for water storage (Figure 12). More details about water-induced water swelling inside composites is written in **Section I.3.b.ii**.

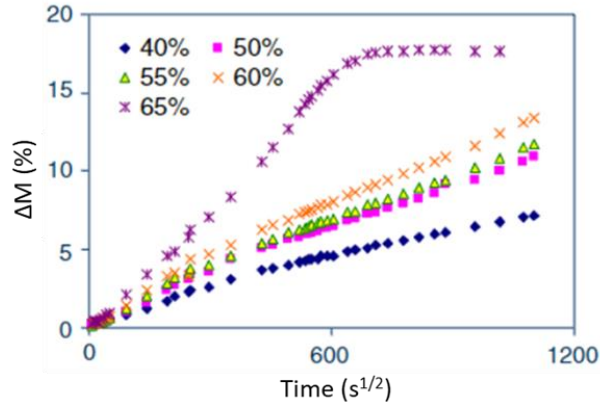


Figure 10: Impact of fiber content on sorption behavior of natural fiber reinforced composites (adapted from [32])

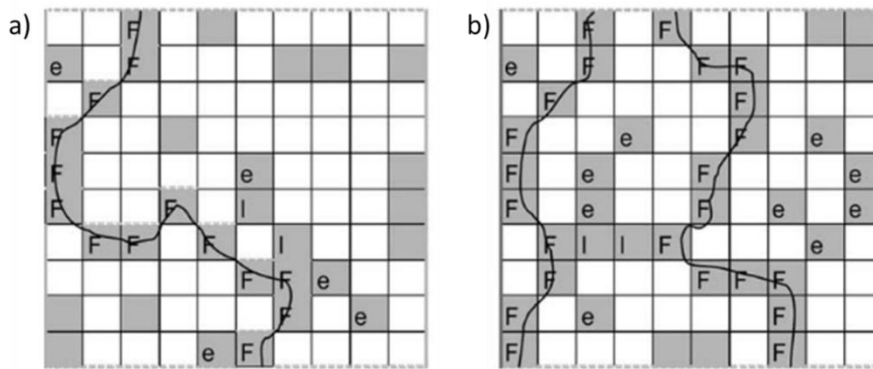


Figure 11: Schematized a) one-path and b) two-path water diffusion inside natural fiber reinforced composites. "F" represents fiber which takes part in the diffusion process, "I" represents the isolated fibers forming loops with diffusion path and "e" represents the end of located clusters [32]

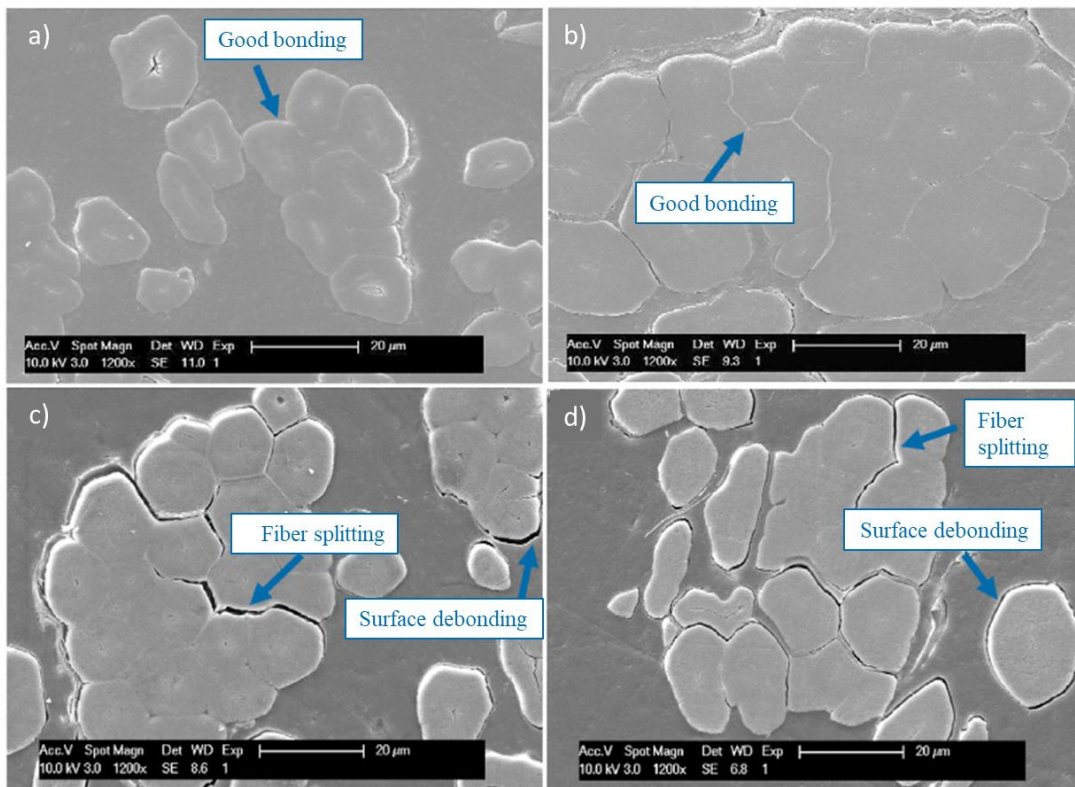


Figure 12: Microcavities induced by flax fiber swelling at the fiber/matrix interface [29]

### I.3.b. Hygroexpansion

The parameters used to describe the hygroscopic behavior of biocomposites are : moisture content ( $\Delta M$ ) and hygroexpansion ( $\epsilon_{\text{hyg}}$ ). Following their evolution along time, the hygroscopic coefficient  $\beta_{\text{hyg}}$  is obtained (i.e. slope of the curve  $\epsilon_{\text{hyd}} = f(\Delta M)$ ). The higher the hygroscopic coefficient, the greater the hygroexpansion of biocomposites at low moisture content. It worth noting here that the term hygroexpansion represents the swelling process of a material subjected to various humidity range, whereas hydroexpansion symbolizes the swelling process of a material in total water immersion [35]. In this section, a deep look is given to the hygroscopicity of natural fibers and natural fiber reinforced biocomposites.

#### *I.3.b.i. At the fiber scale*

The water uptake of natural fibers generate local rearrangement of polysaccharides chains and cellulose fibrils that induces the swelling mechanism. This anisotropic reshaping is controlled by both microfibrillar angle and biochemical composition [36]. Water-induced swelling is an anisotropic feature of natural fibers [37]. It is based on the water molecules that penetrates into the lignocellulosic network. However, water does not penetrate the cellulose fibrils. For this reason, a major parameter regulating fiber swelling is the microfibrillar angle since water will increase the volume occupied by the matrix leading to the spacing of microfibrils. Closely oriented along the fiber axis, the spatial shift of microfibrils is accentuated in the radial direction while longitudinal swelling is negligible.

For example, factor triggering the hygroexpansion of paper have been examined [38]. Among the constitutive elements constituting the wood cell wall showed in Figure 13b, hemicellulose, lignin and elementary cellulose fibrils do not have the same accessibility for water molecules. Hemicellulose chains exhibit the highest contribution considering their higher sensitivity to water (and so water sorption) while lignin chains reduce the water retention capacity and thus

amplitude of hygroexpansion ([35]). For instance, Pejic et al. [39] observed a 20% increase in water retention of modified hemp fiber whose lignin content is equal to 3% compared to unmodified hemp fiber (lignin content = 6%). An opposite trend is reported by decreasing the hemicellulose content from 10.7 % (unmodified hemp fiber) to 3.6% (modified hemp fiber) which generates a 10% decrease in water retention. Then, the microfibrillar angle also impacts the mechanisms. Indeed, a higher MFA tends to increase the longitudinal swelling but reduces the transverse one [40]. Therefore, MFA-value influences the contribution of polysaccharide swelling on the entire hygroexpansion process [41].

At the fiber scale, wood cell wall is composed of three different layers made of crystalline cellulose and hydrophilic matrix (amorphous cellulose, hemicellulose and lignin) captured in Figure 13a. Using X-ray nano-tomography, Rafsanjani et al. [42] evaluated the swelling ability of elementary layers containing S1, S2 and middle lamella. Volumetric strains induced by water has shown a total expansion of S2-layer of  $\epsilon_v=0.25$  that is decreased by adding a surrounding S1-layer ( $\epsilon_v=0.17$ ). The presence of S1 layer limits the radial swelling strains due to the high MFA compared to S2. In conclusion, the swelling behavior of plant cell wall is due to the hydrophilic effect of amorphous matrices (hemicellulose and pectin). The resulting interactions with water molecules induces a reorganization of tissues pictured by the swelling behavior.

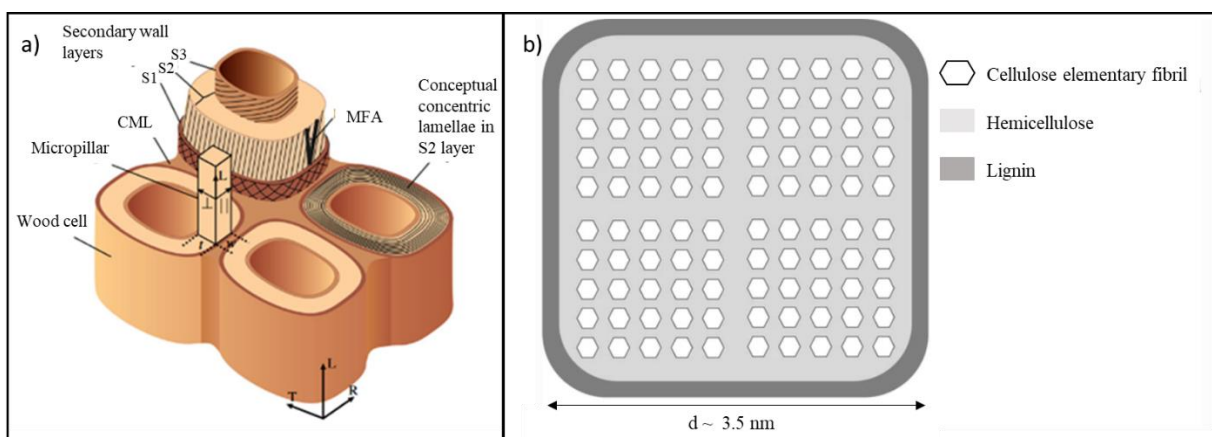


Figure 13: a) Inner scheme of wood cell wall (adapted from [42]). b) Microfibril section made of arranged cellulose elementary fibrils and hemicellulose delimited by lignin layer (adapted from [38]).

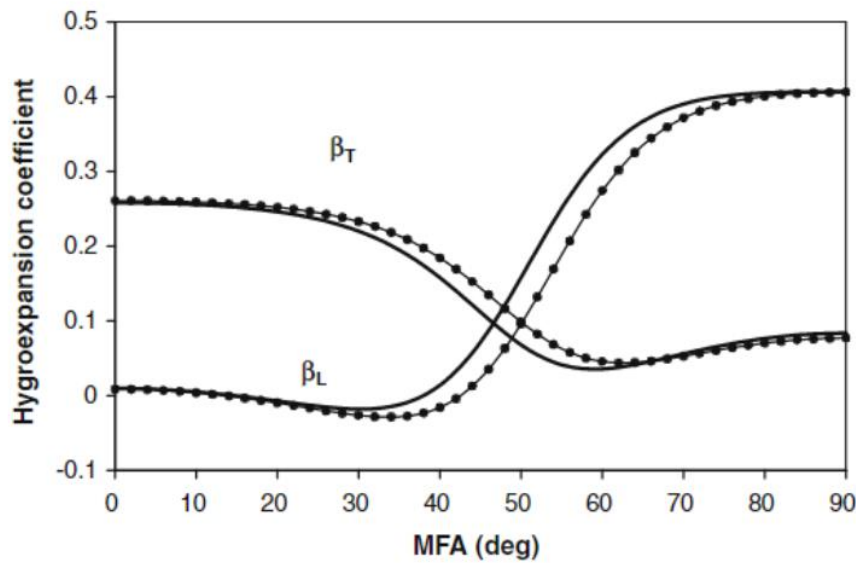


Figure 14: Hygroscopic coefficient as a function of MFA in the S2 layer of wood fiber [43].

S2 layer is a fundamental stakeholder of fiber's hygroscopicity [43]. Since it represents the organized layer where microfibrils are specifically oriented, the MFA dictates cell wall swelling. As illustrated in Figure 14, changing the MFA in the S2 layer will affect the hygroexpansion coefficient in transverse and longitudinal direction.

Regarding macromolecular arrangement, amorphous/crystalline cellulose ratio has also an impact on hygroexpansion process as long as MFA exceeds 20° [44]. Besides, a distinction can be done on the importance of lignin and hemicellulose chains on longitudinal and transverse expansion. The high number of hydroxyl groups in hemicellulose chains is basically used for increasing mechanical performance of lignin-carbohydrate network surrounding fibrils and promoting its association with hemicellulose and lignin matrices [18]. Since water interacts with OH<sup>-</sup> groups, this function is not realized anymore and mechanical properties drop down. Importance of interlayer is also tackled and a strong connection between considered components (S1-part and S2-part) and anisotropic swelling is observed.

Same study has been conducted on other natural fibers such as flax. Figure 15 displays the hygroscopic behavior of elementary flax fiber. Regarding the linear part of the curve, a

regression can be done to evaluate the slope, that represents the hygroscopic coefficient (previously defined) of elementary flax fiber, here equal to 1.14 [45].

At the bundle scale, the expansion mechanism is a cumulative effect of constitutive elementary fibers (Figure 16). The radial expansion occurs in the fiber cell wall, i.e. where cellulosic fibrils are located, and in the middle lamellae formed of hydrophilic lignocellulosic macromolecules. Bound water interacts within middle lamellae and cell wall; increasing transverse and out-of-plane dimension and reducing the lumen section. Free water does not intervene in the swelling mechanism. Taking back the example of flax fiber, the hygroscopic coefficient of flax fiber bundle reaches 1.06 [46]. This is slightly lower than the hygroscopic coefficient of elementary flax fiber ( $\beta_{\text{hyg}} = 1.14$  [45]) because of the additional free water at the fiber/fiber interface.

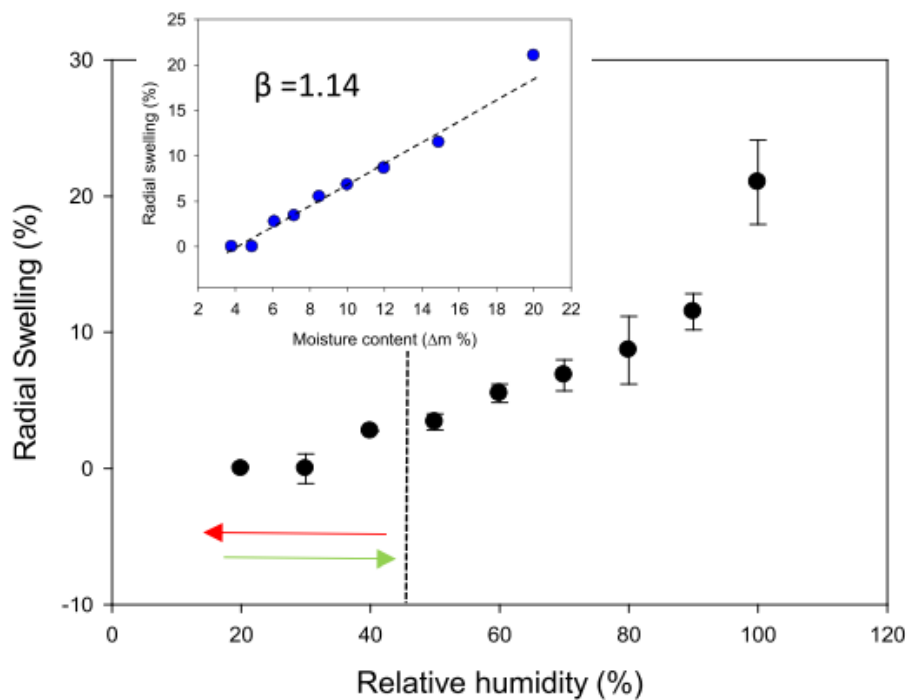


Figure 15: Hygroscopic behavior of flax fiber bundles. Inset represents the linear regression that allows to evaluate the hygroscopic coefficient [45]

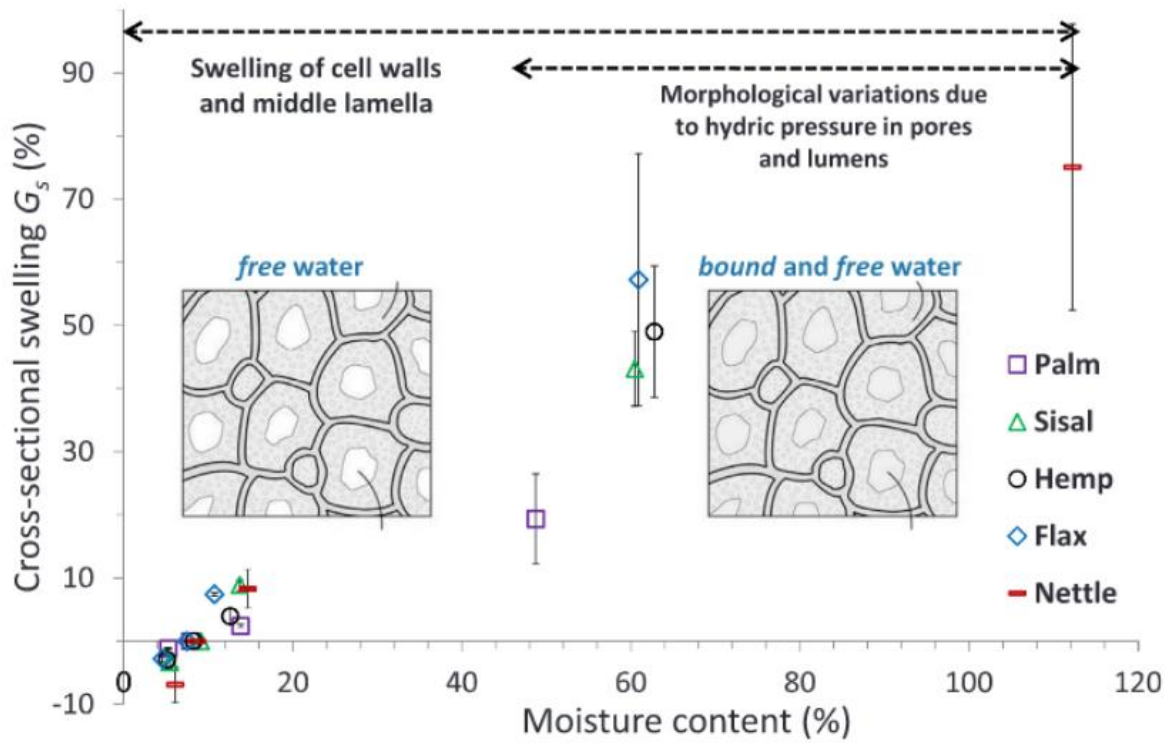


Figure 16: Swelling mechanism of wood bundle upon moisture gradient [35].

Therefore biochemical composition and morphological features give to natural fiber a personal sensitivity and hygroscopicity governed by their functionality [35]. Table 1 exhibits the various hygroscopic coefficients measured for five different fiber bundles (Palm, Sisal, Hemp, Flax and Nettle) related to their inherent properties.

Table 1: Connection between radial hygroscopic coefficient ( $\beta_{r,hygro}$ ), biochemical composition and MFA of five natural fiber bundles (adapted from [35]).

Plant species	$B_{r,hygro}$	Cellulose (%)	Hemicelluloses (%)	Others (%)	Lignin (%)	MFA (°C)
Palm	0.42	45.1 ± 3.4	27.7 ± 4.9	11	16.2 ± 0.3	44
Sisal	1.49	60.1 ± 1.2	23.3 ± 2.1	9	9.3 ± 0.1	20
Hemp	0.92	68.8 ± 1.3	9.8 ± 1.8	17	4.7 ± 0.3	9
Flax	1.67	64.9 ± 2.9	9.9 ± 3.9	21	3.7 ± 0.3	8
Nettle	1.70	51.7 ± 0.9	9.9 ± 1.2	34	4.6 ± 0.2	8

### I.3.b.ii. At the composite scale

Swelling of natural reinforcements induced by water sorption and ingress between the plant tissues causes structural variations of the laminates reflected by an in-plane and out-of-plane



expansions. Responsible for the anisotropic properties of the material, plant fiber is the main component to configure the hygroscopic expansion (rate and curvature) to composites.

When surrounded by PLA-matrix, wood fibers exhibit a swelling capacity twice lower than for unconstrained fibers, downgrading from 0.2 to 0.4-0.5  $\epsilon/\text{RH}$  (Figure 17a) [47], that shows the swelling restriction by the matrix being less-sensitive and less-swellable to water uptake.

Variations in the cross-sectional shapes denotes this impact, as illustrated in Figure 17b.

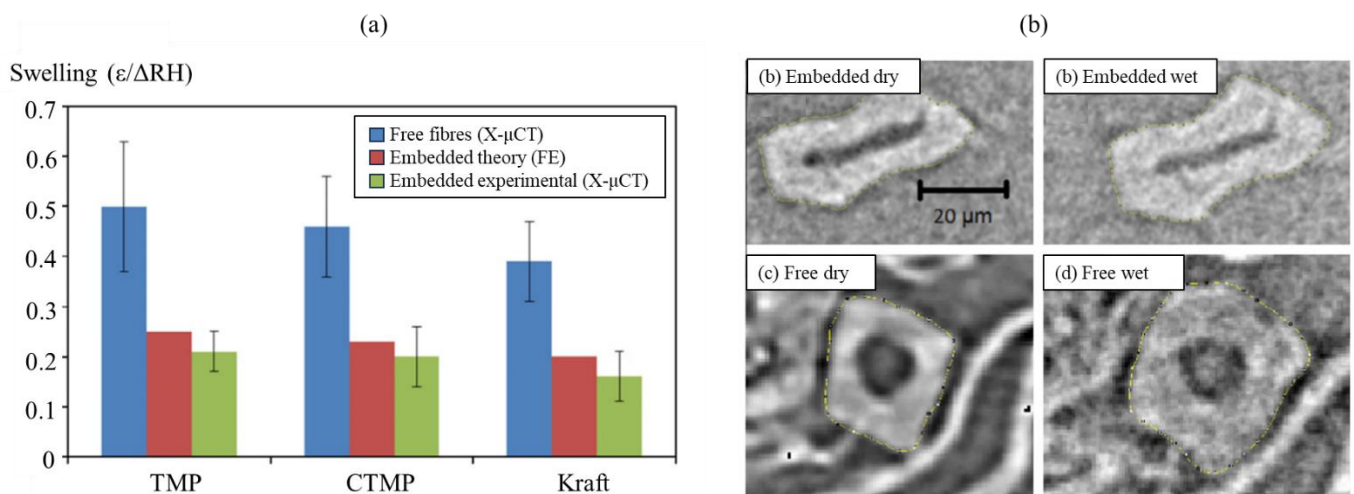


Figure 17: a) Swelling amplitude of free and embedded wood fibres for three extraction techniques : thermomechanical pulping (TMP), chemithermomechanical pulping (CTMP) and kraft pulping (Kraft). b) Qualitative study of structural variations between embedded (a-b) and free (c-d) wood fibres at dry and wet state (adapted from [47]).

Similar results are obtained with technical fibers. For example, Le Duigou et al. [45] studied the relation between fiber hygroscopic expansion and residual stress of flax/PP+MAPP composites. When surrounded by PP+MAPP matrix, the flax fiber swelling is constrained which generates internal stresses in the interfacial area (Figure 18) where microcavities appear (Figure 12). The maximum radial swelling of 21% for flax/PP+MAPP biocomposites was reached at 98% RH. The residual stress evaluated was defined as the sum of the radial stress and thermal contribution generated during process (compression molding) and hygroscopic stress generated during storage. Consequently, the higher the relative humidity during storage, the greater the swelling of the flax fiber and the higher the residual stress at the fiber/matrix interface.

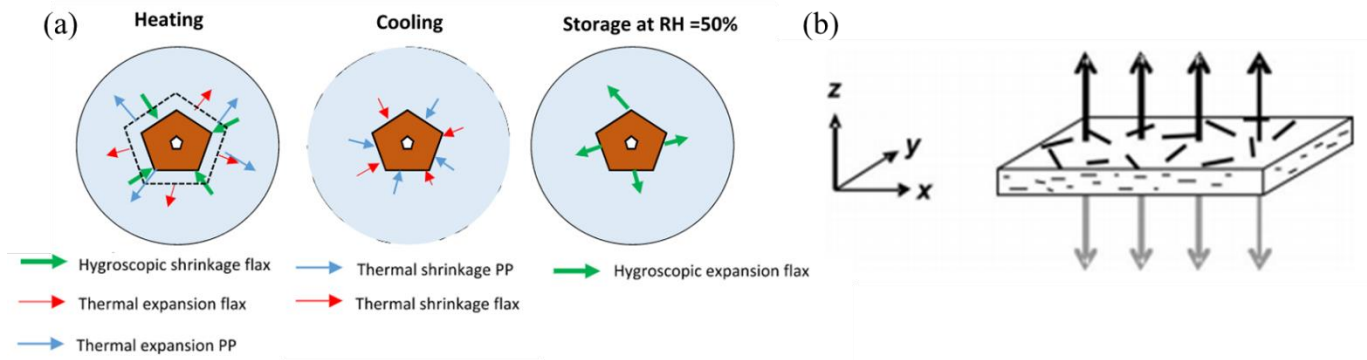


Figure 18: a) Schematic residual stresses generated by technical flax fiber expansion upon moisture uptake [45]. b) Out-of-plane hygroexpansion of beam-like biocomposite reinforced with short natural fibers [48].

Abida et al. [46] also tried to get knowledge about the swelling mechanism of flax fiber within flax/epoxy composites. The measured radial swelling coefficient of flax yarn was of 1.06 while the transverse and out-of-plane hygroscopic coefficients of composites was up to 0.13 and 0.85. These low expansions in the weft and out-of-plane directions can be explained by the low hygroscopic coefficient of the epoxy matrix preventing the maximum swelling of flax yarns in both directions. Almgren et al. [48] conducted researches on the impact of the matrix choice (PP and PLA) on the hygroexpansion of randomly oriented wood-fiber reinforced composites. According to their results, using a hydrophobic matrix PP represents a lock for the out-of-plane hygroexpansion of wood fibers. Since they worked with randomly oriented wood fiber-reinforced composites, transverse and axial hygroexpansion could not be studied. Moreover, they evaluated the role of chemical treatment on hygroexpansion process. Introduction of additive (BTCA) increases the cross-linking state of the matrix and thus lowers the hygroexpansion of wood fibers [49]. A transverse coefficient of hygroexpansion equal to 0.28 was found for unmodified dispersed short wood fiber-reinforced molded composites.

### I.3.c. Hygroelastic properties

One highly targeted aspect of biocomposites is the impact of water sensitivity induced by natural fibers on their mechanical properties. While the insensitivity of synthetic fiber, i.e. carbon or glass fiber, to water absorption means that they retain good tensile properties [50],

[51], composites reinforced with natural fibers show a notable reduction in their mechanical performance. In load-bearing applications, it actually represents a lock to their development.

At the composite scale, the drop of hygroelastic properties can be due to several factors as described for seawater ageing of flax/PLLA composites (Figure 19a) [52]. Firstly, water uptake brings chain scissions of the PLLA matrix (representing the hydrolysis mechanism) that affects the mechanical behavior of biocomposite. Secondly, the higher anisotropic swelling of flax fibers compared to PLLA-matrix creates stress at the fiber/matrix interface. Moreover, water going through flax cell walls reacts with hydrophilic groups of hemicellulose and pectin chains lowering the stress transfer ability of the material. In this sense, a systematic decrease of the tensile modulus in hemp/polyester composites were reported by Dhakal et al. [53] between dry to wet specimens. This loss of performance was accentuated by the fiber content, going from 11%-reduction when  $V_f = 10\%$  to 46%-reduction when  $V_f = 26\%$ . Besides, an interesting difference between fracture mechanisms of dry and wet flax-reinforced biocomposites during a flexural test is revealed. While the dry biocomposite exhibits a clear brittle fracture, the wet one presents a lot of secondary cracks which are induced by the water diffusion at the interface between fibers and matrix causing debonding and delamination. Interfacial properties of biocomposites are also significantly reduced in humid environments ([54], [55]) For instance, Réquillé et al. [56] attested a 13% reduction of tangent modulus for hemp/epoxy biocomposites (Figure 19b). Finally, the kinetic and amplitude of mechanical loss as a function of water sorption is dictated by the water accessibility to fiber cell wall. A higher number of fiber cross sections along the length will improve the hydrophilicity of the surface leading to a better water percolation [57].

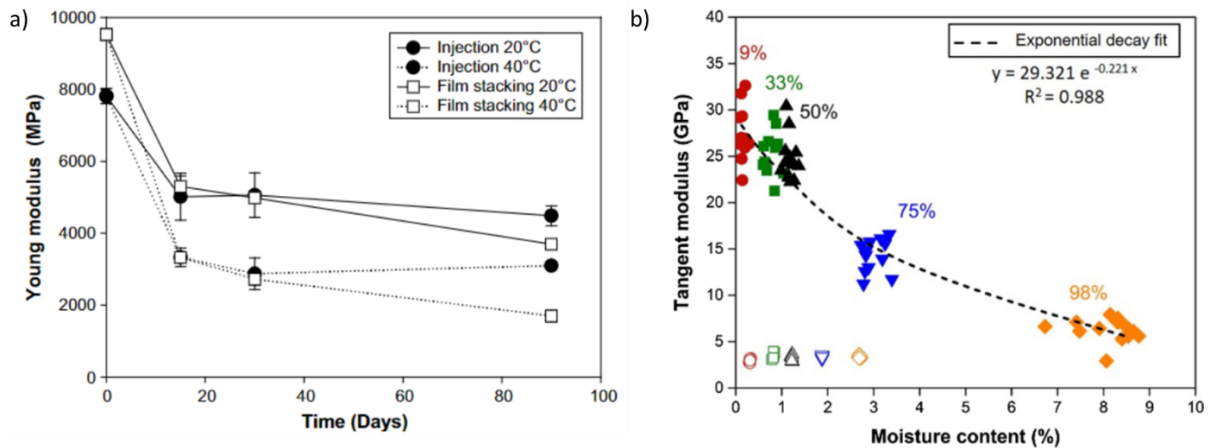


Figure 19: a) Evolution of Young modulus of flax/PLLA biocomposites as a function of immersion time [52]. b) Evolution of tangent modulus of hemp/epoxy biocomposites as a function of moisture content [55].

At the fiber scale, the evolution of mechanical properties in humid environments relies once more on the proportion and accessibility of hydrophilic lignocellulosic chains within its cell wall. However, a minimum water content is indispensable in flax cell wall to ensure cohesion of cellulose microfibrils and rearrangement of lignocellulosic chains during load transfer [58]. However, in contrast with synthetic fibers which do not exhibit a significant sensitivity to water uptake, natural fibers appear as a perfect reinforcement for the development of water-induced shape-changing biocomposites, referring to Hygromorph BioComposites (HBC). This attracting research topic is increasingly quoted in the scientific literature ([24], [40], [59]) since its development could allow the creation of smart performance tools in medical, building, load-bearing, artistic and environmental fields.

## I.4. HBC : a new range of shape-changing materials

### I.4.a. What triggers the actuation of HBC ?

Since the natural fibers on mechanical and hygroscopic properties of biocomposites has been unveiled in previous sections, time has come to finely describe HBC and how it is activated. HBCs represent a new range of moisture-induced shape-changing materials. The actuation of HBC arises from a biomimetic approach in which the differential expansion between two

asymmetrical layers generating a moisture-induced reconfiguration of the material reproduces biological self-deploying process.

Asymmetric structures are often reported as bilayers. This mechanism has been defined by Timoshenko for thermal bilayers [60] but can be applied to hygromorph materials ([61]–[63]).

The given equation allows for evaluating the response curvature of the HBC as function of hygroelastic properties and structural features :

$$\Delta K = \frac{\varepsilon_{hyg} * f(m,n)}{h} \quad (\text{Equation 1})$$

$$f(m,n) = \frac{6(1+m)^2}{3(1+m)^2 + (1+mn)(m^2 + \frac{1}{mn})} \quad (\text{Equation 2})$$

With hygroexpansion strains ( $\varepsilon_{hyg}$ ) defined by the multiplication of the hygroscopic coefficient  $\Delta\beta$  and the moisture content after saturation  $\Delta M$  of the material. The structural parameters affecting the bilayer curvature are symbolized by  $h$ ,  $m$  and  $n$ , where  $h$  represents the sample thickness,  $m = \frac{t_p}{t_a}$  the thickness ratio and  $n = \frac{E_p}{E_a}$  the stiffness ratio between passive and active layers respectively (Figure 20).

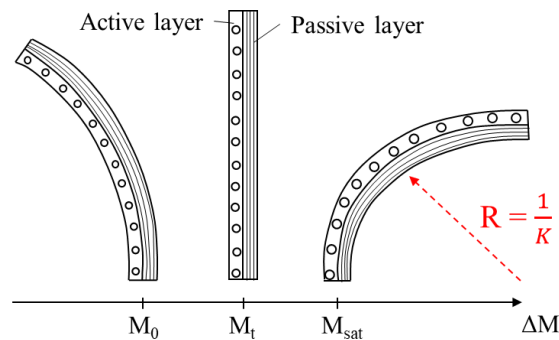


Figure 20: Schematic actuation of bilayer structure.

The key parameter governing the actuation mechanism of Hygromorph BioComposites is the hygroexpansion of plant fibers. Increasing the natural fiber content within HBC promotes both maximal curvature, i.e. responsiveness (Figure 21a), and actuation speed, i.e. reactivity (Figure 21b) [64]. Wide range of natural fibers, e.g. flax, jute, kenaf and coir, may act as potential actuators within Hygromorph BioComposites. Depending on the selected natural

reinforcement, significant differences in actuation properties (reactivity and responsiveness) are identified (Table 2) [40]. This is linked to the specific morphology, microstructure and biochemical composition of each natural reinforcement but also their intrinsic swelling properties (Figure 22 and Table 1). For example, anisotropic ratio and lignin content are the main criteria to identify a plant fiber usable for HBC design with durable actuation over wetting/drying cycles. As a reminder (Section I.3.a.i), flax and jute fiber are mainly composed of hydrophilic components, i.e. between 10 and 20% of hemicellulose and pectin part, and a low content of hydrophobic lignin chains, i.e. from 2 to 3% for flax fiber and from 12 to 13% for jute fibers [40]. This specific composition promotes the water uptake and makes jute and flax fibers more interesting reinforcements for HBC, reaching a final curvature of  $0.095 \text{ mm}^{-1}$  for Flax/MAPP and  $0.094 \text{ mm}^{-1}$  for Jute/MAPP composites. In comparison with a more hydrophobic plants such as coir (lignin content = 40-45 %), the curvature potential of coir/MAPP is outmached ( $\Delta\kappa = 0.027 \text{ mm}^{-1}$ ) [40]. However, the lignin content plays an important role in the sustainability and life span of biocomposites since they prevent the sugar release during sorption/desorption cycles, thus slowing down the biodegradation process by hydrolysis. Then, the lumen size (Figure 22) and MFA are both primordial parameters considering the microstructure of the plant. Low MFA enhances the bending deployment by increasing the curvature response [40]. Reaching the greatest curvature is based on a thorough optimization of the material selection but also on the mesostructure/dimension of passive and active layers (Figure 20).

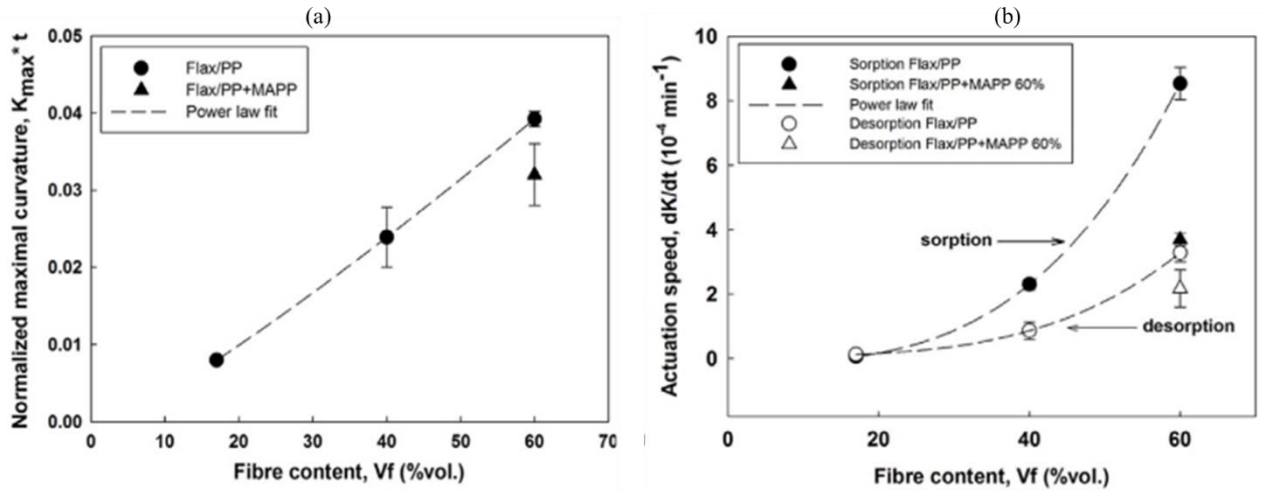


Figure 21: Evolution of a) normalized maximal curvature and b) actuation speed of FF/PP composites as a function of fiber content [64]

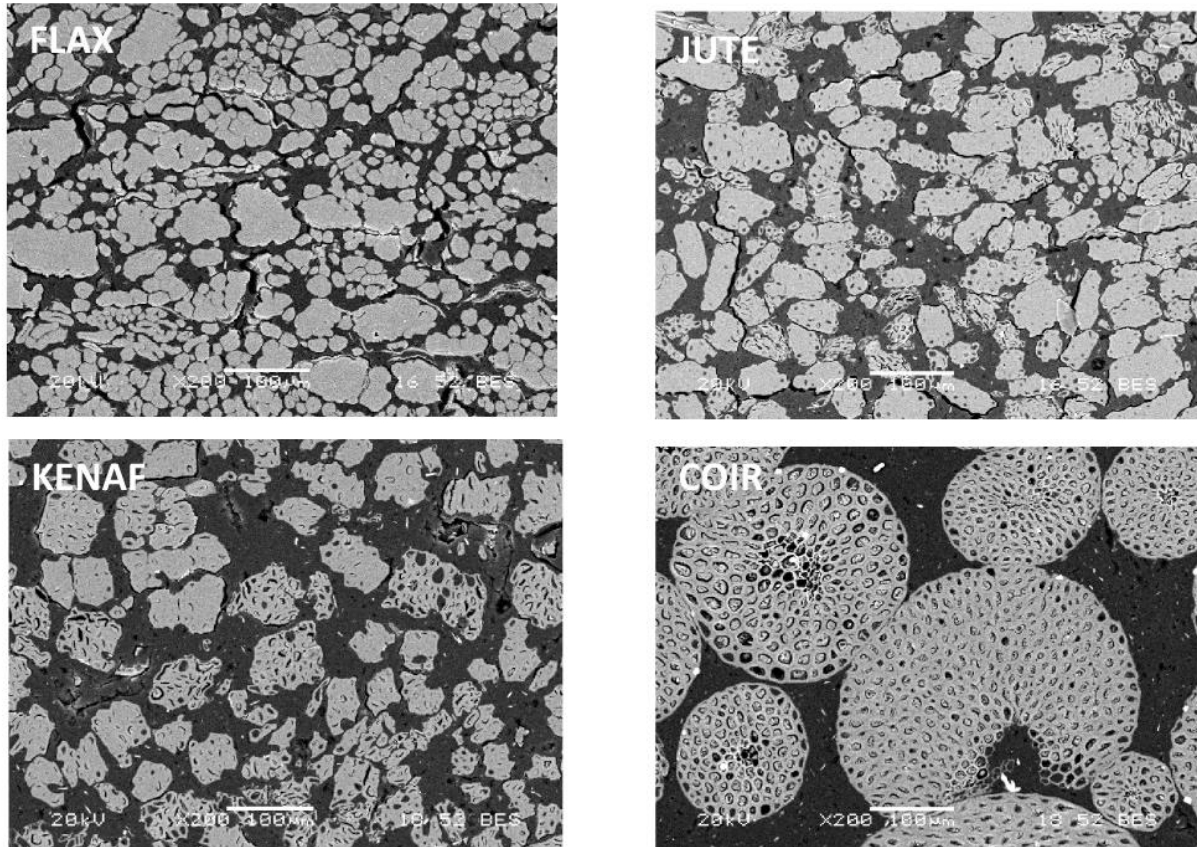


Figure 22: Microstructural differences between several natural fibers [40]. Scale bar = 100 μm.

Table 2: Hygroelastic and shape-changing potential of HBC reinforced with various natural fibers (adapted from [40])

Materials	$\Delta\beta$ ( $\epsilon/\Delta m$ )	$\epsilon_{hygro}$ (%)	$n$ (wet state)	$K$ (mm <sup>-1</sup> )	$K/\text{thickness}$
Flax/MAPP	0.107	3.55	10.9	0.095	0.044
Jute/MAPP	0.11	3.70	9.95	0.094	0.043
Kenaf/MAPP	0.07	2.80	9.1	0.088	0.040
Coir/MAPP	0.03	1.10	2.1	0.027	0.013

In this perspective, Le Duigou et al. [24] have quantified the bending actuation of flax/PP bilayer biocomposites by studying the effect of the thickness ratio between the passive and active layers on the amplitude of response. As displayed in Figure 23, a thickness ratio of 0.5 allows for exacerbating the amplitude of curvature at 0.052 mm<sup>-1</sup>, which is 30% and 40% higher than when thickness ratio is of 0.05 or 1, respectively. Bending actuation can be predicted by controlling hygroelastic properties and layer thickness ratio according to Timoshenko's equation (Equation 1) [60]. Differential swelling between passive and active layers is the source of biocomposite actuation but can also promote fiber/matrix debonding.

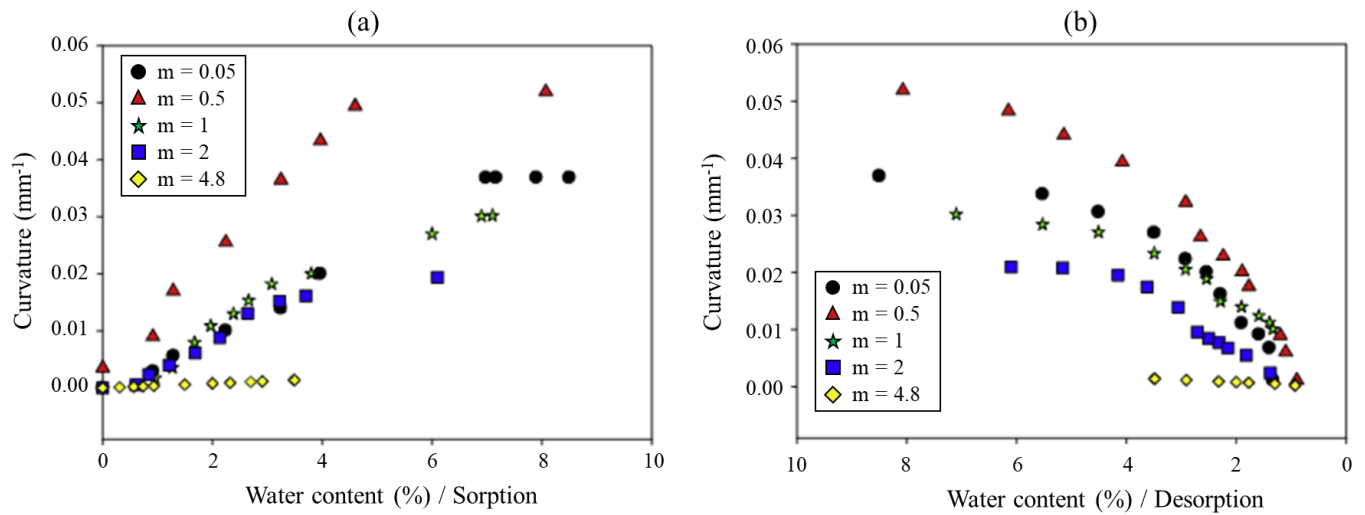


Figure 23: Curvature evolution of Flax/PP HBC during (a) sorption and (b) desorption cycles (adapted from [24]).

Each of these influencing factors must be considered in the material selection and structural optimization to elaborate complex shape-changing biocomposites designed to cover specific applications. However, some limitations remain unsolved such as the role of matrix and structural features (distribution of rigidity between layers, porosity, specimen dimension) on actuation potential and are tackled in **Section I.5**.

#### I.4.b. Water ageing of HBC

Shape-changing has an impact on structural features and matter cohesion inside bilayers. Internal stresses are developed through the smart structure at the fiber/matrix interface where



unsensitive matrix constraints the fiber swelling. Consequently, as observed by Popineau et al. [65] on flax/PP-MAPP made by Vacuum Bar Only Moulding and and Péron et al. [66] on flax/MAPP composites made by hot pressing process, both submitted to numerous sorption/desorption cycles, micro-cracks in the matrix are generated which influence both sorption and mechanical properties of biocomposites.

Figure 24 displays the evolution of longitudinal and transverse moduli of flax/PP-MAPP biocomposites ( $V_f = 42\%$ ) overcoming several hygrothermal cycles with different ranges of humidity at saturation. From 11% to 50% RH, the decrease of longitudinal and transverse moduli is of 9% and 26%, respectively. Furthermore, from 11% to 99% RH, the drop is exacerbated, reaching 30% and 50% respectively. The hornification mechanism, i.e. the restructuration of pores and reorganization of H-bonds linking polysaccharides when removing water from the fiber, may play a significant role in the loss in dry mass along cycles and the modification of mechanical properties [67]. Besides, permanent out of plane swelling is reaching 3% in saturated conditions and 1% for transient one-week cycle conditions.

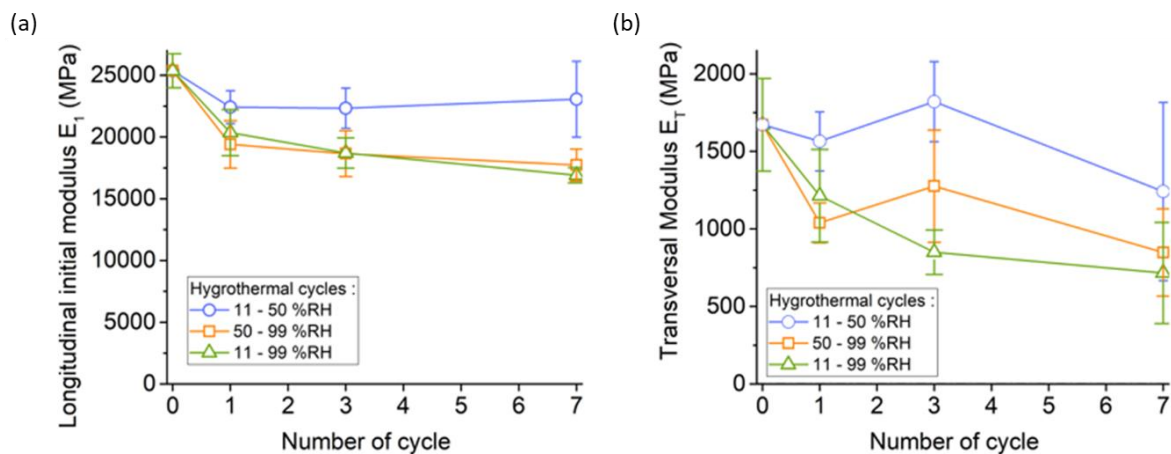


Figure 24: Evolution of (a) longitudinal and (b) transverse modulus of flax/PP-MAPP biocomposites under several sorption/desorption cycles at various range of humidity [65]

With regards to internal stress, increasing the moisture content inside the structure seems to decrease its impact owing to the relaxation effect resulting from plasticization of the matrix.

The stress state of bilayers depends on the cycling conditions. When stored at 50% RH until

saturation and placed at 99% RH until saturation, the fiber swelling has a sufficient time interval to be completed. The applied pressure on surrounding matrix is maximal at the fiber/matrix interface, even if relaxation of matrix allows for a decrease of internal stresses. Placing specimens back to 50% RH until saturation, fibers shrink at the maximal point generating cracks inside the structure (Figure 25a). Moreover, the hygroscopic stress evaluated in transitional regime gives insights on the stress state evolution over moisture content (Figure 25b). For this reason, both amplitude of humidity range and duration of exposure to specific relative humidity are of paramount importance in the climatic ageing of biocomposites.

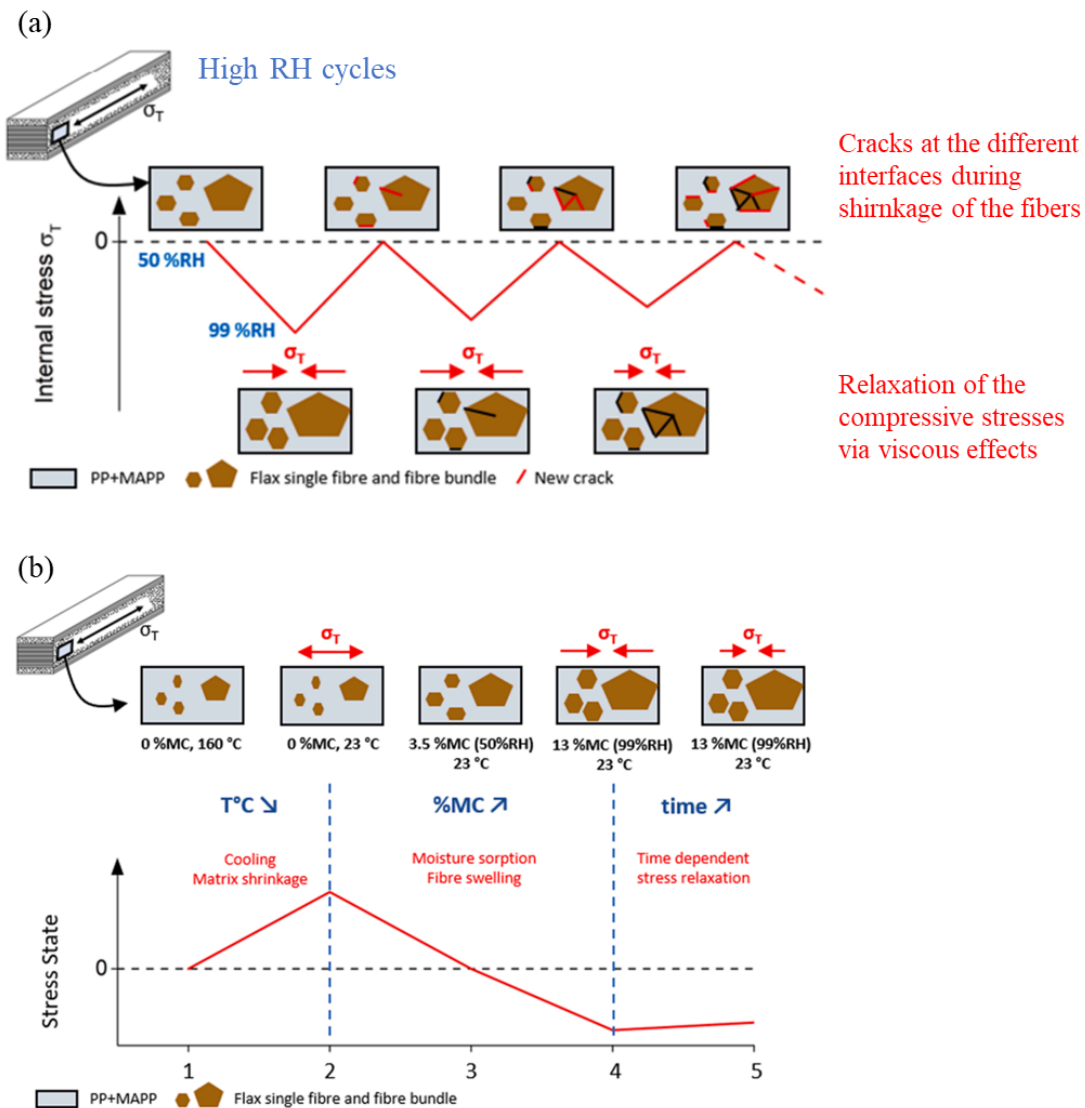


Figure 25: Evolution of internal stresses inside flax/MAPP bilayers over various desorption/sorption cycles a) at saturation and b) in transient conditions [65].

#### I.4.c. Range of applications and development

Hygromorph Biocomposites are more and more designed to join performing and environmental standards. In load-bearing applications, it is possible to find them in the deployment of new innovative systems such as autonomous houses (Figure 26a) [68]. Thanks to hygroscopic material properties, bilayer-made windows can adapt their shape to environmental changes to promote brightness in the house in sunny weather and closure of the windows in rainy days. These characteristics of natural fiber reinforced bilayers are also developed for solar tracking purposes to optimize solar energy recovery [69].

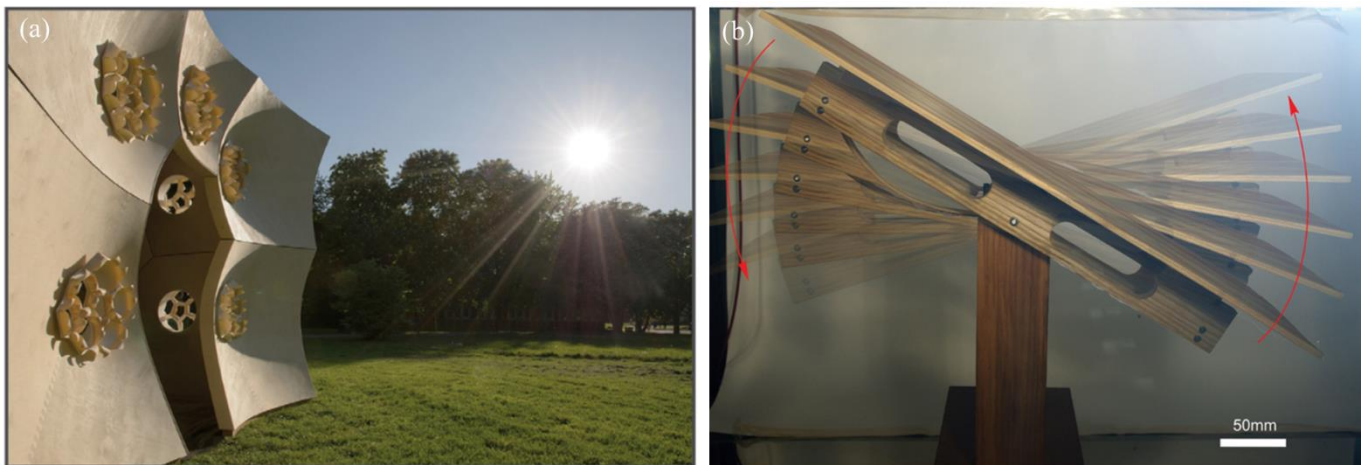


Figure 26: (a) Meteorosensitive house made of moisture-induced morphing windows as innovative prototypes for environmentally-friendly and energy-saving applications [68]. (b) Moisture-sensitive solar tracker prototype. [69].

Still on load-bearing structures, flax/PP HBC have emphasized a promising blocking force, i.e. generated force during water uptake, of 0.45 N assessed by increasing fiber content and improving interfacial strength. Even if this value is very low compared to blocking force of biological model, e.g. from 2.2 to 3.6 N for a pine cone scale, it opens an interesting door to the creation of autonomous water-driven force-generator devices [70].

## I.5. Current locks regarding the actuation of HBC

Despite being an innovative and ecological materials, the development of Hygromorph BioComposites has encountered a number of challenges. This encourages scientists in their quest for knowledge about more suitable structures and associations of materials to broaden the field of application of HBC.

### I.5.a. Limited reactivity

Hygromorph BioComposites are emphasized by the swelling behavior of natural fibers that dictates the motion. However, the fiber swelling outmatches composites swelling owing to the constraining effect of biopolymer matrices ([29], [35], [56]). Indeed, while natural fibers are water-sensitive compounds, biopolymer matrix is mainly insensitive to interactions with water. For this reason, the expansion mismatch between fibers and matrix reduces the actuation potential of HBC. There are three solutions to this problem : (a) increasing the fiber volume fraction inside the material and/or (b) optimized the selection of biopolymer matrix to liberate the morphing potential of natural reinforcements and/or (c) designing the structure to accelerate water sorption and actuation.

Tackling the first solution, fiber content exacerbates actuation performances as previously illustrated in Figure 21. However, increasing fiber volume fraction is not so trivial since an optimal proportion of fibers is important to maintain both the mechanical properties and the integrity of the material (Figure 27). Besides, it is also limited by the feasibility of manufacturing processes and the resulting quality of the specimen [71]. Consequently, deeper insights must be obtained on the matrix selection to unshackle as much as possible the fiber swelling. Then, architectural design promoted by novel manufacturing techniques also represents an important aspect to consider.

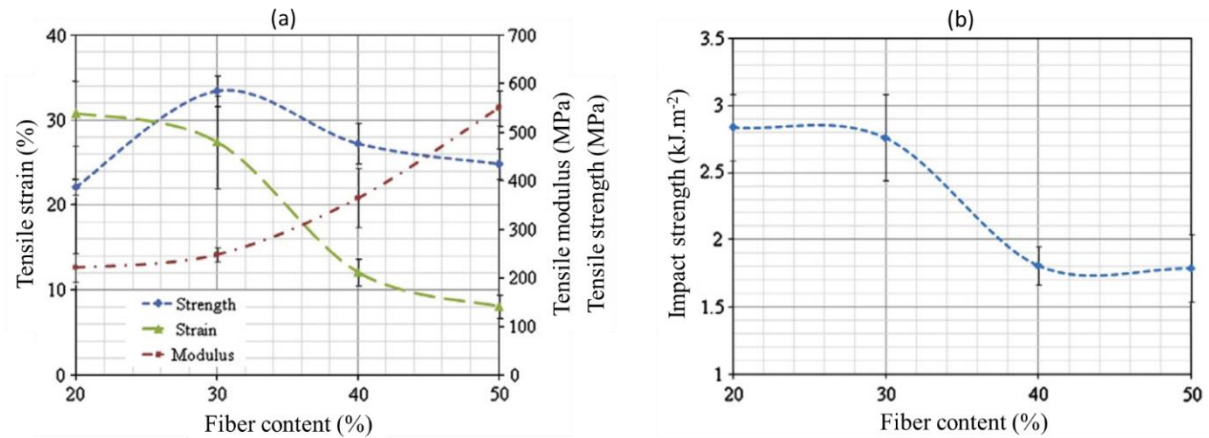


Figure 27: Impact of fiber content on (a) tensile modulus, stress and strain and (b) impact strength of kenaf/TPU composites (adapted from [72]).

### I.5.b. Limited shape-changing pattern and responsiveness

In the development of HBC, the bending potential has figured as the most investigated shape-changing pattern in the scientific society since it allows for quantifying the morphing potential of HBC based on Timoshenko's theory (Equation 1) [60].

However, many structural features might widen the range of deployment of these smart structures, e.g. layers rigidity, thickness ratio or matter distribution. Although conventional manufacturing processes (e.g. injection molding, compression molding, vacuum infusion) have represented a bottleneck in the designability of complex architectures and control of these architectural features, 3D-printing, i.e. an innovative technique for polymer, composite and metal fabrication, is today proposing a more extended approach of material distribution and control of the targeted structure.

## II. The revolutionary role of additive manufacturing in the design of HBC

### II.1. Fused Filament Fabrication (FFF)

Additive manufacturing has recently been getting attention from industrials, scientists and designers. Based on a layer-by-layer deposition, this manufacturing process aims to design complex and exclusive parts to meet structural and architectural expectations. There are several additive manufacturing techniques that can be of interest depending on the structure and dimensions of the material (photopolymerization, powder bed fusion, fused filament fabrication). Stemming from the invention of the stereolithography by Charles Hull in 1983, the Fused Filament Fabrication belongs to the 3D-printing category of material design. 3D-printing presents a wide range of applications going from pure polymer ([73], [74]), composites ([75], [76]) to metals ([77], [78]).

Among them, continuous fiber-reinforced composites have attracted great interest owing to their significantly higher mechanical performances than short fiber reinforced composites [79]. Their benefits have been highlighted in several articles ([80]–[83]).

In this work, materials positioned at the interface between mechanical performances and environmental consciousness are biocomposites reinforced with natural fibers. Their place on the load-bearing market has been growing from the start of the 21th century ([84]–[86]). Knowledge about the printability of this class of composites and how slicing and printing parameters tend to influence the printing quality and material integrity is being acquired ([69], [70]).

#### II.1.a. Filament production

Before tackling the architectural asset given by 3D-printing, some general information on filament production must be developed. Up to now, there are two different ways to fabricate continuous natural fiber reinforced filament for 3D-printing purposes. The first one is a two-

step manufacturing process that distinguishes between filament production and filament printing. In Figure 28a, Kurihara et al. [89] used co-extrusion process that allows for the production of continuous flax fiber filament coated by a chosen matrix inside a heat nozzle. The second is the in-nozzle impregnation of the filament prior to printing (Figure 28b), as used by Matsuzaki et al. [90] to produce continuous jute/PLA (cJF/PLA) filament.

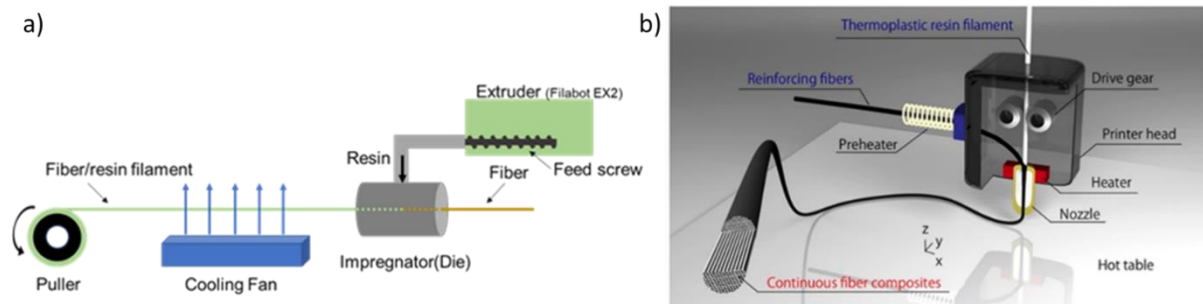


Figure 28: a) Co-extrusion process used to fabricate continuous fibers/polymer filament [89]. b) In-nozzle impregnation of continuous fiber/polymer filament [90].

Adding continuous reinforcements inside raw filaments exacerbates the complexity of 3D-printing. Optimization of fiber impregnation and fiber content of filament must be standardized to ensure printing quality and reproducibility of prints. One particular asset of in-nozzle impregnation is the ease with which the filament diameter can be changed between prints to optimize 3D-printed structures. Filament diameter has already unveiled significant impact on tensile properties of continuous flax fiber/PLA (cFF/PLA) composites. Indeed, the diameter of the manufactured filament is directly correlated to its fiber volume content and impregnation properties. Using 68-Tex continuous flax fibers, Zhang et al. [91] showed that a diameter of 1mm after the impregnation of the matrix was optimal to get both satisfying fiber volume fraction and homogenous surface.

### II.1.b. 3D-printing of continuous fiber reinforced composites

Lanzotti et al. [92] devoted an important part of their work on the study of printing process parameters on the dimension accuracy of 3D-printed PLA parts. They were especially focused on three impacting factors; the layer thickness, the deposition speed and the flow rate. It appears

that the deposition speed represents the most impacting parameter considering the process reliability. However, it might be possible to optimize the dimensional accuracy by running the printing in a reasonable amount of time. Indeed, the flow rate factor has also an important influence and could maintain a balance between these two related factors. In the same idea, Ficzero et al. [93] evaluated the relative fracture in response to a change of layer height in PLA printed parts. However, adding natural reinforcements inside filament complexifies the 3D-printing process. A thorough and accurate adjustment of slicing and printing parameters is primordial.

At the composite scale, Matsuzaki et al. [90] published the first study tackling the 3D-printing of continuous natural fiber reinforced structures. Combining jute fibers with PLA matrix, the gap in performance was reported compared with continuous carbon fiber reinforced composites. However, investigations have recently proved the potential of continuous fiber to challenge the stiffness and strength of synthetic reinforcement inside the structure. cFF/PLA biocomposites belong to these range of materials ([79], [94]). Thanks to the stiffness of flax fibers, 3D-printed biocomposites achieve the tensile modulus and strength of conventional 3D-printed continuous fiber composites as illustrated in Figure 29.

Furthermore, there are still ways of achieving higher mechanical performances [87]. Firstly, the fiber content driving material resistance over mechanical loadings is limited inside 3D-printed biocomposites. A low fiber content ( $< 30\%$ ) enables a compliant filament viscosity for 3D-printing process. Increasing this content creates an irregular material flow through the nozzle which generates poorly printed parts. Secondly, fiber aspect ratio should be considered since it reduces the load transfer at the fiber/matrix interface causing debonding (low aspect ratio) or promotes clogging (high aspect ratio). Last, the formulation requires optimization (fiber type, crop conditions, matrix selection) to maximize the mechanical performances.



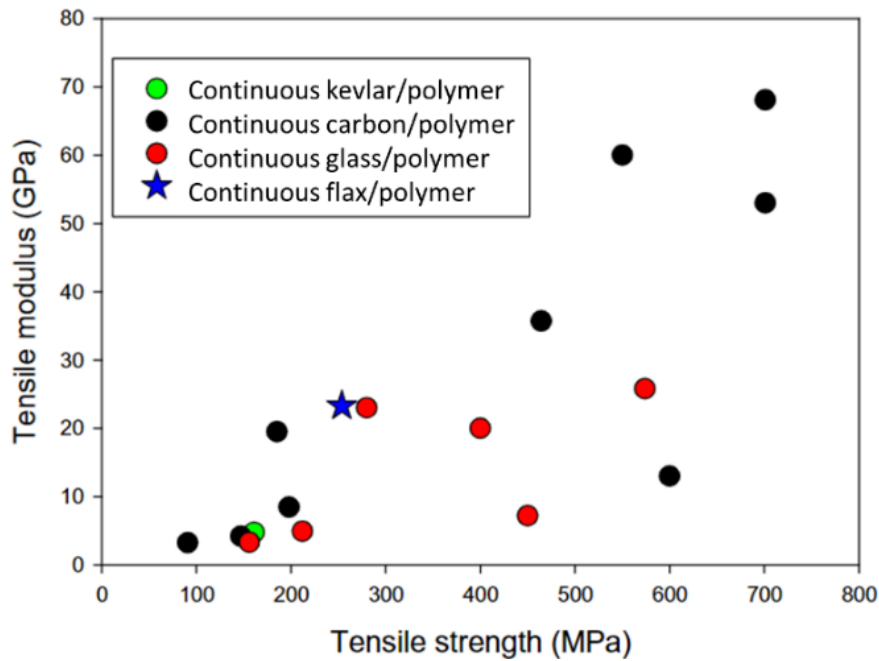


Figure 29: Comparison of tensile modulus and tensile strength between 3D-printed continuous synthetic and natural fiber reinforced composites (adapted from [79]).

Slicing parameters give to designers a relatively wide range of adaptation in the control of the final 3D-printed structures. Among them the Interfilament Distance (ID), the Number of Layers (NL), the Layer Height (LH) and the Number of Trips (NT), have shown an impact on final mechanical properties of cFF/PLA biocomposites (Figure 30a) [88]. The closed connection between slicing parameters and mechanical properties relates to the presence of porosity (Figure 30b). For example, increasing LH from 0.2mm to 0.6mm lowers the compression ratio about during printing which results in higher porosity content (+15%) and lower mechanical properties from 17.2MPa to 9.5MPa [88]. Optimizing the slicing parameters to minimize the porosity content enhances the mechanical performance and are essential to get the best balance between mechanical, interfacial and thermal properties [95].

Along with the 3D-printing of natural fiber reinforced biocomposites, some investigations were conducted to quantify the impact of water-sensitive fiber on mechanical performances of the material. Undergoing a stage in various humid environment (from 11% RH to 98% RH), cFF/PLA 3D-printed biocomposites show an exponential decrease of 64% in longitudinal

modulus, 64% in transverse modulus and 48% in shear modulus (Figure 31) [96] as induced by yarn matrix debonding and PLA softening.

Finally, as a guide of the complexity of printing architected materials, Fudos et al. [97] configured a printability score which translates the capability of a 3D sample to be successfully printed. This factor takes into account the geometrical complexity of the model as well as the used design process (FDM, Binder jetting and Material jetting). The structural control is a fundamental point to develop shape-changing or shape-memory materials gathered in the so-called smart materials, i.e. when 4D-printing substitutes 3D-printing.

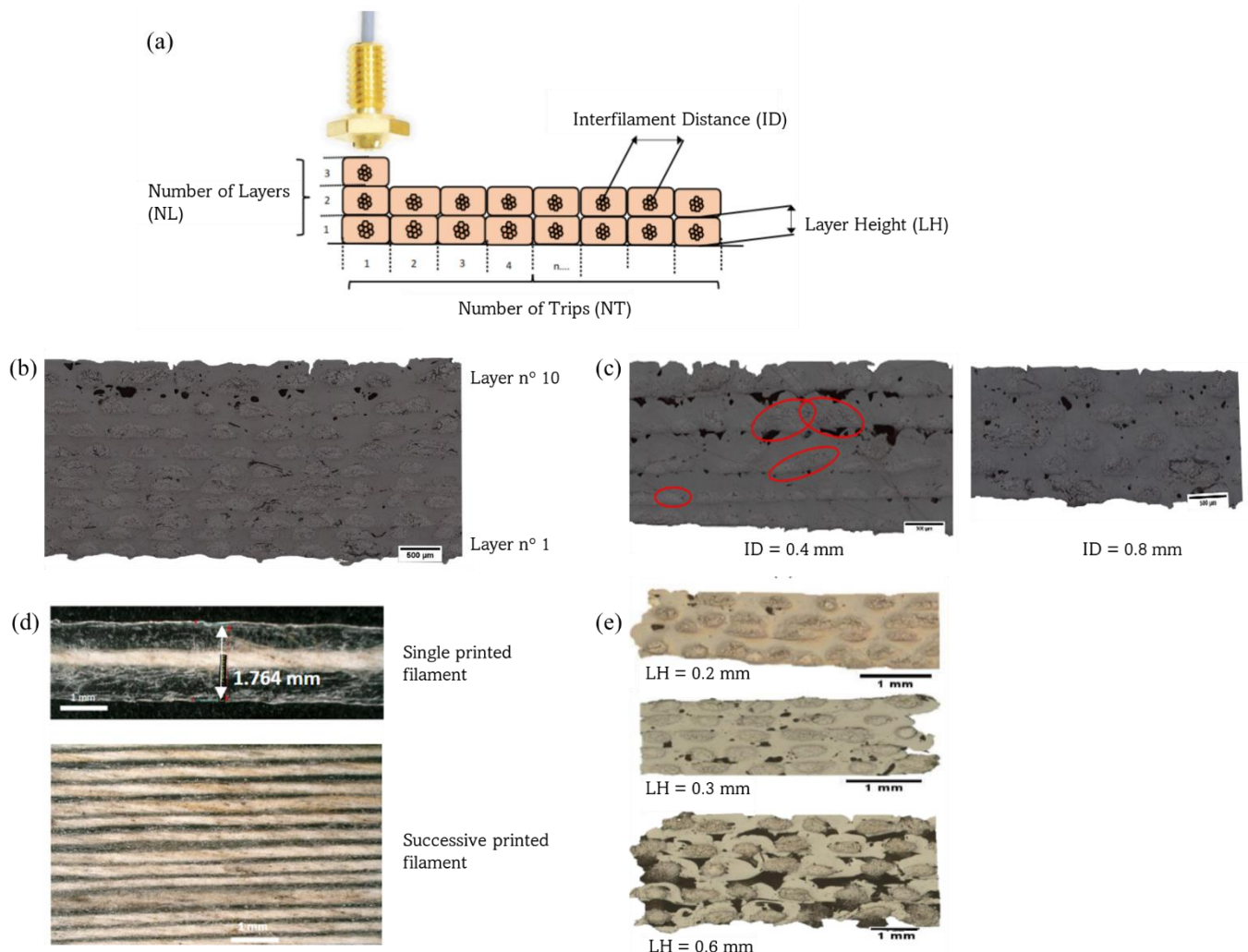


Figure 30: (a) Scheme representing 3D-printing of continuous flax-fiber reinforced composites and the impact of (b) number of trips, (c) interfilament distance, (d) number of trips and (e) layer height on composite mesostructure. This figure is adapted from Le Duigou et al. [88]

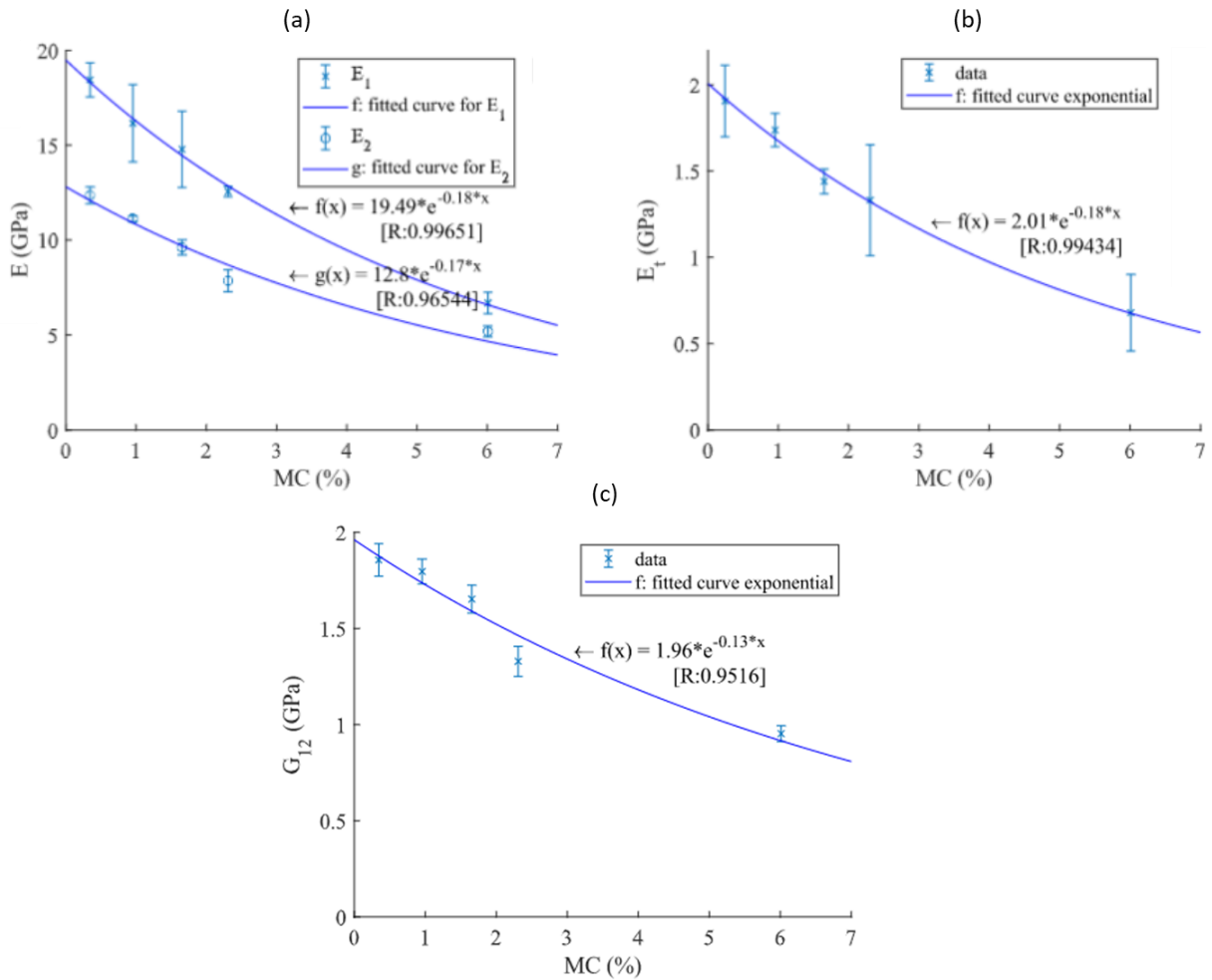


Figure 31: Evolution of (a) longitudinal modulus, (b) transverse modulus and (c) shear moduli of 3D-printed cFF/PLA biocomposites as a function of moisture content [96]. Regarding the longitudinal modulus,  $E_1$  and  $E_2$  curves correspond to the two measurable elastic moduli of biocomposites when reinforced by natural fibers. The calculation is explained by Shah et al.[98]

## II.2. 4D-printing

The strategy of gathering mechanical performances and adaptive structure regarding the external environments was a pioneer in the development of 4D-printed materials ([99]–[101]). Nowadays different printing techniques are used to get access to a wide range of programmable materials whose initial architecture (after printing) differs from its architecture of application (after stimulus). The paradigm of 4D-printing is regulated by three laws introduced in Figure 32 [102]. 1) The shape-changing ability of smart materials actuated by external stimulus (pH, thermal gradient, water uptake, UV-radiations) is induced by a differential expansion between an active and a passive layer. 2) Main physical changes inside smart materials are categorized

in four phenomena : mass diffusion, thermal expansion, molecular transformation and organic growth. 3) Actuation kinetic is governed by the inherent expansion of active and passive layers respectively.

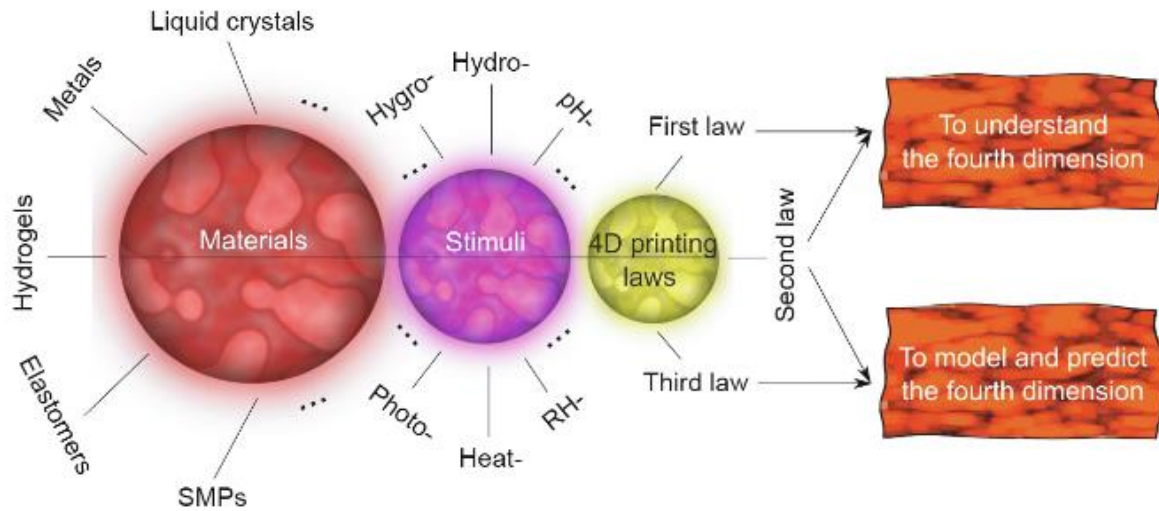


Figure 32: Scheme of the paradigm of 4D-printing and the three governing laws [102].

The emergence of 4D-printing has given rise to two morphing strategies. One consists of using the internal stresses generated through the 3D-printed structures to generate the reshaping stage. It relies on the restructuration of components such as fiber swelling or sensitive polymer when facing a specific stimulus [103]. The second one uses residual stresses induced by 3D-printing process as a tool to tune the shape-changing pattern. By entailing mechanical energy inside the structure, the structure will rearrange towards an optimal configuration when deployed in a compliant environment [104]. Therefore, 4D-printed samples can be configured by tuning the formulation and/or matter distribution in the structure.

### II.2.a. Actuation based on material selection

The field of 4D-printing is not applied to one specific range of materials but gathers multiple families such as hydrogels [105], sensitive polymers [106], composites [107] and metals [108]. Formulating the bilayer structure is of importance to reach a significant curvature of response.

Rajkumar et al. [109] compared different unreinforced thermally induced shape-changing thermoplastics (i.e. PLA, HIPS, ABS) based on a thorough analysis of printing and slicing parameters (printing speed, infill density, thickness). The internal stresses/strains gradient generated between the layers by the FFF process, explaining this actuation, could be maximized by controlling the printing speed, the infill density, the printing orientation and the material thickness (Figure 33).

Besides, the printing order in the design of a bilayer actuator has also emphasized an actuating factor [1]. Indeed, this parameter needs to be taken into account regarding the final curvature achieved by the structure after its full deployment. In the case of PLA/TPU thermomorphs materials, An et al. [110] explained that printing firstly the active layer, i.e. PLA layer, will lead to a higher residual stress/strain implemented inside the laminates. This is due to the temperature of the printing bed which is lower than the one of the constraint layer, i.e. TPU layer. By printing the active layer first, the matrix gets into a fixed shape very quickly which does not let enough time for a reorganization of the macromolecular chains, making the layer in high energy mode with a considerable stress concentration (Figure 34).

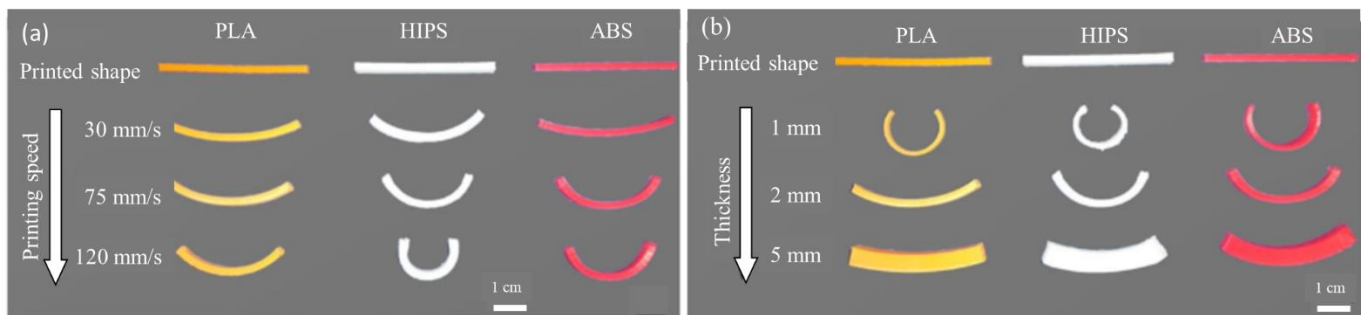


Figure 33: Impact of (a) printing speed and (b) sample thickness on actuation response of PLA, HIPS and ABS 3D-printed specimens (adapted from [109]).

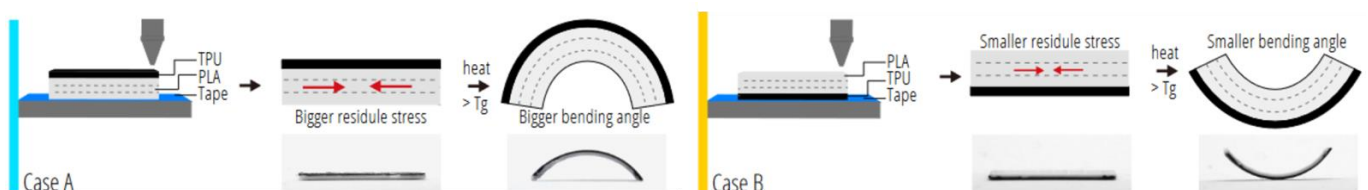


Figure 34: Impact of printing order on actuation behavior of PLA/TPU thermomorph materials (adapted from [110]).

## II.2.b. Actuation based on matter distribution

While a perfect overlap of passive/active layers leads to bending behavior, increasing the complexity of the distribution of passive layer, active layer or both will change the final response. For instance, Wang et al. [111] developed two strategies allowing to switch from 3D-printed simple linear elements to complex self-deployable structures. The first strategy consists in printing a straight line composed of one or more linearly connected active segments. The other rests on the combination of active and passive segments which will generate a swelling differential between layers. Emphasized in Figure 35, the anisotropic distribution would allow to construct multiple bending directions within one simple linear piece.

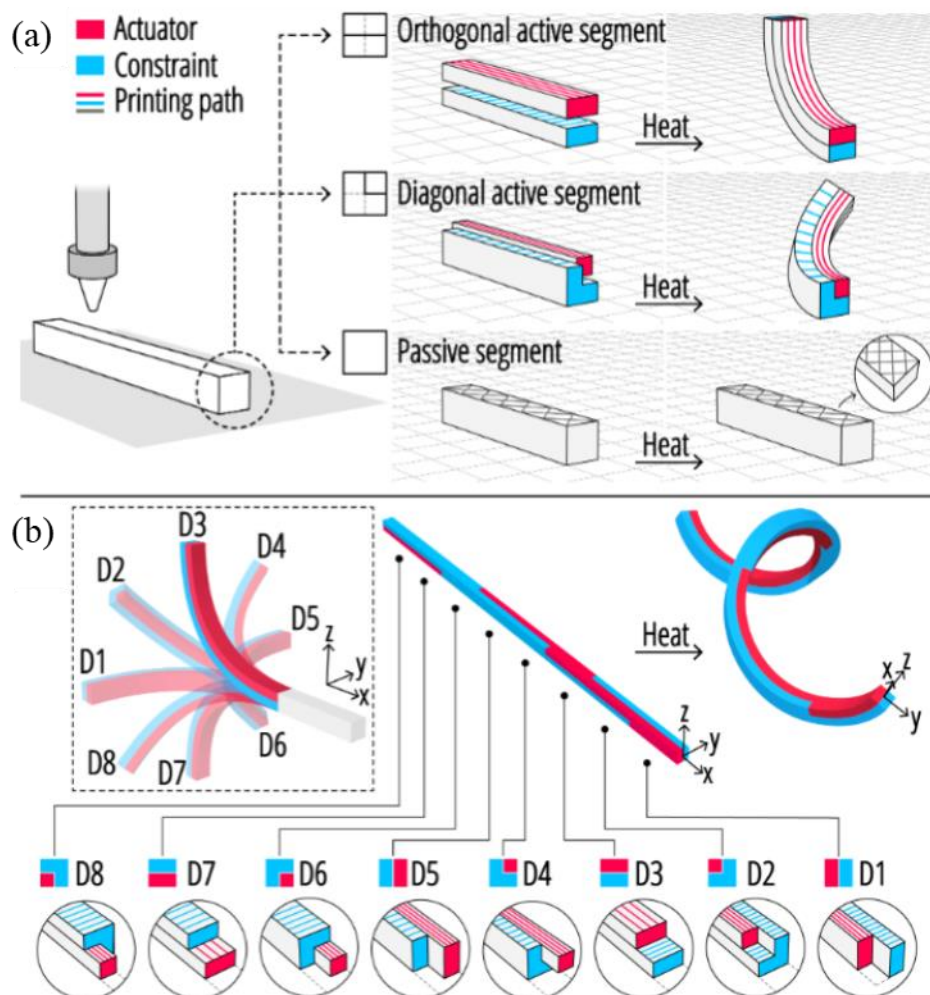


Figure 35: (a) 4D-printing of linear bendable structures and (b) reachable shape-changing patterns [111]

In a parallel approach, Ueda et al. [112] gave some clues about the understanding of locally controlled shape-changing mechanisms of short carbon fiber (sCF)/PA66 composites. To control the bending process of short carbon fibers reinforced composites, they arranged the printed layers very specifically. Their printed parts are composed of a solid one and a bendable one. Whereas the first part exhibited a 100% filling rate, the second one displays a parallel cross shape structure with a filling rate of 44%. Local orientation of the griders, i.e. printed filaments, in the bending part influences significantly the bendability of the final part. Besides, a phase-shift structure is more reluctant to bending because of the constraining effect of its overlapped griders. This type of architecture can be assimilated to hybrid hinge structures where a zone is kept free of motion by using a monolayer set up. This area is called the hinge (Figure 36a). In line with this structure, Yamamura et al. [113] investigated the conception of hybrid hinges composed of shape memory TPU in glassy state combined with a soft TPU in rubbery state (Figure 36a). The influence of the hinge length on the self-folding angle was evaluated in order to design an origami compliant mechanism gripper. Results showed that lower hinge length leads to a decrease of the self-folding angle, quantified by an approximate 50%-drop when the hinge length decreases from 10 mm to 5 mm. Besides, hinge pattern is a tunable parameter that modifies the bending actuation. Zolfagharian et al. [114] tested three hinge patterns: honeycomb, zigzag and squared-patterns. Depending on the slicing parameters (number of layers, layer pattern), the authors made possible to control the bending amplitude (Figure 36b). This influence relates to the hinge ability of the black printed ink (= actuator) to absorb IR-light and heat up the underlying PS film which results in a shrinkage mechanism of macromolecules. Because of the different amount of deposition for each patterns, the shrinkage step is not the same and modifies the final bending angle (going from 178° for honeycomb, 165° for square to 122° for zig-zag patterns). Number of layers also plays a role in this folding process since increasing this number leads to a reduction of the bending potential.

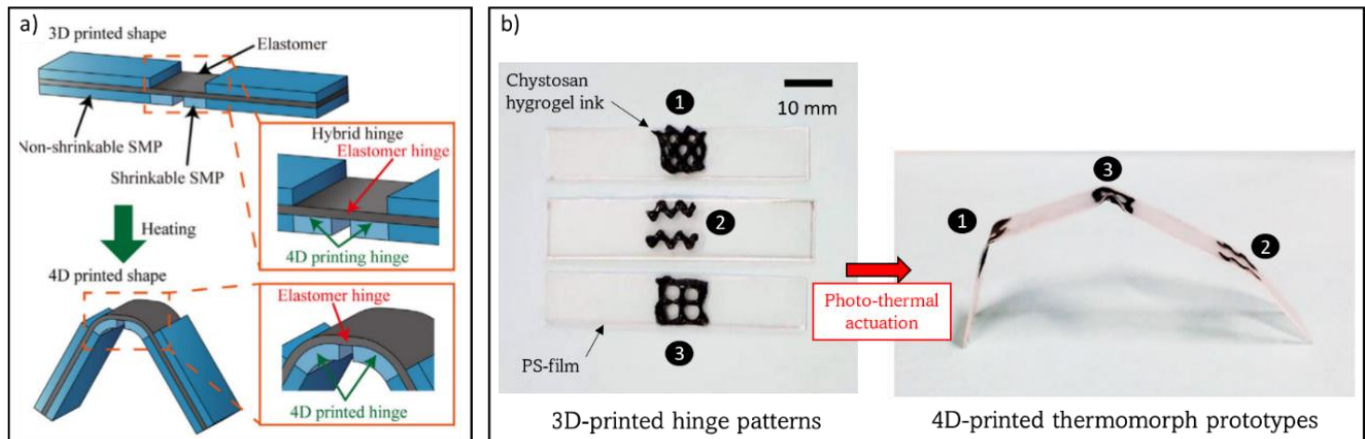


Figure 36: a) Scheme of 4D-printed elastomer/SMP materials relying on hinge area [113] and b) curvature distribution of 4D-printed chitosan ink/polystyrene actuation filled with various hinge patterns: honeycomb (1), zigzag (2) and square (3) (adapted from [114]).

Then, more complex structures are imagined to broaden the range of applications of 4D-printed metamaterials. For example, Wang et al. [115] enlightened the morphing ability of thermally induced shape-changing bilayers by developing a theoretical model allowing to predict the shape-changing behavior of cCF/PA66 composite by programming its printing trajectory, i.e. fiber orientation. The error between the model and the real curvature of bilayers did not exceed 6% which testified a highly accurate model. The final purpose is to generate any shape of deployable surface by controlling the distribution of fibers and especially the angle between intersecting fibers and the bisector angle of the printed fibers (Figure 37).

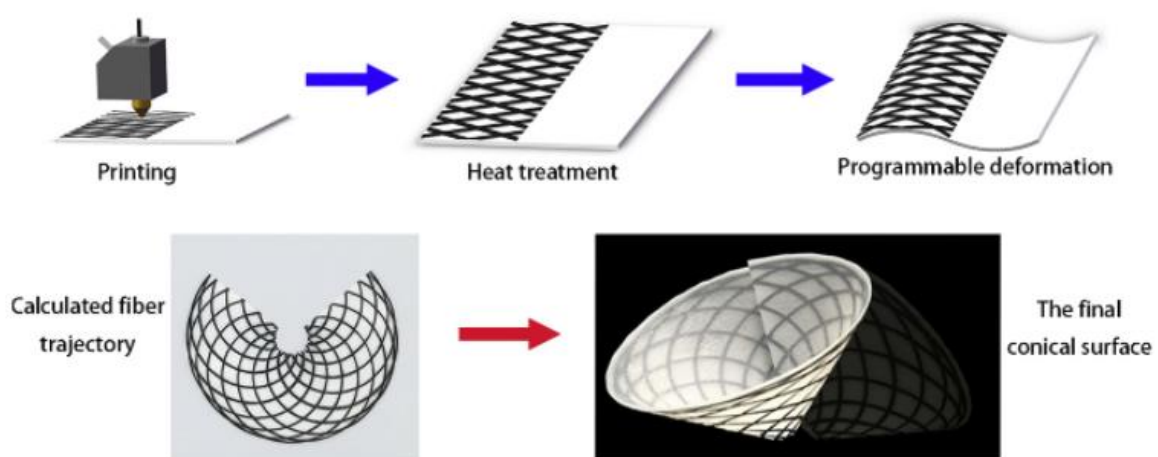


Figure 37: 4D-printing of cCF/PA66 thermo-induced conical prototype exhibiting a specific fiber distribution [115]



Multiple complex shape-changing patterns driven by matter distribution are presented in the scientific database such as strip pattern (Figure 38a-b), flat hollow disc (Figure 38c), lattice (Figure 38d) and star-shaped structure (Figure 38e) or even one inspired from flower's petals (Figure 38g).

Then, Dong et al. [116] also worked on the design of 4D-printed programmable continuous Kevlar fiber (cKF)/PLA composites displaying a triangular cellular structure. In lattice structures, the resistance and rigidity are directly linked to structural parameters related to the cell dimensions (especially cell length) and the thickness of printed layers. This concept remains very interesting in the idea of maximizing the exchange surface with the narrowed environment.

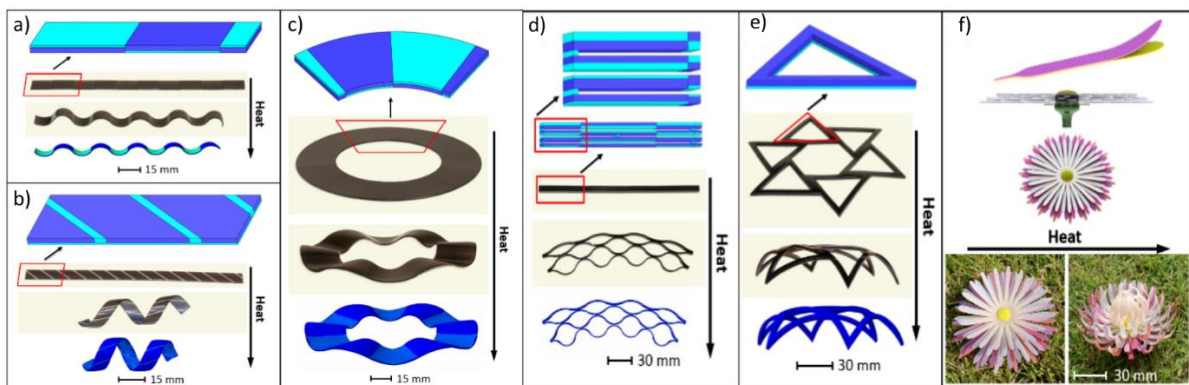


Figure 38: a-b) Flat strips with divers mesostructured and c) flat hollow disc represent fundamental 4D-printed elements driven by in-plane and out-of-plane matter distribution. d) Cellular structure, e) star-shaped structure and f) prototype of flower's petals represent complex 4D-printed structures made of combination of fundamental elements. These illustrations are adapted from Ding et al. [117].

### II.2.c. The case of cellular structures

Among the possible 4D-printed mesostructured actuators, lattice structures are represented by a local distribution of matter and voids that enables lightweight designs to be developed and mechanical properties to be exacerbated (e.g. honeycomb structure). For this reason, growing interest is related to the smart behavior of cellular structures to open doors for innovation and performance.

Cellular materials are more than just part of our daily lives. One of the most accurate examples is the washing sponge whose cellular structure promotes water diffusion through it. The result is an enlargement of the cells, leading to swelling. Another popular example is bread baking. Among the bread constituents, yeast ensures the swelling of the mixture when increasing the temperature. The density change relies on a chemical reaction inside the bread that releases carbon dioxide gas. Because stacked inside the bread structure, CO<sub>2</sub> gases generate the inner porous structure observable when cutting the bread. This mechanism inspired Saint-Jean et al. [118] in their development of thermal-induced cellular structure made of a silicone elastomeric matrix in which bubbles of ethanol, i.e. a volatile liquid, are trapped (Figure 39a). Introducing a restrictive material to this porous network allows for programming the shape-changing pattern (Figure 39b) to incorporate functions to the structure.

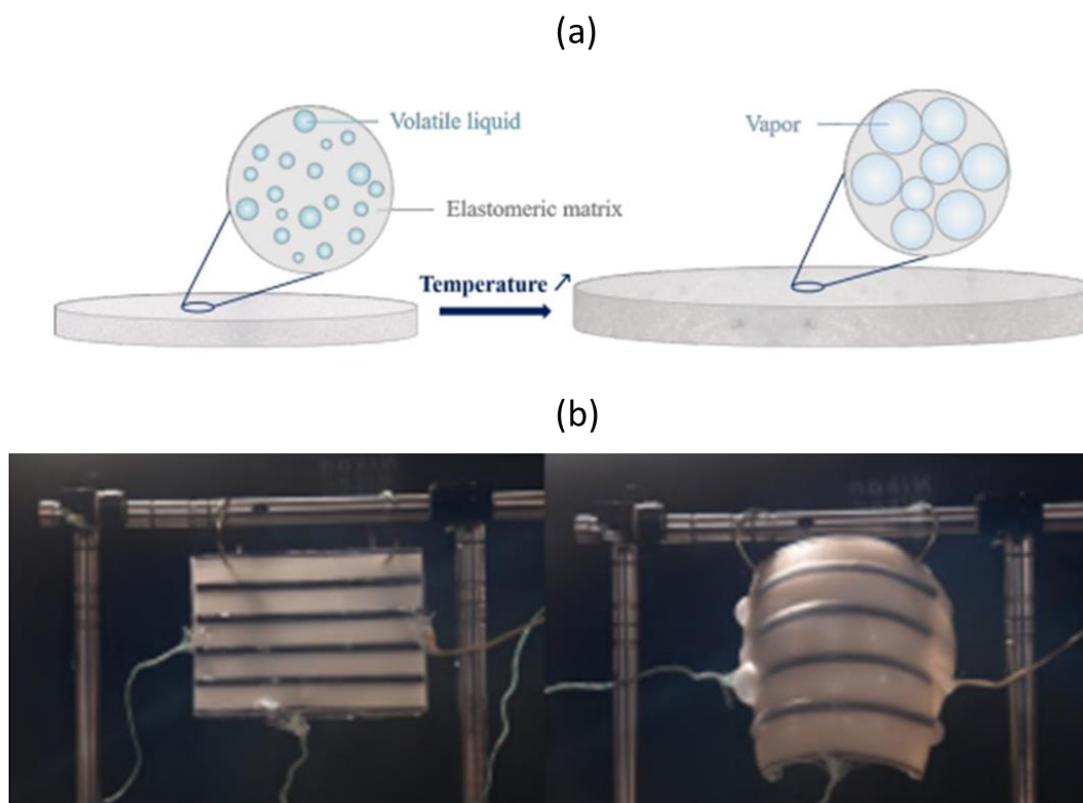


Figure 39: (a) Swelling process of elastomeric matrix caused by the vapor bubbles dilatation when increasing the temperature. (b) Pictures of swelling matrix with integrate restrictive lines. The same sample is stored at room temperature (left) and 90°C (right). Restrictive lines drive the shape-changing pattern. (adapted from [118])

Lattice structures belong to the family of cellular structures. They have the particularity to exhibit a repetitive cellular pattern inside the structure called “lattice”. The lattice expansion can be realized by linking successively several bilayers. Using an unspecified elastomer/shape-memory polymer (SMP) bilayer, Ding et al. [117] reached a 900% expansion of the lattice network. Tuning the slicing parameters to modify the cellular pattern (Figure 41a), layer thickness or cell dimension is precious. This expansion potential is a real inspiration for the development of prototypes where an increase in surface area is desired.

Although well-known for their good mechanical properties, their shape-changing ability has not been a priority in the recent exploration of 4D-printed composites. However, some insightful papers focusing on continuous synthetic fibers are accessible in the literature. Among them, Dong et al. elucidated a strong link between shape-memory ability and specific strength of 4D-printed continuous carbon reinforced lattice structures [116]. Either by testing various cell lengths or layer thicknesses, the specific strength and shape-memory ratio display an unproportional trend meaning that lattice stiffness must be neglected for maximizing its shape memory behavior. Besides, the shape recovery takes a longer time and has a lower recovery ratio when the fiber content increases. According to the authors, it is owing to irreversible slippage at the fiber/matrix interface during the deformation.

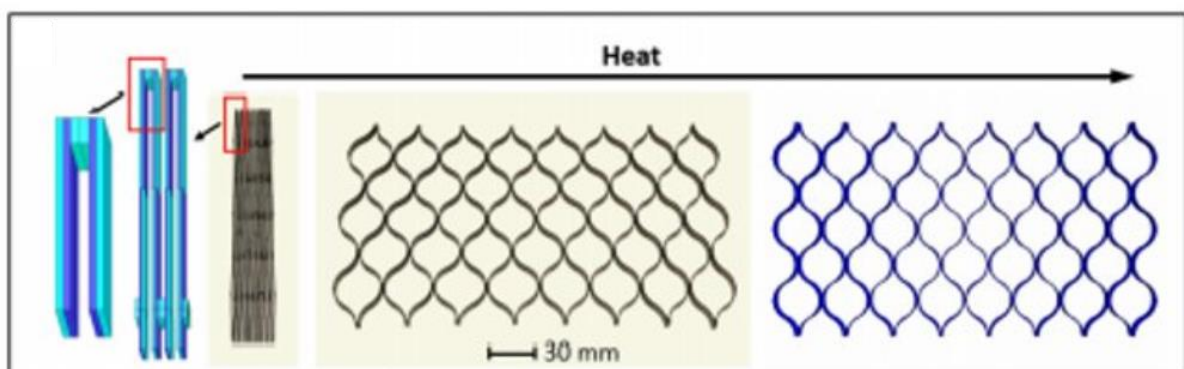


Figure 40: Cellular expansion of lattice structure made of elastomer/shape-memory polymer [117].

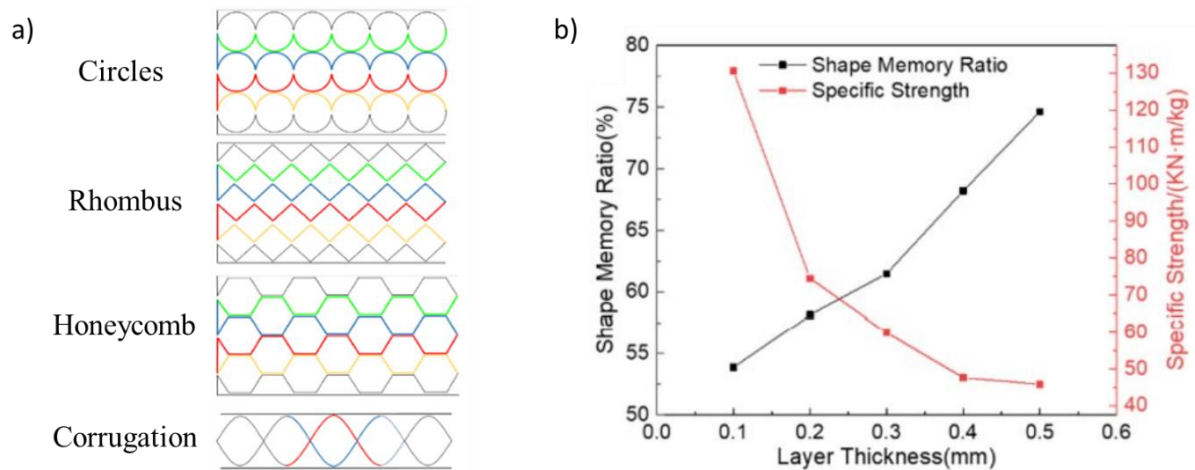


Figure 41: a) Several programmable and printable cellular patterns. b) Evolution of the shape memory ratio and specific strength of continuous carbon fiber reinforced composites as a function of layer thickness. (adapted from [116])

In light of this development, Van Manen et al. [119] explored the different strategies to generate a sequential folding mechanisms within thermally actuated 3D-printed materials. Reducing the thickness of restrictive layers and promoting the presence of internal porosities tends to facilitate the heat transfer and thus to accelerate the shape-changing process. The authors also gave credit to lattice structures by considering how the shrinkage/expansion of adjacent layers would maximize their opening.

To sum up, the paradigm of 3D and 4D-printing has been especially carried by the development of thermomorph materials. However, actuation stimulus is not exclusive to thermal gradient. Humidity gradient or water sorption/desorption are also interesting options that could widen the use of 4D-printed materials where plant fibers trigger the actuation. Understanding the link between 3D-printed path, mesostructured and actuation properties is an essential step to improve the functionality of Hygromorph Biocomposites. In the following section, a collegial reflection is dedicated to water-induced reconfigurable biological models on biochemical and structural approaches.

### III. Reconfigurable water-induced biological models

Nowadays, the opportunities brought by self-deploying materials in the design of multi-structural parts are obvious. Inspired from plant metabolism, smart materials are developed in a strategy of energy-efficiency and multifunctionality to build more adapted and sustainable solutions for the future. To do that it is essential to understand the synergy between biochemical and structural properties of plants and the stimuli impact generated by climatic factors. For this reason, there is a particular wish to solve problems and develop solutions in a biomimetic approach.

The biomimicry concept relates to the wish of humans to take example on natural concepts to improve home-made inventions, replace their actual way of thinking and innovate in a promoting and eco-friendly approach with a view turned towards the future. The standard ISO 18458:2015 conceptualizes the biomimetic approach. The biomimetic logic is divided into several steps going from the definition of the technical problem to the bioinspired improved product (Figure 42).

Natural species representing concept for humans interest are numerous. Burgert [36] and Poppinga [120] summarized the wide range of plant movements listed as a source of inspiration for the development of programmable materials. The main typical physical motions (bending, folding and buckling) remain the most observable in natural mechanisms. Though well developed in the recent decade, Hygromorph BioComposites are facing limitations regarding their actuation performance (**Section I.5**). To overcome this lock, there is a particular motivation to design HBC from biomimetic structures. As the triggering factor, the water displacement through the structure triggers responsiveness and reactivity. It represents an essential lever for boosting HBC deployment and must therefore be optimized. In the following section, the structure of the pinecone, flytrap, waterwheel and Lily plant have been taken as

models whose smart behavior is based on an inter-functional architecture and synergy with the flow of water.

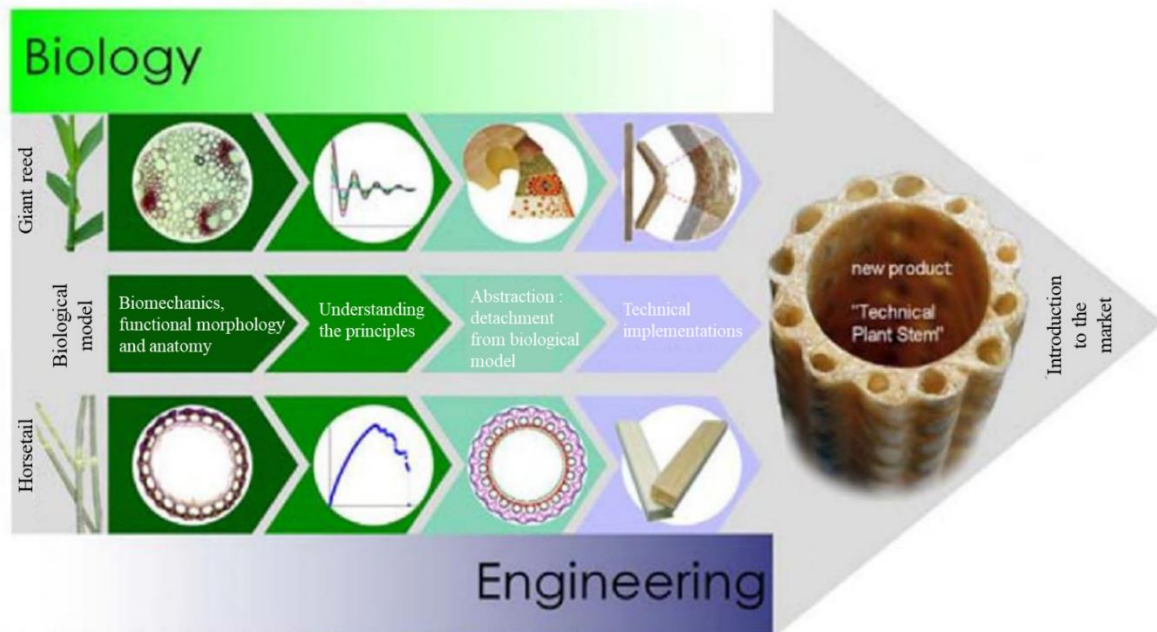


Figure 42: Schematic biomimetic approach (adapted from [121]).

### III.1. Water transport through plant tissue

Transport and diffusion of water within biological structures have been and remain today a risky research topic, since nature displays a multitude of complex mechanisms ([122]–[127]). A particularly interesting phenomenon is the ascent of liquid flow within trees and flowers. Indeed, the way that water and sap are hoisted to the top of the stem is essential for the survival of the plant. The role of water in plant movement is also of paramount importance since it dictates the pressure state within cell walls and thus initiates the plant restructuring. Water can go through plant structures by three different ways: across porous cell walls, across the semi-permeable plasma membrane and by following the flow of adjacent cells [128]. These three points represent the intrinsic options of water displacement inside their structures.

Ascension is a common term when speaking about plant morphology and cohesion of its parts. The flow of water toward the leaf follows a tortuous path from the multilayers arrangement of

roots, passing through the tracheids and vessels of the stem, to finally reach the leaf tissue and supply water to the dehydrated apical buds (Figure 43).

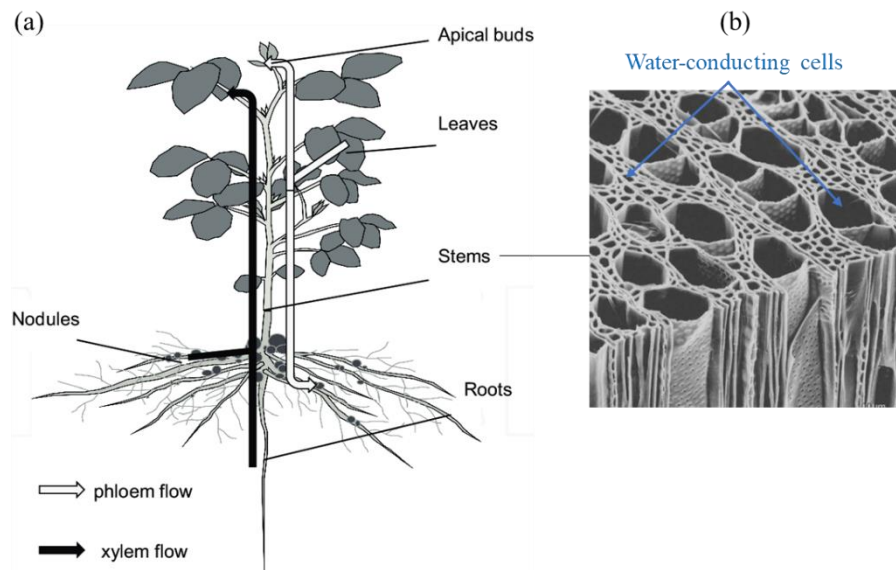


Figure 43: a) Water and nutrients transport within xylem and phloem conducts of in a soybean plant [129]. b) Zoom on the water conduction cells of plant stem called tracheary elements.

### III.2. How water sorption generates motion

Water not only penetrates the structure of plants but also modifies its inherent micro- and mesostructure. Depending on its water sensitivity and local architecture, plants react in a different way to water uptake that attributes specific functionalization to the structure. Transport of water inside plant cells is characterized by two different parameters. At the cell scale, the first parameter quantifying the timescale of plant movement is the relaxation time of the cell when water goes through. It depends directly on the intrinsic properties of the cell (cell radius  $R$ , cell bulk modulus  $\mathcal{E}$  and membrane conductivity  $Lp$ ). Finally, the smaller the cell, the faster the water transport. Water may also displace from one cell to another to pass through the entire plant tissue. For this reason, another representative time must be set: the poroelastic time. This parameter is triggered by the tissue properties (size  $L$ , permeability  $k$  and elastic modulus  $E$ ) as well as water viscosity  $\eta$ . Finally, this point relates to the cell volume changes. Passing through plant tissue, interactions are created between water molecules and plant constitutive entities generating motion of the structure.

### III.2.a. Slow hydraulic movements

The slow hydraulic movements within plants are summed up in this section. Growth symbolizes the main trivial hydraulic movement in plants. It is based on the cellular expansion over time and the ability of the cell to hold water molecules. These irreversible structural modifications are limited by the maximal cell extensibility and conductivity. Growing up, plants increase their exchange surface with environmental factors to receive more supply in vital resources (water, light, heat). Then, osmotic gradients also play a key role in water-driven plant opening. Indeed, the specific turgor pressure presents inside each cell leads to a swelling/shrinking of the cell. This mechanism can be optimized by the tissue and cell wall properties (cell bulk modulus, elastic modulus). Stomata appears as a recurring example in this water-driven mechanism which enables the leaf transpiration and gas exchange with the narrowed environment. The relation between stomata expansion and turgor pressure has been deeply investigated ([130], [131]). The last motion is induced by hygroscopic movements inside natural systems (pine cone, seed pods). More details on this hydraulic mechanism are proposed in **Section III.3.a.ii**.

However, physical limits appear in plant movements. The main parameter involved in the morphing potential and resistant process of plant is the presence of a smoother or stiffer cell wall which prevents the cell from being overinflated by the turgor pressure and enables mechanical resilience [132]. To categorize the referring mechanism, the poroelasticity of the considered biological system is stated. The poroelastic time  $\tau_p$  represents the time needed to equilibrate the pressure between plant cells after the passage of water. It must be minimized to design water-induced materials with faster response. Looking at Figure 44 illustrating the time scale  $\tau$ , i.e. duration of the plant movement, as a function of the cell wall dimension  $L$ , it is possible to identify two movements within biological structures. If  $\tau > \tau_p$ , the plant movement



is slow due to a weak and slow penetration of the liquid. If  $\tau < \tau_p$ , the plant movement is fast and induced by mechanical instabilities in the structure.

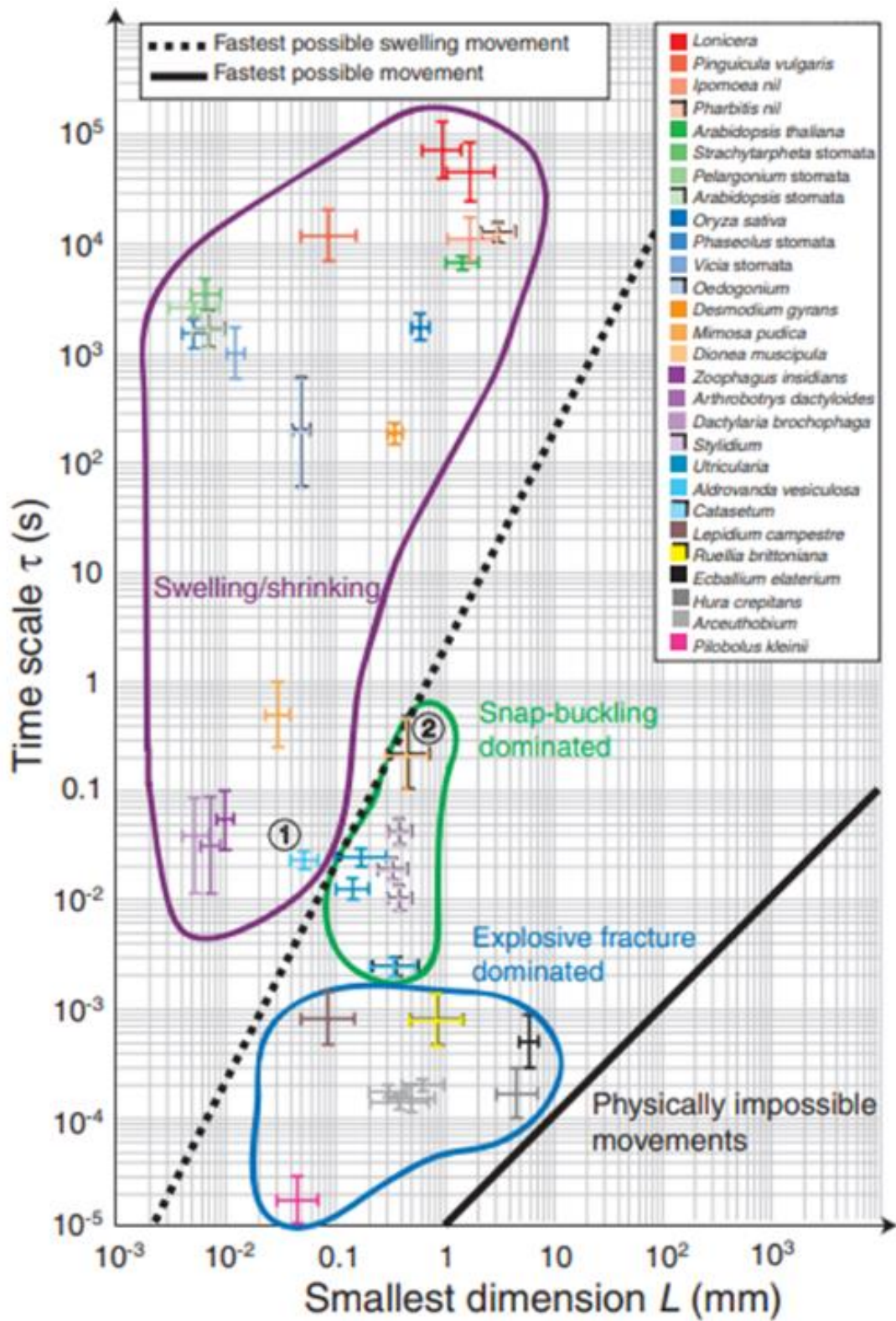


Figure 44: State of the art of time scale used by plant and fungal species as a function of the smallest macroscopic dimension of the moving part  $L$ . Three categories can be distinguished. The slow hydraulic motions (purple circle) of which  $\tau > \tau_p$ . The fast snap-buckling mechanism (green circle) and explosive fracture mechanism (blue circle) of which  $\tau < \tau_p$  rely on elastic instabilities [132].

### III.2.b. Mechanical instability

A second strategy allowing plant motion relies on mechanical instability caused by internal stresses of the biological structure (Figure 44). Some of the fastest shape-changing motions do not rely on the complete hygroscopic properties of plant components but on the naturally pre-programmed mechanical instabilities. Here are some examples explaining this biological morphing ability.

#### III.2.b.i. The elastic snap-buckling

Snap-buckling opening can be found in carnivorous plants. For example, Venus flytrap uses a sequenced shape-change based on a first slow motion of its lobes ( $L = 20$  mm) arises from the variation of turgor pressure causing the swelling of the tissue and modifying the geometrical shape of the lobe. These geometrical variations generate a rapid release of the stored elastic energy allowing a fast closure of the lobes and the capture of the prey between 100 and 300 ms (Figure 45a), known as snap-buckling [133]. Evolution of the elastic energy stored in plant tissue as a function of the lobe curvature is drawn in Figure 45b.

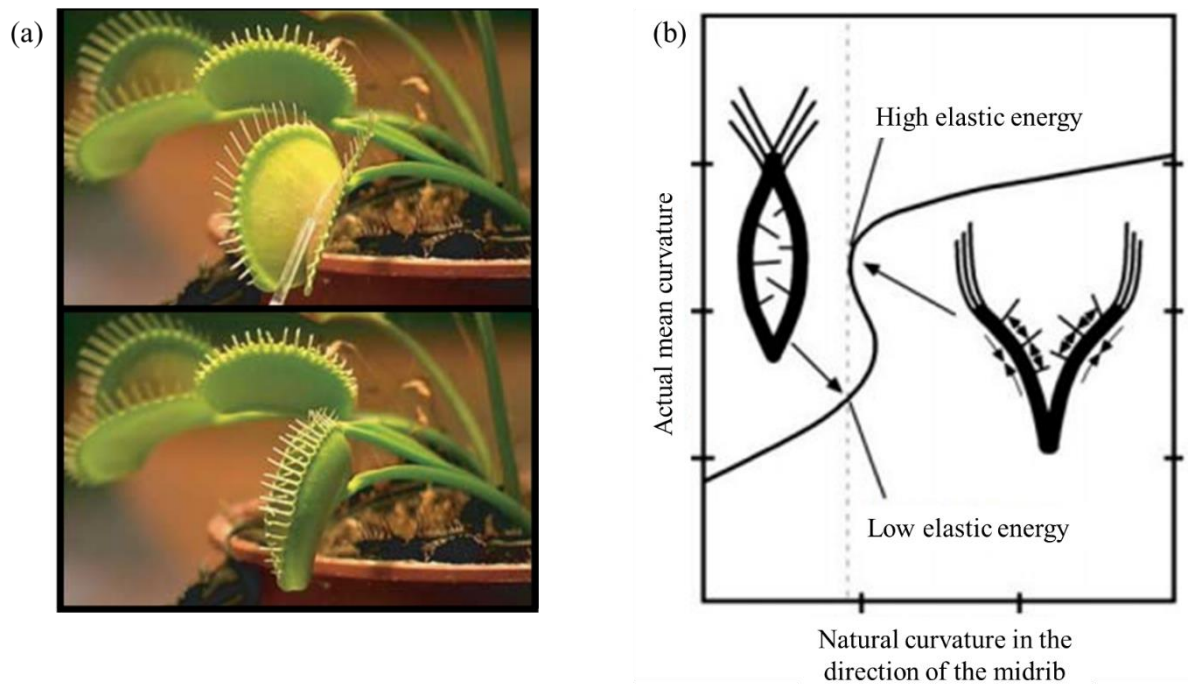


Figure 45: (a) Picturing snap-buckling of Venus flytrap [134]. (b) Evolution of elastic energy stored in Venus flytrap tissue allowing snap-buckling process [135].

Having the same capture function, the waterwheel plant displays a faster response (20-100 ms) triggered by a fast localized turgor change near the initially bent midrib which, by releasing the stored energy, causes a quicker snap-buckling of the lobes ( $L = [2-4]$  mm) [136].

#### *I.2.b.ii. The explosive fracture*

Water presence might also affect the interfacial stresses between cells. For this reason, switching between wet and dry environments drives to an increase/reduction of some hydrophilic cells which, depending on their size and wall rigidity, can present fracture mechanisms useful for seed release. This is for example the case of the *Fern Sporangia* also known as catapult plant (Figure 46a). During dehydration, water molecules are removed from plant cell walls which induces a shrinkage of the tissue by macromolecular rearrangement. These structural changes lead to the collapse of the outer cell walls and the release of stored elastic energy. Seeds are then projected at an initial velocity of  $10 \text{ m}\cdot\text{s}^{-1}$  [137]. This observation can be compared to the bursting process of *Cornus canadensis* during pollination process (Figure 46b) [138]. Its opening is achieved in 1 ms which is the fastest reported dehiscence process to the author's knowledge. Besides, the triggering force of 0.1-0.5 mN prevents the flower opening by small and less mobile colonizers (ants) and targets bigger colonizers (bees, wasps, bumblebees) moving rapidly from flower to flower and promoting fructification. The height of ascent of pollen represents 10 times the height of the flower. This fosters the pollen spread by wind, water or animals [139]. Another popular vegetal showing explosive fracture is the *Erodium cicutarium* belonging to Geraniaceae species ([140], [141]). Well-known for its self-burying motion [142], this vegetal ejects its seeds over a drying period. Fracture occurs at the interface between two constrained awns. Nonetheless, fracture mechanism is very critical to seed dispersal as it correlates with energetic cost. Minimum energetic cost is required to propel the seed as high as possible while avoiding detrimental premature fracture.

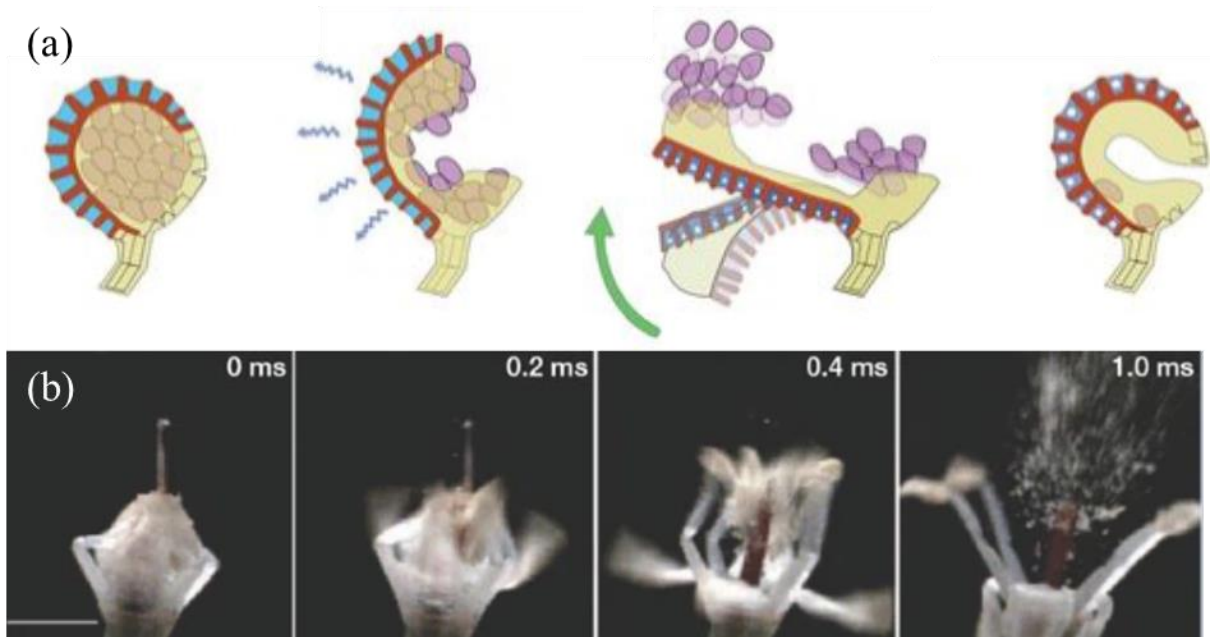


Figure 46: a) Schematic cavitation catapult of Fern sporangia [143]. b) Propelling mechanism of *Cornus canadensis* [138]

To sum up, several motions appear in a plant when subjected to water sorption. While natural systems display a hydraulic slow water-induced motion such as pine cone scale or waterwheel plant, other biological models execute fast motion, e.g. Venus flytrap or Fern sporangia for feeding or dissemination purposes.

### III.3. Example of biological hydraulic actuators

#### III.3.a. Reconfigurable biological models

##### III.3.a.i. Case of pine cone scale

- Description of the mesostructure

Among biological models able to reconfigure their arrangement with moisture gradient, pine cone scale represents one of the most widespread. The complex and unique morphology of cone scales has been widely explored over decades and remains truly inspirational for scientific advances ([144]–[147]).

Different intrinsic and structural parameters have been estimated to understand the thorough mechanism of the reversible folding achieved by cones for its survival. To date, the relation between opening process of pine cone and relative humidity of narrowed environment is a

scientific fact (Figure 47a). The scale of a pine cone is divided into two parts: the bract and the scale (Figure 47b and Figure 48a-c). Bract and scale both exhibit specific amplitudes of curvature which tend to increase when going toward the cone base [144]. This difference may be explained by the thickness gradient along the scale (Figure 48b). This structural organization impacts the tissue swelling after sorption with a change of 34% for bract thickness and 1.7% for scale thickness of the tested *Pinus Rigida*.

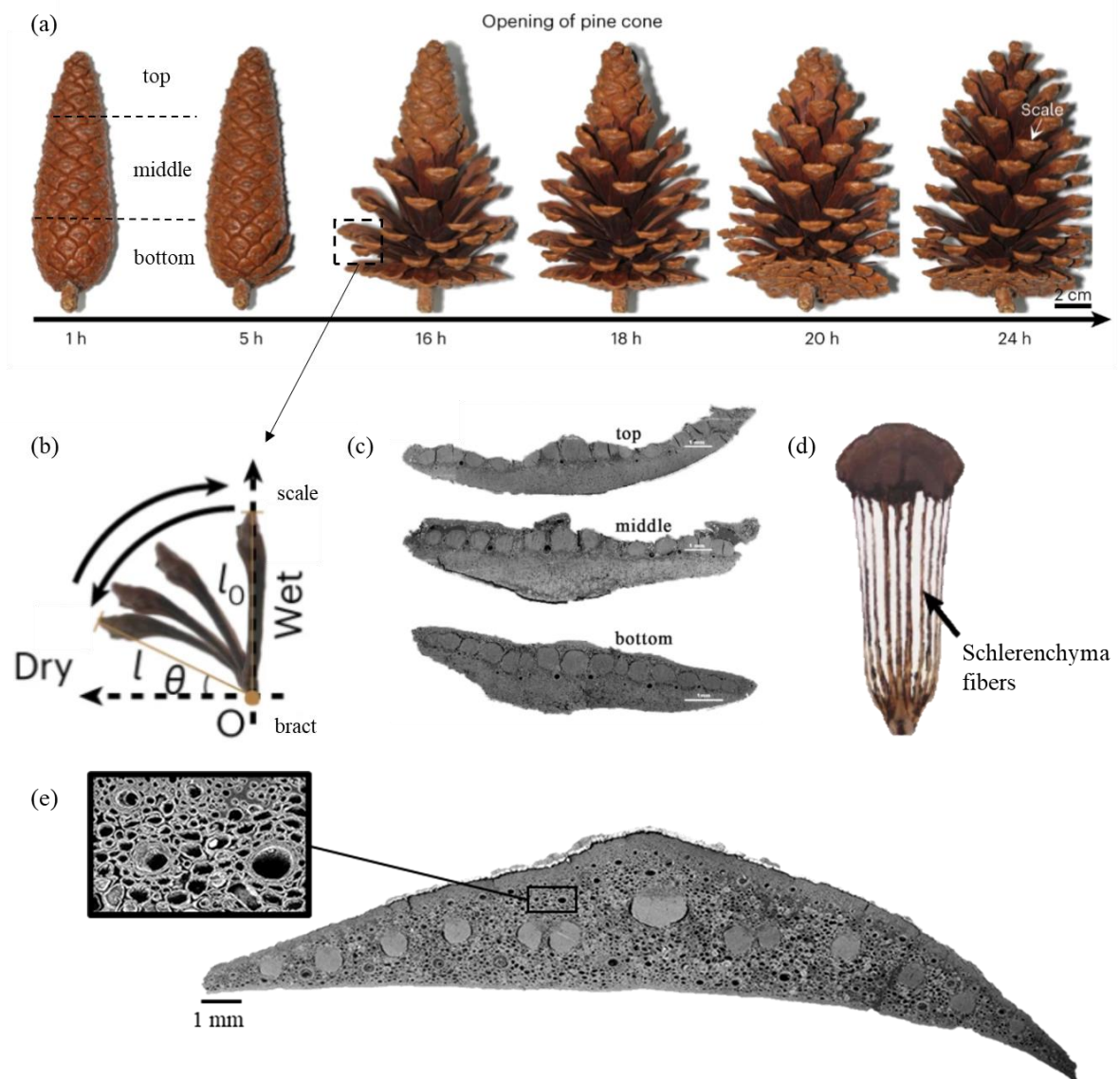


Figure 47: a) Opening mechanism of pine cone at 35°C and 30%-40% RH [148] b) Curving behavior of pine cone scale. c) Middle section of pine cone scale as a function of the location on the cone axis [70]. d) Inner structure of the scale exhibiting schlerenchyma fibers along the length [148]. e) Section of pine cone scale highlighting the presence of resin ducts that intervene in the water transport mechanism.

Sectional slicing of pine cone allows for observing the thorough mesostructure of its scale. Dawson et al. [145] identified several features hidden behind shape-changing ability of the pine cone when facing various humid environments. Actuation occurs thanks to the bilayer configuration of the scale of which inner surface is made of sclerenchyma fibers (Figure 47d) and outer surface of sclereids (i.e. smaller and thicker version of sclerenchyma, more lignified). These two layers do not exhibit either significant variations in biocomposition (cellulose =20%, rest is lignin, hemicellulose and pectin) and water uptake under humid conditions. However, mechanical properties are heavily distinguishable ( $E_{\text{fiber}} = 4.53 \pm 0.90$  Gpa,  $E_{\text{sclereid}} = 0.86 \pm 0.05$  GPa) as well as hygroscopic coefficient ( $\beta_{\text{fiber}} = 0.06 \pm 0.02$ ,  $\beta_{\text{sclereid}} = 0.20 \pm 0.04$ ). Consequently, sclereid (MFA =  $74^\circ$ ) plays the role of active layer while sclerenchyma fibers (MFA =  $30^\circ$ ) act as constraining layer.

The hydro actuation is correlated to the ability of the material to absorb water. The most relevant way nature has found to control the water ingress inside plants relies on the presence of tubular channels which act as water diffusion tunnels to impregnate the different parts. The void distribution is induced by tracheary elements and resin ducts heterogeneously spread within the scale (Figure 47e). In a general manner, voids represent functionalized tools in nature unlike in composites where it is more considered as defects causing the loss of mechanical properties ([149], [150]). Recently, the simplified bilayer configuration of pine cone scale was questioned. A gradient of voids exists inside the sclereid layer. In addition, thickness ratio ( $t_p/t_a$  or  $t_{\text{sclerenchyma}}/t_{\text{sclereid}}$ ) is not constant over the scale's length (Figure 48a-b) and width (Figure 48c-d) thus modifying the geometrical response over moisture change. Therefore, design tools, e.g. 4D-printing, have an important role to play in architecting complex bioinspired prototypes.

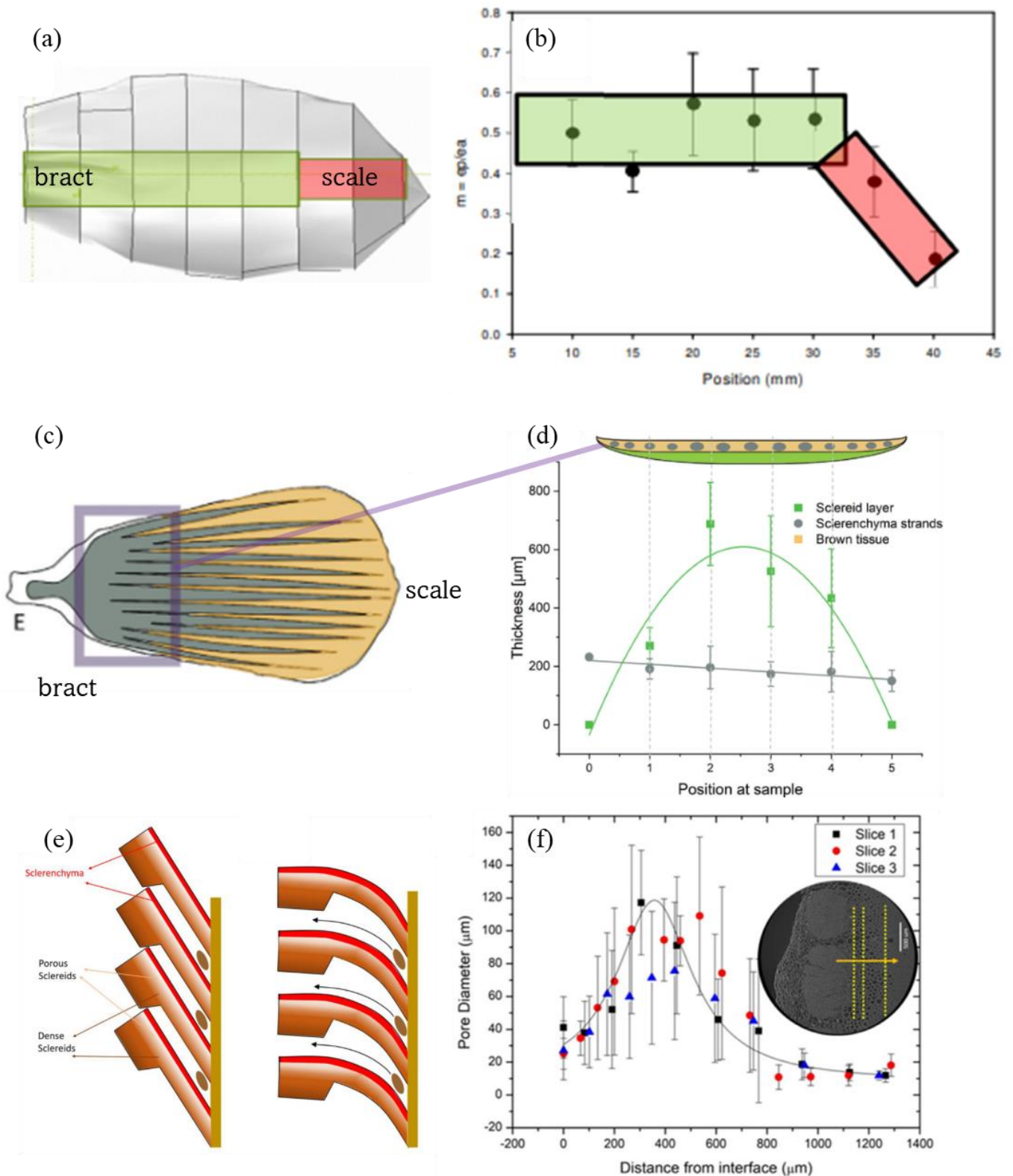


Figure 48: Structural features of pine cone scale. (a) Scale opening relying on a trilayer-configuration and (b) Evolution of pore diameter inside porous sclereid as distance with sclerenchyma layer increases [151]. Thickness ratio between sclereid (passive) layer and sclerenchyma (active) layer (c-d) in the scale length [152] and (e-f) in the scale section [146].

- Specific motion and sequentiality

Originally based on single curvature interpretation of pine cone scale motion during moisture change ([62], [145]), recent works on pine cone scale have evidenced a more complex motion ([153], [154]). Indeed, cones are natural prototypes able to exhibit a multiple curvature of their scales to maximize either the seed protection or dispersal. Following a multi-phase curvature occurring at different time scale (Figure 49). A bifurcation of curvature occurs around 30% of relative humidity where the longitudinal curvature, i.e.  $K_x$ , overcomes the transverse one, i.e.  $K_y$  ([153]). As well as speeding up response, this actuation scenario makes the scale more compact and reduces its geometric rigidity to improve longitudinal actuation.

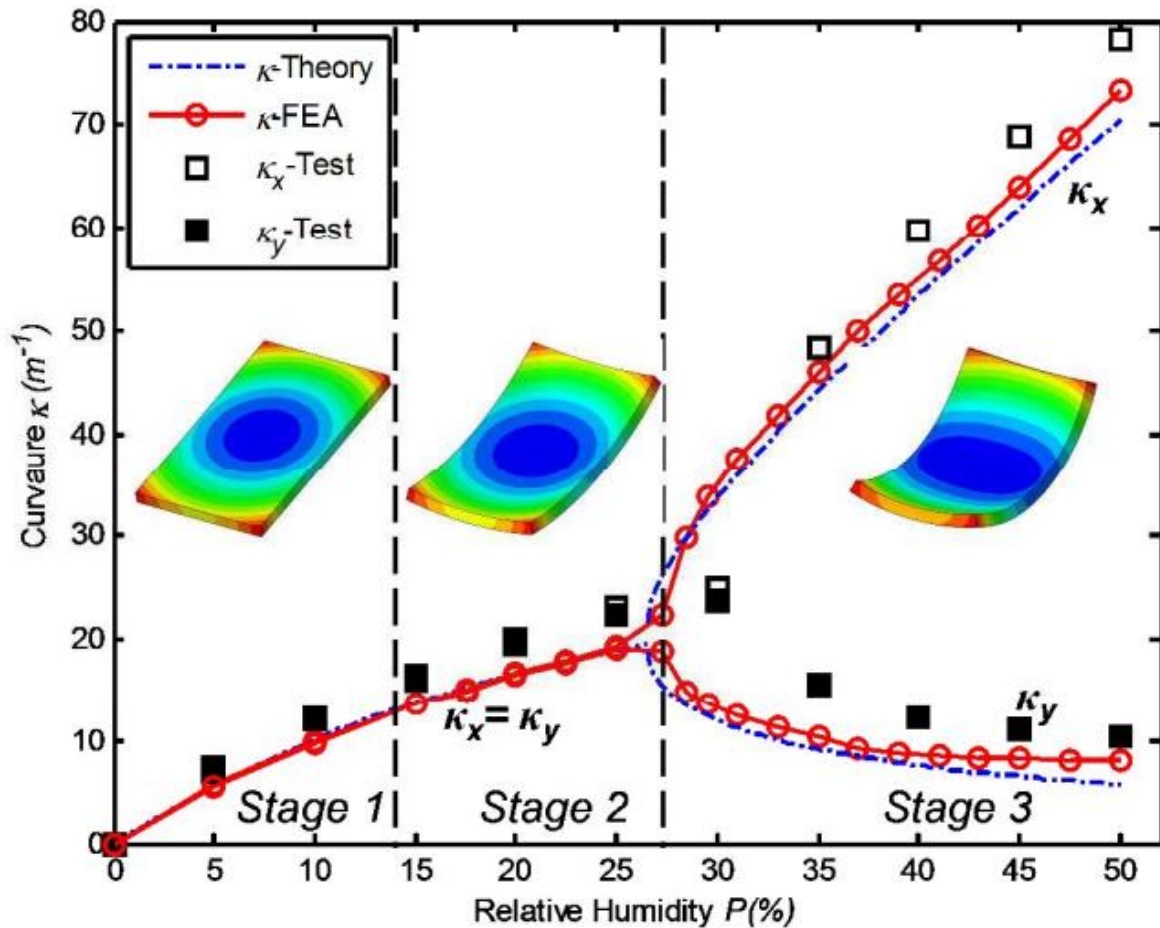


Figure 49: Evolution of longitudinal ( $K_x$ ) and transverse ( $K_y$ ) curvatures as a function of relative humidity. The intersection ending stage 2 represents the bifurcation point [153]. The bistability represents the two stable shape states that a material can reach due to an external action, the transition between those states is highlighted through the bifurcation between the longitudinal deformation  $K_x$  and the transversal deformation  $K_y$  and the profile of the main curvatures.



### III.3.b. Towards 4D-printed Hygromorph biomimetic prototypes

Inspired from the bending behavior of pine cone scales, Reyssat et al. [62] were the first to convert this empowering natural mechanism to the design of artificial hygromorph. They evaluated the kinetic of sorption of a cellulosic paper/polymer composites where only one extremity was in contact with water. Based on Washburn's law, they observed a power law between the position of water front (migration over the material) and immersion time.

Recently, some articles have targeted the potential of 4D-printed HBC to reproduce biological motion. For instance, using 4D-printing for designing pine cone scale is powerful since the in-plane architectural entities totally change along its length and width. Both thickness and aspect ratio evolve to allow a precise and efficient opening/closing transition of the scale upon moisture gradient. This detailed architecture is hardly practicable for conventional manufacturing processes which do not give a local control of matter distribution.

Inspired from Bhutan pine, Correa et al. [154] explored the double-curvature mechanism during the shape-changing of the scale whose transversal and longitudinal curvature were alternately predominant at a specific humidity range. For this reason, they attempted to design artificial prototype made of wood-polymer composite (active layer) and acrylonitrile butadiene styrene (passive layer) by performing water gradient cycle on 4D-printed bilayers. 4DP scales exhibit a two-step water-induced actuation - starting with first transversal curvature followed by longitudinal curvature (Figure 50).

#### *III.3.b.i. Multiple actuation*

This behavior successfully matches with bistable shape-changing pattern of Bhutan scales. However, the process repeatability of 4DP prototypes did not reach the exceptional sustainability of the natural pine cone scale able to overcome 50 successive full motion sequences. Delamination of the artificial scale was noted after 13 full motion sequences in

complete immersion. Finally, printed structural set-up slightly affects the shape-changing behavior of 4DP samples to reproduce such complex biomimetic actuation (Figure 50a) where elasticity gradients governs the double curvature self-shaping [155]. More examples drawing on a shape/deformation relation are available. For example, self-shaping curved folding mechanism reproduces origami-like structures by distributing the actuation throughout the bending surfaces (Figure 50b) [156]. On another strategy, Vazquez et al. [157] took benefit from the elementary bending potential of wood-based bilayers to exacerbate their responsiveness to Kirigami geometries (Figure 50c).

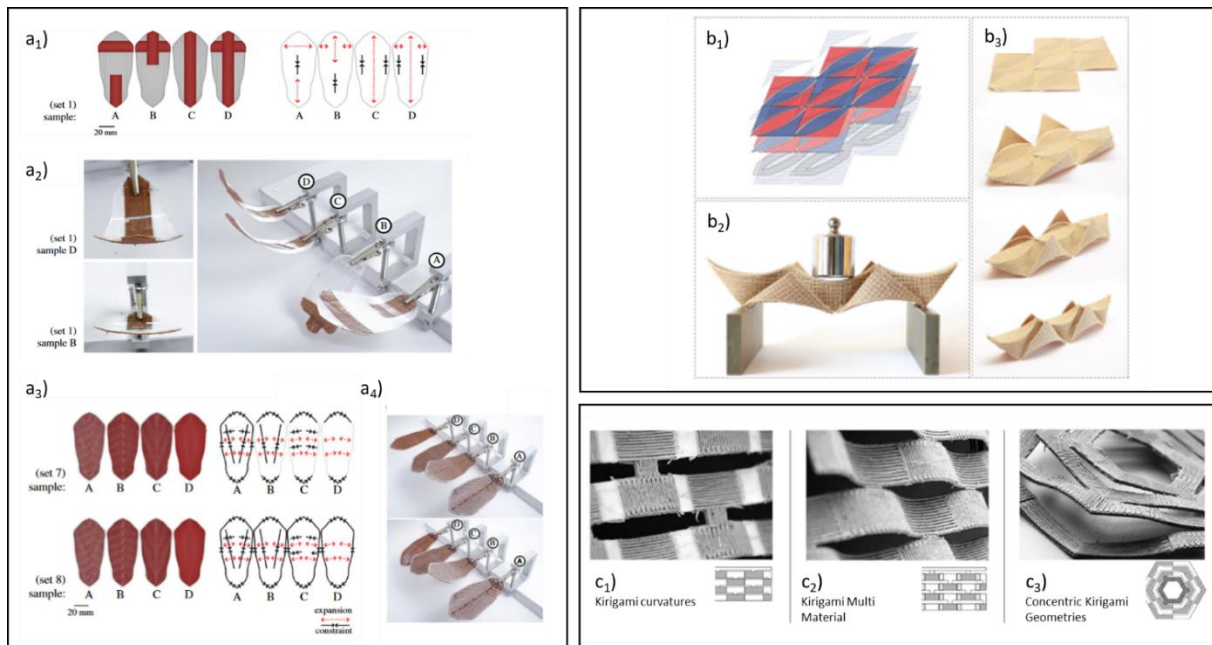


Figure 50: a<sub>1</sub>) Set model and a<sub>2</sub>) 4D-printed specimens of HBC with single curvature. a<sub>3</sub>) Set models and a<sub>4</sub>) 4D-printed specimens of HBC with double curvature due to specific in-plane stress distribution [154]. b<sub>1</sub>) Computational design of 4D-printed wood-based prototypes with multiple actuation. b<sub>2</sub>) Same 4D-printed prototype under 200g load. b<sub>3</sub>) Actuation of curved-folded structures upon drying stage. [156]. c<sub>1</sub>) Kirigami curvatures, c<sub>2</sub>) Kirigami multi material and c<sub>3</sub>) Concentric Kirigami Geometries made of wood fiber composite [158].

Recent review papers on designing 4D-printed HBC have appeared ([87], [159]). The two main fields of application of HBC are biomedical and engineering structures. In biomedical, innovative structures are being developed for drug delivery [160] or bone recovery [161]. Shape-changing abilities of HBC depend on multiple factors related to both mesostructural design and external conditions. Natural fibers and polymers matrix exhibit a difference in

sensitivity to water uptake or thermal gradient. However, in real situations, it is difficult to uncouple these two stimuli.

### *III.3.b.ii. Sequential morphing*

Sequential response is a proof of architectural control and tunable reconfiguration. Its aims to program the kinetic of response of reconfigurable entities to attribute an optimized final shape. One of the examples widely targeted by 4D-printing is the opening of flower's petals such as Lily flower [120]. Methods for encoding temporal shape evolution inside architected shells have recently been published [162]. Spatio-temporal information can be embedded in the geometry of architectural shells that morph from flat to smooth 3D shapes (Figure 51). The presented shells exhibit a trilayered configuration with two recovering 3D-printed polymer layers a pre-stretched elastic membrane. Polymers included inside outer layers are actuated over  $T = 56^{\circ}\text{C}$ . At room temperature, the structure remains flat and the middle layer stores the energy necessary to drive the deformation. Having the same biochemical composition but with a different mesostructure gives a different morphing pattern that can be optimized to avoid collisions of petals as imaged in Figure 51a and Figure 51d.

Other thermomorph bilayers have unveiled new concepts of temporal morphing. Stoychev et al. [163] developed PMMA/thermoreponsive hydrogel six-ray star-like bilayers of which edge-activation allows for tuning the order of folding. After what, they upscaled this strategy to the formation of smart thermomorph pyramids.

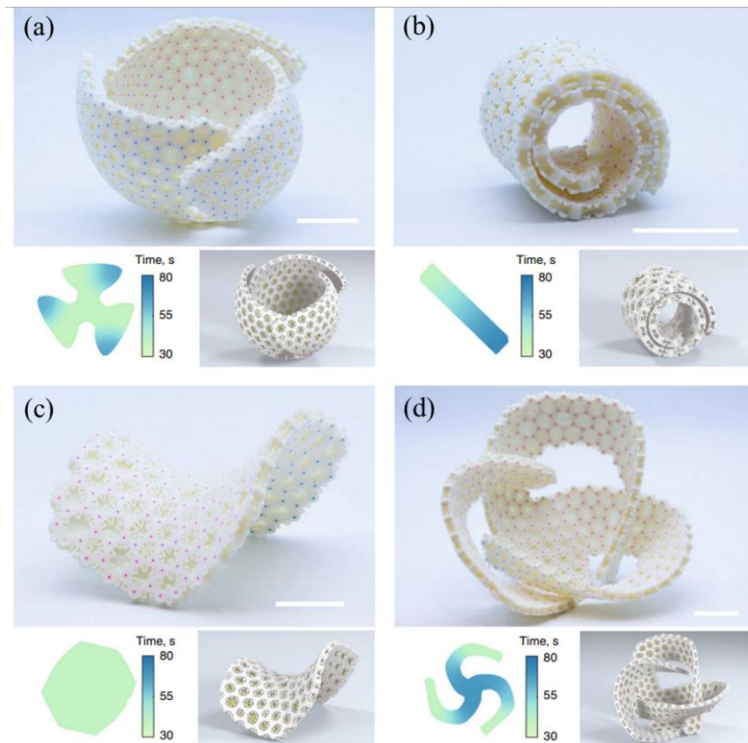


Figure 51: Sequential response of divers shell architectures. (a) Homogenous recovery of petals by slowing down the reactivity of one specific side. (b) Spiral-like configuration reached by maximizing the reactivity of one side of the beam. (c) Saddle-like configuration induced by a hexagonal shape. (d) Complex interweaving architecture optimized by distribution of reactivity from the center to the edges. Scale bars = 3 cm [162].

Regarding HBC structures, interesting first trends are today claimed in scientific literature. The sequential deployment of hygromorph biocomposites was explored by Tahouni et al. [164]. They displayed three strategies to control the timescale motion based on the following parameters: active layer thickness ( $t_a$ ), localized mesostructural cavities within functional layers and the addition of blocking layer regulating the water sorption/desorption within the structure. From the bilayer scale, actuation speed and amplitude can be programmed by the active layer thickness. Being directly linked to the surface-to-volume ratio, an increase in composite thickness leads to a reduction of the actuation rate. Multi-element and single-element composite structures have been successfully engineered as a prototype of natural concepts such as the silver thistle (Figure 52a). By configuring the active layer number  $N_a$  (related to the active layer thickness  $t_a$ ) and the interfilament distance of the passive layer ( $ID_p$ ), sequential motion in multiple stages were proposed (Figure 52b).

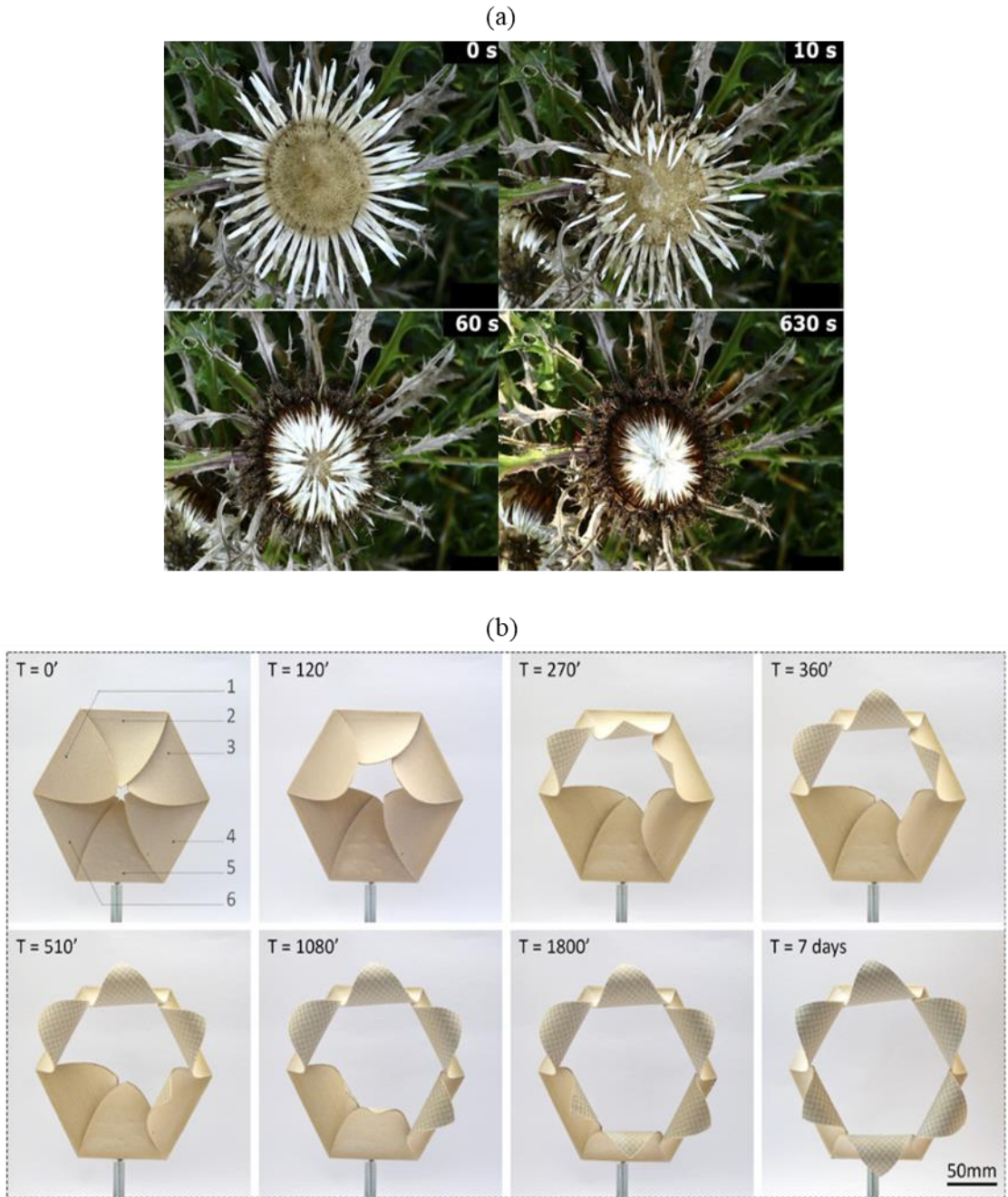


Figure 52: (a) Wetting-induced closing mechanism of silver thistle. (b) Wetting-induced opening mechanism of 3D-printed biocomposite bilayers [164].

III.3.b.iii. Towards more complex deployable structures based on Hygromorph

Today, optimization devices and methodological tools exist to formulate and design HBC prototypes catering targeted functions [159]. The threshold between mechanical stability and morphing ability inside 4D-printed materials remains subtle. Developing smart structures without sufficient mechanical performances would not be relevant for most applications. For this reason, the relation between resistance and actuation of shape-changing metamaterials must be known.

Following this strategy, 4D-printed hydrogels or SMP with variable stiffness / thickness ratio have been successfully designed ([165], [166]). Ren et al. [165] managed to reproduce complex shape-changing motions of which the actuation relies on a moisture and thermal gradient. The printed bilayer was fabricated from the overlaying of Shape-Memory Polymer polyVinyl Chloride (SMPVC) on water-swellaable PolyUrethane (PU) layer. Modifying the thickness of PU-active layer affects the radius curvature of bilayers (Figure 53a).

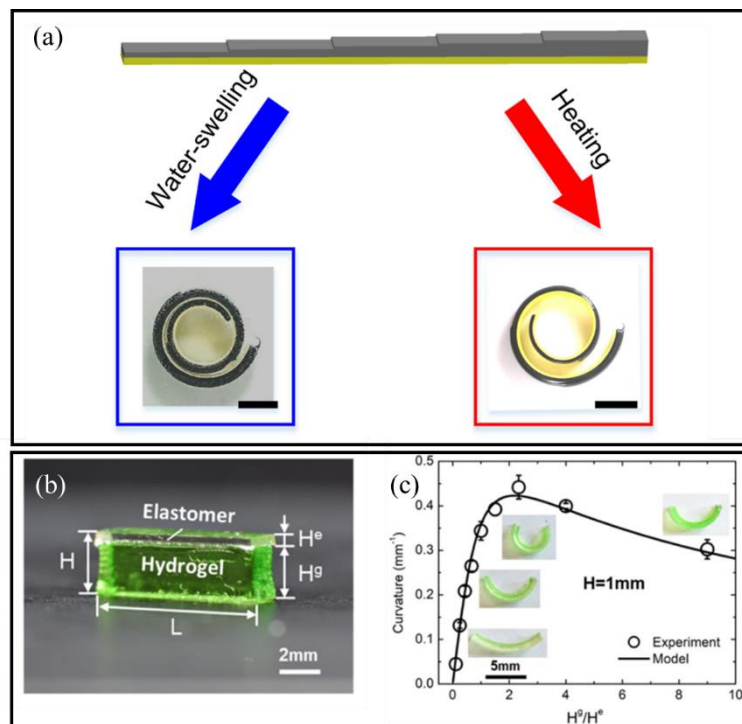


Figure 53: Impact of thickness ratio on 4D-printed (a) water/thermo sensitive PU/SMPVC bilayers [165] and (b-c) water sensitive hydrogel/elastic bilayers [166]

Bastola et al. [167] found inspiration in the *Selenicocus setaceus*, a cactus able to adapt its stem to climb walls and cliffs. One of its assets remains in the adaptation of its morphology along time which directly affects its properties (especially the flexural rigidity). The old part of the stem shows a circle-like cross-section the less mature stem exhibits a triangular cross-section and the youngest part's one looks like a star. They managed to 3D-print water-induced shape-changing materials which mimic the morphing mechanism of the cactus stem from the old stem to the youngest one by targeting the swelling and deswelling process of hydrogels (Figure 54).

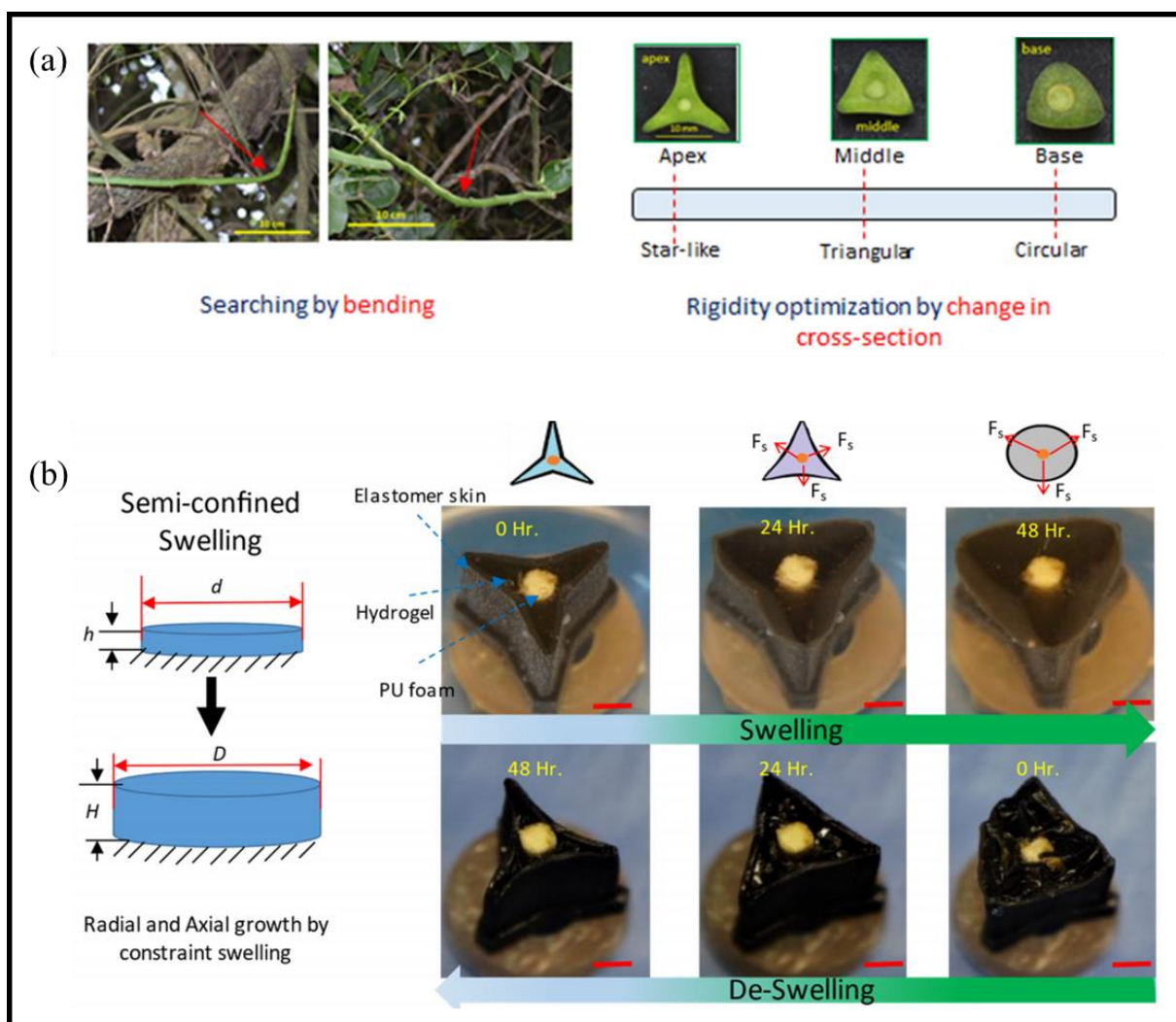


Figure 54: a) Bending behavior of *Selenicocus setaceus* exhibiting a variable stiffness stem and b) 4D-printed inspired prototypes [167].

As a consequence, composites with variable stiffness have been developed in a biomimetic ([168], [169]) and mechanical approaches [170]. Regarding HBC, Cheng et al. [155] succeeded

in 4D-printing a multifunctional orthotropic splint made of an active wood-polymer layer and a passive copolyester layer. Besides promoting the structure warping around the forearm, the variable stiffness of the splint might also maintain an adequate pressure on the desired wound areas exclusively (Figure 55). This complex reshaping results from a thorough relation between design concepts and additive manufacturing [159].

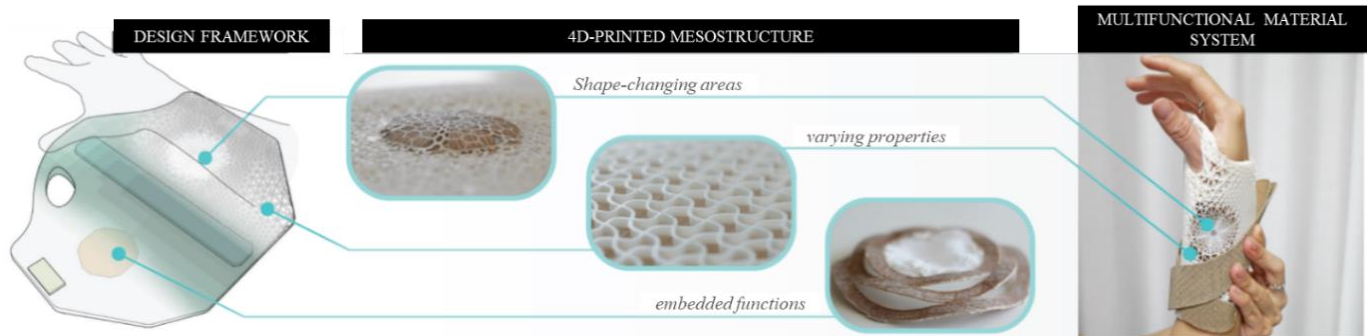


Figure 55: 4D-printed wood/copolyester splint with functionalized areas (adapted from [155]).

Then, based on the fitting of their rigorous analytical model and experimental data, Van Manen et al. [171] aimed to predict the shape-changing properties (curvature and stiffness of lattices) by programming the inner structure of the material (stiffness ratio, thickness ratio, aspect ratio). The control of morphing potential based on these structural features is provided in Figure 56. This work opens the door to incremental progress in redefining the scope of HBC.

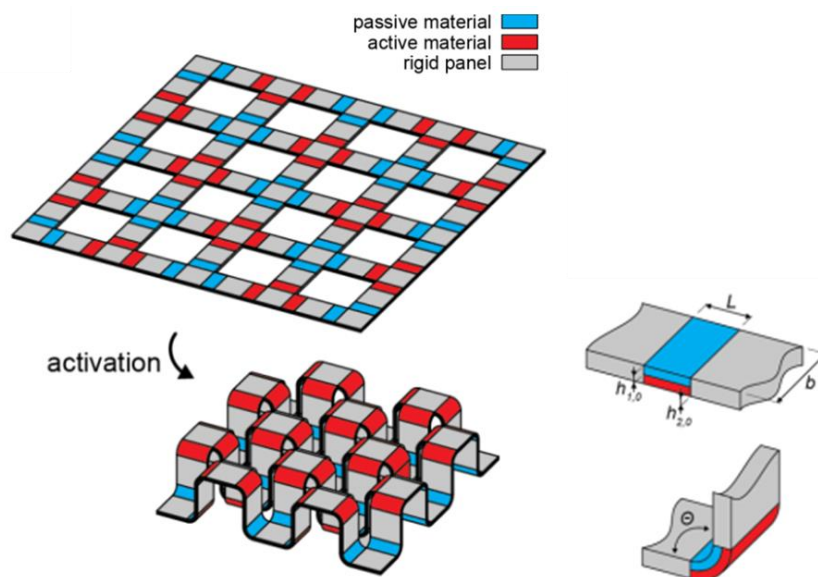


Figure 56: Numerical simulation of shape-changing material with complex distribution of active/passive layers [171].



### III.3.b.iii. Deployable lattice structures

The design of shape-shifting structured lattices has known a high development in recent years for several printed materials (elastomeric ink [172], shape-memory polymer [165], photopolymer resin [173], biocomposites [155], [156]).

Extrapolating the curving behavior of elemental bilayers, scaffold structures may generate cellular expansion. Two successive bilayers bound at the edges (hinge area) may form an active cell (Figure 57). However, the amplitude of actuation given by simple bilayers remain higher than cellular pattern because of geometric constraints that are induced by the rigidity and resistance of the hinge area [174].

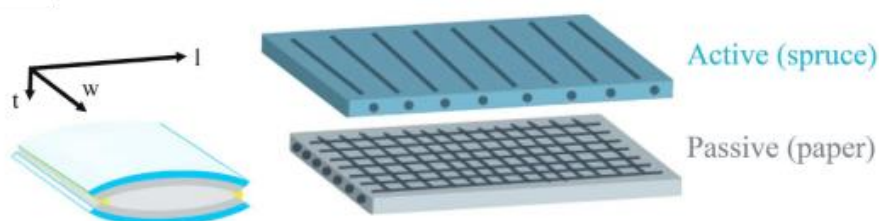


Figure 57: Cell formation by overlaying two bilayers [174]

Besides, the opening of the lattice network such as honeycomb or Gridshell structure have been achieved ([157], [174], [175]). In parallel, Wang et al. [176] designed a biotic bilayer actuator made of a biological block copolymer (SELP) and cellulose nanofiber (CNF). The stimuli-responsive behavior of this system was induced by the swelling of the SELP hydrogel matrix. Changes in temperature or due to the ionic strength of the environment leads to structural modifications of the matrix which alter the water ingress and transport inside the copolymer and affect its deployment process. This kind of actuators remains a source of hope for the biomedical sector ([177], [178]).

Cellular shapes are a triggering point of lattice expansion as highlighted by Figure 58 ([173], [179]). Disclosed by Figure 58, the set anisotropic thickness and elasticity of bilayers drives the direction of expansion via functional patterns (pattern height, resolution, grid distribution,

amplitude and frequency). Although working on thermomorph, Keshavarzan et al. [173] evaluated the shape recovery and shape memory effect of two specific cellular lattice structures: Rhombic and Body-Centered Cubic structures. Made by vat polymerization 4D-printing of a photopolymer resin, their compressive responses related to a temperature gradient were measured. Overcoming a quasi-static loading-unloading cycle at 20°C, Rhombic structures propose a wider range of mechanical properties, i.e. reaching a Young modulus of 26 MPa, and a higher specific absorbed energy of  $7.3 \cdot 10^{-3} \text{ J.kg}^{-1}$ , compared with BCC structures ( $E = 5 \text{ MPa}$ , specific absorbed energy =  $0.2 \cdot 10^{-3} \text{ J.kg}^{-1}$ ). They found out that the processing temperature as well as the structural matter arrangement impacts the energy absorbed and released by the material over different loading/unloading cycles which finally dictate the shape memory effect of a printed material. This can directly be correlated with Ashby's consensus on mechanical properties of cellular structures whose performances are affected by the cell shape [180].

To complement this state of the art, Li et al. [181] described a new epoxy thermoset polymer which could be used for Multifunctional Lightweight Architectures. Their work was devoted to the mechanical and shape memory effect of microlattice networks. Analyzing different lattice shape and length, they showed that the cubic shape presents the best mechanical performances (compressive strength and strain-energy storage) than Kelvin and octet unit cells. Cubic microlattices exhibit interesting properties regarding the shape memory effect. Their strain recovery achieved 83 % at 100 °C and their recovery stress was around 3.4 MPa meaning that they can exert a significant force during their recovery process. However, the most interesting architecture for SME is the cylindrical geometry since it recovers 97 % of its initial shape after a loading/unloading cycle. Finally, they explained that the strength is regulated by the intrinsic properties of the used matrix and the specific architecture given to the 3D-printed material.

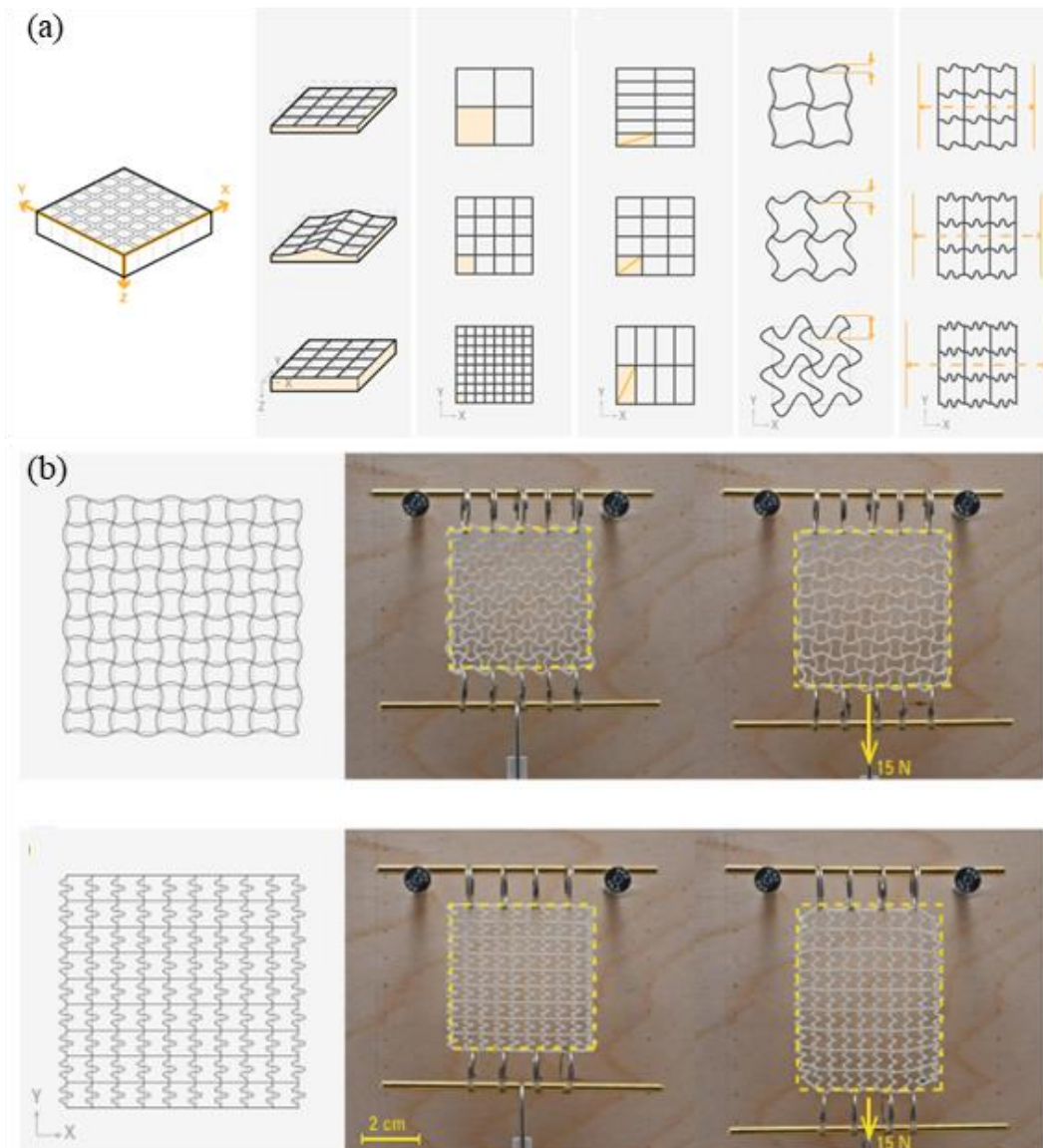


Figure 58: Functional patterns used to design shape-shifting lattice patterns. b) Directed cellular expansion by tuned 3D-printed pattern [179].

Besides, Gridshell structure presents architectural assets for load-bearing applications ([182], [183]). The crossing double-curvature shell in a grid shape is very trendy to fabricate lightweight architectures with significant mechanical stiffness and strength. Innovation led scientists to imagine environmentally responsible Gridshell structures. 3D-printing and slicing parameters (Total Layer Count, Layer Height and Thickness ratio) allows for the shape-shifting of functionalized Gridshell structure. With an optimized tool-paths, active hinges and non-active surfaces, it is possible to recreate structures with sequential reproducible bending/folding [157].

#### IV. Potential asset for marine restoration and artificial reefs

The depletion of biotic resources along coastal zones and in the Oceans, which is a very worrying problem since several decades, continues to alarm society and arises the interest of the scientific community. Highly impacted by overfishing, acidification of the ocean, climate warming and anthropogenic pollution, marine species live today in dramatic conditions which could lead to a massive extinction of the sea wildlife in the coming centuries. According to the GIEC report on the Ocean and Cryosphere [184], the marine biomass is predicted to decrease of  $15.0 \pm 5.9 \%$  at the end of this century. This forecasted drop is the consequence of global warming affecting directly marine ecosystems, i.e. especially coral reefs that are essential for the marine life cycle. This reduction will affect both the marine food chain and the human society since the number of fishing catches is estimated to drop between 20.5 and 24.1%.

For this reason, scientists have imagined different solutions to fix this problem. Boström-Einarsson et al. [185] recently listed a set of investigations carried out the restoration of the coral reef. They elaborated a state of the art of the methods and techniques which have been used over the four last decades to rehabilitate the ocean floor (micro-fragmentation, direct transplantation, larval enhancement, artificial reefs).

Artificial reefs are human deployed structures immersed in water to promote the resettlement and restoration of damaged marine ecosystems. Firstly immersed in Japan 300 years ago [186], many coastal countries have decided to accentuate their investigations on this deployed structure for environmental, fishing and touristic purposes. Strategical thinking has arisen from the conception of artificial habitats to optimize their implantation in seawater all around the World (Table 3). From 1960, the number of publications related to the development of artificial reefs has known an exponential growth, testifying the global interest on this ecological lever (Figure 59) [187].

Table 3: Number of articles published by the main countries with studies on artificial reefs. The category "other" regroups investigations on socio-economical, behavior, management and mitigation, oceanography and environmental impacts (adapted from [187]).

Countries	Ecology	Engineering	Review	Other	TOTAL
United States	95	3	16	41	<b>155</b>
China	21	23	1	19	<b>60</b>
Australia	27	2	10	12	<b>51</b>
Brazil	40	1	3	4	<b>48</b>
Italy	24	3	4	7	<b>38</b>
UK	12	1	8	16	<b>37</b>
Japan	13	7	2	10	<b>32</b>
France	12	2	4	12	<b>30</b>
Portugal	11	5	2	10	<b>28</b>
Spain	7	2	4	8	<b>21</b>
Israel	8	0	1	9	<b>18</b>
South Korea	1	7	1	4	<b>13</b>

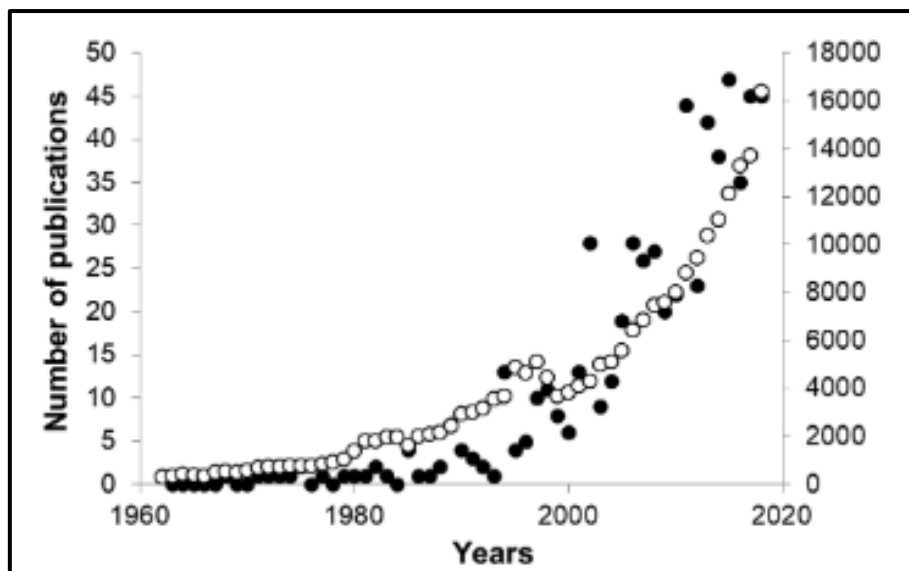


Figure 59: Number of publications tackling the development of artificial reefs (black dots) from 1962 to 2018 in line with the evolution of publication on general ecology (white dots) [187].

Artificial reefs are immersed to supply a substrate for organisms adhesion and biofilm growth. Biofilm formation on an immersed surface can be defined in four steps. At the beginning, organic molecules interact with the substrate where physical bonds are created. As soon as this thin layer named conditioning film has formed, marine organisms such as bacteria and diatoms can interact and hang to the substrate. Then, bacterial metabolism generates an accumulation of microorganisms working together to create a bacterial community called biofilm ([188], [189]). The microbial and biochemical composition of biofilm dictate the diversity and distribution of colonizers. Indeed, as it depends on the microbial community, biofilm can

promote or inhibit the adhesion of bigger marine organisms [190]. Among them, marine bacteria are known to be the first colonizers considering their massive presence in seawater going from  $10^5$  to  $10^6$  cells/mL [191]. Then, bigger organisms, e.g. diatoms or microalgae, are attracted by the nutrient release of the bacterial community. Finally, communities of macrofoulers (e.g. barnacles, invertebrates) develop at the surface to finalize the growing process of marine biofouling (Figure 60).

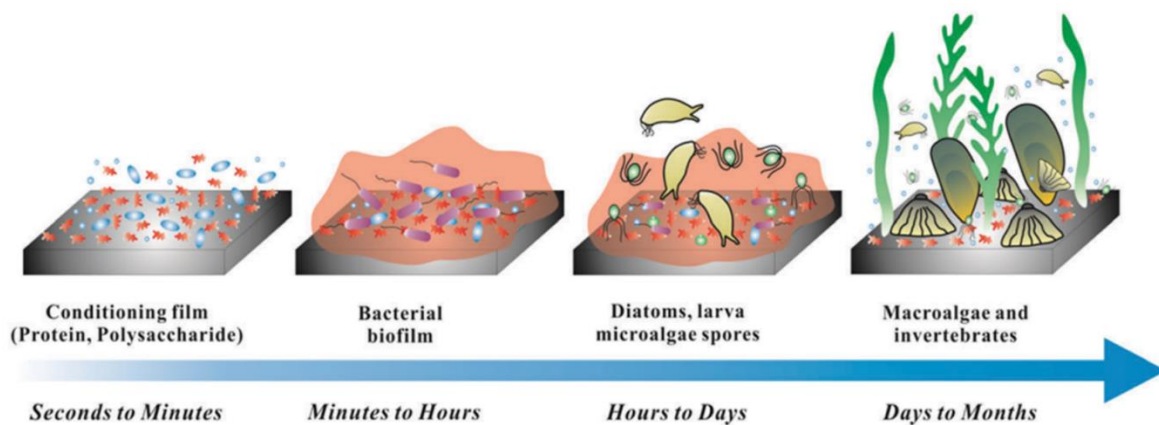


Figure 60: Biofouling mechanism of marine micro- and macroorganisms on a material surface (taken from [192]).

## IV.1. Material selection

A first essential reflection point concerns the biochemical composition of the structure. Two subparts are developed for optimizing the function and efficiency of an artificial reef. At first, the selection of the material to positively interact with marine organisms is tackled. Then, the question of seawater ageing of the material is raised to angle the development towards innovative artificial reef with controlled lifetime. Indeed, the biodegradable aspect of artificial reef has already shown a positive impact on marine restoration as it complexifies the food web and increase the accessed trophic level [193].

### IV.1.a. A promotor of marine biofouling

No need to explain that artificial reefs must be biocompatible with marine organisms. A particular issue was related to the belief that a material favorable to colonization was sufficient

to be considered as an artificial reef. Studying the resettlement of marine species on the reef means studying the interactions between marine flora and the support as well as the end-life process of the material. Fact which is today reviewed since the introduction of materials in some areas has led to a successful reimplant of marine life on initially deserted area but of which the degradation process released toxic and harmful chemicals for the colonizing species and more generally for the marine life cycle. This is especially the case of tires [194] which have been used over several decades as a helpful support in the recolonization process (Figure 61) and are now being removed from the Oceans. More interested by the recruiting potential and life restoration of tire reefs, their environmental impact was rarely handled. Reflection process did not connect with life cycle analysis of the material and toxic agents have been disseminated in seawater. For instance, tires release metallic trace elements - e.g. zinc, copper, lead and cadmium - that were present in several colonizing organisms (hydrozoans, bryozoans and ascidians). While not affecting the restoration of an ecosystem in the early stages, these toxic atoms will impact the sustainability of the reef in a negative way [195].

Making a similar assumption, wrecks have, for a long time, been considered as suitable surfaces for benthic organisms. However, these living organisms do not grow similarly on artificial reefs by comparison with natural reefs (Figure 62). Walker et Schlacher [196] underscored the fouling variations in coverage rate and species richness between artificial reefs and natural reefs. After 3 years of immersion, only 25 species recovered the wreck surface against 48 on natural reefs. To enhance the biodiversity on the wreck, a longer immersion time is recommended. Besides, sessile species such as hard corals needs time to mostly colonize the reef, e.g. around 8 years, while mobile species like fishes are twice as many after only 2.5 years [197].



Figure 61: Picture of tires immersed in seawater off Florida [194]

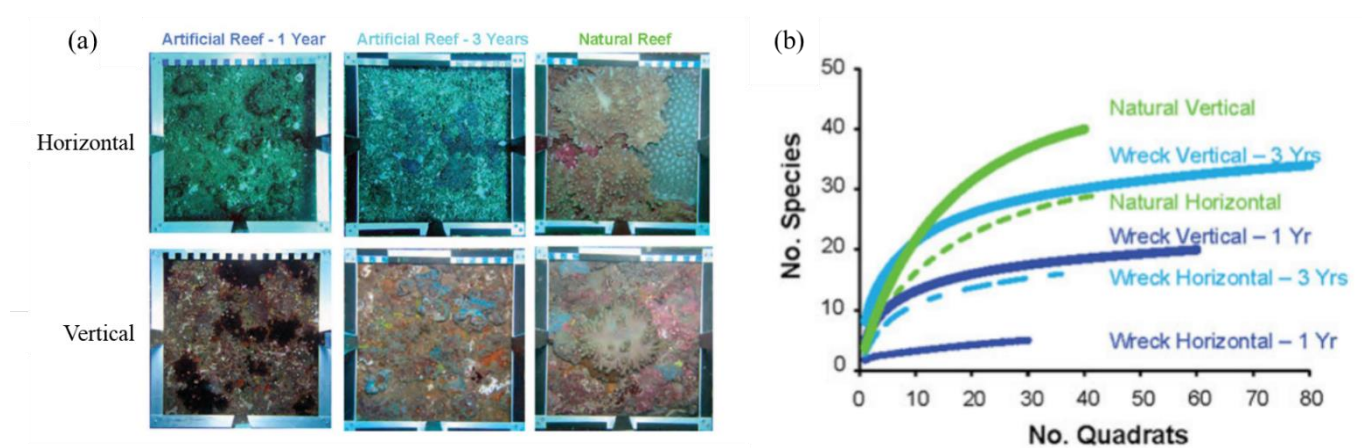


Figure 62: (a) Quantitative and (b) qualitative assessment of marine biofouling on artificial reefs (wreck) and natural reefs [196].

For decades, concrete block has asserted its position as the most adapted material for designing artificial reefs thanks to its toughness, surface roughness, affordability and processibility ([198], [199]). Though resistant to waves as exhibited by the Atlantic Wall vestiges, concrete ends up into irremediable fragments and/or sediment landfills where metals and additives products are released over structural degradation [195]. Unfortunately, concrete blocks are non-biodegradable materials that do not disappear after their immersion in seawater. Since artificial reefs may induce ecological degradation, their installation must be included in the principle of “zero irreversibility”, arguing that any anthropic action on the planet must be reversible [200]. Moreover, overcoming successive colonizing stages over the years, the efficiency of the artificial habitat is abated. Renewing the immersed structure is essential to maintain significant



interactions with marine organisms and reenergize reef restoration. This long-term inefficiency of immersed reefs has been leading scientists to reconsider their strategies. Since the use of permanent reef does not bring general agreements, our thoughts are given to the use of biobased and/or biodegradable artificial reefs with a controlled lifetime as adaptative solutions [193].

In 2019, a state of the art of tested materials for artificial reef creation was published [187]. Figure 63 displays materials widely tested for optimizing biochemical composition of artificial reefs. Besides wrecks and tires, marine biofouling of concrete blocks, oil platforms or conventional polymers such as PolyVinyl Chloride (PVC) were also evaluated. Resulting from human excess and carelessness, plastics has been accumulating in oceans and dramatically deteriorating the survival of marine species ([201]–[203]). Their use as component of artificial reefs seems totally unsuitable, and even counterproductive. However, toxicity of plastics has not shown an unanimous effect on marine organisms. For example, the toxicity of plastic leachates on harpacticoid copepod *Nitocra spinipes* has been investigated [204]. Above the 21 tested plastics, only 8 exhibited significant toxicological effect. Though depending on weather conditions, UV-lights, temperature, pH and surrounding stimuli, the degradation of plastics depends upon macromolecular arrangement. The release of plastic leachates takes a longer time with crystalline polymers. Besides, the rigidity of plastics also seems linked to its ecotoxicity since softer plastics were statistically more dangerous than rigid ones (6 vs 2).

Nowadays, a societal wish to employ greener materials that will only positively interact with marine species is proclaimed. Among them, biomaterials from natural feedstock are seen as promising alternative for the future of artificial reefs [205]. For example, a particular attention was drawn to biopolymer matrices (defined in Section I.1.b.) as their biobased origin and biodegradability by terrestrial microorganisms seemed adapted for environmental applications. Indeed, using bioplastics instead of petroleum-based plastics gives two main advantages : 1) a greener production process and/or 2) a full biodegradability under specific conditions [206].

However, they do not represent an unanimous solution to replace environmentally-destructive petroleum-based plastics yet. One of the biggest challenges consists in creating a bioplastic 100%-biodegradable in seawater and of which the degradation products, i.e. intermediary oligomers and final minerals, would be assimilated by marine microorganisms. Even if research papers treating this topic aren't numerous, the impact of plastics depends on the considered biological specie. For example, PLA-bioplastics have an ecological effect comparable to conventional plastics on certain marine organisms [207] whereas it remains innocuous for other species [208]. The use of bioplastics must not be dropped since only few bioplastics have been aged into seawater to evaluate their ecotoxicity. Indeed, the range of existing bioplastics will still be increasing in the following years and other alternatives to current bioplastics (PBAT, PBS, PHA, starch blends, PCL) should be discovered.

Moreover, a reminder is required on the specificities of suitable substrates for marine biofouling. Coral recruitment does not only rely on the density and volume of colonizing organisms but also on their diversity. The durability, biochemical composition and structural complexity of substratum (roughness, microgroove) promote the biofouling activity. Initial benthic communities drastically influence the coral recruitment. For example, while crustose coralline algae is a promotor of marine biofouling, bryozoans, macroalgae, sponges have an inhibitor impact. Leonard et al. [209] quantified the coverage rate and species richness of several materials (PVC, PLA, concrete, fiberglass, ceramic foam). As presented by Figure 64, biofouling potential and species richness are significantly modified by the chosen material and prove its importance in the selection of benthic community to restore a sustainable ecosystem (Figure 64b).

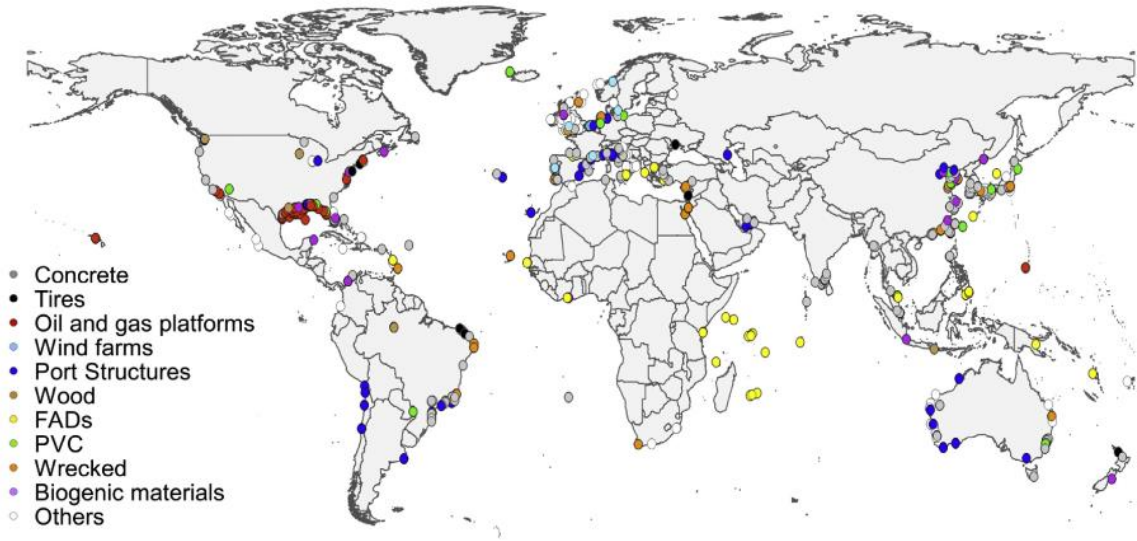


Figure 63: Tested materials as use for artificial reefs all around the globe in 2019 [187]. FAD means fish aggregates devices.

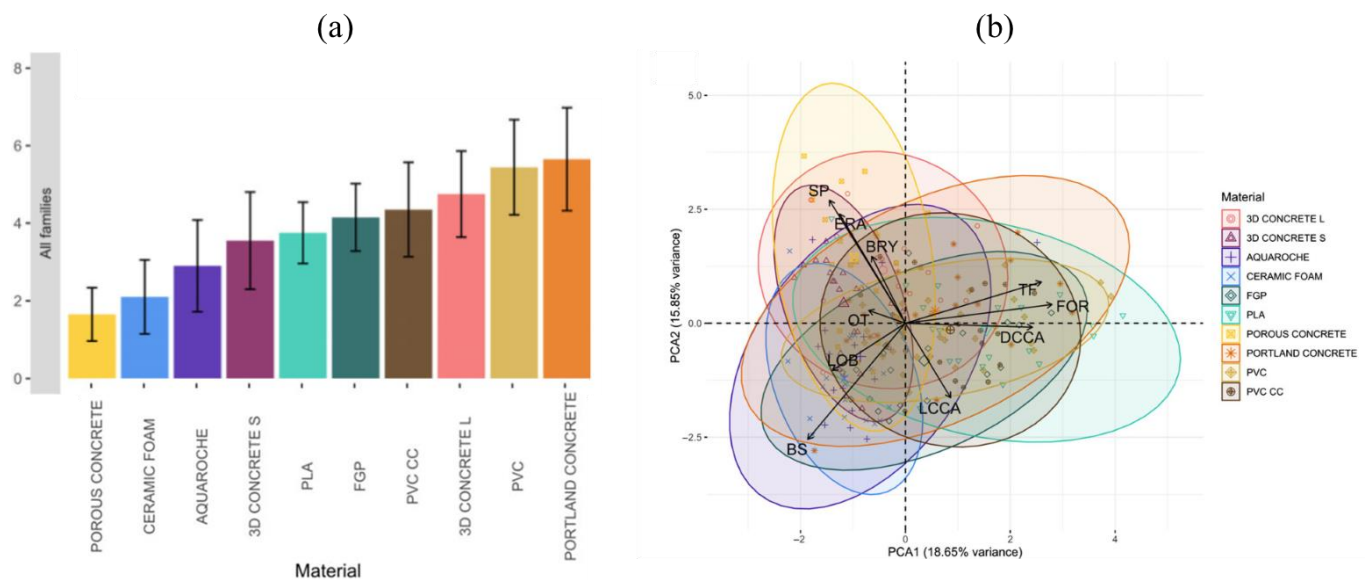


Figure 64: (a) Biofouling potential of various materials. (b) Principal component analysis plot informing about the singular benthic community among the tested materials [209]. The analyzed benthic communities represent Bare substrate (BS), Bryozoans (BRY), dead and alive Crustose coralline algae (DCCA and LCCA), Encrusting red algae (ERA), Foraminiferans (FOR), Lobophora (LOB), Turf algae (TF), Sponge (SP) and other species (OT).

There is still a considerable gap of knowledge on the material selection to design functionalized artificial reefs. The use of natural biocomposites is more and more pronounced in marine engineering for leisure boat essentially [210]. It shows consistent mechanical properties and good stability to vibrations, nevertheless its composition might be optimized for resettlement

purposes. Degradation of natural fibers (e.g. flax fibers) release polysaccharides chains [211] of which the impact on microcellular adhesion has not been explored yet.

#### IV.1.b. Seawater ageing and controlled lifetime of biocomposites

Concrete represents a sustainable and resistant material when immersed in seawater [212]. Comparing to this stiff material, bioplastics are lightweight alternatives of which seawater ageing highly depend on their physico-chemical properties. For example, aliphatic polymers display a variable degradation in seawater that is mainly affected by the environmental conditions (salinity, temperature and living organisms). In Japanese seas, PBAT and PBS matrix exhibited a 7-8% weight loss after 6 weeks of immersion while PBSA and PCL reached a degradation of 80% (Figure 65) [213]. Distilled water and seawater ageing of PLA has been investigated in Lorient harbor (France) by Deroiné et al. [214]. A main impact brought by ageing environment is provided by the presence of mineral salts which makes the water diffusion through polymer chains more complicated. It is specified that PLA does not exhibit significant changes structurally or biochemically until 6 months. This trend is confirmed by Wang et al. [215] which assessed the weight loss of PLA, PBS and PBAT in seawater. None of these bioplastics displayed a weight loss higher than 10% after 6-month immersion time.

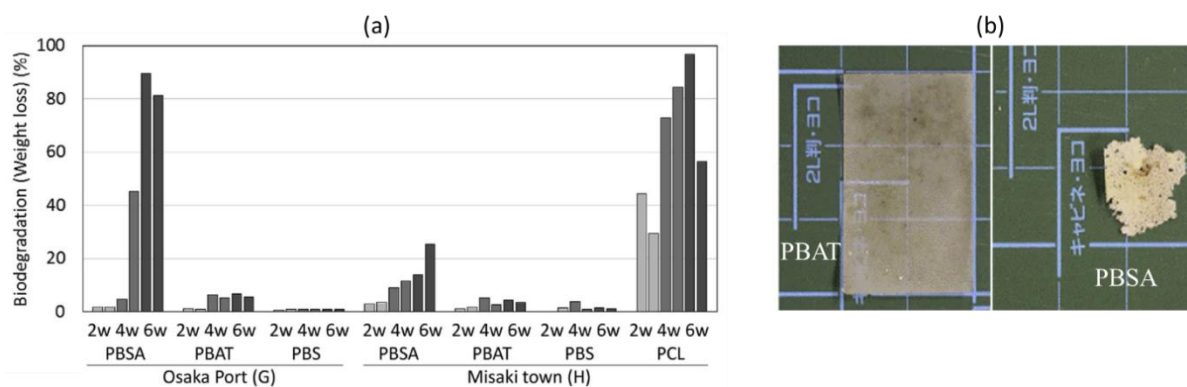


Figure 65: (a) Biodegradation in seawater of aliphatic polymers (PBSA, PBAT, PBS and PCL) in Osaka port and Misaki town for a 6-week immersion. (b) Films of PBAT and PBSA after 6-week of immersion in the sea at Osaka port [213].

In marine applications, the lifetime of a biocomposite is reached when the mechanical properties decrease from 80% of their initial values [216]. The reduction of mechanical

performances of these materials after water uptake is based on different factors. Firstly, water uptake brings chain scissions of the PLLA matrix (representing the hydrolysis mechanism) that affects the mechanical behavior of the biocomposite. Secondly, the higher anisotropic swelling of flax fibers compared to PLLA-matrix creates stress at the fiber/matrix interface. Moreover, water going through flax cell walls reacts with hydrophilic groups of hemicellulose and pectin chains lowering the stress transfer ability of the structure. During fiber leaching, internal compounds are extracted by water flow such as uronic acid and sugar (Figure 66). The loss of functional polysaccharides from the pectin region such as uronic acid is showed to highly impact the fiber stiffness since it is in charge of stress transfer between microfibrils [211].

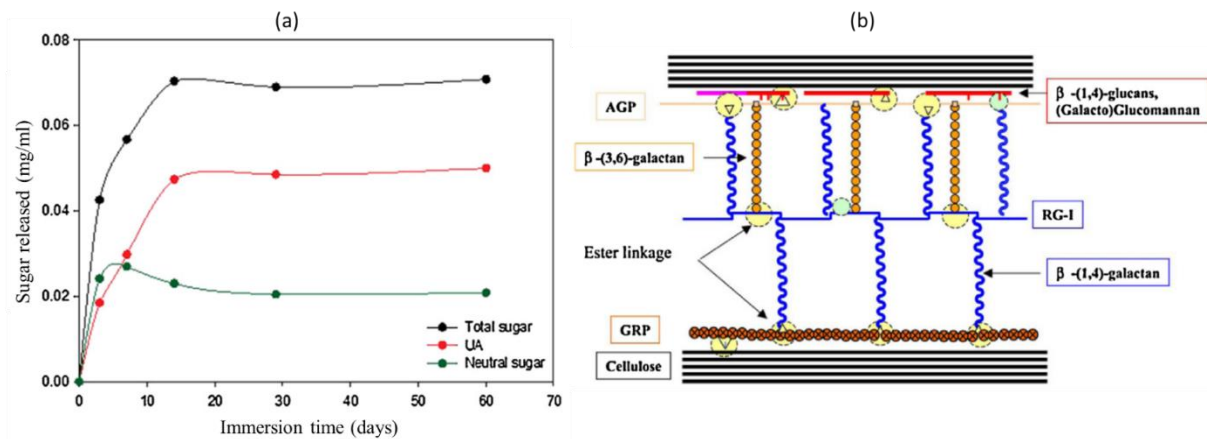


Figure 66: (a) Evolution of sugar released of flax fibers as a function of immersion time [211]. (b) Schematic view of S2 cell-wall of flax fiber [217].

Although more or less resilient to water uptake and marine colonization depending on their formulation, the degradation in seawater of bioplastics and biocomposites is much faster and important than the degradation of concrete blocks. Therefore, in the development of artificial reef, the formulation represents a lever to control the material lifetime.

## IV.2. Choice of the architecture

A second strategy to maximize this marine restoration consists in optimizing the structure of the reef. There are crucial elements to consider before starting the design phase. First, an artificial reef must present a sufficient exchange surface to allow the interactions and adhesion

of species. Then, it must include narrow and non-exposed places to allow the survival of vulnerable macro-organisms. For these reasons, different structures were and are being investigated in scientific research to understand the key of creating the optimal artificial reef. In Europe, the Nazare artificial reef off the western coast of Portugal represents a successful example of hollow concrete blocks. Five years after its deployment in 2010, the fish community and diversity had significantly grown thanks to the presence of refuges acting as protection and overgrowth areas. These biological indicators gave positive perspectives for scientists [218]. Suzuki et al. [219] made researches on the enhancement of the settlement and survival of juvenile corals on artificial reefs based on Gridshell structures. Their results tend to explain that the architectural optimization (i.e. plate arrangement and mesh size) as well as the material selection significantly influence the survival rate of *Acropora* species. Indeed, they succeeded in obtaining a survival rate of 14 % after 6 months of immersion with a mesh size of 2.5 cm. Besides, they investigated the impact of the structure on the settlement and survival process of the marine organisms. Designing a grid structure with narrow and deep cells combined with a plate overlap to limit the light intensity degree was definitely helpful for long-scale restoration of juvenile corals.

Instead of studying the impact of the structure, Ruhl et al. [220] focused their attention on the difference between artificially and naturally conceived reefs and the influence on the colonization trend and rate. Besides, depending on the printed architectures (inspired from marine plants) and used materials, they gave answers about the influence of 3D-printed coral reefs on the viability and sustainability of colonizing marine species. Based on the behavior of coral associated blue-green chromis, i.e. *Chromis viridis*, they showed that the fish did not select a specific habitat during the 15-minutes test. This results proves that 3D-printed corals can compete with natural models in terms of architecture and attraction of marine species. The scientific community has raised concerns about the deployment of artificial reefs. Although

their implantation does not represent the most common method to repopulate damaged marine areas, their presence exhibits a satisfying 66% survival of transplanted corals according to almost 80 sources [185] (research papers, reports, online records, online survey) and represents a source of hope in this fight against the coral extinction.

For this reason, the control of the architecture enabled by 3D-printing represents a big asset to reef design as illustrated by Figure 67 and Figure 68. Architectural features such as void content and structure, inner crevasses or surface roughness are important to recreate a balancer ecosystem ([221], [222]). Then, 3D-printing is also a very used tool in the world of oceanography for diverse applications such as tracking, biomechanics, locomotion, hydrodynamics [223]. The opportunity given by 3D-printed concrete blocks to redesign and optimize the structure of artificial reefs while adding natural components (geopolymer, glass sand, seashell) to the formulation is drawing a growing interest [198]. A statistical survey based on a Multi-Criteria Decision Making Assessment can be conducted to select the best candidate for reef design. This strategy relies on 4 selective criteria: cost, printability, life cycle assessment and bioreceptivity [221].

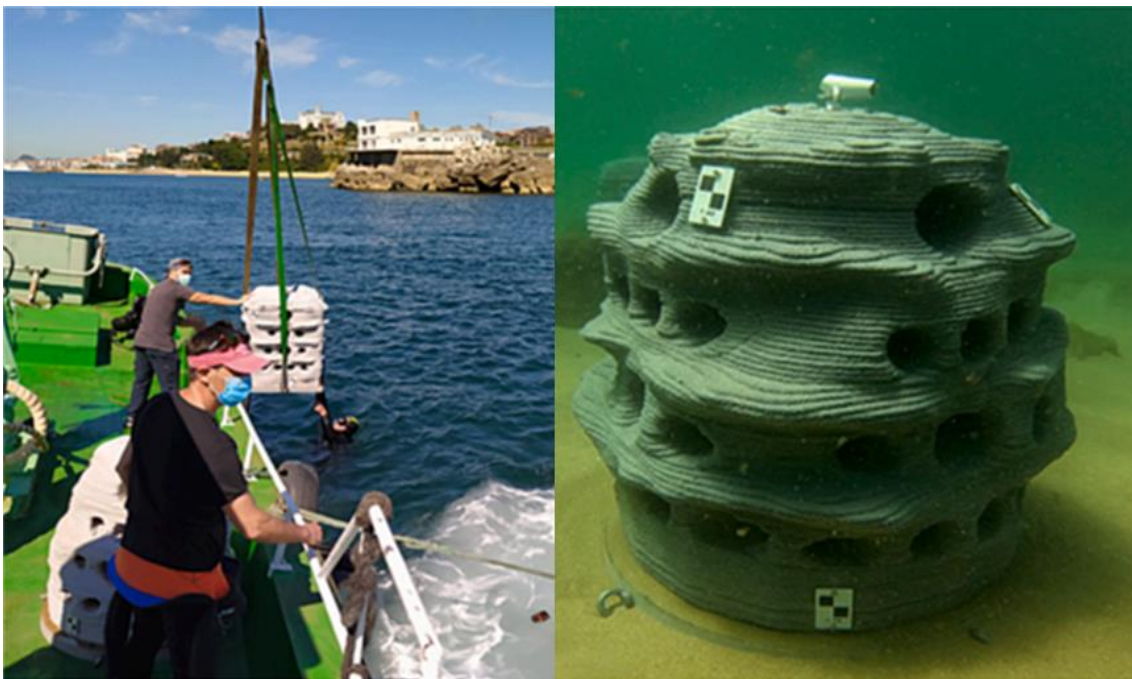


Figure 67: Immersion of an artificial reef at Santander Bay [221]

Finally, Figure 68 lists these three features within bioinspired 3D-printed reefs [222]. According to Leonard et al [209], 3D-printed samples exhibited a satisfying covering rate and colonizing species. Local organisms use to colonize specific areas which have a high roughness/microgrooves to hide from external factors and predators. However, being able to control reef lifetime is an important asset that is not favorable for heavy materials like concrete. Using biobased and biocompatible Hydromorph Biocomposites may open the door towards the fabrication of **compliant deployable artificial reef with controlled lifetime** to widen the scope of applications (from environmental to halieutic purposes).

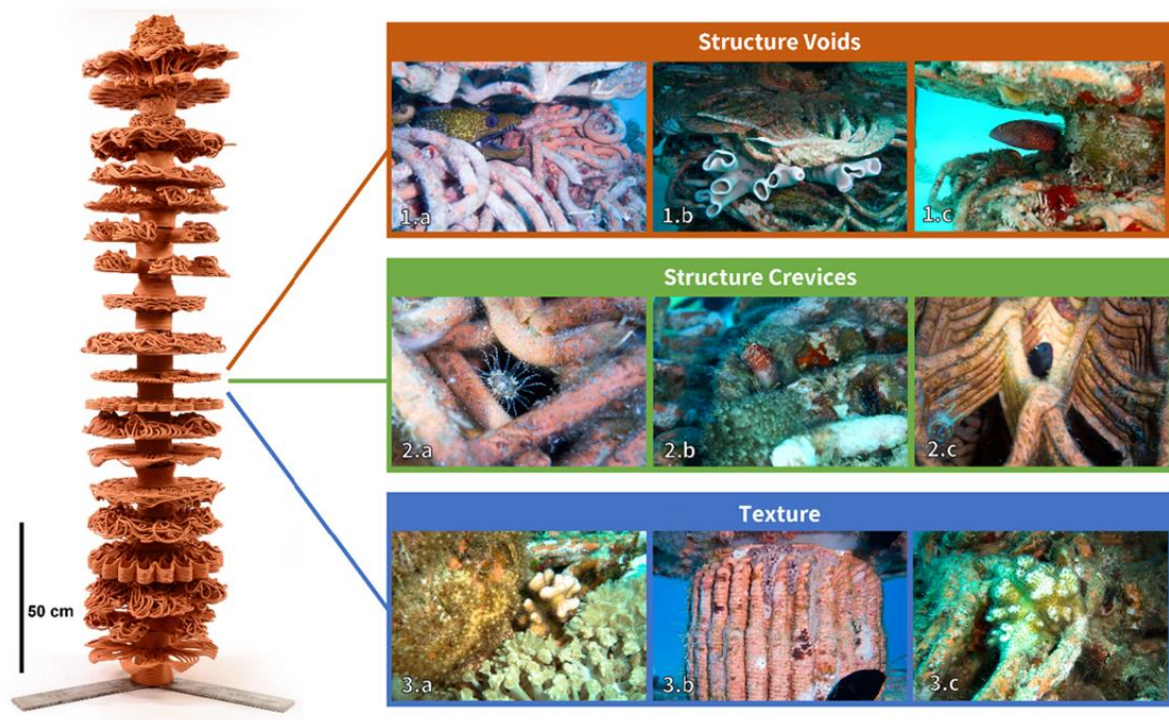


Figure 68: Architectural features made of 3D-printed ceramic elements to promote marine biofouling [222]





# Chapter 2: Materials & Methods


## « Material and Design » survey

## « Biological » survey


### OBJECTIVES

- Widen the shape-changing potential of HBCs by optimizing :
  - Their formulation
  - Their architecture
- Evaluate the potential of biocomposites for restoring marine ecosystems by optimizing
  - Their formulation


### MATERIALS




Flax bundle



Biopolymer granulates  
(PLA, PBS, PBSA, PBAT)




Flax non-woven fabrics



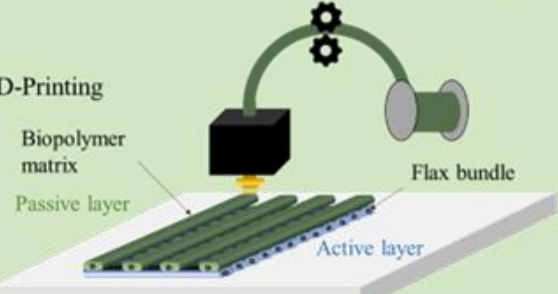
Biopolymer film (PLA, PBAT)

### MANUFACTURING PROCESS

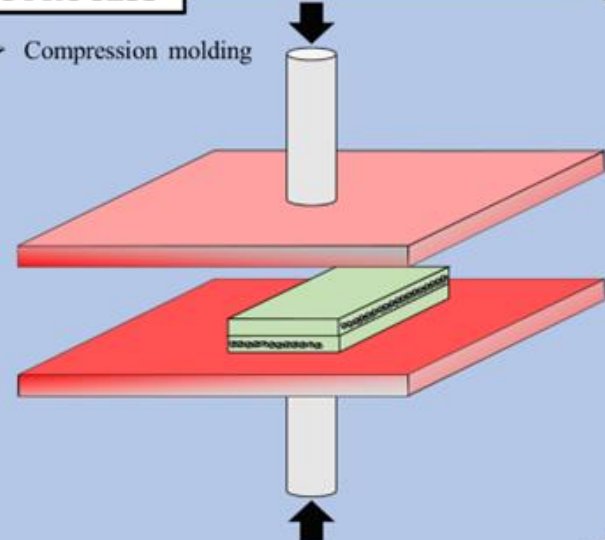
➤ Filament production



➤ 3D-Printing



➤ Compression molding

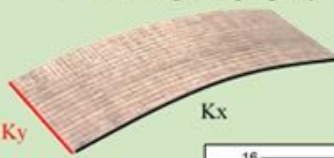
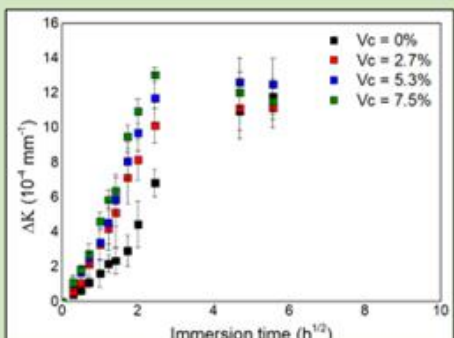


### CHARACTERIZATION METHODS

➤ Characterization of materials

- Tensile tests
- DSC
- Microscopic analysis
- Hydroscopic properties

➤ Final targeted property : Actuation of HBC

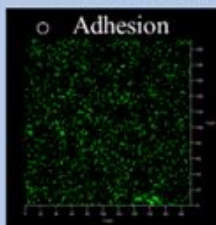



➤ Characterization of materials

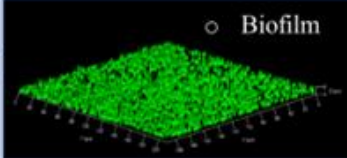
- Contact angle
- Tensile tests
- DSC
- Toughness
- Roughness

➤ Final targeted properties : Biofouling potential

○ Adhesion




72 hours

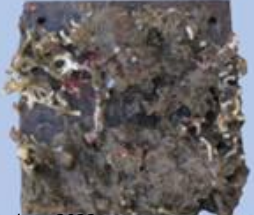


○ Biofilm

○ Macro-fouling



Seawater immersion



## I. Introduction

**Chapter 2** is devoted to the introduction of investigated materials and characterization methods involved in this PhD project. Two distinct investigations have been conducted over these three years period. Firstly, a study period was devoted to improving the HBC's potential. By evaluating the role of formulation (**Chapter 3 and 5**) and design (**Chapter 4 and 6**), 3D and 4D-printing of biocomposites was tackled and different techniques of characterization were required covering microstructural, hydro/hygroscopic and hydro/hygromechanical aspects.

Then this was followed by a shorter but equally important section on the biofouling potential of biocomposite substrates to revitalize marine ecosystems (**Chapter 7**). For this investigation, only the formulation of the substrate was considered, not its architecture. This led to the use of different characteristics, e.g. including physico-chemical properties and biofouling amplitude, and manufacturing techniques of the tested prototypes.

To sum up, in this chapter presenting the “Materials and Methods” section, both parts are successively described as “Material and Design” (**Chapter 3, 4, 5 and 6**) and “Biological” surveys (**Chapter 7**).

## II. “Material and Design” survey

This section is dedicated to the carried out investigations tackling the relation between formulation, architecture, 3D-printing and shape-changing performances of 4D-printed biocomposites.

### II.1. Materials

#### II.1.a. Flax fiber

Continuous flax fiber yarns were provided by Safilin (Sailly-sur-la-lys, France). The selected yarn was twisted (320 tpm) with a linear weight of 68 TEX (g/km). These yarns were used to produce the continuous flax-fiber reinforced filament of which surrounding matrix could be modified along the co-extrusion process (described in **Section I.2.a**).

#### II.1.a. Biopolymer matrices

Four biopolymers were tested in this survey. Polylactic acid (PLA) Ingeo™ Biopolymer 3001D was supplied by Natureworks LLC. Then, two polymers belonging to the Polybutylene Succinate group were used. The first one is a common PBS, BioPBS FZ71PM/FZ71MB (PBS), and was delivered by MCC Biochem. The second one is a Polybutylene Succinate Adipate, Bionolle™ 3001 MD (PBSA), and was produced by Showa Denko K.K. Finally, PolyButylene Adipate Terephthalate (PBAT) Ecoflex F Blend C1200 was provided by BASF. The rheological and thermal properties of these matrices are gathered in Table 4.

Table 4: Density, Melt Flow Rate (MFR), melting temperature and tensile modulus of the investigated matrices. According to supplier (\*).

	<b>PLA</b>	<b>PBS</b>	<b>PBSA</b>	<b>PBAT</b>
<i>Mass density</i> *	1.24	1.26	1.26	1.25 - 1.27
<i>MFR (g/min)</i> *	22	22	3	2.7 – 4.9
<i>Melting point (°C)</i> *	200	115	114	110 – 120
<i>Tensile modulus (Gpa)</i>	3.1 ± 0.3	0.7 ± 0.2	0.3 ± 0.1	0.06 ± 0.03

## II.2. Manufacturing process

### II.2.a. Filament production

The filament used for printing the laminates was produced by the co-extrusion process (Figure 69). By feeding and bringing together the flax yarn and the molten polymer matrix in a heated nozzle, impregnation of the fiber by the matrix occurs. Then, by cooling it to room temperature, the biopolymer becomes more rigid, and the final continuous flax fiber reinforced filament is obtained. This process was developed by Le Duigou et al. [79]. The extrusion conditions for each of the customized filaments are detailed in Table 5.

Table 5: Extrusion conditions for customized continuous flax-fiber reinforced filaments.

	cFF/PLA	cFF/PBS	cFF/PBSA	cFF/PBAT
Die temperature (°C)	200	175	200	200
Oven temperature (°C)	120	RT	RT	RT
Die size (mm)	0.6 (diameter) x 20 (length)			
Puller speed (m/min)	1.00	1.00	0.80	0.80
Extrusion speed (rpm)	3	3	2	2

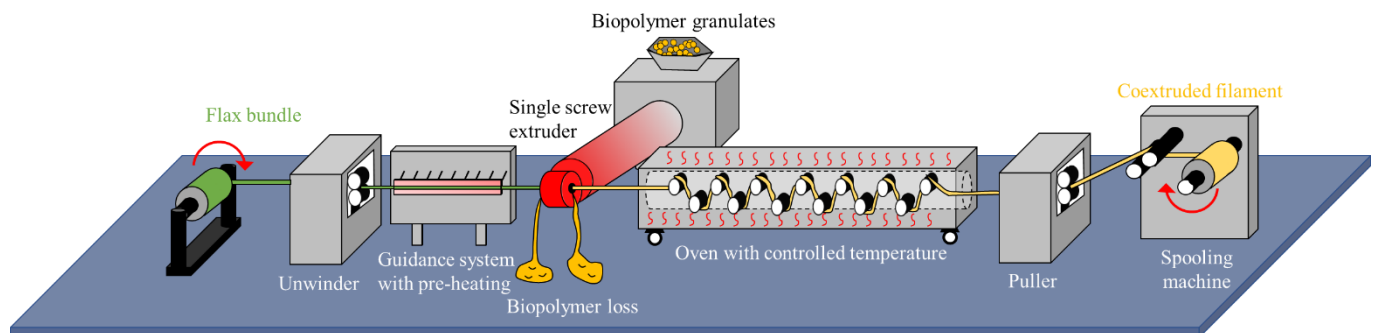


Figure 69: Schematic representation of co-extrusion process used to develop continuous flax fiber reinforced filament.

### II.2.b. 3D-printing of continuous flax fiber reinforced biocomposites

#### II.2.b.i. 3D-printing

The final step in the manufacturing process is the 3D-printing of biocomposite laminates (Figure 70). This part is ensured by a PRUSA MK3s 3D-printer with a custom print head. Allowing architectural control, 3D-printing allows for setting several parameters such as layer thickness  $t$ , interfilament distance  $ID$  within layers and fiber orientation of which both influence the morphing pattern inside 4D-printed bilayers.

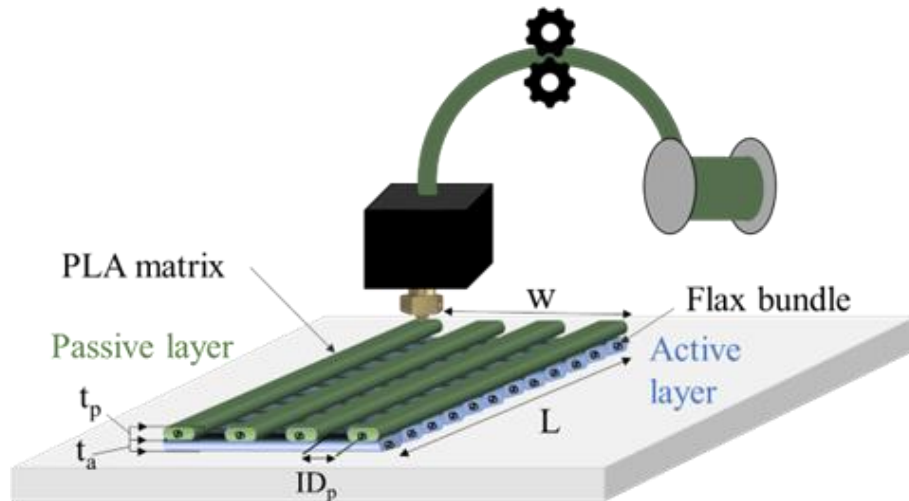


Figure 70: Schematic description of 3D-printing process of continuous flax-fiber reinforced bilayers.  $L$  and  $w$  represent the length and width of printed bilayer.  $t_p$  and  $t_a$  refer to the thickness of passive and active layer, while  $ID_p$  symbolizes the interfilament distance within passive layer.

Depending on the matrix surrounding the flax yarns, the printing bed is heated in order to optimize the deposition process and to avoid high thermal residual stresses inside the structure. The Gcodes are written using FullcontrolGcode Designer [224] which allows a disruptive control of printing parameters. The printing conditions for each material are gathered in Table 6.

Table 6: Printing conditions for flax-fiber reinforced biocomposites.

	<b>cFF/PLA</b>	<b>cFF/PBS</b>	<b>cFF/PBSA</b>	<b>cFF/PBAT</b>
<i>Nozzle temperature (°C)</i>	190	135	145	145
<i>Bed temperature (°C)</i>	60	Room Temp.	Room Temp.	Room Temp.
<i>Printing speed (mm/min) in straight lines</i>	420	420	420	420
<i>Layer height (mm)</i>	0.20	0.15	0.15	0.15

### II.2.b.ii. Post-treated specimens

A batch of printed samples was post-processed by molding them in a hot press at 30 bar to limit the potential effect of 3D-printing on porosity. The 3D-printed samples were placed in a metal mold to minimize misalignment effect of yarn. Then, they were subjected to heating and cooling steps under high compression. The first step is to heat the system to the nozzle temperature for the shortest possible time to prevent thermal degradation [210]. The processing

temperature was adapted to the present matrix in order to optimize its rheological behavior for a better matter cohesion. cFF/PLA, cFF/PBS, cFF/PBSA and cFF/PBAT were heated up at  $T = 200\text{ }^{\circ}\text{C}$ ,  $T = 160\text{ }^{\circ}\text{C}$ ,  $T = 170\text{ }^{\circ}\text{C}$  and  $T = 200\text{ }^{\circ}\text{C}$  respectively. Then, while maintaining an elevated temperature, the system was put under pressure of 50 bar for 2 minutes. Finally, cooling was carried out under 200 bar to room temperature. SEM images of the microstructure of the cross-section of the two laminates are shown in Figure 71.

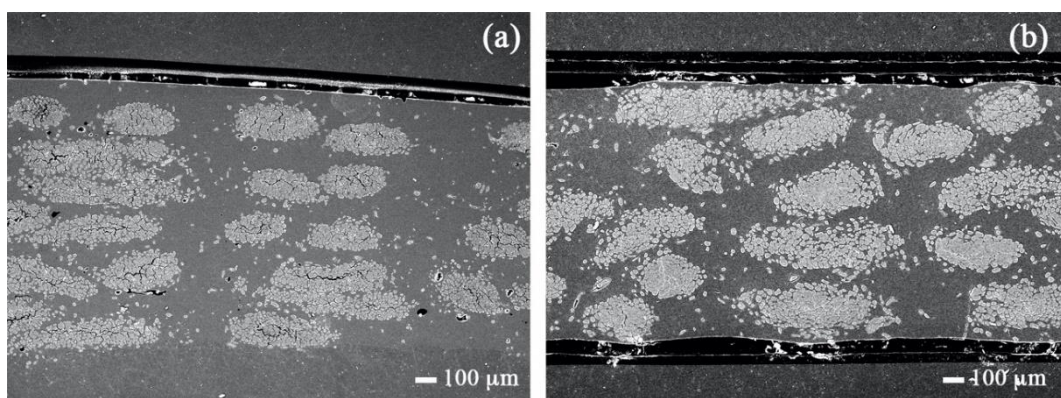


Figure 71: Microscopic analysis obtained by SEM of the microstructure of (a) 3D-printed cFF/PBS and (b) 3D-printed + thermopressed cFF/PBS laminates

## II.3. Characterization techniques

### II.3.a. Microscopic analysis

#### *II.3.a.i. Fiber, porosity and channel content*

The microstructure of custom filaments and 3D-printed biocomposites is evaluated using the KEYENCE VHX-7000 digital microscope and the Jeol JSM-IT500HR scanning electron microscope at 5 kV.

Quantification of the mesostructure of 3D-prints is an essential step to fix structural parameters affecting actuation. At first, porosity and fiber content of co-extruded filament were assessed. Then, regarding 3D-printed unidirectional specimens, three structural entities were evaluated: 1) fiber content, 2) porosity content and 3) channel content. It is important to differentiate fiber and porosity content in filaments and 3D-printed specimens since manufacturing process is

known to induce unwanted porosities. The surface fraction of the channels are related to the architected conducts tackled in **Chapter 6**. They represent localized empty conducts. Both content was measured on the YZ cross section. Figure 72 points out the section of filament and 3D-printed biocomposites. Image analysis was performed using ImageJ software® (National Institute of Health, USA).

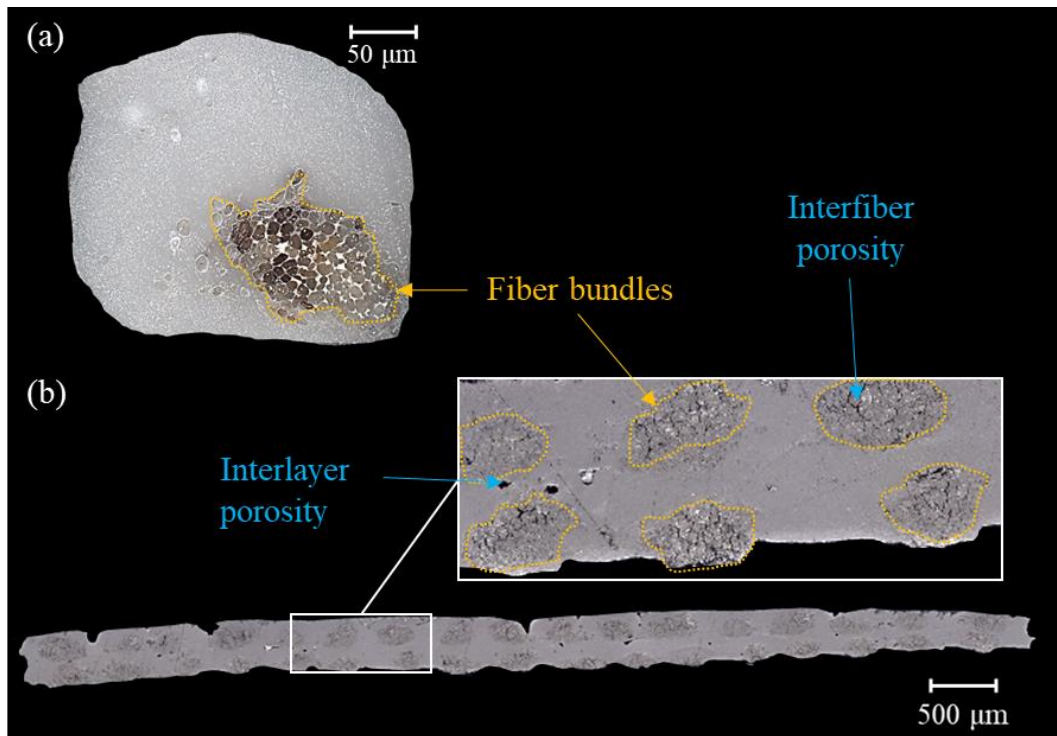


Figure 72: Microstructural analyzes illustrating the section of (a) co-extruded filament and (b) 3D-printed biocomposite.

### *II.3.a.ii. Mesostructural analysis of bilayers*

Relying on Timoshenko's equation (Equation 1), a microscopic analysis was also conducted to evaluate the thickness ratio of 4D-printed bilayers since it governs the morphing ability of HBC (Figure 73).



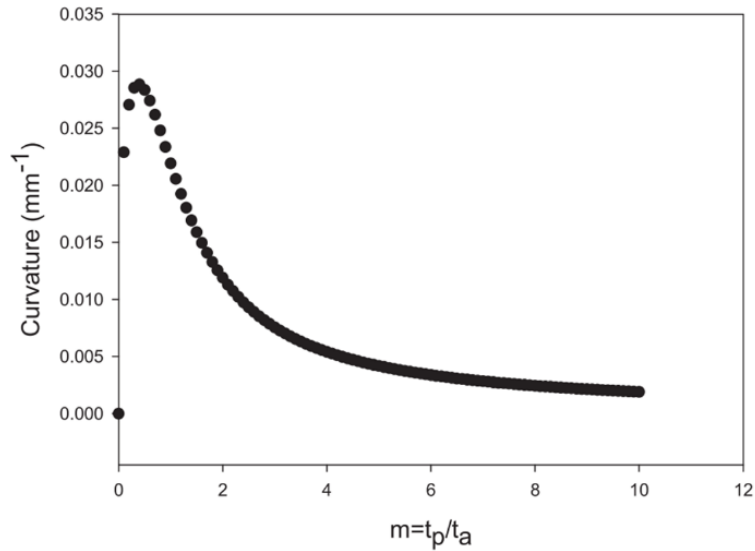


Figure 73: Evolution of bilayer curvature as a function of thickness ratio  $m$  (taken from [225]).

### II.3.b. Hydro- and hygroscopic properties of 3D-printed biocomposites

#### II.3.b.i. Sample conditioning

5-layer printed samples (2 x 2cm<sup>2</sup>) are placed in an oven at 40°C under vacuum until THE stabilization of their mass. After this drying step, which represents the initial state, the samples are either fully immersed (at room temperature) in distilled water (hydroscopic conditioning) or in a wet environment controlled by an active desiccator chamber (hygroscopic conditioning). For a progressive rise of ambient humidity, a full RH (from 0% to 98%) and temperature-controlled enclosure was used. The temperature was fixed at 20°C.

#### II.3.b.ii. Sorption isotherm

The sorption mechanism of 3D-printed biocomposites is evaluated at different relative humidity values to build the sorption isotherms with Equilibrium Moisture Content (EMC) thanks to the active desiccator chamber previously defined. The percentage gain  $M_t$  at any time  $t$  is calculated as:

$$M_t(\%) = \frac{M_t - M_0}{M_0} \cdot 100 \quad (\text{Equation 3})$$

Where  $M_t$  and  $M_0$  are the mass of the sample after exposure to water/moisture and the mass of the initially dry material, respectively. All the data presented here represent the mean values of

a quintuplicated test. During immersion, three parameters of interest are extracted: the final water content ( $\Delta M_{sat}$ ), the coefficient of diffusion ( $D$ ) and the kinetic of sorption ( $dM/dt$ ).  $D$  is obtained by fitting the experimental data with a Fickian diffusion model which is typically used to describe the sorption behavior of thin natural fiber composite ([21]-[22]). To study the hydroscopic properties of continuous flax fiber reinforced composites, the samples can be considered as thin laminates since the thickness ( $e = 1.5$  mm) is much lower than the width ( $l = 20$  mm). The 1D Fick model was used as a simple tool to better understand the role of matrix stiffness on moisture sorption kinetics (**Chapter 3**). Regarding short wood fiber reinforced biocomposites, the same model was used although having a higher width/thickness ( $w/t$ ) ratio. In this case, the fit allows for exploring the relation between water diffusion and biocomposite structure (**Chapter 6**). A more in-depth study of the sorption mechanism using more complex models is beyond the scope of these two surveys.

To quantify the diffusion kinetics of biocomposites, samples similar to those used for hydro- and hygroscopic conditioning were tested. Based on the diffusion curve  $\Delta M = f(\sqrt{t})$  [227] Equation 4 was used.

$$\frac{M_2 - M_1}{\sqrt{t_2} - \sqrt{t_1}} = \frac{4M_\infty}{h\sqrt{\pi}} \sqrt{D} \quad (\text{Equation 4})$$

$D$  symbolizes the coefficient of diffusion,  $M_\infty$  the water content at saturation and  $h$  the thickness of the sample; while  $t_1$  and  $t_2$  was set at the beginning ( $t_1 = 0$  s) and after 1 hour ( $t_2 = 3600$  s) of immersion.  $M_1$  and  $M_2$  are the water content of biocomposites related at both times. Water-induced kinetics of sorption were evaluated after 1-hour of immersion by measuring the slope between biocomposite swelling and immersion time (Figure 74).

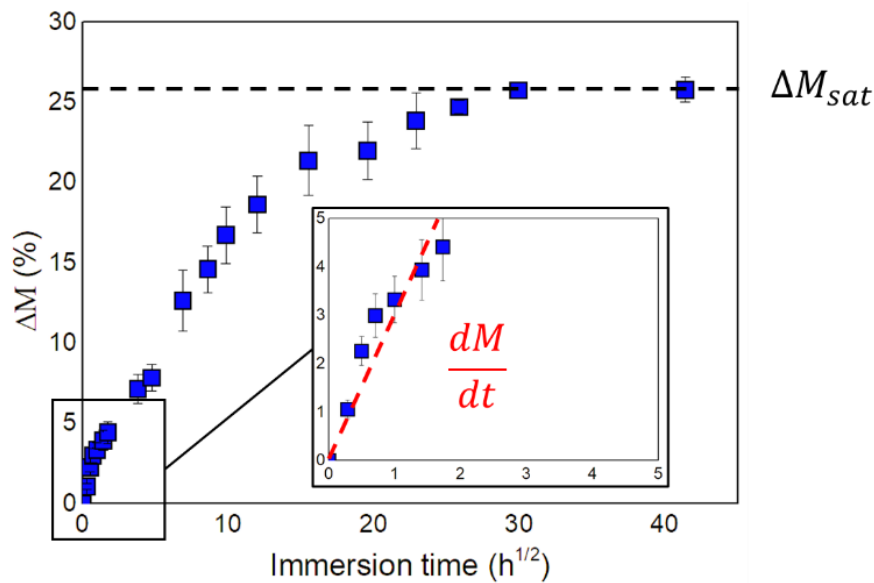


Figure 74: Sorption curve of biocomposite with the measurement of kinetic of sorption ( $dM/dt$ ) on the initial linear part of the curve and the final sorption reached at saturation ( $\Delta M_{sat}$ ).

### II.3.a.iii. Anisotropic swelling

These physical mechanisms are characterized by measuring the swelling of final 3D-printed biocomposites during immersion tests (hydroexpansion) and in several humid environments (hygroexpansion) using the cartographic tool KEYENCE VHX-7000 digital microscope. Five squared samples are analyzed in the longitudinal, transverse and out-of-plane directions and the arithmetic mean of the results is calculated for both continuous flax fiber reinforced biocomposites (**Chapter 3**) and short wood fiber reinforced biocomposites (**Chapter 6**). While longitudinal (x) and transverse (y) directions have been carried out with KEYENCE VHX-7000 digital microscope measurements (Figure 75a), the out-of-plane swelling (z) was assessed by a Mitutoyo micrometer with a resolution of 0.001 mm. The final expansion of the material and its kinetic of expansion evaluated in both directions represent the targeted properties of the test (Figure 75b).

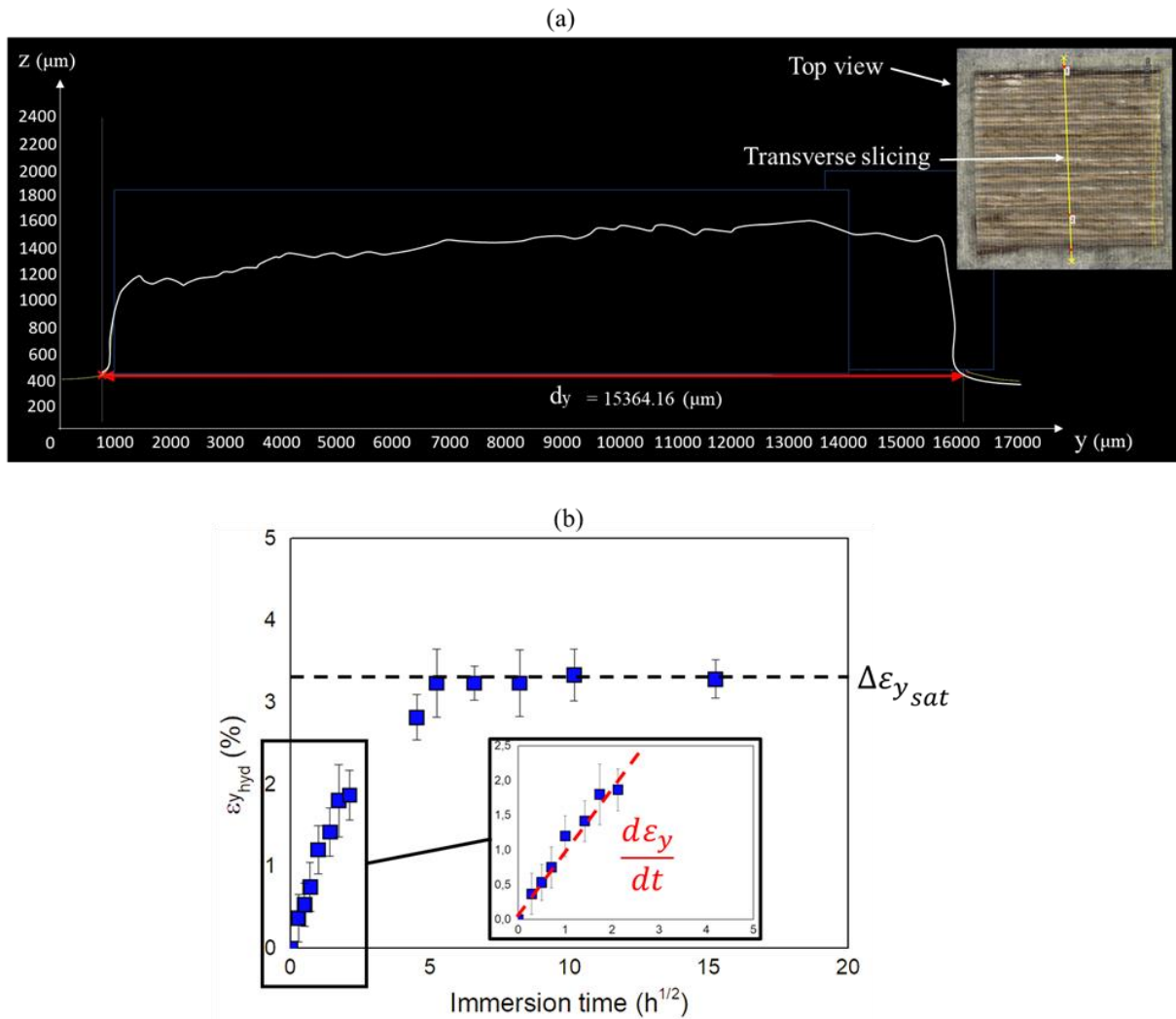


Figure 75: Evaluation of the hydroexpansion phenomenon on a 3D-printed biocomposite. (a) Top view of 3DP cFF/PBAT biocomposite and evolution of the sample's thickness in the transverse direction ( $dy$ ). (b) Resulting graph allowing for measuring the kinetic of expansion ( $d\epsilon/dt$ ) and final expansion reached at saturation ( $\Delta\epsilon_{sat}$ ), i.e. here presented for transverse hydroexpansion.

### II.3.c. Mechanical properties

Mechanical tests on 3D-printed samples whose edges were machine-milled before performing the experiment are replicated five times. Prior to testing, the samples are stored in a vacuum oven at  $40^{\circ}\text{C}$  until a constant weight is reached. This condition implies a minimal amount of water within the material, which is indicated here as 'zero' (anhydrous state). The tensile properties of all specimens are determined by quasi-static tensile tests according to ASTM D638, ISO 527-4 and ISO 14129 standards, using an Instron 5566 universal testing machine (500N or 5 kN cell load depending on the maximal strength overcome by the tested specimen).

The test was carried out with a tensile speed of 1 mm.min<sup>-1</sup>. The in-plane shear properties (stress and strain) are determined by ASTM D3518 standard.

Three different types of test specimens, type A specimen (unidirectional fiber orientation at 0° along the length of the specimen) and type B specimen (unidirectional fiber orientation at 90° along the width of the specimen) are used to determine the longitudinal and transverse mechanical tensile properties, while type C specimen (bidirectional fiber orientation at 45/-45°) is used to evaluate the mechanical shear properties. An extensometer is used for the strain measurement during the longitudinal and transverse tests. The tensile longitudinal modulus named  $E_1$  is determined within a range of strains from 0.05 to 0.1 % [228]. Tensile characterization of pure PBAT, PBSA, PBS, PLA matrices and thermopressed biocomposites is also performed.

#### II.3.d. Physico-chemical properties

##### *II.3.d.i. Thermal properties*

Thermal properties of biocomposites were evaluated by Differential Scanning Calorimeter (DSC). Several features gathering glass transition temperature ( $T_g$ ), recrystallization temperature ( $T_c$ ), melting temperature ( $T_m$ ) and crystallinity index ( $I_c$ ) of the biopolymer matrix were followed throughout the measurement. This characterization step is essential since it is assumed to impact both water sorption and shape-shifting of HBC (**Chapter 3, 4 and 6**) as well as marine biofouling (**Chapter 7**) ([229]–[231]).

##### *II.3.d.ii. Viscoelastic properties*

Dynamic rheological characterization has been carried out on MCR201 rheometer from Anton Paar. The instrument was set up with 25-mm parallel-plate geometry, and the experiments were conducted in oscillatory mode in frequency range of 0.01-100 rad.s<sup>-1</sup> at 170°C, 200°C and 190°C for PBS, PLA and PBAT, respectively. The strain was selected within the linear viscoelastic domain.

### II.3.e. Characterization methods of 4D-printed bilayers

#### II.3.e.i. Actuation properties

To quantify the shape-changing potential of 4D-printed specimens, the radius of curvature was measured by image analysis using the ImageJ software (national Institute of Health, USA). Being directly linked to these radii, the longitudinal curvature (**Chapter 3, 4 and 6**) and transverse curvature (**Chapter 4**) were thus reported (Figure 76).

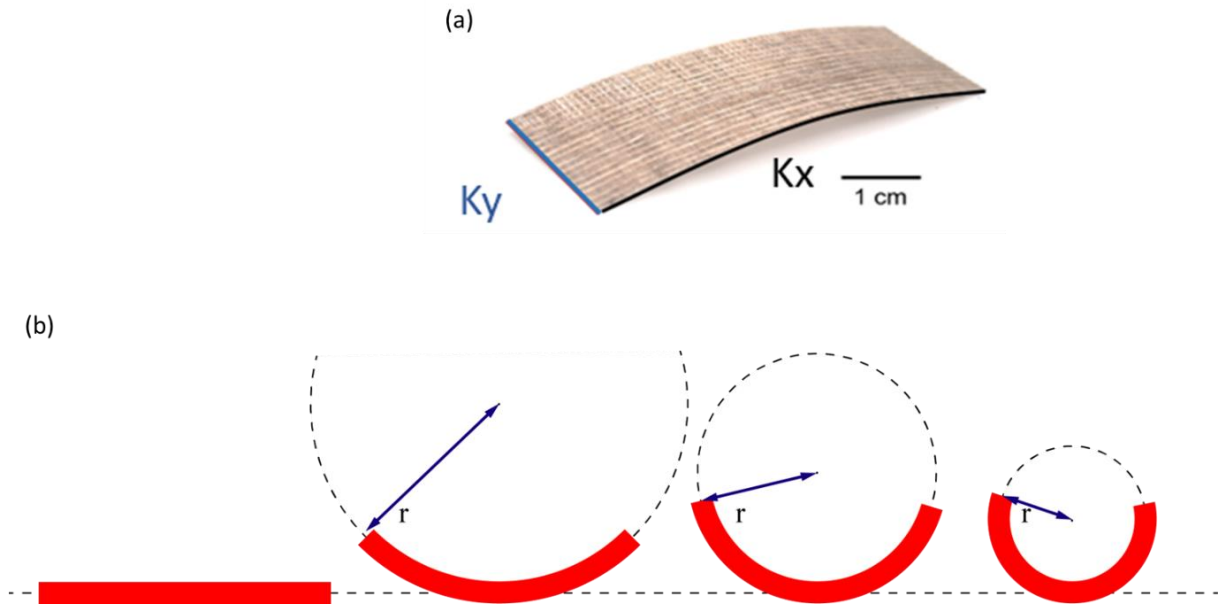


Figure 76: (a) 4D-printed cFF/PLA specimen illustrating the longitudinal  $K_x$  and transverse  $K_y$  curvatures. (b) Schematic description of radius of curvature at different actuation step.

#### II.3.e.ii. Hydro- and hygroscopic stresses measurement

Arising from the fiber swelling that induces shape-changing of the material, hydro- and hygroscopic stresses are generated inside the structure. Via calculations based on the experimental results on the curvature actuation of 4D-printed HBC, elastic and hydroexpansion properties of 3D-printed biocomposites, and internal hydroscopic stresses can be estimated as follows [232].

$$\sigma_{hyd} = \frac{E_{11} \cdot E_{22}}{E_{11} + E_{22}} \frac{t}{\Delta \rho} \left( \frac{1}{2} + \frac{1}{24} \left( 2 + \frac{E_{11}}{G_{12}} + \frac{E_{22}}{G_{12}} \right) \right) \quad (\text{Equation 5})$$

With  $t$  the bilayer thickness,  $E_{11}$  and  $E_{22}$  the respective elastic moduli of the active and passive layers,  $G_{12}$  the shear modulus, and  $\Delta\rho$  the relative variation of curvature between the dry and wet (after saturation) bilayers.

### III. “Biological” survey

#### III.1. Materials

To assess the potential of flax-fiber reinforced biocomposites to repopulate marine ecosystems, three ranges of materials were selected: conventional plastics, bioplastics and biocomposites. Conventional plastics are represented by a transparent commercial polymer, i.e. Polyglass, provided by SEDPA (Pérenchies, France) in opposition to bioplastics composed of PolyLactic Acid (PLA) Biopolymer 3001 supplied by Natureworks LLC (Minneapolis, USA) and PolyButylene Adipate Terephthalate (PBAT) Ecoflex C1200 supplied by BASF. Biocomposites were made of bioplastics (PLA, PBAT) combined with flax non-woven preforms ( $100 \pm 15$  g/m<sup>2</sup>) provided by Ecotechnilin (Yvetot, France). Two flax fiber volume contents ( $V_f$ ) of 15% and 30% added in both bioplastics were investigated. Both bioplastics and biocomposites plates were manufactured by moulding process using a hot press as previously performed by Pantaloni et al. [233]. The physico-chemical properties of both materials are reported in Table 7.

Table 7: Physicochemical properties of plastic, bioplastics and biocomposites. Data provided by the supplier (\*).

Materials	Density	Roughness (mm)	Contact angle (°)	Elastic modulus (MPa)	Toughness (Shore D)	Cristallinity index (%)
<i>Polyglass</i>	$1.29 \pm 0.02$	$0.32 \pm 0.04$	$59.4 \pm 2.5$	$2634 \pm 145$	$76.9 \pm 1.1$	9-10
<i>PLA</i>	1.24*	$2.99 \pm 0.37$	$77.5 \pm 2.0$	$3116 \pm 309$	$82.6 \pm 2.6$	0-1
<i>PBAT</i>	1.25 – 1.27*	$2.55 \pm 0.19$	$84.7 \pm 1.9$	$63 \pm 3$	$42.3 \pm 3.1$	15-16
<i>Flax/PLA (V<sub>f</sub> = 30%)</i>	$1.03 \pm 0.01$	$3.63 \pm 0.92$	$87.9 \pm 6.7$	$17795 \pm 1010$	$83.4 \pm 1.4$	3-4
<i>Flax/PBAT (V<sub>f</sub> = 30%)</i>	$1.05 \pm 0.01$	$3.17 \pm 0.49$	$49.3 \pm 5.2$	$18504 \pm 3262$	$61.8 \pm 2.2$	17-18

### III.2. Manufacturing process

Compression molding avails for two specific surveys. At first, it was employed to compare the hydroexpansion and hydroscopic coefficient of biocomposites between 3D-printed samples and 3D-printed + thermo-compressed samples with a similar formulation (**Chapter 3**) as explained in **Section I.2.b.ii**. Then, the fabrication of thermo-compressed specimens for biofouling investigations (**Chapter 7**) was also carried out. In this investigation, 3D-printing process was not employed since only the influence of biocomposite formulation on biofouling potential was targeted.

### III.3. Characterization of substrates

Numerous analyzes are conducted on the aforementioned materials since many parameters have been identified to influence the colonizing process of marine organisms [209]. As previously described, the characterization of mechanical properties and thermal properties are carried using the same methods as for the “Material and Design” survey.

#### III.3.a. Contact angle

The hydrophilic/hydrophobic behavior of several biopolymer (PLA, PBAT), biocomposites (cFF/PLA, cFF/PBAT) and conventional polymer (Polyglass) was investigated by contact angle measurement. For this test, a KRUSS DSA30 goniometer was employed. Contact angle measurements provides information on the surface wettability and interactions with organic solvents. Three tested solvent were used among which water, formamide and diiodomethane to have more feedbacks on the surface tension and polarity of surface components.

#### III.3.b. Surface roughness

Finally, the last physico-chemical property relies in surface roughness which is a critical parameter to know working on marine biofouling. To characterize the surface roughness of our thermo-compressed samples, a TR 100 Surface Roughness Tester was employed. It allows for measuring manually the arithmetical mean roughness value (Ra) and the mean roughness depth



obtained by averaging the five highest peaks with the five highest depth (Rz). Methods of analysis are illustrated in Figure 77.

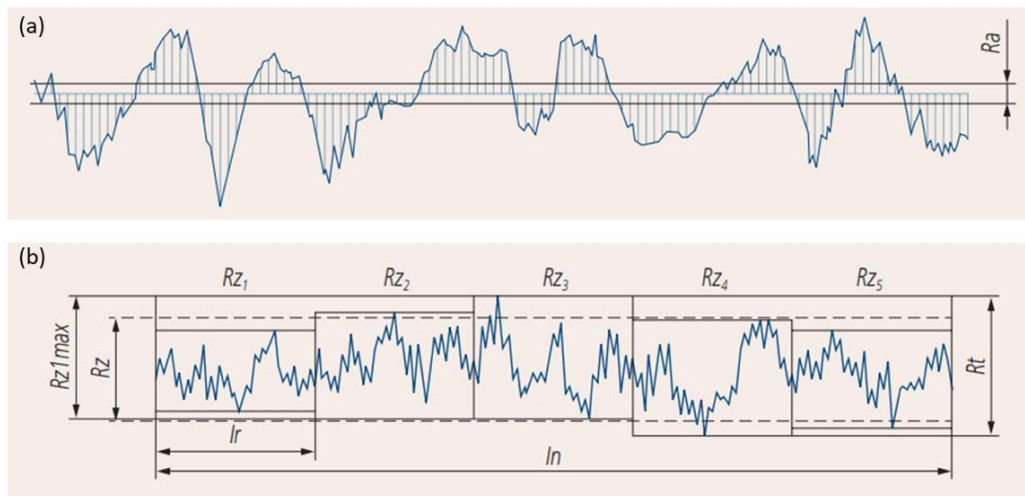


Figure 77: Method of analysis of (a) the arithmetical roughness value (Ra) and (b) the mean roughness depth (Rz) (taken from Mitutoyo reference guide).

### III.4. Cultivation of the biological strains

Two marine microorganism strains were cultivated: *Pseudoalteromonas* sp. 3J6 (Figure 78a) marine bacterium and *Cylindrotheca closterium* diatom (Figure 78b).

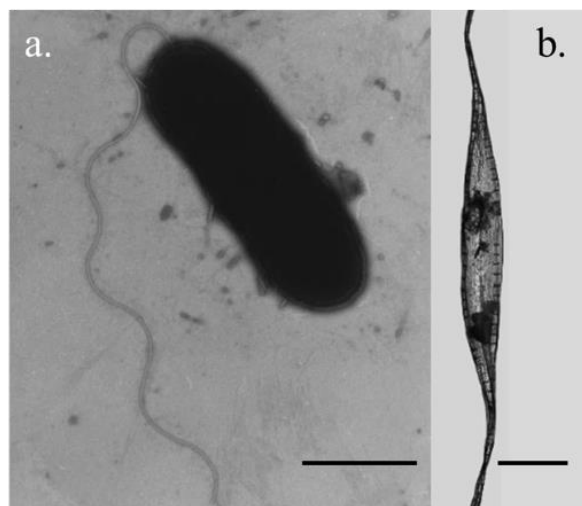


Figure 78: Pictures of (a) *Pseudoalteromonas* bacteria (adapted from [231]) and (b) *C. closterium* (adapted from [232]). Scale bars: 1  $\mu$ m (a), 10  $\mu$ m (b).

#### III.4.a. *Pseudoalteromonas* sp. 3J6

*Pseudoalteromonas* sp. 3J6 was isolated from an immersed glass surface in the Gulf of Morbihan – Bailleron’s island [234]. This bacterial strain was tagged by a GFP encoded

plasmid [235]. Strain was grown on Marine Broth (MB) medium (Difco) at 20°C under orbital shaking (125 rpm) for 3 days.

#### III.4.b. *Cylindrotheca closterium*

*C. closterium* (*Bacillariophyceae*, (*Ehrenberg*) *Reimann and Lewin*) were cultured in a phytotronic chamber (Helios 600 Phytotron) with a 16h:8h light/dark cycle. Growing in an artificial seawater (ASW), diatoms were used at the stationary phase after 14 days of growth. An axenization was carried out before synchronization, i.e. 40h before the experiment, by adding three antibiotics : penicillin G (1 g/L), streptomycin (500 mg/L) and chloramphenicol (100 mg/L) [236]. Before starting the test, diatom counting was realized to make sure that a sufficient population of diatoms was present. The threshold limit was fixed at  $10^6$  cells/mL for investigating the impact of flax leachates on diatom growth and  $10^5$  cells/mL for diatom adhesion test.

### III.5. Sample preparation

#### III.5.a. Samples for microorganism adhesion

For carrying the microorganism adhesion survey of *Pseudoalteromonas* sp. 3J6 and *C. closterium*, three different types of materials were used: conventional plastic (Polyglass), bioplastics (PLA and PBAT) and biocomposites (Flax/PLA and Flax/PBAT) for which fiber volume fraction was of 30%. These materials were cut in small, squared pieces (1 cm<sup>2</sup>) and sterilized by UV ( $\lambda = 365$  nm) for 20 min.

#### III.5.b. Samples for *in situ* macroorganism adhesion

Tests were conducted in the harbour of Etel (Etel, 47°39'32"N 3°12'27"W). Eleven range of materials (10x10 cm<sup>2</sup>) were immersed : bioplastics (PLA, PBAT), biocomposites with various flax fiber content (15%, 30%), the reference plastic (Polyglass) and four concrete formulations with specific additive, i.e. Calcium Diformate (CD), Limestone Filler (LF), Cellulose Ether (CE) and raw concrete (X). The sample distribution was randomly organized to stamp from

combined microbiological attraction. The immersion period started in October 2021 and ended in September 2022. In total, 55 squared samples (replicates = 5) were horizontally fixed on an oyster table (Figure 79) and immersed at a depth of 2.5 m for one year.

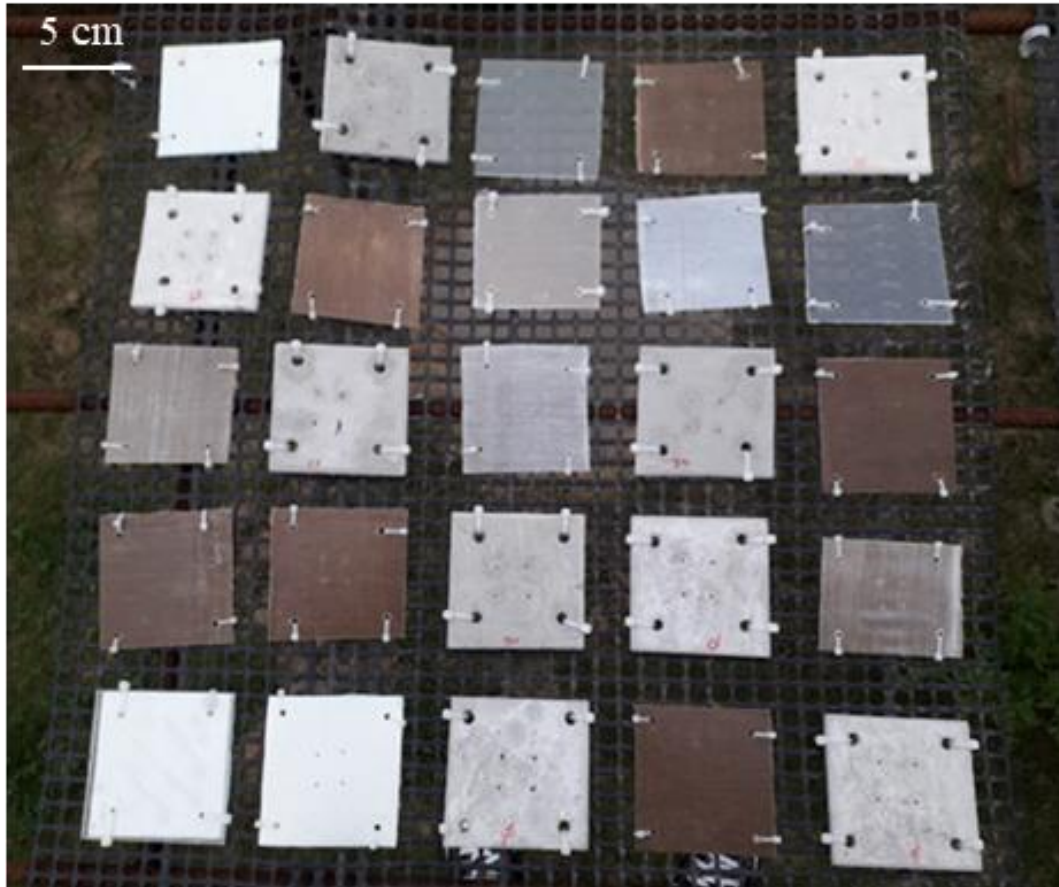


Figure 79: Picture of the sample distribution on an oyster table before immersion.

### III.5.c. Samples for testing the growth of microorganisms

To establish a connection between released degradation products of flax fibers, i.e. flax leachates, and the growing process of marine microorganisms, an extraction of flax leachates was conducted. For that, row non-woven flax fabrics were immersed in artificial seawater (ASW) for 24 h under stirring (150 rpm). The resulting solvent was filtered and evaporated at 40°C. Finally, the extracted product was adjusted with ASW at a concentration of 10 mg.mL<sup>-1</sup>.

1.

### III.6. Microorganism and macroorganism adhesion

#### III.6.a. Microorganism adhesion

For each tested material, technical duplicates and biological triplicates were performed.

##### *III.6.a.i. Pseudoalteromonas sp. 3J6*

- Bacterial adhesion

Each sterilized squared sample of Polyglass, bioplastics (PLA and PBAT) and biocomposites (Flax/PLA and Flax/PBAT) was dropped in a 24-well microtiter glass bottom plate (Figure 80). Polyglass samples were used as control samples. Once the samples are positioned, 2 mL of the tested bacterial solutions recovered the material surfaces. The time allocated for bacterial adhesion was 3 hours [234]. After washing and removing the non-adhered organisms, the covering rate is characterized by Confocal Laser Scanning Microscopy (LSM 710, Zeiss, Oberkochen, Germany) using a 40x oil immersion objective. The covering percentage was measured by ImageJ software (National Institute of Health, USA).

- Biofilm formation

Once the bacterial adhesion was analyzed, feeding medium (MB) was added to each well in order to promote bacterial biofilm growth. A confocal analysis using a x40 oil immersion objective is realized after 72-hours of maturity to quantify the biovolume ( $\mu\text{m}^3/\mu\text{m}^2$ ) and average thickness ( $\mu\text{m}$ ) of the bacterial biofilm. The final targeted properties (average thickness and biovolume) are measured by Comstat from MATLAB software.

Figure 81 illustrates the test carried out from bacterial adhesion of *Pseudoalteromonas sp. 3J6* to the final conceived biofilm.



Figure 80: 24-well microtiter glass bottom plate. Microorganisms adhesion takes place in the well containing a material sample. Empty spots are used to flip the samples and analyze the covering surface by confocal analysis.

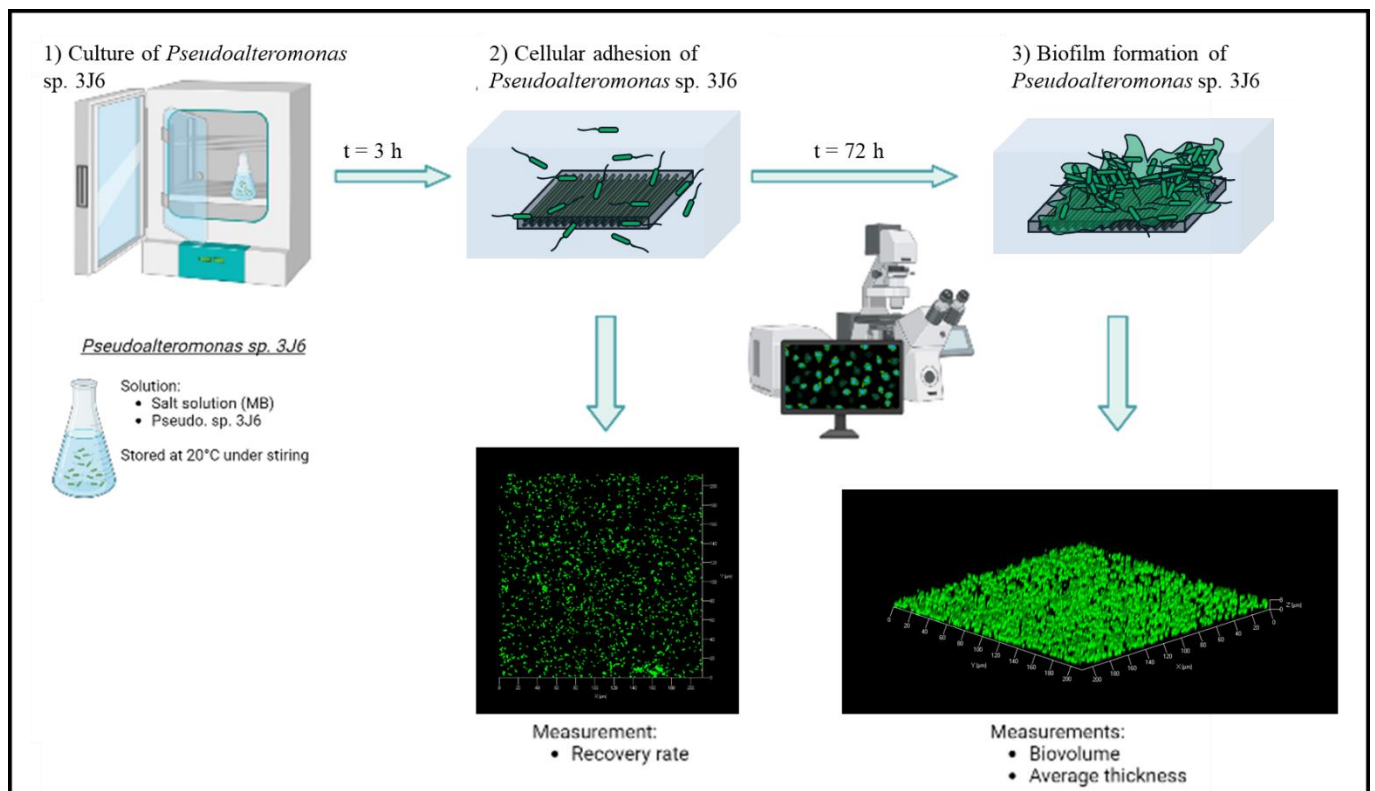


Figure 81 : Schematic protocol from strain culture to biofouling characterization of *Pseudoalteromonas* sp. 3J6. Scheme was created on Biorender.com.

### III.6.a.ii. *Cylindrotheca closterium*

- Diatom adhesion

Considering *C. closterium* diatoms, the adhesion mechanism was characterized after 72 hours [237] of incubation by confocal analysis using a 20x water immersion objective.

- Biofilm formation

As with the bacterial survey, the formation of diatoms biofilm was assessed after 72 hours of incubation by confocal analysis using a x20 water immersion objective. The final targeted properties (average thickness and biovolume) are measured by Comstat from MATLAB software.

### III.6.b. *In situ* macroorganism adhesion

The measurement of macrofouling was performed during the favorable period, i.e. between March and September, for scuba diving in Brittany. Underwater pictures (Figure 82) of the macrofouling were taken with a CANON® G12 digital camera equipped with Ikélite® watertight enclosure.

At the end of the 1-year immersion period, samples were picked up and the identification of colonizing organisms was carried out. Only sessile species were considered.

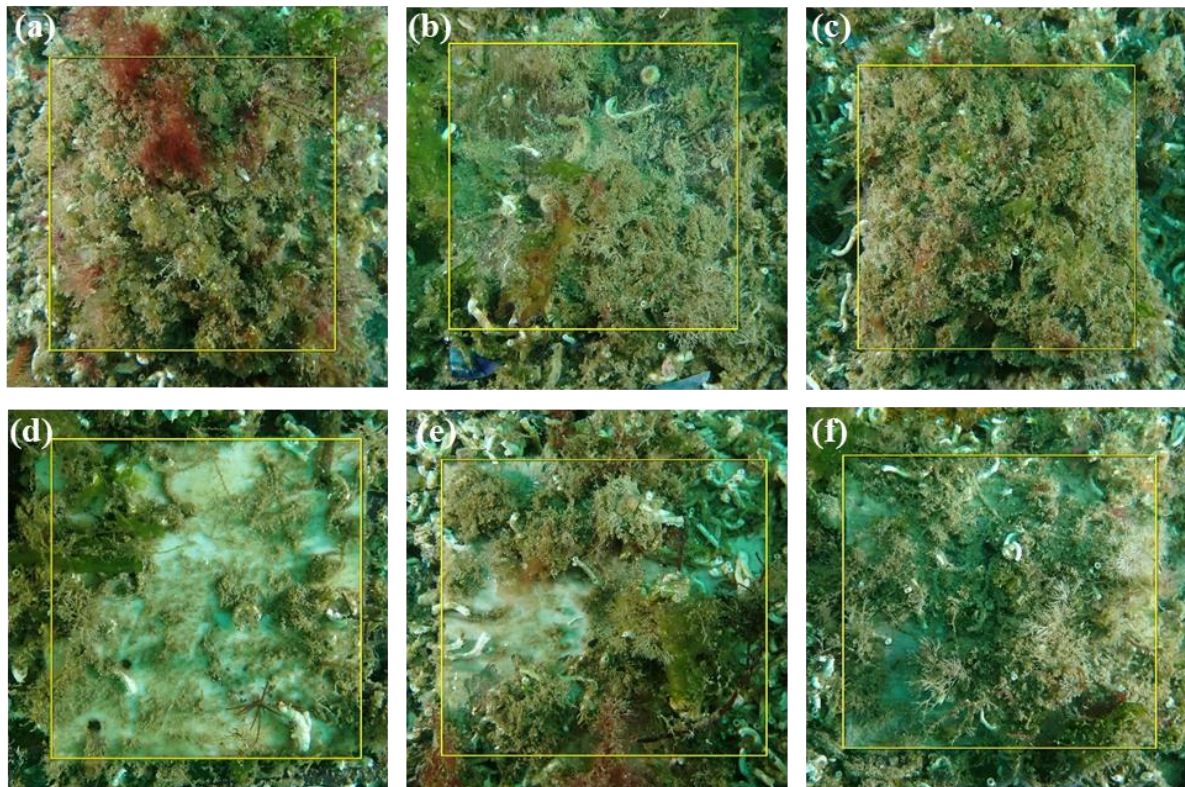


Figure 82: Underwater pictures of slabs made of (a) PLA, (b) Flax/PLA ( $V_f = 15\%$ ), (c) Flax/PLA ( $V_f = 30\%$ ), (d) PBAT, (e) Flax/PBAT ( $V_f = 15\%$ ) and Flax/PBAT ( $V_f = 30\%$ ) after 1 year of immersion (from June 2022 to June 2023).

### III.7. Influence of flax leachates on the growth of microorganisms

Extracted from flax fibers, the influence of the lixivium was evaluated on the growth of *C. closterium* diatoms and *Pseudoalteromonas* sp. 3J6 bacteria.

For evaluating the impact on the growth of *Pseudoalteromonas* sp. 3J6, 96-well microtiter plates were filled with solutions of MB/flax leachates with a variable concentration of flax leachates going from 0.08, 0.16, 0.31, 0.63, 1.25 to 2.5 mg.mL<sup>-1</sup>. This survey is carried out by using the optical density of solutions, i.e. retracing the growing rate of the bacterium [238], after 1 day of interactions.

Regarding *C. closterium*, similar microtiter plates were filled with ASW/flax leachates following the same range of leachate concentration. The resulting fluorescence generated by living diatoms after 4 days of interactions was used as an indicator for measuring the growing rate of diatoms [237]. The schematic organization of both microplates is presented by Figure 83.

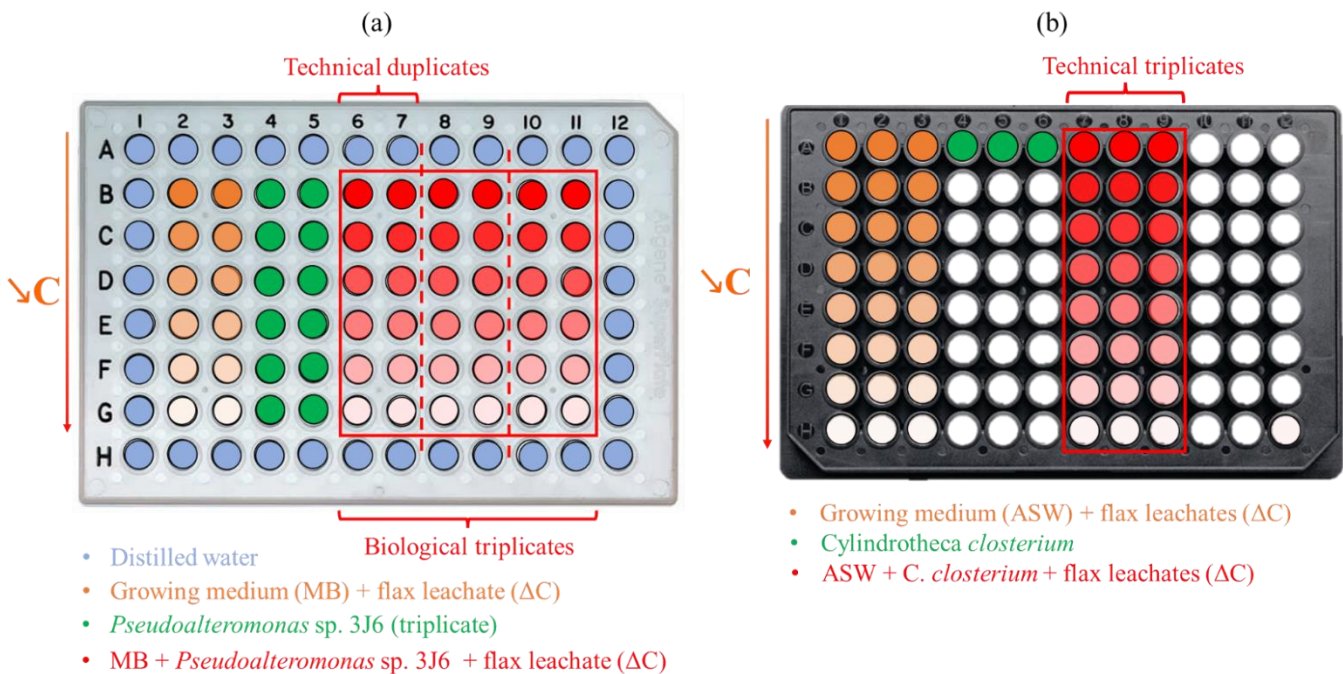


Figure 83: Schemes of 96-well microplate for following the growth of two biological models: (a) *Pseudoalteromonas* sp. 3J6 by absorbance and (b) *C. closterium* by fluorescence in the presence of flax leachates. Blue spots symbolize water-filled wells to prevent interferences from the outside. Gradient orange spots are dedicated to the growing medium/flax leachates. The green areas are dedicated to the growing medium/biological model solutions used as reference and control for bacterial/diatom growth. The gradient red spots represent the biological triplicates inducing technical duplicates to get higher reliability in the results. For both microplates, the flax leachate concentration decreased from the top to the bottom.



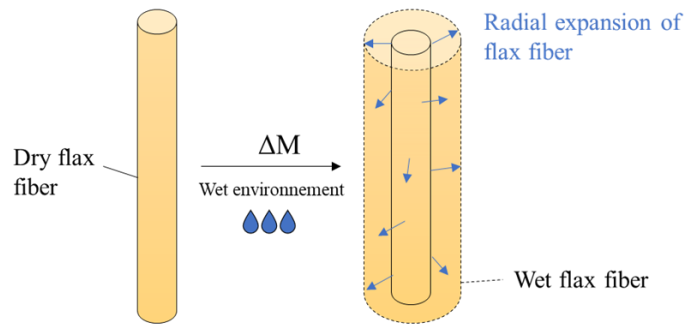




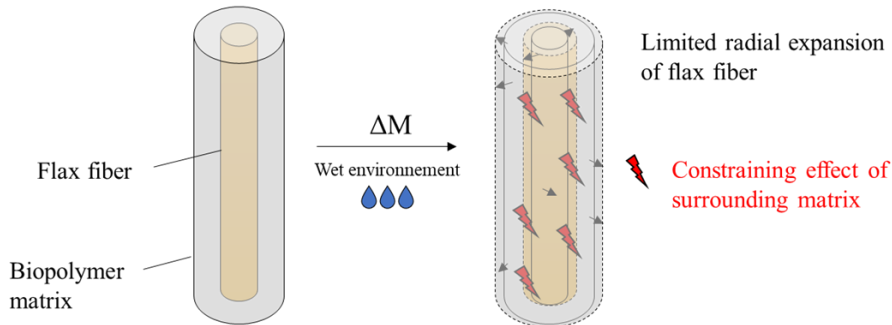
# Chapter 3: Matrix selection: a key towards wider actuation ?

Fiber swelling  $\Leftrightarrow$  Constrained by surrounding matrix

➤ Water-induced swelling of elementary flax fiber

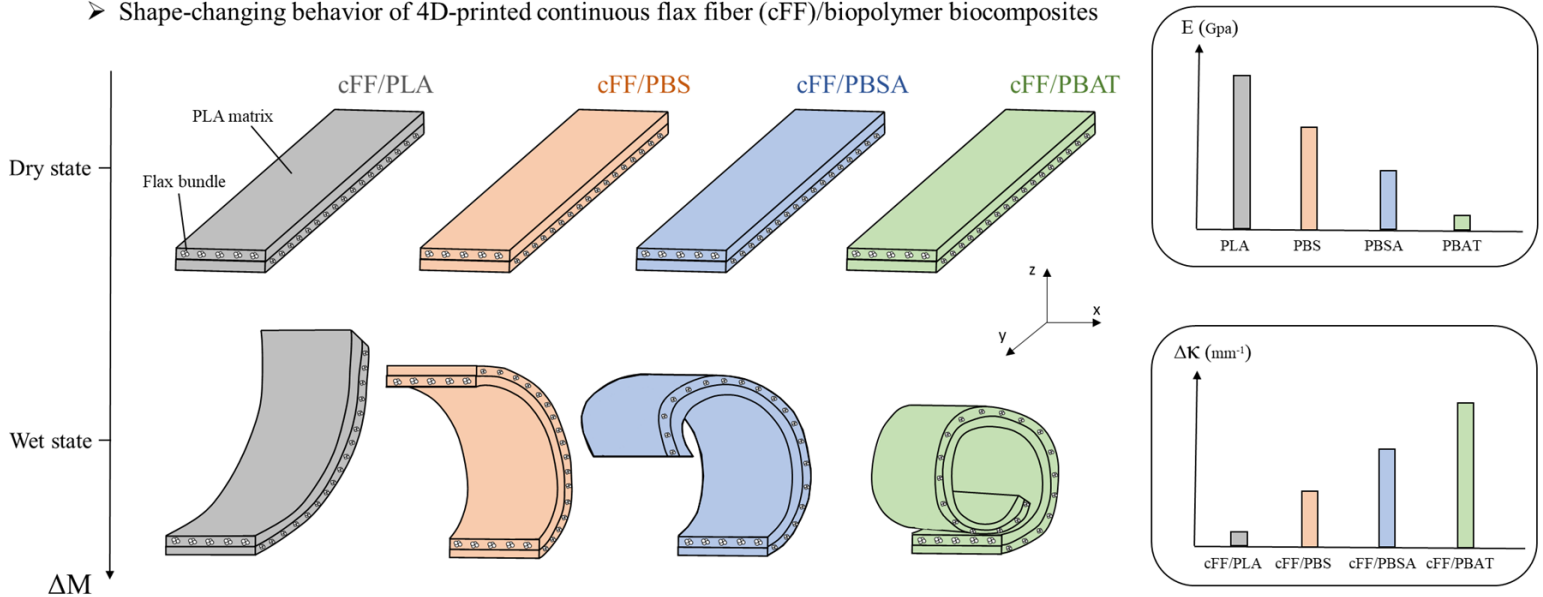


➤ Water-induced swelling of flax/biopolymer filament



Matrix selection  $\Leftrightarrow$  Promotor of actuation

➤ Shape-changing behavior of 4D-printed continuous flax fiber (cFF)/biopolymer biocomposites



## I. Introduction

The recent rise of continuous fiber reinforced composites developed by 3D printing has opened the way to complex and multifunctional load-bearing materials. First introduced by Matsuzaki et al. [90] in 2016, the controlled distribution of continuous fibers within the printed composite achieved unprecedented mechanical performance and strengthened the anisotropic behavior of fiber-reinforced materials. In this context, the development of 3D-printed continuous natural fiber reinforced biocomposites (CNFRB) has been presented ([87], [91], [239]) as a new sustainable approach in load-bearing applications but also for morphing purposes [87]. An antagonist feature between load-bearing application and shape-changing of biocomposite is its moisture-induced hygro/hydroexpansion, caused by the local swelling of the natural fibers. Indeed, it induces a reduction of mechanical performance but increases the actuation potential of shape-changing materials. To this point, it is important to differentiate two physical mechanisms contributing to the expansion of material in presence of water. Hydroexpansion of material relates to its swelling behavior under immersion while hygroexpansion targets its swelling behavior under variable relative humidity [35].

Providing the interactions of their hydroxyl groups with water molecules, hydrophilic polysaccharides (hemicelluloses, pectins) facilitate the sorption of water [240]. This phenomenon induces a reorganization of the local arrangement of the polymer chains and a modification of the dimensional [241] and mechanical properties of the fiber [58]. The hygroexpansion mechanisms within plant fibers depend strongly on their microstructure and composition ([38], [45], [242]). For example, single flax fibers show a radial hygroscopic coefficient  $\beta$  of 1.14 [45]. However, Joffre et al. [47] have shown that when surrounded by a polymer matrix, natural fibers do not reach the same levels of swelling because of the constraining effect applied to them. This trend was confirmed by Abida et al. [46] who also underlined the constraining effect of the epoxy matrix on the radial swelling of the flax yarns.

They observed a significant difference between the radial hygroscopic coefficient of the flax yarns ( $\beta=1.11$ ) and the transverse coefficient of the flax fiber-reinforced composites in weft ( $\beta=0.13$ ) and out-of-plane ( $\beta=0.85$ ) directions. In addition, Réquillé et al. [56] and Le Duigou et al. [59] have demonstrated hygroscopic swelling of an orthotropic nature in natural fiber-reinforced composites. It was stated to be due to an asymmetric pressure distribution and the release of elastic potential energy during the processing step, although this remains open to debate.

The differential swelling between the fiber and the matrix as well as between the orthogonal plies involves the generation of hygroscopic internal stresses that have been recently investigated [243]. These stresses can sometimes exceed the transverse tensile strength of the composite ply and result in internal damage (crack, delaminating, etc). The hygroscopic expansion of natural fibers and their related stresses are considered a drawback for structural applications and mitigation strategies should be implemented to limit its influence.

Based on a biomimicry approach and asymmetric architecture, the hygroscopic expansion of natural fibers can be efficiently used in Hygromorph BioComposites (HBC) with shape-changing functionality. These materials are both sensors and actuators and react passively (without an external energy source) to changes in humidity. Belonging to stimuli-responsive materials, HBC with slender geometry display responsiveness and reactivity to actuation that depend directly on various global parameters described by the modified Timoschenko equations [62] (tensile modulus ratio, laminate thickness, ply thickness ratio and hygroexpansion of each ply). Experimental investigations have demonstrated that interfacial shear strength, fiber architecture and composition, and fiber content are material parameters that affect their spatio-temporal response [64].

The hygroscopic and anisotropic expansion of natural fibers is considered as an opportunity for morphing applications of biocomposites because the shape-changing mechanism and the

amplitude reached is based on large differential swelling within the asymmetric mesostructure. Hence, a better understanding of biocomposite expansion is essential to exacerbate the amplitude potential of morphing biocomposites.

**Chapter 3** aims at understanding the matrix contribution on the hygro- and hydroscopic properties and internal stresses for load-bearing and morphing applications of 3D-printed hygromorph biocomposites (continuous reinforcements).

For that, an investigation is conducted on the effect of matrix stiffness and the role of the biopolymer matrix in the swelling process, with tensile moduli ranging from  $63 \pm 3$  MPa for PolyButylene Adipate Terephthalate (PBAT), to  $313 \pm 87$  for PolyButylene Succinate Adipate (PBSA), to  $658 \pm 16$  for PolyButylene Succinate (PBS) and to  $3116 \pm 309$  for PolyLactic Acid (PLA). The effect of the 3D-printing process is first analyzed by comparing the results obtained with similar materials processed by thermo-compression. Water and moisture sorption tests are performed in combination with hygro-/hydroexpansion measurements to show transient and stationary behavior. Tensile properties are also evaluated, while the curvature of asymmetric lay-up is assessed to track the internal hydroscopic stress state.

Finally, the influence of matrix stiffness is discussed in the framework of controlling hydroexpansion for opposite purposes such as structural and morphing applications.

## II. Microstructural description

Fiber content and porosity are two essential parameters for qualifying composite materials and their related manufacture, as they drastically influence mechanical, hydro- and hygroscopic properties. Porosity is not a simple parameter to evaluate for natural fiber composites as it depends on the characterization method as well as the input data (e.g. fiber density) used for the calculation [244]. The microstructure features of the different flax-based printed biocomposites as a function of the biopolymer matrix (PBAT, PBSA, PBS and PLA) are presented in Table 8. They are compared to printed samples that have been submitted to subsequent thermocompression step.

Table 8: Fiber volume fraction ( $V_f$ ) and porosity content ( $V_p$ ) of (a) 3D-printed and (b) 3D-printed- thermocompressed biocomposites

	cFF/PLA	cFF/PBS	cFF/PBSA	cFF/PBAT
<b>(a) 3D Printing</b>				
$V_f$ (%)	32.6 ± 0.5	29.1 ± 2.5	29.2 ± 3.0	33.0 ± 4.2
$V_p$ (%)	2.1 ± 0.1	4.1 ± 0.9	3.7 ± 1.2	4.5 ± 1.5
<b>(b) 3D Printing + thermocompression</b>				
$V_f$ (%)	33.8 ± 0.3	28.8 ± 4.1	32.9 ± 1.0	30.9 ± 3.3
$V_p$ (%)	0.6 ± 0.1	0.5 ± 0.4	0.6 ± 0.2	1.2 ± 0.2

The fiber volume fraction is targeted around 30%vol during filament production, which is respected for all samples, taking into account the standard deviation. Although considerably higher than the pioneering work of Matsuzaki et al. [90], this achieved fiber fraction is limited by technical reasons such as yarn twist and partial impregnation. As far as we know, there is currently no off-the-shelf industrial filament containing continuous natural fibers on the market. This suggests that the current results can be further improved by additional technical work on filament production.

Although, De Kergariou et al. [244] suggested that the optical measurement tends to underestimate the porosity of the biocomposite, i.e. porosity content, and evidences moderate values attesting for a good printing quality compared to the literature data on discontinuous

fiber biocomposite [87]. This is due to a careful material selection, comprehensive humidity control during the process and optimization of printing and slicing parameters. Therefore, hydro- and hygromechanical analysis can be achieved without being dramatically biased by defects.

In order to evaluate the effect of the 3D-printing process on the microstructure but also on the hygroscopic properties, an additional molding step was applied while the potential thermal degradation is assumed to be of low importance. In fact, the porosity content of thermo-pressed materials decreases drastically to 0.5 % for cFF/PBS and 1.2 % for cFF/PBAT (Table 8).

### III. Hygroscopic behavior

#### III.1. Sorption isotherm

Prior to the biocomposites, each biopolymer matrix with different tensile moduli, e.g. 0.06 GPa for PBAT, 0.3 GPa for PBSA, 0.7 GPa for PBS, and a relatively stiff polymer with a value of 3.1 GPa for PLA, were tested and showed similar moisture content after water saturation ranging from  $1.05 \pm 0.07$  % for PBAT,  $1.13 \pm 0.09\%$  for PBSA,  $1.21 \pm 0.25$  for PBS and  $1.04 \pm 0.23$  % for PLA. These results were collected from molded samples to obtain a porosity content close to 0%.

Figure 84a represents the evolution of the moisture content of 3D-printed biocomposites with the different biopolymer matrices in a wet environment (from 0 to 98% RH). A sigmoidal behavior can be observed for all biocomposites, regardless of matrix type and stiffness, which is typical of porous cellulosic materials with a multi-step sorption mechanism [245], [246]. Assuming negligible microstructural difference (porosity and fiber content) (Table 8) within these biocomposites and similar moisture uptake of the matrices, matrix stiffness is assumed not to affect the sorption mechanism of the biocomposites in a humid environment.

Figure 84b exhibits the evolution of moisture content as a function of immersion time for similar materials. Difference between sorption at high relative humidity and immersion conditions are evidenced with a higher sorption for immersion. This may be due to the free volume filling at different scale by free water [15].

Again, the sorption behavior is broadly similar between the biocomposites, although the diffusion coefficient and moisture content at saturation are altered.

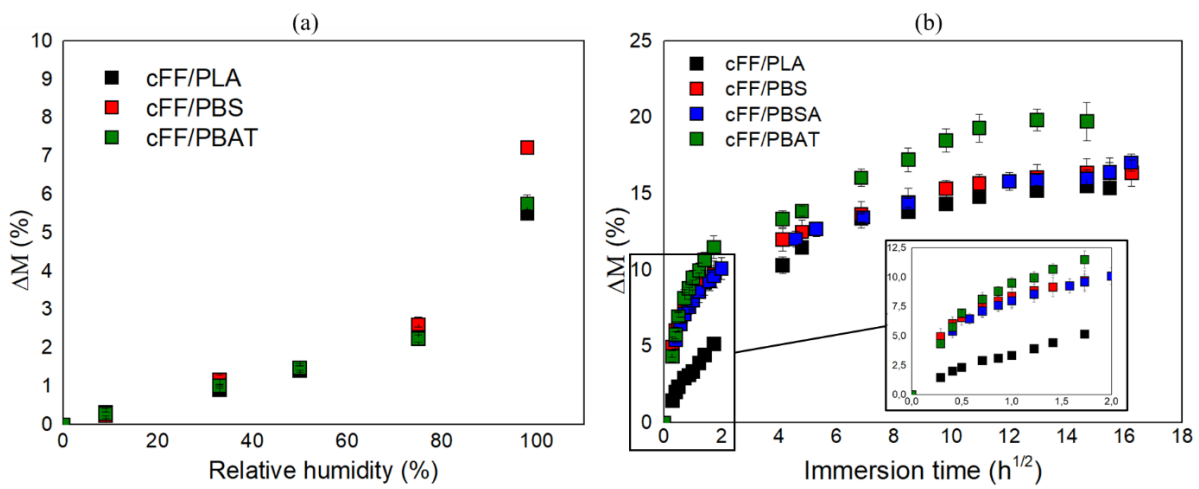


Figure 84: (a) Evolution of moisture content of 3D printed biocomposites with different biopolymer matrices (PBAT, PBSA, PBS and PLA) as a function of Relative Humidity (RH). (b) Water uptake as a function of time during immersion of 3D-printed biocomposites.

Thus, cFF/PBAT samples are slightly more sensitive to water uptake as they reached a post-saturation water content of  $19.7 \pm 1.2\%$ , compared to  $17.0 \pm 0.6\%$  for cFF/PBSA,  $16.4 \pm 0.9\%$  for cFF/PBS and  $15.4 \pm 0.2\%$  for cFF/PLA. Regarding the sorption kinetics of pure matrices, PLA, PBS, PBSA and PBAT samples exhibit a diffusion coefficient of  $5.5 \cdot 10^{-6} \text{ s}^{-2}$ ,  $6.9 \cdot 10^{-6} \text{ s}^{-2}$ ,  $8.5 \cdot 10^{-6} \text{ s}^{-2}$  and  $7.5 \cdot 10^{-6} \text{ s}^{-2}$  respectively (Table 9). At the biocomposite scale, cFF/PBAT, with the softest matrix, has the highest diffusion coefficient, while cFF/PLA takes the longest to absorb water, with a diffusion coefficient 5 times lower.



Table 9: Parameters extracted from water diffusion models for (a) 3D-printed and (b) post-thermopressed biocomposites

	<b>cFF/PLA</b>	<b>cFF/PBS</b>	<b>cFF/PBSA</b>	<b>cFF/PBAT</b>
<b>(a) 3D Printing</b>				
<b><math>\Delta m, \text{ sat (\%)} </math></b>	$15.4 \pm 0.2$	$16.4 \pm 0.9$	$17.0 \pm 0.6$	$19.7 \pm 1.2$
<b><math>D (10^{-6} \text{ mm}^2/\text{s})</math></b>	6.8	29	31	34
<b>(b) 3D Printing + Thermocompression</b>				
<b><math>\Delta m, \text{ sat (\%)} </math></b>	$9.8 \pm 0.5$	$7.4 \pm 0.6$	$8.6 \pm 0.3$	$10.7 \pm 0.5$
<b><math>D (10^{-6} \text{ mm}^2/\text{s})</math></b>	0.5	2.0	3.3	3.7

A clear decrease in terms of water mass at saturation and diffusion kinetics is visible between 3D-printed biocomposites and those 3D-printed and then thermocompressed, with for example for absorbed water mass, a decrease of 93%, 94%, 78% and 89% for cFF/PLA, cFF/PBS, cFF/PBSA and cFF/PBAT, respectively. This is due to the reduction in porosity both at the ply and yarn scale (Figure 71) emphasizing a better fiber impregnation that results from the application of additional pressure (Table 8). Regarding the trend and influence of matrix stiffness, results suggest that water transport kinetic within biocomposites is influenced by matrix stiffness. Actually, it is well established that moisture uptake within biocomposites is accounted for by the hydrophilic nature of flax fibers [240]. However, the moisture sorption of these fibers is altered by the residual stress state at fiber/matrix interface which originates from the constraining effect of the matrix [247]. Thus, it appears that the matrix constraining effect induced by matrix stiffness represents a key factor for controlling water diffusion in biocomposites. Besides, underlying effect such as matrix crystallization might be another potential explanation to this decrease of porosity content and should be more deeply investigated.

### III.2. Hygroscopic expansion

The hygroscopic expansion of the biocomposites and the associated hygroscopic deformations were measured and plotted in Figure 85. They are induced by the swelling of the natural fibers

and the biopolymer matrix during sorption. The axial swelling  $\epsilon_{\text{hydro},x}$  is the lowest owing to the negligible swelling of the flax fibers in the longitudinal direction compared to the transverse and out-of-plane directions.

At the laminate scale, moisture sorption induces a linear increase in transverse and out-of-plane swelling strains with time, followed by a steady state plateau.

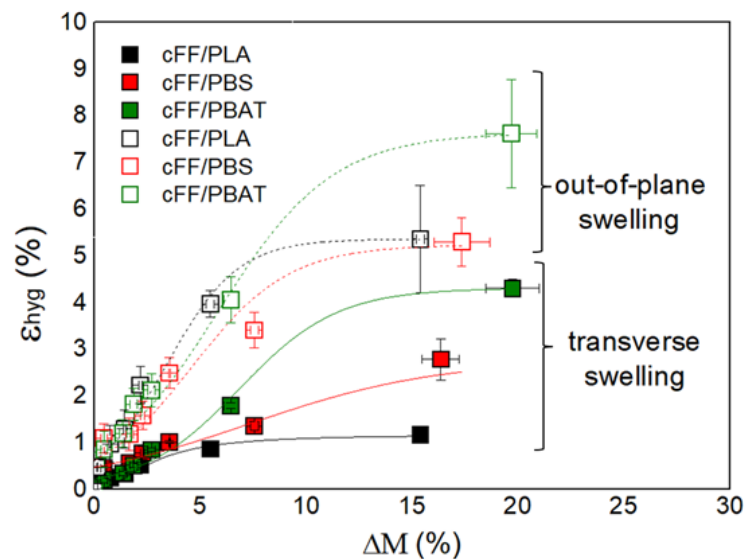


Figure 85: Evolution of transverse and out-of-plane hydroscopic strains of 3D-printed biocomposites as a function of moisture content. Solid lines represent a sigmoidal fit.

The similar behavior also observed in biological structures such as pine cones [62] is probably due to the microstructure, interactions with water, and internal hygroscopic stresses. Indeed, bonded water appearing at the first time of sorption is responsible of the hydroexpansion of the fiber cell-wall [35] while the free water that is transported by the internal multi-scale porosity implies an increase of water content but only slightly contributes to the deformation of the material.

Steady-state plateau differences appear between the different matrix-based biocomposites with lower maximum transverse hydroexpansion ( $\epsilon_{\text{cFF/PLA}} = 1.5\%$ ) for stiff PLA-based biocomposites compared to soft PBAT-based biocomposites ( $\epsilon_{\text{cFF/PBAT}} = 4.0\%$ ). Similarly, the hydroexpansion coefficient ( $\beta$ ) which takes into account hydroexpansion strain and moisture content is influenced by the choice of matrix. As the stiffness of the matrix increases,  $\beta$

decreases. It was evaluated by measuring the slope between initial (dry) and final (saturated) state.

Considering that the fiber content is similar in biocomposites and that single flax fibers are mainly responsible for the expansion of the biocomposite due to their radial expansion of 20-25% ([45], [248]), the matrix and its stiffness therefore also play an important role in the hydroexpansion of biocomposite. Their chemical composition must also be considered even though PLA, PBS, PBSA and PBAT have slightly different hydroexpansion ( $\epsilon_{PLA} = 0.2 \pm 0.1\%$ ,  $\epsilon_{PBS} = 0.4 \pm 0.1\%$ ,  $\epsilon_{PBSA} = 0.2 \pm 0.1\%$  and  $\epsilon_{PBAT} = 0.5 \pm 0.1\%$ ).

The hydroexpansion kinetics is also greatly affected by the change in polymer stiffness with values of  $3.5 \cdot 10^{-7} \text{ s}^{-1}$  to  $32.8 \cdot 10^{-7} \text{ s}^{-1}$  for PLA and PBAT-based biocomposites respectively and PBS together with PBSA with intermediate values. All the values of the transient and stationary regimes are gathered in Table 10 for all the 3D-printed biocomposites. The values obtained are in a similar range as in the literature ([46], [56], [242], [249]).

Applying a subsequent thermocompression molding step after 3D-printing involves a twofold increase in the hygroscopic coefficient compared to the printed sample (Table 10). This is in agreement with the observation made on 3D-printed short wood fiber reinforced polyester in a previous article [79]. Indeed, even if a slight reduction of the hygroscopic strain is observed, the moisture content is drastically reduced due to the decrease of porosity. Thus, the influence of the matrix stiffness on the maximum value and the expansion kinetics is again confirmed.

Finally, a stiffer matrix leads to a lower expansion of biocomposites, which may be interesting for structural application of a biocomposite in an outdoor environment. Soft matrices, on the other hand, allow for greater expansion, which is the key factor in the design of hygromorph and hydromorph biocomposites.

Table 10: Hydrosopic parameters of 3D-printed and 3D-printed + thermocompressed biocomposites.

	cFF/PLA	cFF/PBS	cFF/PBSA	cFF/PBAT
<b>(a) 3D Printing</b>				
$\epsilon_{y,hyd}$ (%)	$1.5 \pm 0.3$	$3.0 \pm 0.3$	$3.8 \pm 0.4$	$4.0 \pm 0.4$
$d\epsilon_{y}/dt$ ( $10^{-7} s^{-1}$ )	$3.5 \pm 1.1$	$16.3 \pm 5.5$	$20.2 \pm 6.2$	$32.8 \pm 3.7$
$\beta_{y,hyd}$ (%)	$0.06 \pm 0.01$	$0.13 \pm 0.01$	$0.14 \pm 0.01$	$0.19 \pm 0.01$
<b>(b) 3D Printing + Thermocompression</b>				
$\epsilon_{y,hyd}$ (%)	$1.4 \pm 0.1$	$1.6 \pm 0.2$	$3.0 \pm 0.1$	$3.7 \pm 0.1$
$d\epsilon_{y}/dt$ ( $10^{-7} s^{-1}$ )	$1.1 \pm 0.1$	$2.9 \pm 0.1$	$10.4 \pm 2.9$	$21.4 \pm 0.4$
$\beta_{y,hyd}$ (%)	$0.14 \pm 0.01$	$0.20 \pm 0.02$	$0.30 \pm 0.02$	$0.31 \pm 0.01$

## IV. Hygro-/Hydromechanical behavior

### IV. 1. Hygro-/Hydromechanical properties

Figure 86a and b display the influence of water content (implied by relative humidity and immersion) on the longitudinal ( $E_{11}$ ) and transverse ( $E_{22}$ ) elastic moduli. First of all, the matrix stiffness has a dramatic effect on longitudinal stiffness, with 3D-printed cFF/PLA, cFF/PBS, cFF/PBSA and cFF/PBAT having  $E_{11}$  moduli of  $15799 \pm 2154$ ,  $11175 \pm 1250$ ,  $10300 \pm 700$  and  $12748 \pm 1847$  MPa respectively. This is due to the moderate fiber volume ratio (about 30%). The trends observed for the transverse modulus are similar.

The data for cFF/PLA biocomposite are similar to those published previously [88]. To our knowledge, there are no data available on cFF/PBS and cFF/PBAT in the literature. With respect to transverse stiffness, the cFF/PLA composite also exhibits higher properties than cFF/PBS and cFF/PBAT biocomposites, but beyond the effect of matrix stiffness, the interfacial shear strength also has a large influence on the transverse properties. Using microbond tests, Pantaloni et al. [233] showed that cFF/PLA has an interfacial shear strength (IFSS) almost twice as high as cFF/PBS.

Then, the presence of water, induced by the RH conditioning or immersion, inside the composites plies and fiber cell-walls causes an exponential decay of the  $E_{11}$  modulus for all

biocomposites toward a nearly constant value (Figure 86a). The intensity of the decrease is similar (-60%) regardless the matrix chosen. However, as noted earlier, a stiffer matrix results in slower moisture uptake. Thus, it can be stated that the stiffness of the matrix can also influence the kinetics of rigidity loss. For example, reaching a moisture content of 5% (Figure 84b) and the corresponding stiffness (Figure 86a) requires about 4 hours for cFF/PLA versus about 24 minutes for cFF/PBS and cFF/PBAT biocomposites.

For  $E_{22}$ , a linear decrease is noticed with a larger slope for cFF/PLA compared to the cFF/PBS and cFF/PBAT counterparts (Figure 86b).

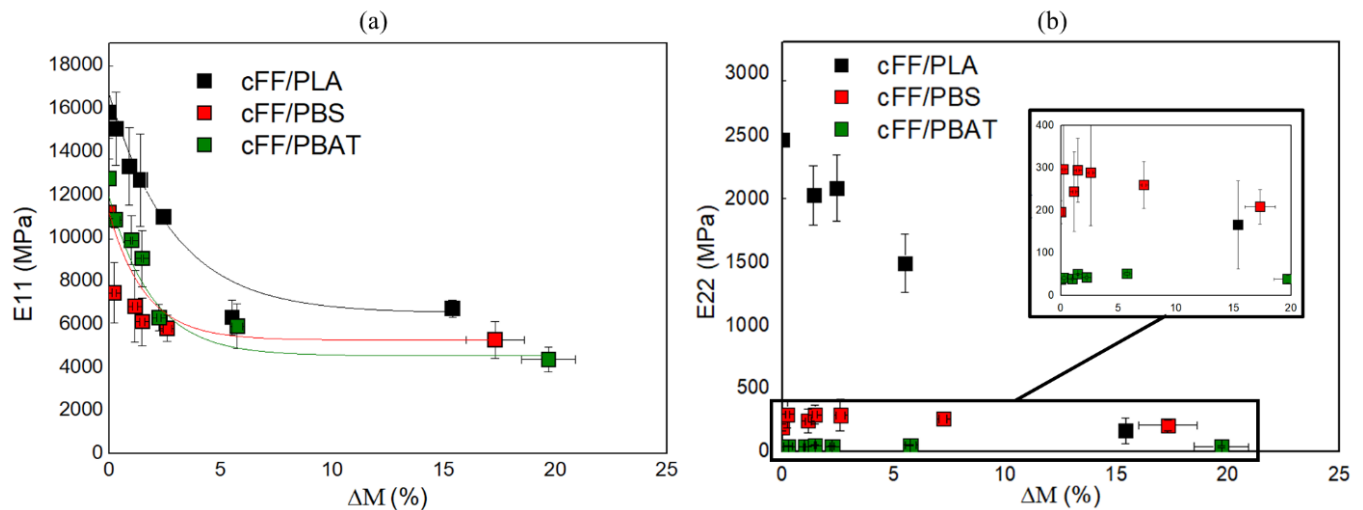


Figure 86: Evolution of (a) longitudinal ( $E_{11}$ ) and (b) transverse ( $E_{22}$ ) elastic modulus of 3D-printed biocomposites for various moisture content. The inset shows a magnification of the y-axis (b). Solid lines are decreasing exponential fits.

Actually, moisture induces swelling and plasticization mechanisms that alter the elastic properties of composites. In addition, the moisture content and its gradient within the material generate hygro- and hygroscopic internal stresses that can exceed the transverse tensile strength of the composite ply and degrade the interactions both between the components and within the fiber cell wall ([50], [51], [250]). This results in a lower ability to transfer load stresses during mechanical loading and a failure of the material at lower loading stress.

## IV. 2. Evaluation of the internal stress

Curvature analysis, i.e. the difference between the initial dry curvature and the final saturated curvature after immersion in water, was performed on asymmetric biocomposites. To better understand the relationship between hydroexpansion and matrix stiffness, the radial internal stresses generated in asymmetric laminates by moisture sorption are estimated using Equation 5 [251]:

$$\sigma_{22} = \sigma_{radial} = \frac{E_{11} \cdot E_{22}}{E_{11} + E_{22}} \frac{t}{\Delta\rho} \left( \frac{1}{2} + \frac{1}{24} \left( 2 + \frac{E_{11}}{G_{12}} + \frac{E_{22}}{G_{12}} \right) \right) \quad (\text{Equation 5})$$

With  $t$  the total thickness of the sample ( $t = 0.65$  mm),  $\Delta\rho$  the differential curvature radius due to differential expansion between layers ( $\Delta\rho_{\text{after printing}} = \rho_{\text{after printing}} - \rho_{\text{after actuation printing}}$ ,  $E_{11}$  and  $E_{22}$  are the values of longitudinal and transverse modulus at saturated state,  $G_{12}$  is the in-plane shear modulus. A wide range of radial compressive stresses from 16.0 to 0.8 MPa for cFF/PLA and cFF/PBAT respectively is calculated, confirming the lower constraining effect of PBAT on flax fibers compared to PLA counterparts. cFF/PBS also exhibits a lower radial stress of 2.1 MPa. Higher matrix stiffness restricts fiber swelling due to higher internal compressive stresses. Conversely, lower matrix stiffness allows the fiber to expand. This confirms that the constraining effect of the matrix on the flax fiber and consequently on the internal hydroscopic stresses can be controlled by selecting the appropriate matrix stiffness. However, it must be kept in mind that local plasticization generated by water ingress might be considered during matrix selection. Indeed, it would induce the matrix to be more deformable so that the biocomposite swelling may be altered.

## V. Matrix selection as a promotor of HBC actuation

A global representation of the evolution of the transverse hydroscopic strain of the different 3D-printed biocomposites is presented as a function of the matrix stiffness (Figure 87a).

Interestingly, the hydroexpansion results correlate well with matrix stiffness with a continuous decrease in hydroexpansion with increasing polymer stiffness. Thus, a constraining effect of the matrix implies a linear reduction ( $R^2 = 0.91$ ) in the expansion of the embedded fiber compared to the free fibers [47]. Increasing matrix stiffness helps to increase the stresses at the fiber/matrix interface and promotes dimensional stability which is one of the bottlenecks in load bearing applications. On the contrary, reducing the matrix stiffness allows the fiber to expand considerably more and faster which can result in a faster response, potentially relevant for actuator/shape-changing applications. Although not significant compared to the radial swelling of flax fibers, the swelling of the matrix may contribute slightly to the expansion of the biocomposite.

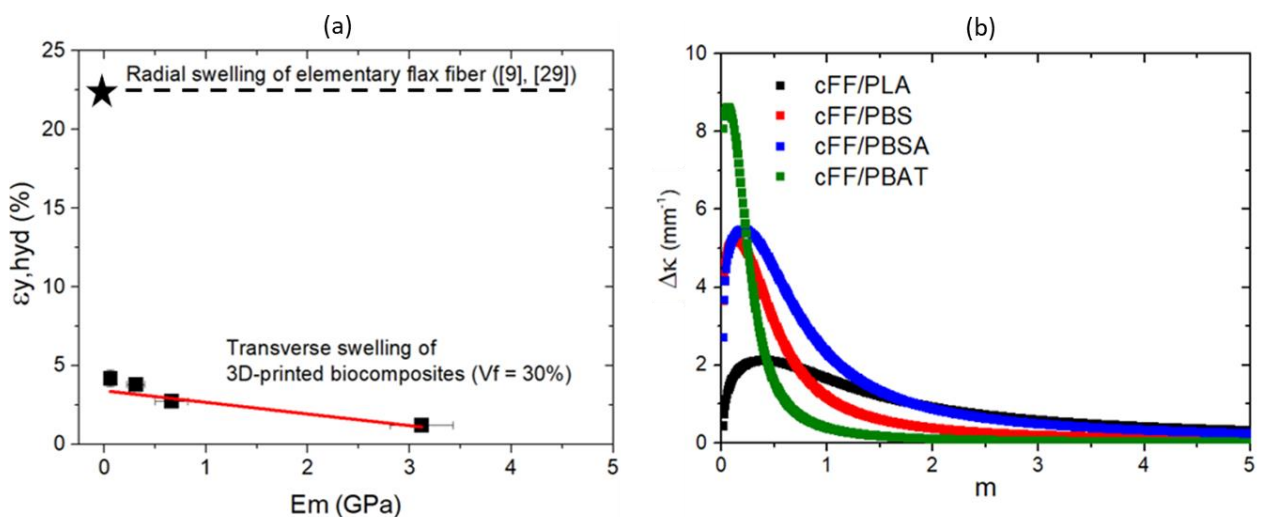


Figure 87 (a) Evolution of hydroscopic expansion of 3D-printed biocomposites ( $V_f=30\%$ ) as a function of matrix stiffness. (b) Evolution of the curvature amplitude of 4D-printed bilayer biocomposites in the dry and wet state as a function of the active-to-passive layer thickness ratio ( $m$ ).

The open question remains, what boundary conditions might allow the design of biocomposites with negligible hygro- and hydroexpansion for load bearing applications and, on the contrary, with maximum hygro- and hydroexpansion for morphing purposes ?

Based on a linear trend as observed in Figure 87a, two points can be discussed regarding the boundary conditions. First, extrapolating a linear regression to  $\epsilon_{hyd,y} = 0$  leads to a matrix stiffness equal to 4.33 GPa. It is interesting to note that this value is close to the transverse

modulus of the fiber ([252], [253]). This explains that the hygroexpansion of biocomposites occurs if the stress generated by the fiber swelling is higher than the stress induced by the matrix, thus if the rigidity of the matrix is lower than the transverse modulus of the fiber. However, stiff polymers often induce low toughness and potentially high processing temperature which are not compatible with natural fibers (e.g. PEEK or other). Formulating the matrix with short fibers to enhance its stiffness can be imagined and would deserve further work. On the other hand, maximization of hydroscopic strains for morphing purposes can be achieved by decreasing the matrix stiffness, for a specific fiber content (Figure 87a). Assuming  $E_m = 0$  GPa, the maximal transverse hydroscopic strain would be of 4.2% considering the linear equation. In this condition, the natural fibers would be the only component to exhibit water-induced swelling. Based on a specific Rule of Mixture, multiplying the fiber volume fraction ( $V_f = 30\%$ ) by the radial swelling of elementary fiber ( $\epsilon_y = 22.5\%$ ) gives a final transverse swelling of 6.75% at the biocomposite scale. The difference between experimental and theoretical values can be explained by the variation of swelling between single and bundle of fiber as explained elsewhere [35]. The natural swelling potential of the free flax fiber could be reached by the combination of restricted matrix stiffness and higher fiber content. Indeed, based on the Timoshenko equations (Equation 1) the actuation curvature (actuator responsiveness)  $\Delta\kappa$  can be evaluated to illustrate the role of the matrix stiffness.

Figure 87b presents the predicted evolution of actuation curvature as a function of layer thickness ratio  $m$  for biocomposites based on the different matrices. The maximum curvature achieved by the bilayers covers a wide range from  $21.3 \cdot 10^{-3} \text{ mm}^{-1}$  for cFF/PLA,  $52.2 \cdot 10^{-3} \text{ mm}^{-1}$  for cFF/PBS,  $54.9 \cdot 10^{-3} \text{ mm}^{-1}$  for cFF/PBSA to  $86.3 \cdot 10^{-3} \text{ mm}^{-1}$  for cFF/PBAT. Interestingly, HBC with a softer matrix, i.e., PBAT, reaches almost similar curvature values (responsiveness) to FF/MAPP with 60% vol manufactured by thermocompression [59]. Assuming that responsiveness clearly depends on the fiber content [64], the present work shows that the matrix



stiffness drastically and positively modifies the stationary actuation performance of HBC. The Timoschenko's equations do not provide any information on the transient performance of HBC; however, previous results dealing with the effect of matrix stiffness on the swelling kinetics of biocomposites suggest that it may also be positive for HBC. This point should be investigated further.

## VI. Conclusion

3D-printed biocomposites reinforced with plant-fibers are increasingly competitive with the performance of composites reinforced with synthetic-fibers. The intrinsic swelling of natural fibers has often been considered a major drawback limiting the development of biocomposites for outdoor applications. However, turning this drawback into an advantage can be achieved by designing shape-changing materials, i.e. hygromorph/hydromorph biocomposites (HBC).

**Chapter 3** brings additional insights into the effects of matrix stiffness on the sorption, hydroexpansion, mechanical properties and internal stresses generation of biocomposites manufactured by the 3D-printing process. Thus, various filaments were produced and then printed with biopolymer matrices with a wide range of stiffness from 63 MPa to 3.1 GPa. Similar fiber content and porosity level were achieved.

The increase in matrix stiffness implied a reduction in moisture content and sorption kinetics. The cFF/PBAT biocomposites had a hygroscopic coefficient of 0.19, followed by PBSA, PBS and PLA with coefficients of 0.14, 0.13 and 0.06, respectively. This was followed by a loss of elastic mechanical properties of the different composites for a similar moisture content.

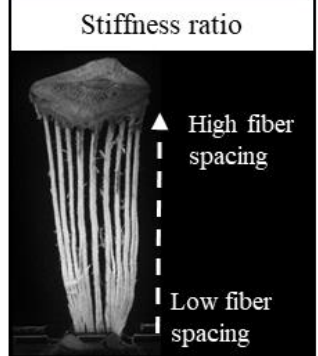
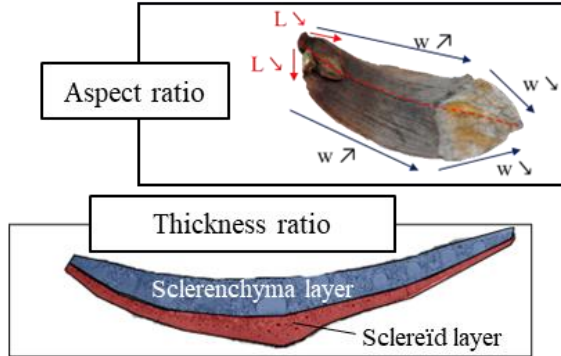
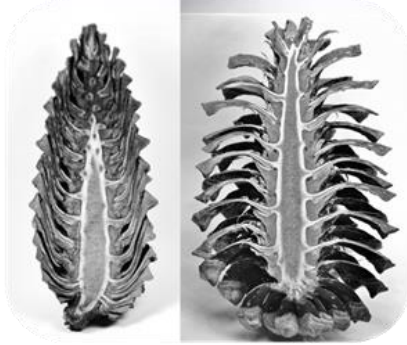
It was established that the constraining effect of the matrix was modified by the matrix stiffness as found by evaluating the hygroscopic internal stresses. The evolution of hygroscopic strain as a function of matrix stiffness showed a linear decreasing trend. It seems theoretically possible to cancel the hydroexpansion in the case of a structural application of the biocomposite by selecting a matrix whose stiffness is higher than 4.3 GPa. Conversely, for an application

targeted towards morphing, maximum hydroscopic deformation can be achieved with low matrix stiffness. Thus, the composite based on the softer matrix, i.e. cFF/PBAT, exhibits encouraging actuation performance similar to that of FF/MAPP 60%vf manufactured by thermocompression. Linear extrapolation of  $\epsilon_{\text{hyd}}$  as a function of matrix stiffness toward zero values of matrix stiffness proposed a value around 4%. Further work should be done to design Hygromorph BioComposites to take benefit of the full radial expansion of the elementary flax fiber ( $\approx 20\text{-}25\%$ ).

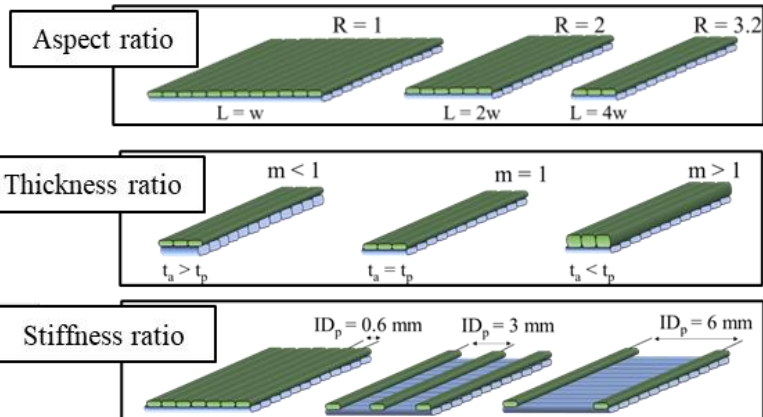
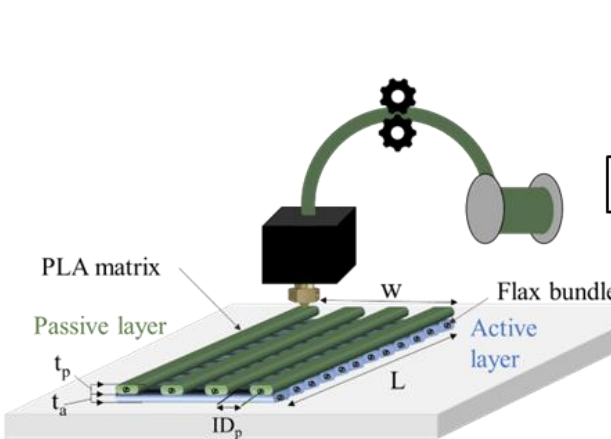


# Chapter 4 : How bioinspired design fosters the morphing behavior of HBC ?

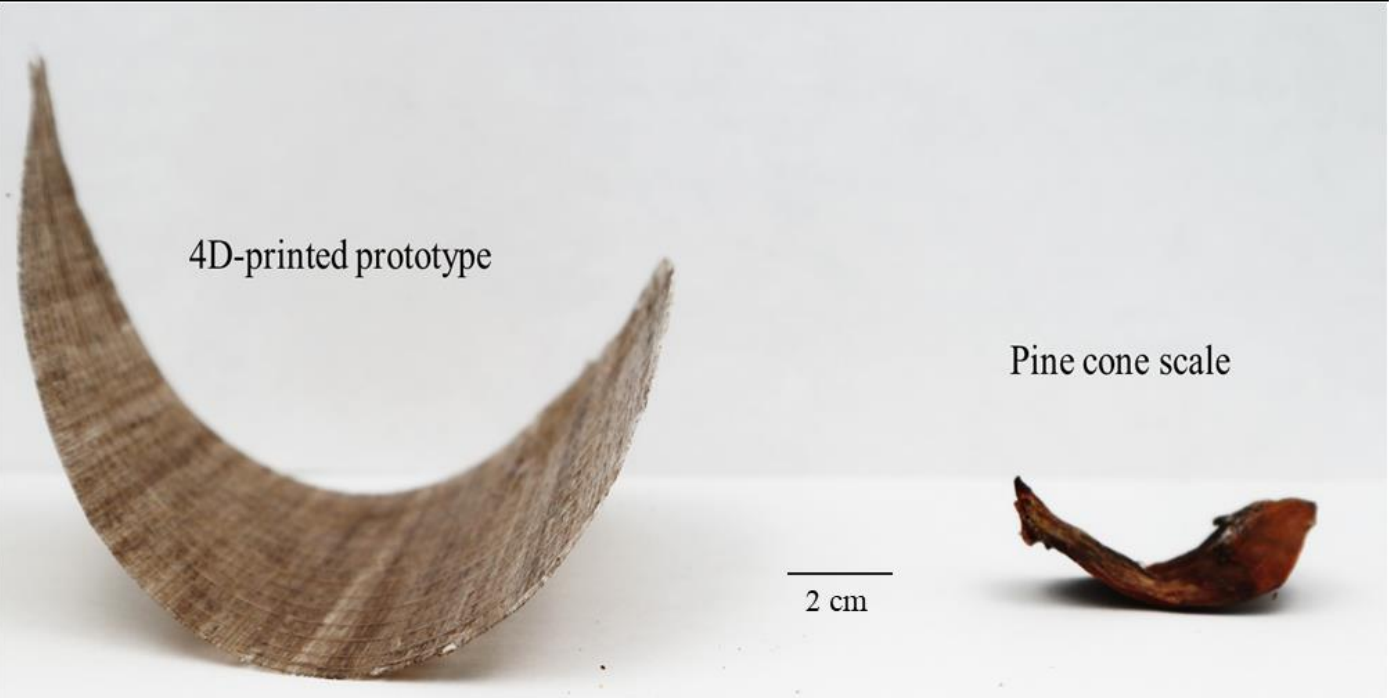
## Biological Inspiration



## 3D-printing



## 4D-printing



## I. Introduction

Originally based on single curvature interpretation of pine cone scale motion during moisture change ([62], [145]), recent works on pine cone scale have evidenced a more complex motion than the single longitudinal curvature ([254], [255]). Actually, pine cone scale actuation follows three states of humidity-driven deformation considered as a multi-phase curvature occurring at different time scale. A bifurcation of curvature occurs around 30% of relative humidity where the longitudinal curvature  $K_x$  overcomes the transverse one  $K_y$  [254]. The bistability represents the two stable shape states that a material can reach due to an external action. The transition between those states is highlighted through the bifurcation between the longitudinal deformation  $K_x$  and the transversal deformation  $K_y$ , when a change of predominant curvature is noticed.

More than fasten the response, this actuation scenario allows a better packing of the scale and reduces the geometrical rigidity of the scale to enhance the longitudinal actuation. For pine cone scale, the transition between various shape is rather slow. Indeed, fast bifurcation named as snap through effect is often used in plant kingdom to overcome the only diffusive based actuation. This is the case of carnivorous plants that use mechanical instability i.e. fast change of curvature to fasten their response ([133], [134], [136], [256]). Bistable mechanisms are also used by animals. For example, the specific displacement of crabs reveals a complex physical synergy at its leg level. Made of five different parts, the crab leg overcomes successive mechanical loads induced by motion. The shape-changing curvature of the legs allows for consistent forward and backward motility [257].

Unlike these natural examples, pine cone scale has a very low velocity [148]. Instead of using mechanical instabilities, its bifurcation mechanism is built on a slow continuous reshaping process. The pine cone scale is made of two distinguishable layers : sclerenchyma and sclereid layers. Among thousands of pine cone scale species, internal structure and biochemical

composition vary and modify the responsive curvature. Sclerenchyma layer is embedded into a brown tissue that limits the fiber expansion. It is considered as restrictive layer. In the opposite, the sclereid fibers exhibit a 20%-length variation at saturation [258].

The attainable design space is greatly limited by the difficulty to locally tailor the pre-strain field and material anisotropy due to the inherent orthotropic nature of the conventional manufacturing techniques employing fiber-reinforced composites or mechanical pre-straining. This strongly limits their applicability to systems with simple shapes and geometries. More complex designs thus require enhanced control particularly for obtaining locally tailored strain fields with large anisotropy gradients.

4D-printing represents a disruptive approach to manufacture complex novel smart materials with morphological predetermined response. This is an incredible opportunity for natural fiber biocomposite to be developed in the same time scales as synthetic counterparts [87]. Correa et al. [255] have proposed a programmable 4D-printed Hygromorph Biocomposites exhibiting a dual curvature response to moisture variation. Their methodology was based on trial-and-error approach to find the architecture, i.e. printing trajectory and material distribution that would enable a temporally delayed double curvature. Gladman et al. [259] and Van Manen et al. [119] proposed similar investigations on cellulose/hydrogel and pure PLA polymer. Even if the bifurcation term is not used in these works, the reshaping mechanism is similar although not strictly investigated. Moreover, in addition to material build-up composition, the lay-up, the geometry and aspect ratio of a bilayer geometry also affects the shape transformation ([6], [16], [17]).

Different studies have dealt with the possible programming and mastering of the bifurcation thanks to the combination of different bistable elements [261], the optimization of the structure [262], the external environment [263], the orientation of fibers [115], the using of tunable

stiffness mechanism [264] and through other biomimetic models in order to control the bistability of composites. Some of them tackled the influence of the length to width (L/W) aspect ratio on the bifurcation and the modes of stability encountered (horse saddle, double cylindrical curvature) ([16], [23], [24]). However, these studies address a bistability prediction resulting from a thermal action ([263], [265], [266]) or from an external force [267] and not from a hygroscopic action.

The management of the bifurcation is essential to be able to program the response even if it depends on many factors which are all interrelated [262]. Different ways of predicting the bistability of multi-layered laminates are proposed. Through the double curved beam model and finite element analysis ([268], [269]), we can predict its shape transformation as a result of an external force. The semi-analytical approach of the relations of Rayleigh Ritz and Von Karman ([23], [25], [28], [29]) allows to predict the bistable structure following environmental action as temperature or humidity.

The aim of **Chapter 4** is to target the material and 4D-printing processing parameters making possible to control the bistability of a Hygromorph Biocomposite to program its morphing. Different aspect ratio and thickness ratio through 4D-printed bilayer samples are tested on a wide range of humidity to point out the best geometrical configuration and analyze the bifurcation behavior. Besides, bifurcation and the subsequent actuation performance gain are discussed in term of passive layer stiffness thank to various processing parameters (e.g. interfilament distance, material selection). Finally, a prototype approach is realized to reproduce the complex motion of pine cone scale by design control in order to upgrade the actuation potential of 4D-printed HBC.

## II. Results

### II. 1. Conceptualization of pine cone architecture and geometry

Pine cone scale relies on a combination of structural features and biochemical components that promotes its deployment under water uptake [146]. While sclereid fibers appear as elongated cells, sclerenchymous fibers are made of embedded small cells [272]. Besides, the water sensitivity of both layers also exhibits interesting differences with a 27%-thicker and 22%-longer sclereid layer after reaching saturation state. In the opposite, dimensions of sclerenchyma layer are almost unmodified (3%-thinner and 1%-longer at saturation state compared to dry state). Based on this difference of water-induced expansion of the scale tissues, the sclereid layer can be considered as the active layer while sclerenchyma layer acts as the restrictive layer (Figure 88).

Focusing on the mesostructure of the scale (Figure 88), the sclereid layer exhibits a thick area close to the rachis ( $t = 0.7\text{mm}$ ) and then exponentially decreases approaching the apophysis ( $t = 0.15\text{ mm}$ ). The sclerenchyma layer remains almost constant along the length ( $t = [0.2-0.3]\text{ mm}$ ). Therefore, the passive-to-active thickness ratio that controls the longitudinal curvature actuation according to the bimetallic theory of Timoschenko (Equation 1) exhibits an exponential decay along the scale length (Figure 89a).  $t_p/t_a$  evidences an optimum curvature close to the rachis as it is observed elsewhere [62].

Along the width (Y direction),  $t_p/t_a$  ratio is also changing and is here responsible of the transverse actuation responsiveness and reactivity. Along Y, the sclerenchyma strands appear also to have constant thickness while the sclereid layer evidences a parabolic trend. Hence,  $t_p/t_a$  also evidences a parabolic evolution with value tending to infinite value on the edge and 0.3 close to the center (Figure 89b). Following Timoschenko's equations, a curvature distribution is expected with maximal value on the center which geometrically constrains the



synclastic behavior of the curvature. Although this parameter evolves through the length and width of the scale [146], thickness ratio in pine cone scale is around 0.5 [273].

Another dimensional variation is the aspect ratio of the scale, i.e. its length/width (L/W) ratio. Although this ratio has been estimated at 5/3 for pine cone scale [254], a gradient of aspect ratio may be more suitable considering the non-rectangular shape of the scale. Therefore, the scale can be represented as a polygonal association whose the different aspect ratios promote the double curvature mechanism (Figure 88). For example, the higher width at the apophysis, i.e. apical area, generates a transverse curvature  $K_y$  while the thin width at the rachis, i.e. also called hinge area [273] or basal area [255], promotes the longitudinal curvature  $K_x$  [255].

Then, the distance between sclerenchyma fibers is also an observable architectural feature exhibiting an evolution through the length of the scale [146]. Made of thick lignified cell walls, the sclerenchyma fibers are very stiff and contribute to the hardness of the scale [274]. The increase of the distance between sclerenchyma fibers [146] along the length of the scale might ensure the mechanical coupling of the rachis and apophysis parts (Figure 88). However, this point requires further biological surveys.

To carry out this investigation, the geometry and mesostructure of pine cone scale are abstracted into sliceable building blocks such as aspect ratio (Length/Width)  $R$ , passive-to-active thickness ratio  $m$  and interfilament distance  $ID$  respectively. Since interfilament distance dictates the passive-to-active stiffness ratio  $n$ , only the interfilament distance in passive layer ( $ID_p$ ) was investigated. Both parameters were individually analyzed by fixing the two others. The preset values are the following ones:  $R = 3.2$ ,  $m = 0.7$  and  $ID_p = 0.6$  mm. Investigation on aspect ratio was conducted by keeping a fixed length ( $L = 8$  cm) while changing the width ( $w = [2.5; 4; 8]$  cm) to finally obtain three aspect ratios of 3.2, 2 and 1. By programming Layer Height printing parameter, the passive-to-active thickness ratio fluctuates from 0.5, 0.8, 1, 1.7 to 2 [87]. Then, by modifying interfilament distance in the gcode, specimens with various  $ID_p$

were built ( $ID_p = [0.6, 1.5, 3, 6]$  mm). Inter-filament distance in active layer ( $ID_a$ ) was fixed at 0.6 mm all along the investigation. 3D-printing process and aforementioned tested parameters are mapped in Figure 90.

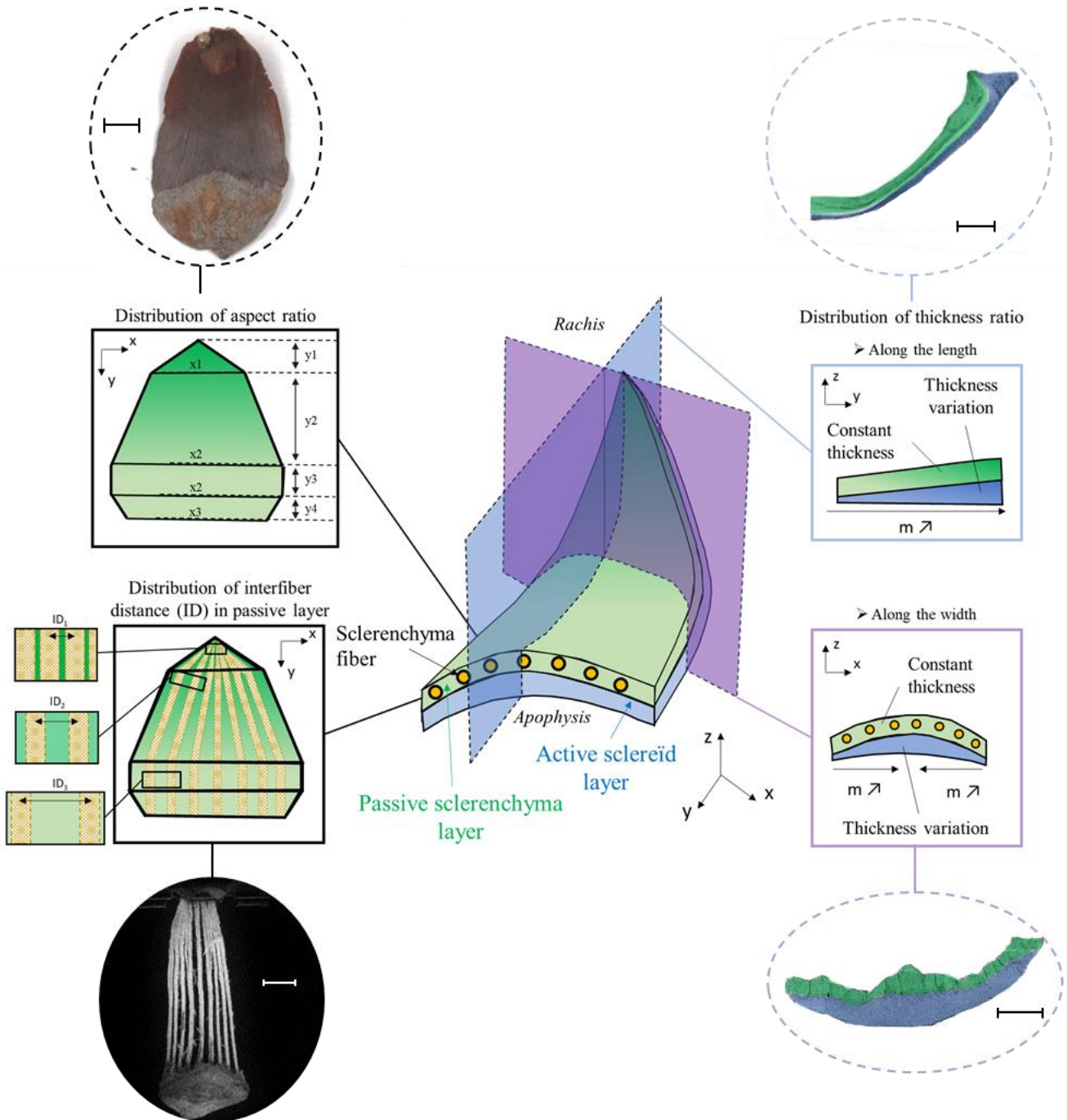


Figure 88: Discretization of the architecture of the scale in four sliceable blocks. Rachis and apophysis are also defined as basal and apical parts.

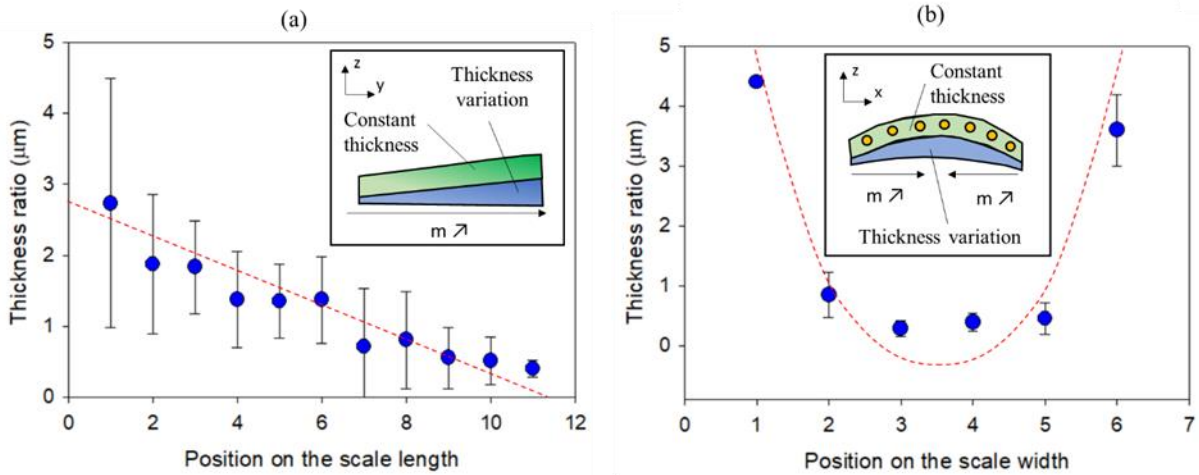


Figure 89: Distribution of passive-to-active thickness ratio through (a) longitudinal and (b) transverse section of *Pinus wallichiana* scales. Green layer represents the passive sclerenchyma layer while the blue layer symbolizes the active sclereid layer. Graphics are based on the data of Eger et al. [146]

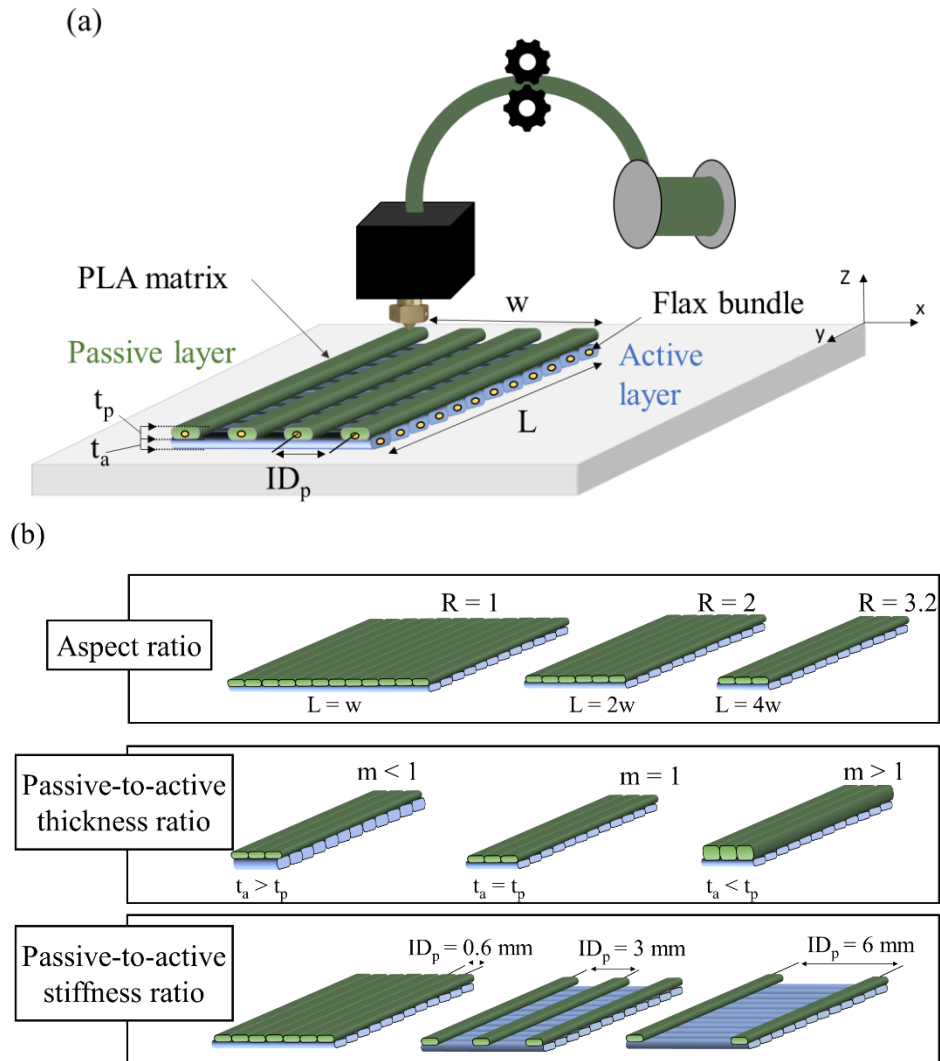


Figure 90: (a) 3D-printing process of cFF/PLA bilayers and (b) the three investigated architectural features : aspect, thickness and stiffness ratios. Green layer represents the passive layer ( $0^\circ$  orientation) while the blue layer represents the active layer ( $90^\circ$  orientation).

## II. 2. Influence of the length to width (L/W) aspect ratio of HBC

Figure 91 gives the evolution of the longitudinal ( $K_x$ ) and transverse ( $K_y$ ) 4D-printed cFF/PLA HBC caused by water sorption for different length to width ratios. Starting from positive curvature values at dry state ( $RH = 0\%$ ), an initial increase of  $K_x$  could arise from the residual stresses generated by 3D-printing process. The HBCs flatten out around  $\Delta C \sim 5\%$  which corresponds to the free stress state where residual and internal stresses are equal. This confirms a previous work dedicated to cycling behavior of HBC [65]. The effect of aspect ratio is clear. The slender the beam the higher the change of curvature. The beam-like bilayer ( $R = 3.2$ ) produces a change of longitudinal curvature sign while the squared bilayer ( $R = 1$ ) ends up in a flat shape (Figure 92). This difference reflects the higher differential swelling for a beam-like structure of which orthotropic expansion is promoted and leads to the inversion of the longitudinal curvature. On the opposite, neither active or passive layers are identifiable in a square-like bilayer. It results in an antagonist swelling that geometrically restricts the actuation potential. In parallel, increasing the width to thickness ratio makes the swelling more orthotropic, promoting the out-of-plane expansion [56]. In this test, increasing the aspect ratio promotes the transverse expansion of the active layer, resulting in a higher longitudinal expansion.

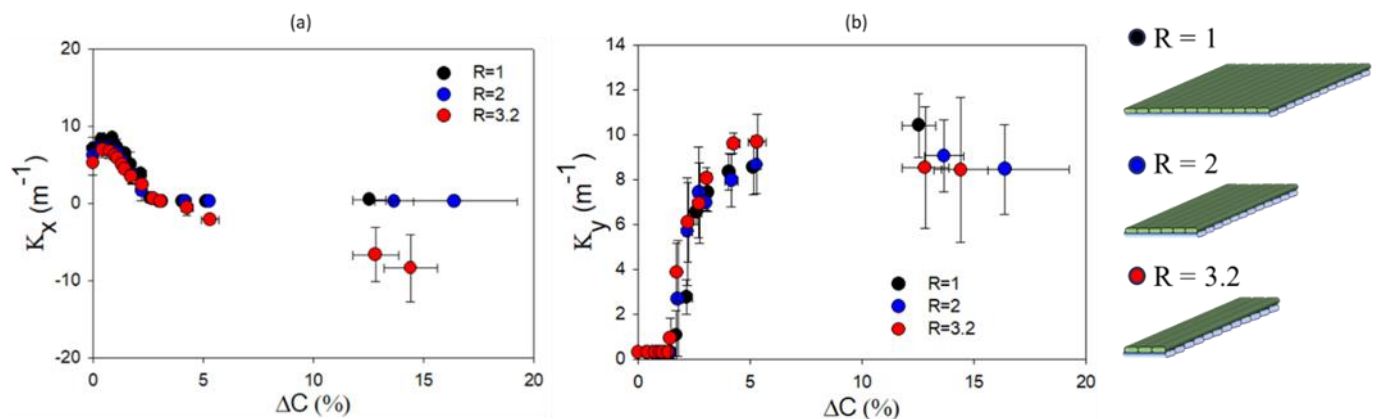


Figure 91: Evolutions of longitudinal ( $K_x$ ) and transverse ( $K_y$ ) curvatures of 4D-printed cFF/PLA biocomposites as a function of moisture content for various aspect ratios. ( $m = 0.7$ ,  $ID_p = 0.6$  mm)

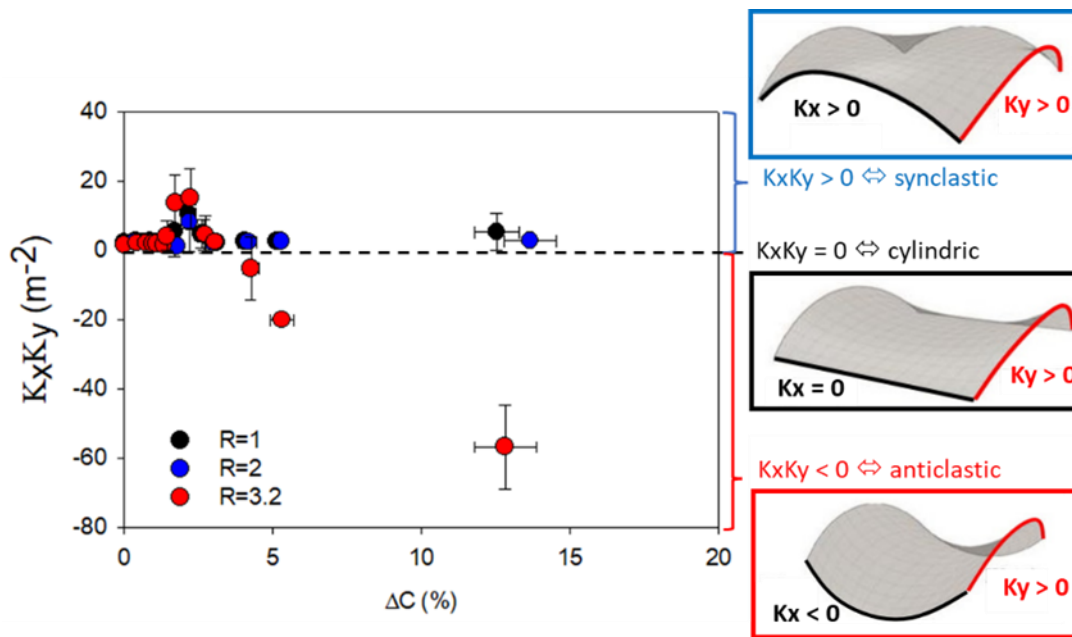


Figure 92: Gaussian curvature as a function of moisture content for cFF/PLA bilayers with different aspect ratios. Depending on the  $K_x K_y$  product, both synclastic, cylindrical and anticlastic shapes are illustrated. ( $m = 0.7$ ,  $ID_p = 0.6$  mm)

Arising from the product of curvatures ( $K_x K_y$ ), Figure 92 exhibits a variation in the Gaussian curvature as a function of water sorption. The beam-like bilayer ( $R = 3.2$ ) went from a cylindrical shape transformation, to a synclastic shape and finishing with an anticlastic shape. For lower aspect ratio, the bilayer does not exhibit any change of Gaussian curvature sign. Gigliotti et al. [260] already pointed out this relation on synthetic composite material subjected to thermal gradient. They informed that increasing aspect ratio drives the bifurcation mechanism by losing the geometric symmetry. It induces an anticlastic curvature along the length. Besides, it is important to mention the synclastic shape occurring for each aspect ratio for a moisture content around 2%. This observation emphasizes the actuation of the transverse curvature  $K_y$  (Figure 91b) before the change of sign of the longitudinal curvature  $K_x$  (Figure 91a). This shows similarities with actuation mechanism of pine cone scale, where transverse actuation outstrips the longitudinal curvature [255].

The moisture content at bifurcation  $\Delta C^*$  is an important parameter to follow as it establishes a link between the overall hygroscopic stress induced by water sorption, the bifurcation and the aspect ratio. A slightly higher  $\Delta C^*$  is required to reach bifurcation for squared bilayers ( $\Delta C^*$

=  $2.2 \pm 0.2\%$ ) compared to rectangular bilayers as it is hypothesized that higher actuation force is required to overcome the constraining effect of the passive layer. In rectangular bilayers ( $R = 3.2$ ), the hygroscopic internal stress is lower and less strain energy is required to perform the bifurcation ( $\Delta C^* = 1.7 \pm 0.1\%$ ). Moreover, due to the orthotropic water diffusion through biocomposites, modifying the aspect ratio should affect the diffusion kinetics and strain distribution over transitional swelling [275]. On the other hand, the curvature at bifurcation  $K^*$  does not significantly fluctuate between specimens. Therefore, the aspect ratio enables to tailor the physical configuration (synclastic, cylinder or anticlastic shapes) of cFF/PLA bilayer while keeping the curvature at bifurcation  $K^*$  unchanged.

Applied to pine cone scale, the aspect ratio decreases along the length, as the width significantly increases from the rachis to the apophysis (Figure 88). Thus, the transverse curvature should be fostered in the apophysis area to ensure scale closure and seed protection. At the rachis, the trend is opposite. Relying on a high aspect ratio, the longitudinal curvature would be exacerbated while the transverse curvature would remain insignificant. Besides, the high aspect ratio could change the sign of longitudinal curvature to facilitate the seed release in dry environment.

### II. 3. Cross-sectional distribution of tissue : Influence of the passive-to-active thickness ratio

The second investigated structural parameter is the passive-to-active thickness ratio  $m$ , defined as thickness ratio here, as referred in Timoshenko's equation [60]. Figure 93 displays the curvature in longitudinal and transverse directions of cFF/PLA bilayers for various thickness ratios.

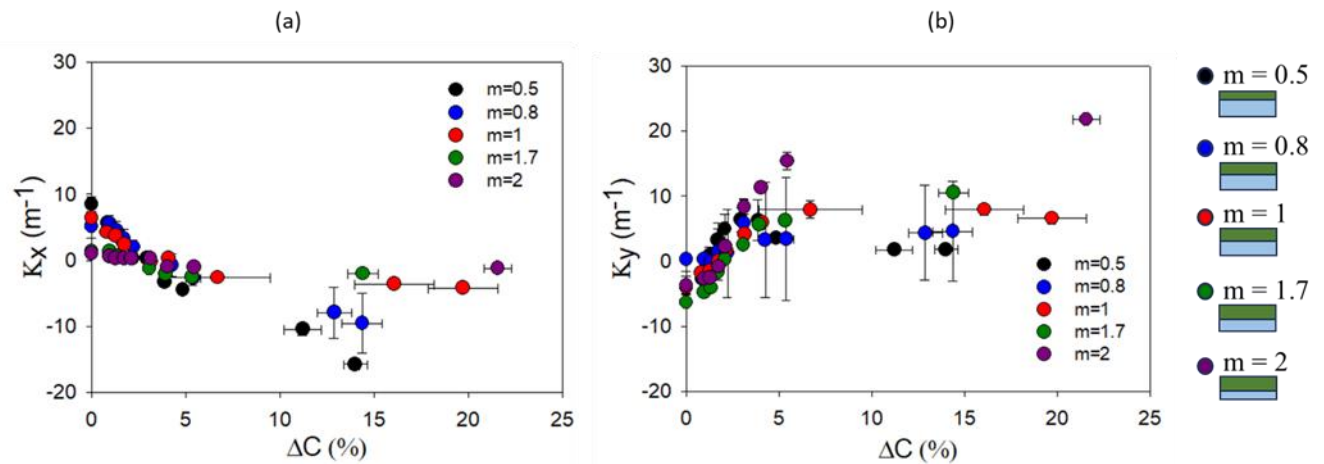


Figure 93: (a) Longitudinal and (b) transverse curvature of cFF/PLA bilayers as a function of water content for various passive-to-active thickness ratios ( $R = 3.2$ ,  $ID_p = 0.6\text{mm}$ )

Regarding Figure 93a, various actuation behaviors along the longitudinal direction are observed. A high thickness ratio ( $m = 2$ ) evidences a dominant contribution of the passive layer in the longitudinal bilayer direction and thus almost a constant zero-curvature along this axis. Conversely, a higher transverse curvature is observed (Figure 93b) since role of layers are reversed. The opposite trend is logically observed for low thickness ratio ( $m = 0.5$ ). Several results are proposed in the accessible literature dedicated to thermal stresses calculation within composite laminates [260]. For example, for square composite plates, the reduction of the  $[0/90^\circ]$  thickness ratio makes the curvature of one side negligible.

As shown in Figure 94, Gaussian curvatures are not impacted by thickness ratio while increasing the moisture content. As this part of the study was performed with slender HBC ( $R = 3.2$ ), changing the thickness ratio will essentially change the main contributing layer. In each extreme cases ( $m = 0.5$  and  $m = 2$ ),  $K_x$  and  $K_y$  annihilates each other one until bifurcation occurs. It results in a major presence of anticlastic shape except at bifurcation point where cylindrical shapes prevail.

Applied to pine cone scale, the gradient of thickness ratio along the length and width (Figure 94) induces an in-plane distribution of elastic strains, triggering the double curvature mechanism.

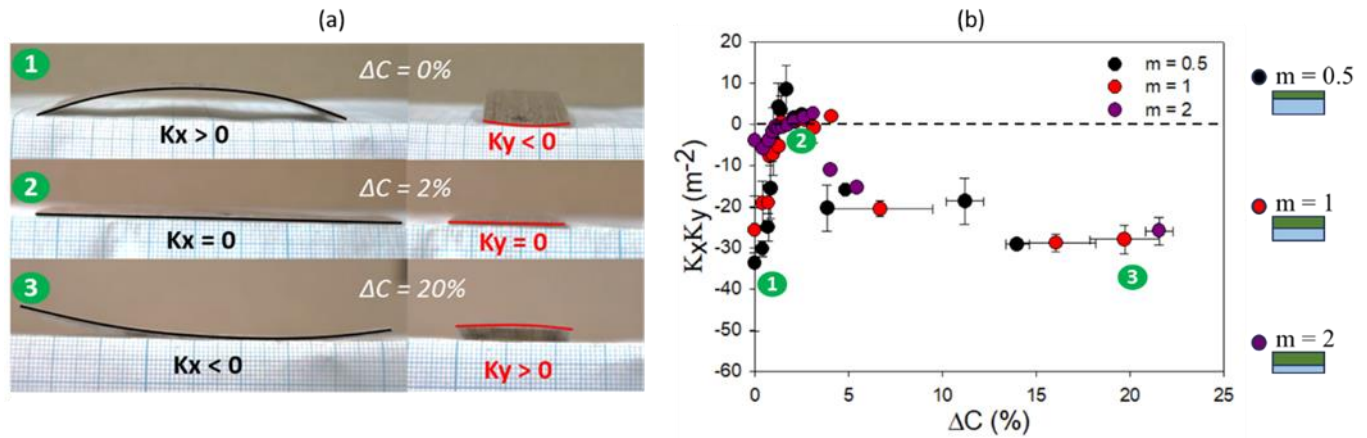


Figure 94: (a) Transitional shapes of cFF/PLA bilayers as relative humidity increases ( $m=0.5$ ,  $R=3.2$ ). (b) Gaussian curvature as a function of moisture content for cFF/PLA bilayers with different thickness ratio ( $R = 3.2$ ,  $ID_p = 0.6$  mm).

Table 11 illustrates a strong dependence of the moisture content  $\Delta C^*$  and the curvature  $K^*$  at bifurcation with the thickness ratio for slender beams ( $R = 3.2$ ). In biocomposites, moisture sorption is promoted by hydrophilic behavior of natural fibers ([26], [276], [277]). Since exchange surface between water molecules and flax fibers is unchanged between specimens, variations related to critical parameters are linked to bilayer mesostructure.

Regarding the moisture content at bifurcation  $\Delta C^*$ , low values ( $\Delta C^* \sim 1.6 \pm 0.1\%$ ) are obtained for extreme thickness ratios ( $m = 0.5$  and  $m = 2$ ) against higher values for balanced thickness ratio ( $\Delta C^* = 2.0 \pm 0.1\%$  for  $m = 1$ ). The cross-sectional distribution of tissues accelerates the bifurcation mechanism by promoting the transverse expansion of the active or passive layer ( $m = 0.5$  or  $m = 2$ ). When  $m = 1$ , the hygroscopic contributions of active and passive layer are closer, increasing the strain energy to reach bifurcation.

Then, by changing the cross-sectional distribution of tissues, a predominant expansion is attributed to the active or passive layer, affecting the resulting  $K^*$ . For example, low passive-to-active thickness ratio highlights a dominant active layer and a greater longitudinal curvature  $K_x$ .



Table 11: Critical parameters of cFF/PLA specimens for several thickness ratio

$m$	$K^* (m-1)$	$\Delta C^* (\%)$
0.5	$2.7 \pm 0.9$	$1.6 \pm 0.1$
1	$1.0 \pm 0.2$	$2.0 \pm 0.1$
2	0	$1.7 \pm 0.1$

## II. 4. Influence of passive-to-active stiffness ratio in the bifurcation behavior

Passive-to-active layer stiffness ratio of the HBC, referred as stiffness ratio here, affects the actuation mechanism according to Timoshenko's equation [60]. Stiffness of the passive layer is given by 0° longitudinally oriented flax/PLA materials while active counterparts is brought by 90° transversally oriented. Optimal values are expected as the curvature starts decreasing when HBC behave like a beam-like behavior rather than a bilayer [225]. Two strategies can be conceptualized through 4D-printing to bring deeper insights on the impact of stiffness ratio on the double-curvature mechanism. Firstly, slicing parameter such as the interfilament distance of the passive layer (IDp) is used to adjust its restrictive effect on actuation and be potentially modified along the HBC X-Y plane. Then, change in the material formulation used for the HBC production is employed to modify the stiffness ratio between active and passive layers.

### II.4.a. In-plane distribution of tissue : Influence of the Interfilament Distance in the passive layer (IDp)

Thanks to the design range proposed by 4D-printing, the layer stiffness can be tuned by setting the printing path. The first strategy consists in increasing the interfilament distance of the passive layer (IDp) from 0.6 to 6 mm to modify its amplitude of hygroexpansion as well as the composite layer stiffness. It has been established that the in-plane stiffness is directly linked with the composite surface ratio [278]. Figure 95 displays the longitudinal and transverse curvature of HBC as water sorption increases.  $K_x$  starts from slight positive values and monotonically decreases towards negative values. Increasing IDp generates a reduction of the

stiffness and the restriction effect on the 90° oriented active layer so that  $K_x$  curvature change increases [225].  $K_y$  is also modified with IDp but on a lower extent and again contrary results. Indeed, the role of IDp is changing to and become IDa due to the HBC anisotropy. Thus, generating an in-plane distribution of ID is beneficial for localizing the actuation, which mostly relies on the differential of hygroexpansion (1<sup>st</sup> order parameter) rather than using the restrictive effect induced by the stiffness ratio (2<sup>nd</sup> order parameter) according to Timoshenko's equation (Equation 1).

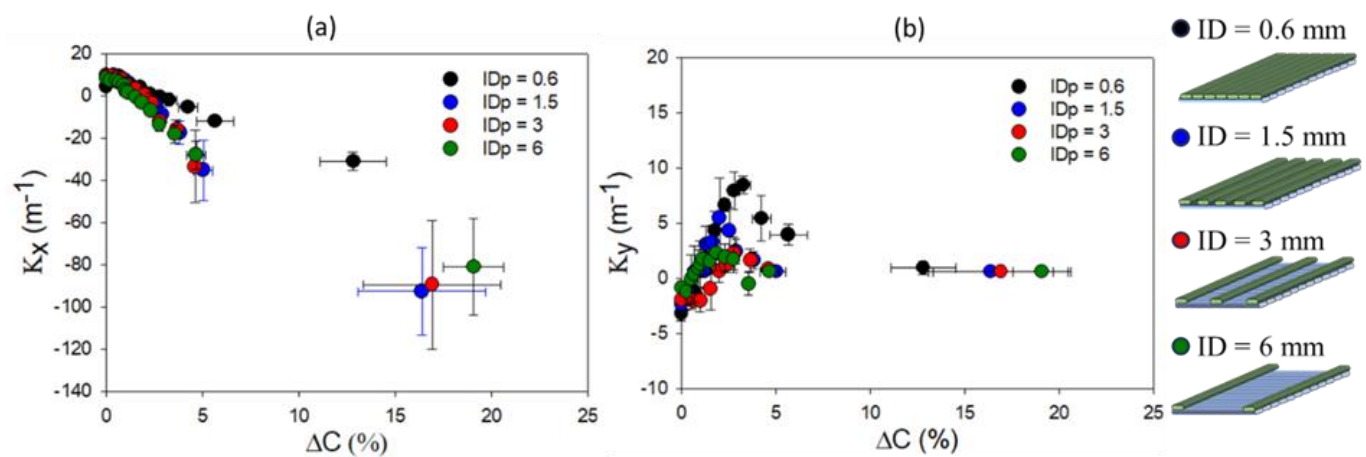


Figure 95: (a) Longitudinal and (b) transverse curvature of cFF/PLA bilayers as a function of water content for various interfilament distance within the passive layer. ( $R=3.2$ ,  $m=0.7$ )

#### II.4.b. Impact of the selected material

Biocomposite formulation is another option to control stiffness ratio. Relying on the inherent mechanical properties of the selected materials, it is possible to optimize the contributions of passive and active layers in the actuation process. For conducting this investigation, 4D-printed cFF/PLA and cFF/PBS specimens, with aspect and thickness ratio of 2 and 0.7 respectively, were tested. The stiffness ratio of cFF/PBS and cFF/PLA in dry state is given in Table 12 [279]. This ratio is 9-time lower when flax fiber is surrounded by a rigid PLA matrix ( $E = 3.1$  GPa) instead of a soft PBS matrix ( $E = 0.7$  GPa). A slight difference is observed in the evolution of  $K_x$  and  $K_y$  curvature as functions of moisture content (Figure 96). At dry state, curvature amplitude of cFF/PBS started at higher values in the longitudinal side compared to cFF/PLA

prints. This difference may result from a lower constraining effect on flax expansion and thus larger biocomposite expansion [279]. This observation is also made for different aspect ratios ( $R = 1$  and  $R = 3.2$ ).

Table 12: Stiffness ratio of cFF/PLA and cFF/PBS biocomposites in dry (taken from [28]).  $n$  represents the passive ( $E_{11}$ ) to active ( $E_{22}$ ) stiffness ratio.

	$E_{11}$ (MPa)	$E_{22}$ (MPa)	$n$ ( $E_{11}/E_{22}$ )	$\Delta\varepsilon_{hyd,y}$ (%)
cFF/PLA	$15799 \pm 2154$	$2476 \pm 470$	$6.4 \pm 2.1$	$1.5 \pm 0.3$
cFF/PBS	$11175 \pm 1250$	$196 \pm 27$	$57.0 \pm 14.2$	$3.0 \pm 0.3$

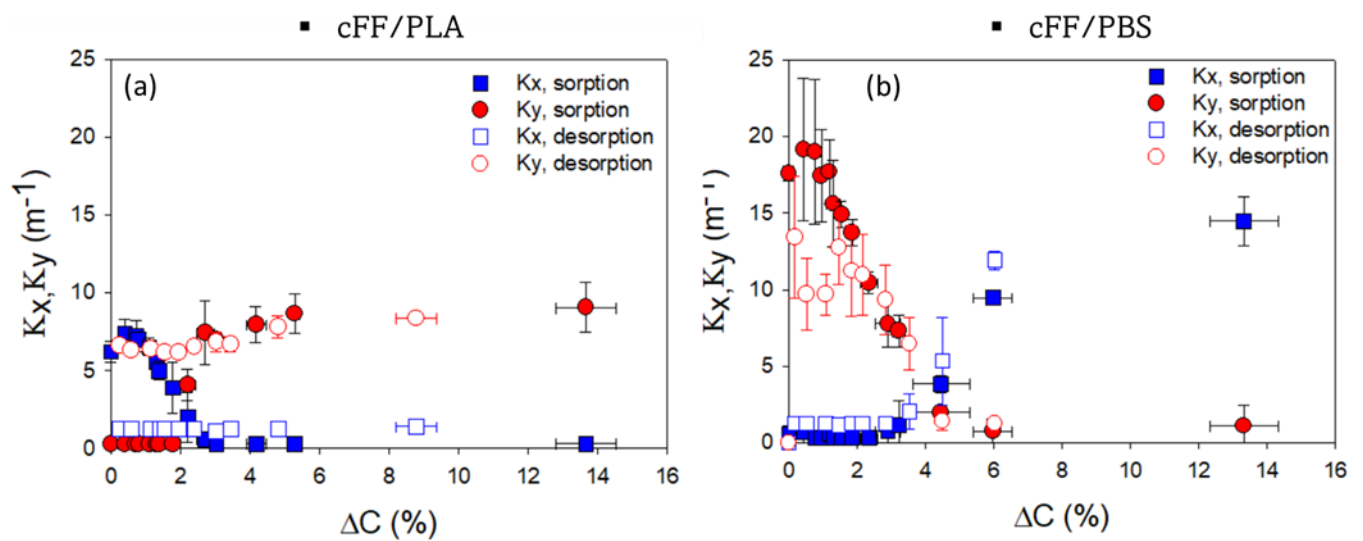


Figure 96: Evolution of longitudinal ( $K_x$ ) and transverse ( $K_y$ ) curvature of 4D-printed (a) cFF/PLA and (b) cFF/PBS biocomposites. ( $R = 2$ ,  $m = 0.7$ ,  $IDp = 0.6\text{mm}$ )

Though having a different stiffness ratio and swelling ratio, the cFF/PLA bilayer evidences a curvature bifurcation at a moisture content of 2.2% compared to 4.0% for cFF/PBS. Indeed, cFF/PBS HBC generates lower hygroscopic internal stresses and slows down the bifurcation mechanism [279]. However, other parameters such as water-sensitivity, plasticization and crystallinity of polymers should also be considered.

Another interesting aspect of optimizing the formulation of 4D-printed HBC relies in the reversibility of actuation. Indeed, both  $K_x$  and  $K_y$  curvatures of cFF/PBS bilayers recover almost entirely their initial values (Figure 96b) unlike cFF/PLA bilayers which do not exhibit reversibility of the bifurcation mechanism (Figure 96a). Embedding flax fibers with soft matrix

such as PBS leads to a reduction of internal stresses and a better process reversibility. This approach strengthens the possibility given by 4D-printed prototypes to mimic shape-changing behavior of pine cone scale. However, it must be mentioned that reversibility of pine cone scale does not only rely on a significant mismatch in hygroscopic and mechanical properties of sclereid and sclerenchyma layers [145] but also on the presence of porous channels called resin ducts. The reduction of internal stresses enabled by this porous area increases the interfacial toughness and thus strengthens the reversibility of the bending actuation in pine cone scales [151] although having no impact on expansion mechanisms [147].

### III. Reshaping 4D-printed HBC with dual actuation

Reproducing the complex dual stage curvature of pine cone scale requires a control of the local hygroscopic anisotropies through the scale to generate both longitudinal and transverse curvatures. The nastic behavior of Bhutan pine scale is marked by a bifurcation phenomenon from dry to humid conditions. The desiccation-stage, i.e. opening stage of the scale, shows a decrease in transverse curvature ( $K_y$ ), flattening the scale in its length. In other words, the longitudinal curvature ( $K_x$ ) of the scale is controlled by the evolution of transverse curvatures through the scale's length.

As explained by Correa et al. [255], primary  $K_y$  is generated by the apical flaps, i.e. edges of the scale. Then,  $K_x$  is strictly initiated at the basal part of the scale. To discretize and mimic this complex dual stage motion, several decisions were taken regarding slicing parameters, i.e. governing architectural features, of the cFF/PLA 4D-printed scales (Figure 97). Three prototypes have been designed to reproduce dual curvature mechanisms. The only impact of the stiffness ratio is investigated in this part. Thickness and aspect ratios are kept constant for both 4D-printed scale prototypes. At first, a gradient of  $ID_p$  along the length (from 0.6 to 6 mm) was tested on **Prototype A**. Then, a gradient of  $ID_p$  combined with an increase of  $ID_a$

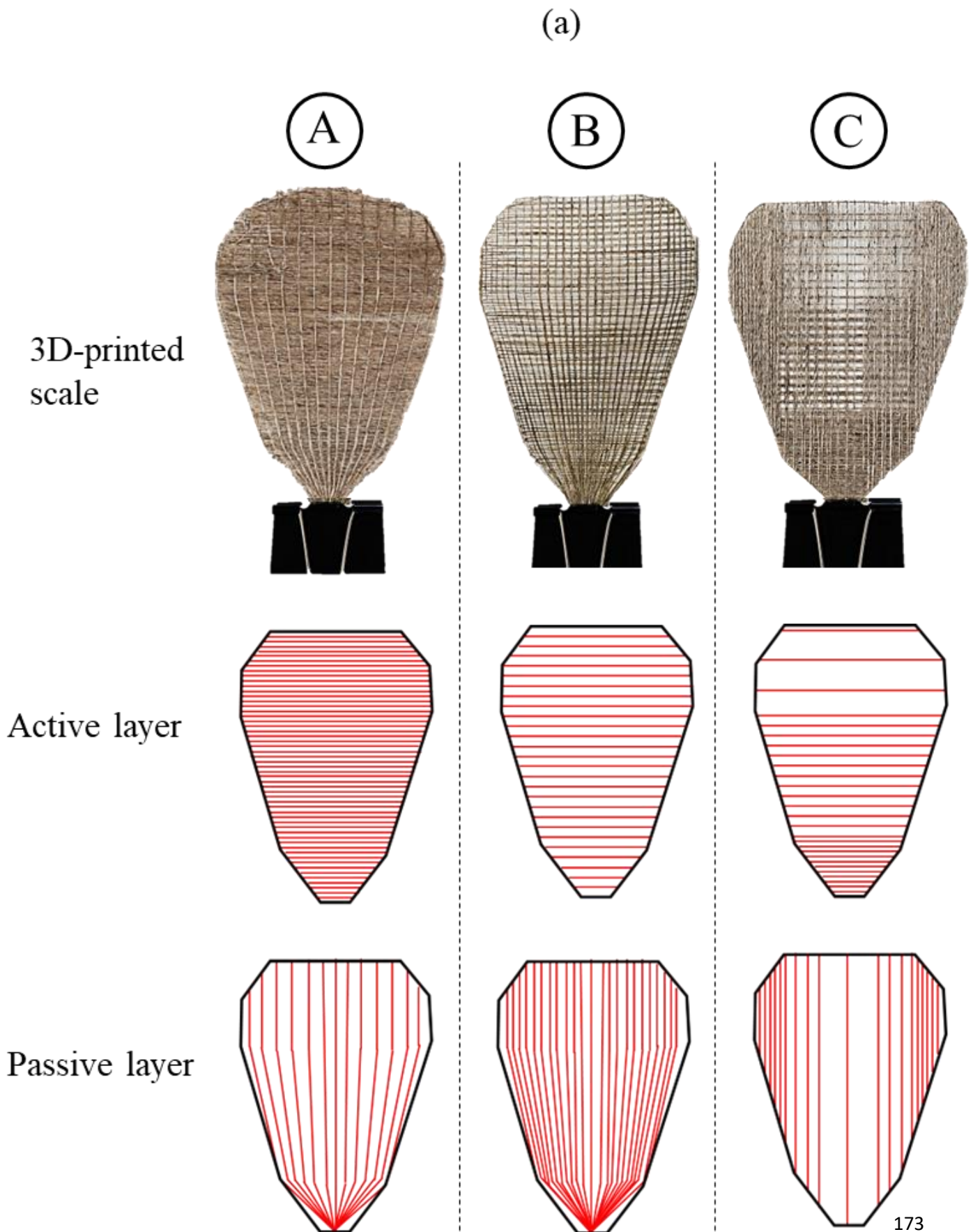
(IDa = 1.5 mm) compared to **Prototype A** (IDa = 0.6mm) was programmed to enhance the transverse curvature and reduce the curvature potential in the longitudinal direction (**Prototype B**). Finally, a gradient of IDp from the sides (IDp = 0.6 mm) to the center (IDp = 3 mm) was investigated to accentuate the transverse curvature. Besides, in order to promote Kx in the basal area, a gradual increase of IDa was set from the rachis (IDa = 0.6 mm) to the apophysis (IDp = 6 mm) (**Prototype C**). These three prototypes are illustrated by Figure 97a.

Figure 97b displays the opening mechanism of each prototype from dry conditions (RH = 0%) to immersion state. **Prototype A** is the most representative of the biological structure of pine cone scale [146]. However, the strong fiber density in its active layers combined with a low distribution on the passive layer (Figure 97a) exacerbates the longitudinal curvature and prevents the apparition of the transverse curvature.

Then, **Prototype B** tends to limit longitudinal curvature by increasing IDa (IDa = 1.5 mm) and decreasing IDp (from 0.6 mm at the basal area to 3 mm at the apical area). However, this printing strategy is not successful either to observe the double curvature mechanism. Although having a lower amplitude compared to **Prototype A**, the longitudinal curvature still dominates the shape-changing mechanism due to the favorable evolution of aspect ratio. The transverse curvature is not apparent at the apex area but can be observed at the base area due to the high density of fibers in the passive layer. However, it does not fit with the transverse curvature of the pine cone scale at its apophysis.

Finally, the double curvature mechanism was reached by **Prototype C**, where a gradient of IDa and IDp through the length and width allowed both longitudinal curvature at the base area and transverse curvatures at the apical parts (Figure 97b). However, the generated double curvature mechanism remains very localized and not distributed within the entire scale. More thoughts

must be given on the role of other slicing parameters such as aspect ratio and thickness ratio to improve this bioinspired motion.



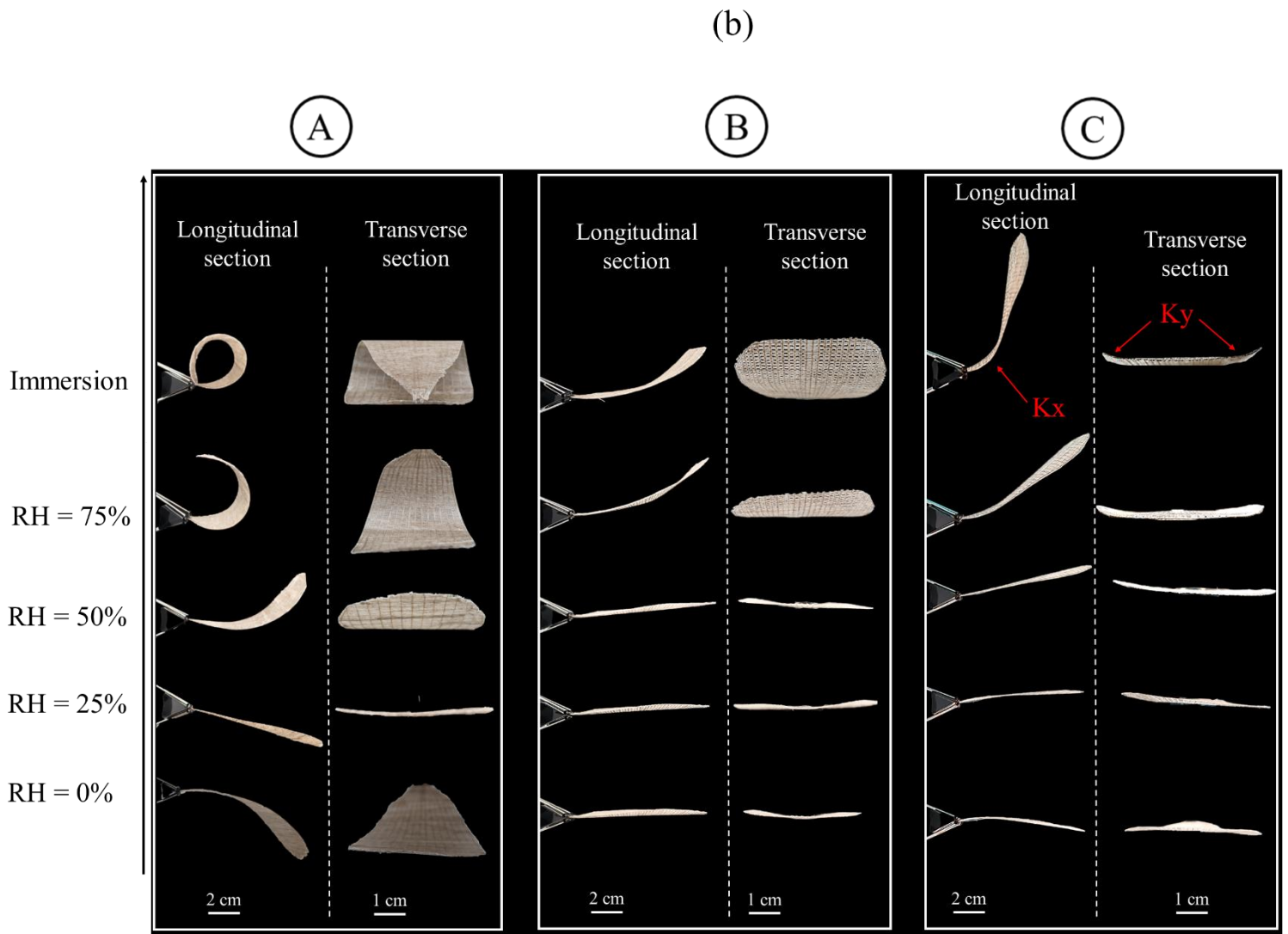


Figure 97: (a) 4D-printed pine cone scale and the filament distribution inside active and passive layers. (b) Actuation mechanisms of the 4D-printed scales from 0%-RH to total immersion.

## IV. Conclusion

Widely observed in nature, the bifurcation behavior ensures precious functions to biological models (e.g. pine cone scale, Venus flytrap). Pine cone exhibits a slow double-curvature mechanism of its scale to promote efficient seed dispersal and full protection against bad weather. This natural phenomenon relies on a specific configuration of the scale using various architectural features (e.g. aspect ratio, thickness ratio, stiffness ratio).

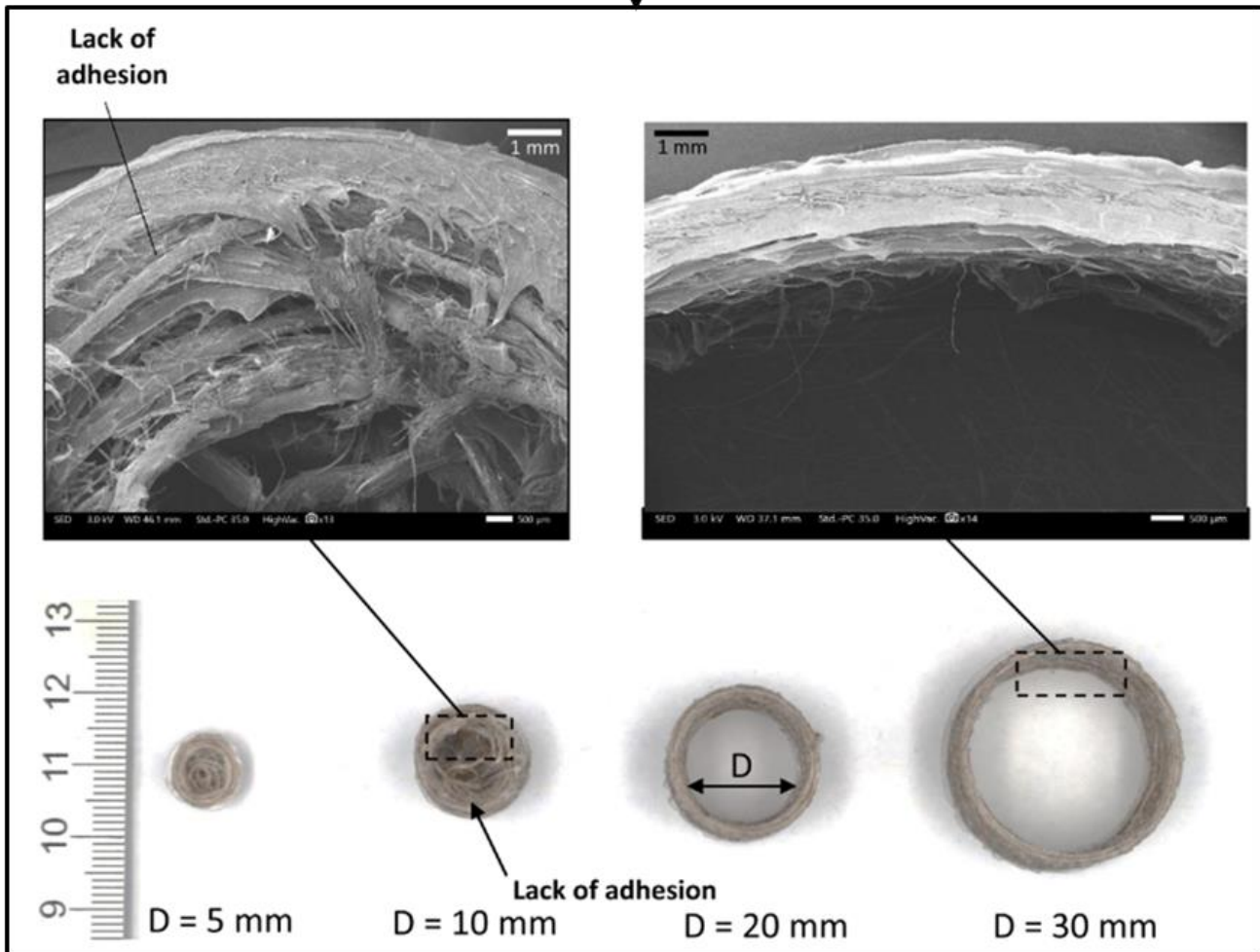
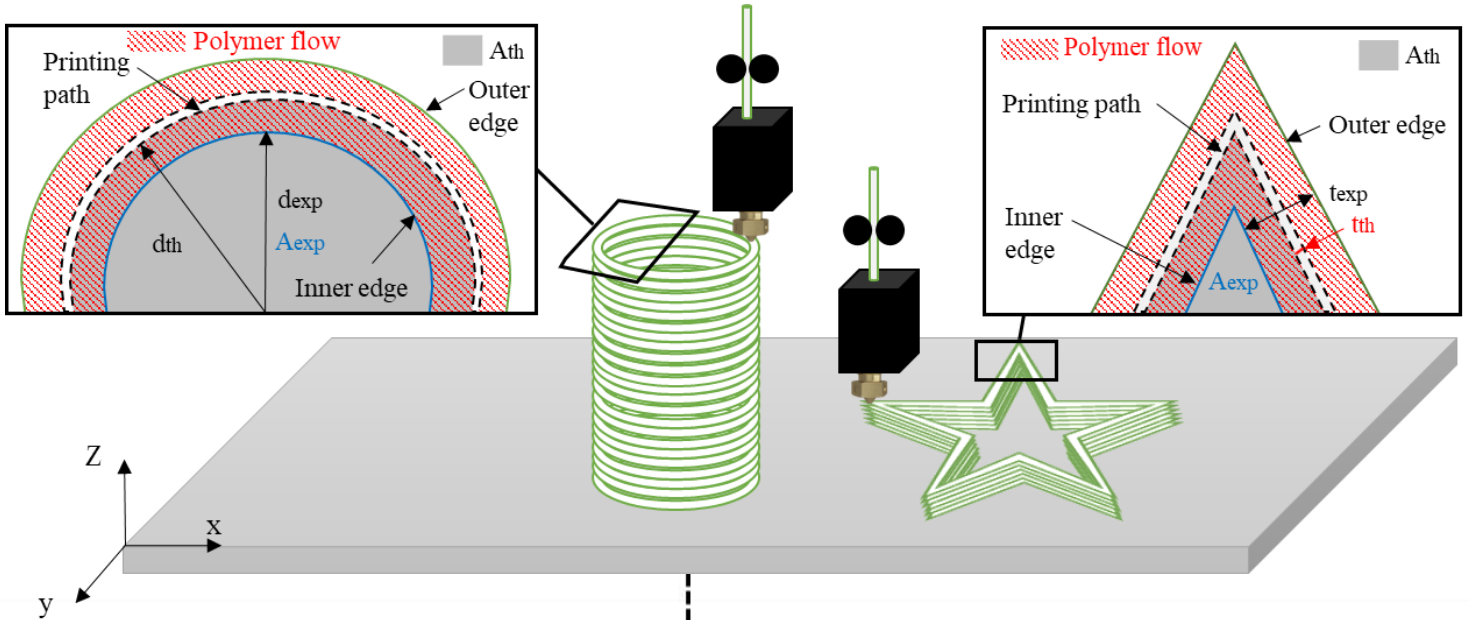
Thanks to 4D-printing, the development of water-induced shape-changing biocomposites, called Hygromorph Biocomposites (HBC), creates new energy-efficiency arising from biomimetic approaches. In Chapter 4, an exploration is realized on the impact of several

architectural features on the bifurcation behavior of 4D-printed continuous flax fiber/PLA biocomposites. Controlling both aspect, thickness and stiffness ratio of 4D-printed biocomposites leads to a control of the double-curvature mechanisms and allow for reaching more complex meteorosensitive architectures for a wider range of applications. By controlling the slicing parameters, a representative 4D-printed scale prototype is proposed. However, further thoughts must be given to widen the range of 4D-printed HBC able to double curve in a controlled time lapse.





# Chapter 5 : Technical limitations of 3D-printing in the deployment of continuous natural-fiber HBC



## I. Introduction

3D-printing of biocomposites is a subset of 3D-printed composites that aims to limit the use of non-renewable resources in order to reduce its ecological footprint [87]. The production of continuous natural fiber reinforced filaments for 3D-printing has significantly improved the mechanical performance of composites compared to those reinforced with short fibers [79]; in addition to expanding the possibilities for shape-changing materials such as Hygromorph BioComposites (HBC) [225].

3D-printing represents a “material by design” approach in the manufacturing process with the highest degree of freedom as it enables the possibility to tailor the mesostructure, i.e the structure at the ply scale. This direct manipulation of the micro and meso-scale architecture of the material composition has been demonstrated to have a direct effect on the corresponding performance characteristics at multiple levels ([280]–[282]). By designing the optimal material organization through the deposition process, the structures are developed with the desired amount of material and the intended direction dependent properties that are needed for the targeted application; following a similar model to that encountered in a biological structures ([120], [154], [283]–[285]).

Although 3D-printing is almost exclusively applied to polymeric materials, there has been an increasing amount of research into expanding the possibilities of cellular parts with short and continuous fibers composites ([76], [286]–[288]). Matsuzaki et al. [288] evidenced the difference between programmed and 3D-printed round-like structures for continuous carbon reinforced PolyAmide (cCF/PA) composites. By modifying the radius of the circles, they observed that the printed radius was always smaller than the programmed radius, which could be due to the twisting motion of the yarns during printing. Their numerical model evidenced that the stiffness of the filament due to the fiber content and the quadratic moment (diameter) were the key factors in producing high fidelity printed cCF/PA composites parts.

**Chapter 5** emphasizes the geometric limitations of 3D-printing continuous flax fiber/PLA biocomposites (cFF/PLA) as it represents a crucial point to widen the field of printability of sustainable structures and their range of applications in the future. Geometric limitations incorporate both limit printed angle and limit printed diameter of out-of-plane tubular and pentagonal architectures. By assessing the difference between programmed and real trajectories, it aims to boost the deployment of continuous flax fiber reinforced biocomposites (cFF/PLA) with complex 3D-printed structures. A comparison with pure polylactic acid (PLA) and short flax fiber polylactic acid (sFF/PLA) 3D-printed parts is presented. Finally, a discussion on future parameters to improve printing fidelity is initiated.

## II. Results

The results shown in Figure 98 illustrate the noticeable difference between the programmed and experimental shapes made with cFF/PLA, pure PLA and sFF/PLA. The influence of the set diameter to build tubular pieces is a particular concern. With a diameter between 20 to 30 mm, the printing fidelity for cFF/PLA is at its maximum, between 70 and 80% of the programmed area (Figure 99a). However, these values are lower than those obtained with pure PLA and sFF/PLA biocomposites, for which a fidelity of over 90% has been calculated. Furthermore, whatever the printed filament, none of the final structures reach a 100% fidelity because of polymer flow occurring along the process (Figure 98). Reducing the print diameter of the cellular pattern generates some issues (low bed adhesion, distortion angle) for cFF/PLA, to ensure proper filament deposition. The design of a cellular material (e.g. for the sandwich core) with cFF/PLA biocomposite may be limited to an internal diameter of 15 mm whereas the geometric limitations (i.e. minimum printable diameter) is lower for pure PLA and sFF/PLA (about 5 mm with a similar fidelity range) for the set slicing and printing parameters. Similar tests were done with cCF/PA which exhibited a minimum achievable diameter of 8 mm by optimizing the filament size [288].

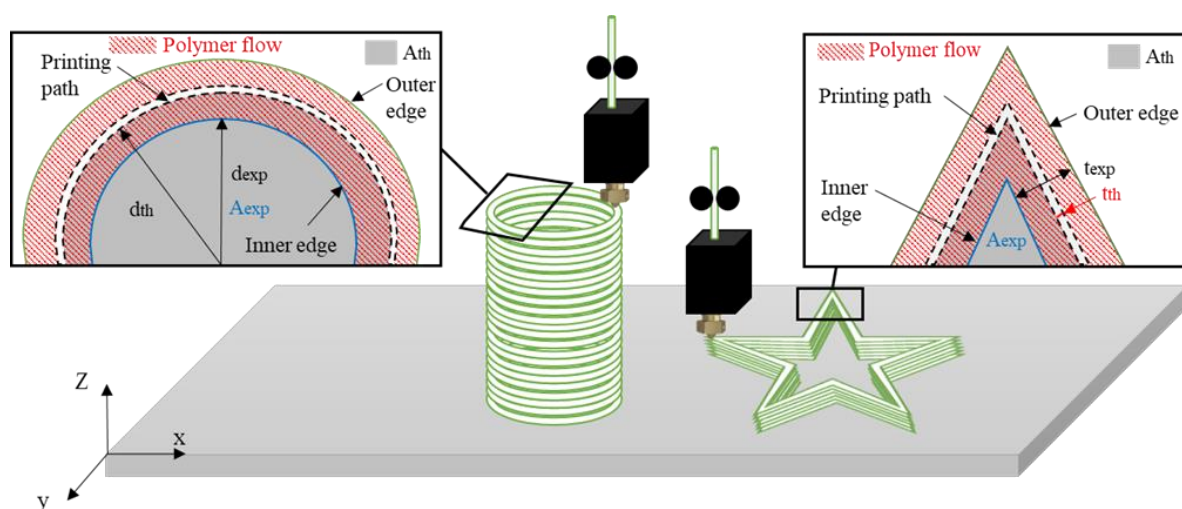
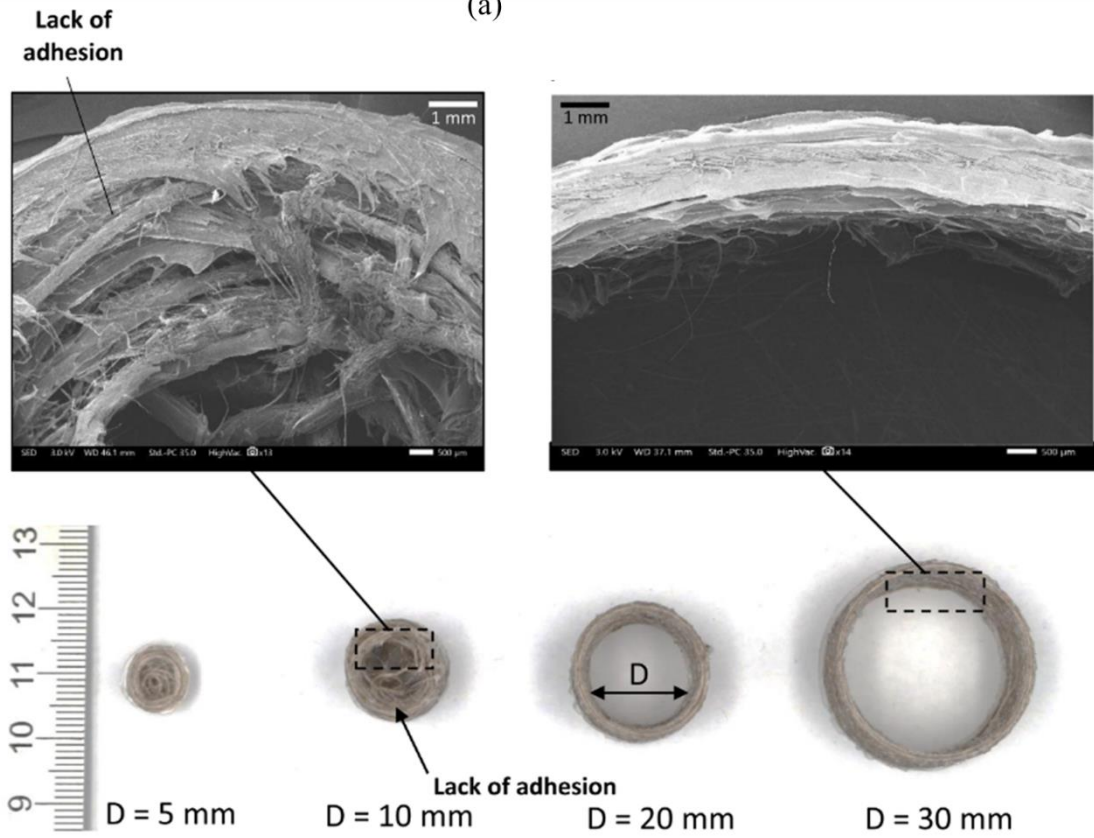
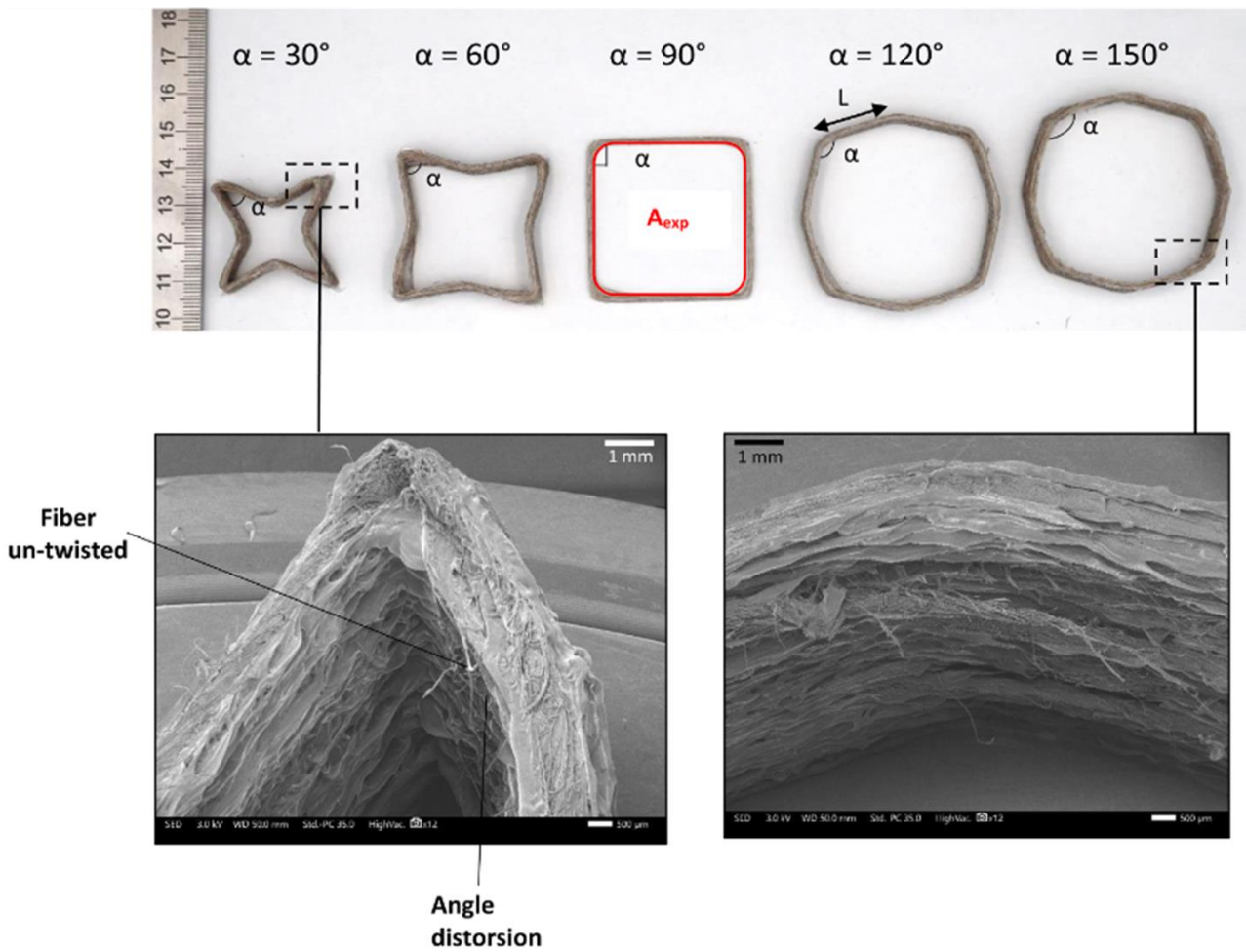


Figure 98: Parameters considered to quantify set and measured printed area for both circular and polygonal sections. The red hatched area represents the polymer flow along printing while the dark area defines the theoretical area depending on the printed pattern. The dotted and blue lines delimit the printing path followed by the nozzle and the experimental area depending on the printed pattern.

(a)



(b)



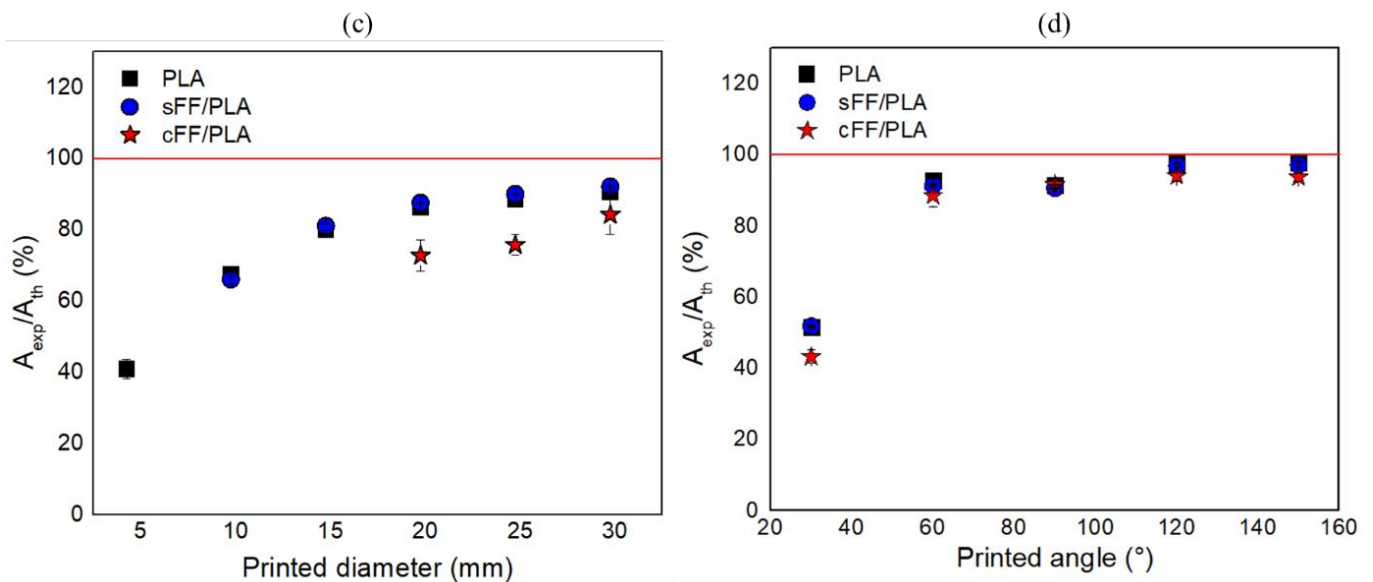


Figure 99: (a) Circular shape and (b) star/octagonal shape of continuous flax fiber/PLA biocomposites. Comparison between theoretical and experimental area as a function of the set (c) diameter and (d) angle of PLA polymer, short flax fiber/PLA and continuous flax fiber/PLA lattice-structured biocomposites.

When the programmed diameter is less than 15 mm, the area could not be experimentally quantified correctly. The images indicate that the position of the deposited filament has significantly deviated from the initial circular position, instructed by the print path, towards the central area of the shape. This deviation is likely the result of the short time dedicated to solidifying the matrix on the previous layer, which is further exacerbated by an increase in tangential stresses with respect to the bonded area. This tangential stress results from the direction of movement of the nozzle in relation to the print path. Another reason for this deviation on the material deposition may be the result of a mismatch between the filament diameter ( $d = 0.4 - 0.6$  mm) and the nozzle diameter (0.9 mm). The dimensional discrepancy between the nozzle and the filament has been technically needed in order to reduce filament damage during printing. A smaller nozzle has already been tested, but it tends to cause either clogging or filament breakage due to the increased shear stress.

A similar strategy is already used in a commercial printer with continuous carbon fiber composites [250] where the nozzle diameter is 1 mm with a filament diameter of about 0.35 mm. This difference increases the degree of freedom of the filament during deposition, which affects the control of the final cylinder shape.

In considering the influence of the programmed angle, it is essential to note that the length between the angles ( $L$ ) was kept constant for this test to ensure a similar “length of adhesion” before applying the change in nozzle direction. Figure 99d shows that the relatively high printing fidelity (around 90%) of cFF/PLA is observed at around  $60^\circ$ , which is very similar to pure PLA and sFF/PLA biocomposites. It is also important to notice that there is a large difference in material stiffness ( $E_{11_{\text{PLA}}} = 3.1 \pm 0.3 \text{ GPa}$ ,  $E_{11_{\text{cFF/PLA}}} = 15.8 \pm 2.1 \text{ GPa}$ ) ([225], [279]) but a similar range of printed filaments and quadratic moments that influence geometric bending stiffness.

Below  $\alpha = 60^\circ$ , a large discrepancy between the programmed and experimental data is observed due to the lack of adhesion with the printing bed or between the layers. Lower angles induce more radical changes in the direction and position in which the filament is deposited, which can generate greater in-plane tangential stress. Indeed, depending on their relative position within the bundle, the elementary flax fibers can be subjected to damage by buckling due to compressive stress. Flax fiber and all natural fibers are known to be prone to buckling failure due to their internal microstructure [289]. Similar observations have been made on cCF/PA parts ([250], [290]).

### III. Conclusion

In line with the ongoing development of 3D-printed biocomposites reinforced with continuous natural fibers, a first insight into the design space of cellular pattern has been proposed. Although custom designs are easily programmable, certain limiting parameters, such as cylinder diameter and printed angle, restrict full control of the printing process. It is interesting to note that patterns with non-acute angles can be achieved in a similar way between cFF/PLA, pure PLA and sFF/PLA and should therefore be preferred to circular pattern design.



The observed variations between the programmed and experimental observations are assumed to be mainly due to:

- Relatively high in-plane stiffness of cFF/PLA due to biocomposite composition (fiber type and content)
- Twisted structure of flax yarns that may imply damage and reduce the strain accommodation of single fibers within the filament flexibility during printing.
- The uneven stress loading of the elementary fibers within the yarn that promotes the buckling of the fibers at acute angle.
- Limitations of interlayer bonding that result from the above-mentioned fibers characteristics but also due to the dimensional tolerances needed in the nozzle selection where the nozzle size is much larger than the fibers.

It is important to keep in mind that these results were obtained for specific printing and slicing parameters of which an adjustment might modify the printing quality. Further developments should be done to promote greater fidelity of cFF/PLA biocomposites but limiting the reduction in intrinsic material stiffness that is required for semi-structural application. Thus, the production of smaller diameter ( $< 0.5$  mm) cFF/PLA filaments may be relevant, especially if rovings are used instead of twisted yarns. Roving will help the single fiber to conform during printing. In combination, the nozzle diameter should be as close as possible to the filament diameter. The temperature-printing speed coupling could also be adjusted as it governs viscoelastic properties of the matrix and adhesion process in order to optimize matrix deposition and reduce structural flaws. Finally, geometric limitations can also be overcome by incorporating an offset factor during programming/design that can account for such deviations. This offset could be similar to factors used to accommodate for polymer shrinkage that results in warpage issues for certain materials. Thus, taking the fidelity ratio into account during

programming can expand the design space for cFF/PLA 3D-printed biocomposites with cellular patterns.

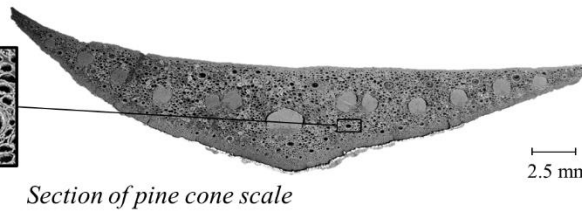
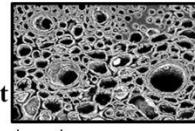


# Chapter 6 : How bioinspired designs speed up the actuation of HBC ?

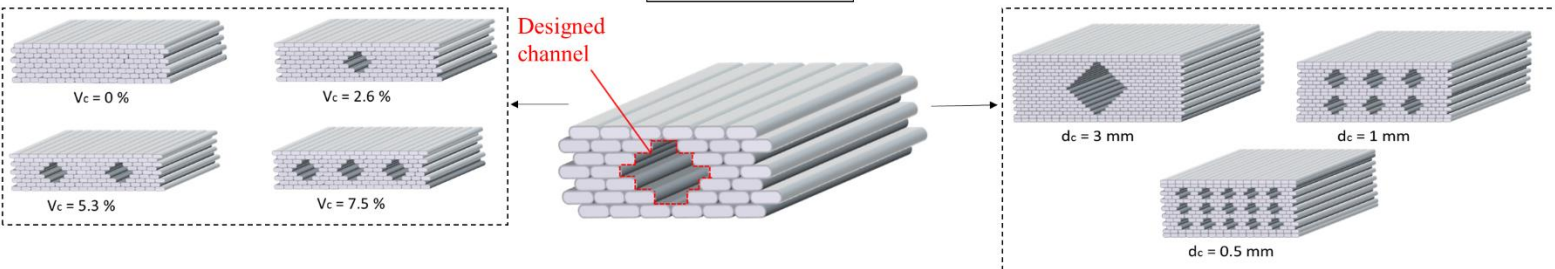
## Biological Inspiration

Sclerenchyma strands

Promote water transport and morphing

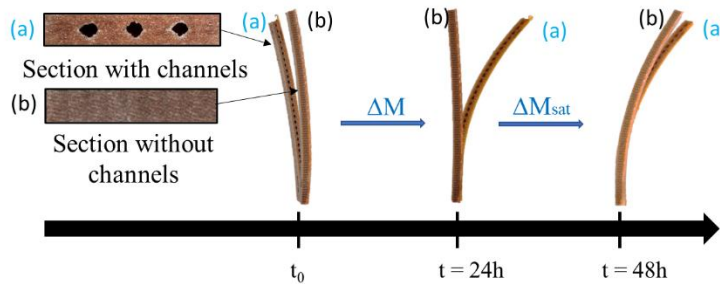


## 3D-Printing

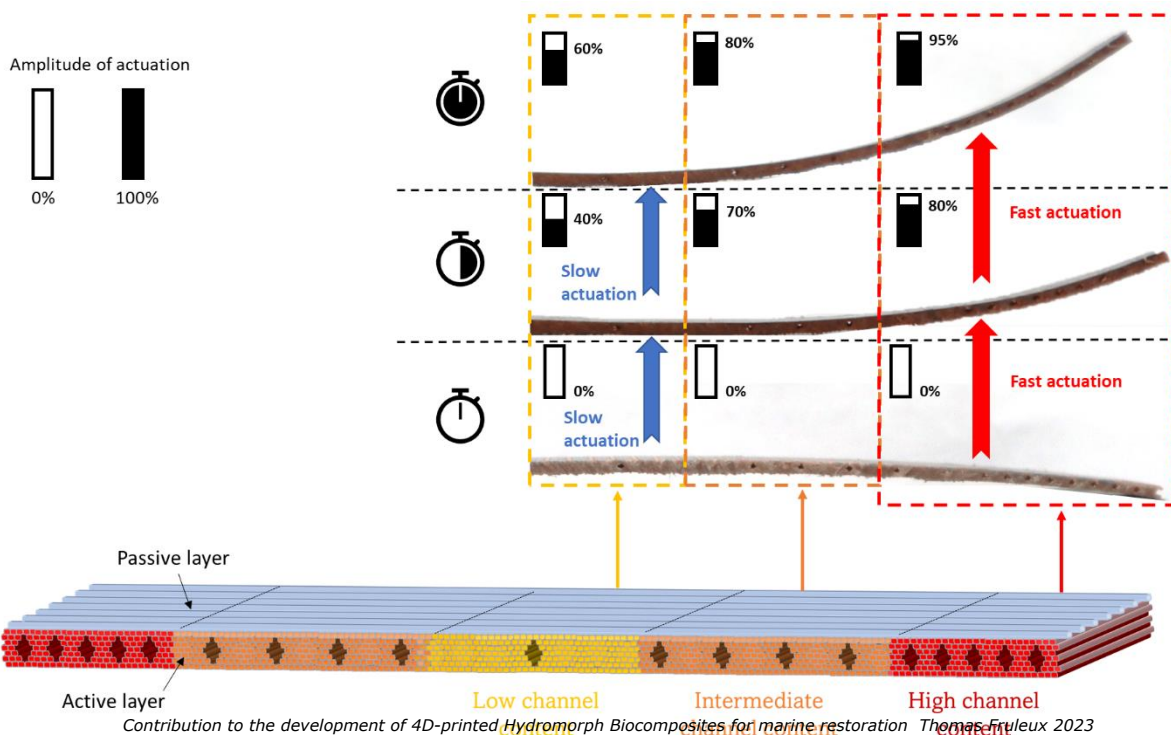


## 4D-Printing

➤ Channels promote reactivity of Hydromorph BioComposites



➤ New opportunity for deploying smart actuators with sequential responses



## I. Introduction

Sorption mechanism of biocomposites follows two strategies [59]. Chemically, hydrophilic biopolymers (hemicellulose, pectin) present in the middle lamellae and surrounding the fiber cell-walls interact with water molecules by forming hydrogen bonds ([291], [292]). Physically, free water might also remain within cavities (lumen, porosities) by capillary forces [35]. Since natural fibers are surrounded by a hydrophobic matrix, the water uptake process is slowed down ([56], [225], [279]). Thus, their reactivity, i.e. kinetic of actuation, is relatively slow and is currently limited by the moisture transport within the natural fiber-reinforced composites.

Water transport can be affected by the porosity content and distribution within the material [149]. In the engineering field of 3D-printed polymeric composite materials, porosities are currently assumed to be inherent defects because of their detrimental effect on the mechanical properties [293]. These porosities occurred either in the interfilament or in the interlaminar area and are implied by a lack of pressure during processing ([75], [294]). However, the presence of voids is not always categorized as a flaw. For example, the porous structure of plants promotes and controls the supply of nutrients and water transport through plant tissues. This step is essential to plant metabolism and survival ([123]).

**Chapter 6** proposes a new concept of 4D-printed HBCs where the water transport and actuation are controlled by tailored channel architectures. In this chapter, channels are defined as intentionally designed cavities predetermined by the toolpath design. These designs involve intentional changes in the spacing between print path lines across the co-planar raster pattern of a layer or through the combined effect of such intentional print path spacing across multiple vertical layers. Thus, the printed mesostructured will be inspired by those biological mesostructured where porosities or voids provide essential functions (lightness, inertia, moisture transport and actuation). First, an investigation of solely the active layer of the subsequent 4D-printed wood fiber-reinforced biocomposites printed HBC bilayers is done. No

bending actuation is expected, and the purpose is to bring deeper insights on the relationship between channel content (from 0% to 10%), size (from 0.5 to 3 mm), distribution patterns across the samples and moisture ingress, hygroscopic expansion, and finally hydromechanical properties. Then, these functional channels will be implemented in the mesostructure of 4D-printed HBC bilayers and morphing potential will be analyzed in terms of reactivity and responsiveness. Finally, the design of an HBC with sequential response capability, thanks to localized channels, is tackled and similarities with scale functionality are disclosed.

## II. Results

### II.1. Concept

Most plants require a continuous supply of water and dissolved substances to survive. The importance of conducting elements in supplying water of various natural systems was pointed out, as in the case of the channel-like structure of the tracheids in plant stems ([295]–[297]). The variation of tracheid sections within the wood mesostructure was also discussed by Krabbenhoft et al. [297], showing that it affects the fluid ascent. In the pine cone scale (Figure 100), the size of channels or vascular bundles is distributed heterogeneously between the different tissues. The sclerenchyma layer acts as a mechanical reinforcement and displays vascular bundles with narrow channel and a high filling factor. Besides, the sclereid layer has a denser architecture and consists of individual cells, which form a cell size gradient between the region close to sclerenchyma tissue and the dorsal side of the scale [151]. This structural gradient within the pine cone scale has been proposed recently to prevent critical stress concentration between the different layers so that reversibility of the passive-hydraulic actuation mechanism is guaranteed.

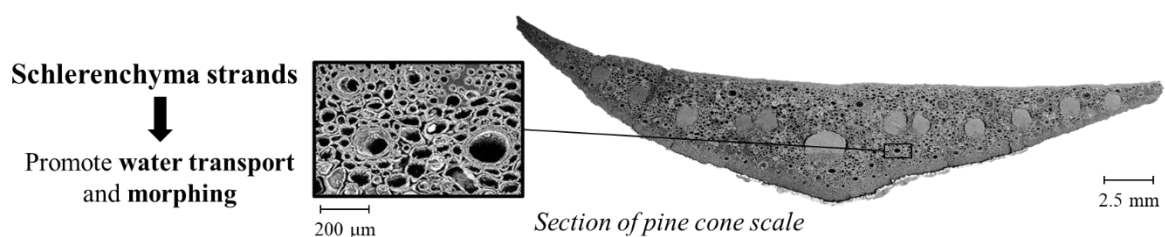


Figure 100: Transverse section of a pine cone scale exhibiting a void-induced mesostructured.

We hypothesize that it is possible to create programmed printing paths to generate 3D-active layers of different typologies, composed of short natural fiber biocomposites with variable channel content and distribution, inspired by pine cone scale mesostructure. A dedicated design of the active layer is then transferred in two steps towards 4D-printing of HBCs to enhance their morphing properties. First, simple HBCs with active layers upgraded in terms of size,

content and channel distribution will be produced. Then, the meso-scale architecture of the active layer will be functionally designed with a distribution of channel size and content across the section in order to provide a tailored spatio-temporal actuation.

## II.2. Investigation of the active layer scale

### II.2.a. Mesostructure qualification

Here again, we consider the channels to be intentional architectural features designed to improve the functional characteristics of the system. This is different from unwanted microscopic porosities, which are common defects induced by the printing process (Figure 101). Channel content in the active layer was set from 0% to 7.5% (Figure 102a) based on the geometric assumptions of material comparison and their printability. Although 3D-printed biocomposites are far from being model materials, the porosity content (calculated by image analysis) is very low (Table 13). Values above 7.5% were considered outside the scope of this study for a number of reasons, including 1) maintaining effective mechanical resistance, and 2) facilitating trajectory programming.

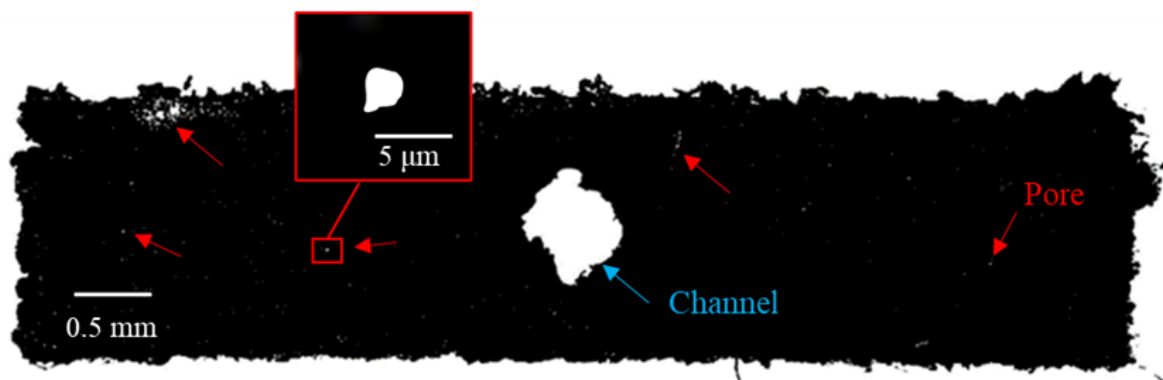


Figure 101: Macro- and microporosities inside the active layer of 4D-printed HBC illustrating a channel cross-section (blue arrow) and pores (red arrows).

Illustrated in Figure 102b, channel diameter ( $d_c$ ) ranges from 0.5 mm to 3 mm, which was achieved by tailoring the slicing parameters (Layer Height, Interfilament Distance and Filling Ratio). Finer diameters were too complex to print because of the size of the nozzle (0.4 mm), but also due to the rheological behavior of the biocomposite filament. In addition, we decided to target three diameter values that have significant impact on the wicking mechanism



according to Jurin law [298]. The results for channel ( $V_c$ ), porosity content ( $V_p$ ) and channel diameter ( $d_c$ ) are presented in Table 13 and Figure 103.

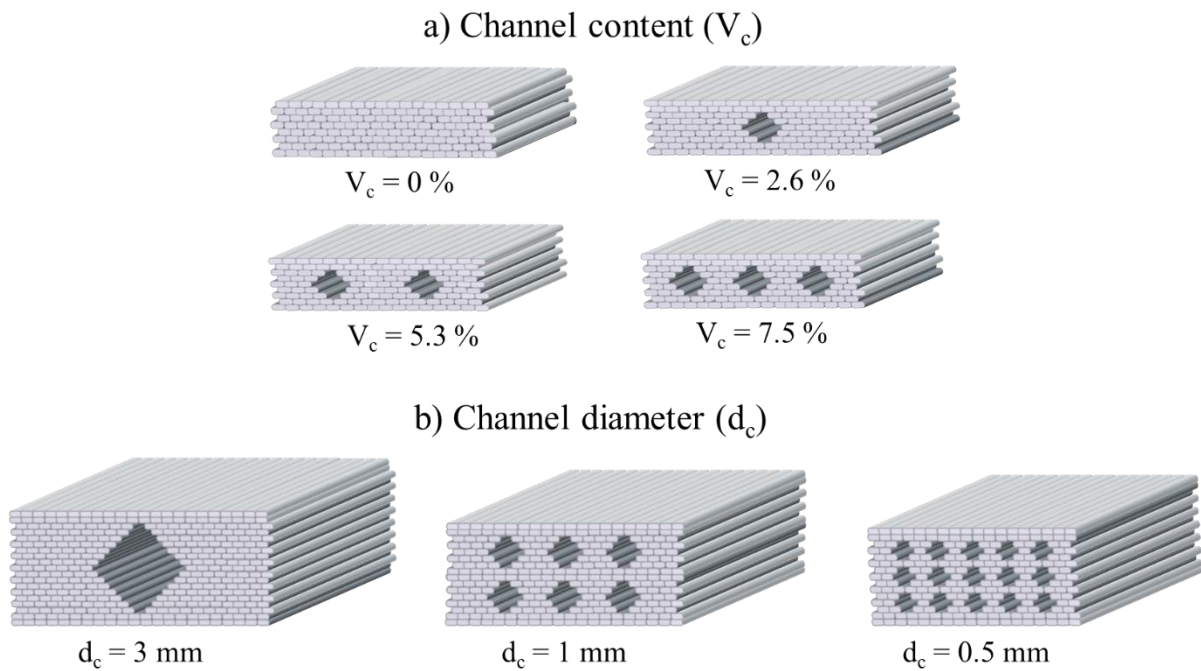


Figure 102: Set printing patterns of 3D-printed biocomposites cross section displaying various (a) channel content ( $V_c$ ) and (b) diameter ( $d_c$ ).

Channel distribution is controlled by keeping a similar channel volume content while varying the size of the channels. It is worth noting that the distance between the edges of the channel and the edges of the workpiece remains constant between samples ( $d = 0.6$  mm) to prevent any disturbance for the analysis of the sorption behavior.

Table 13: Mesostructural parameters (channel content  $V_c$ , porosity content  $V_p$  and channel diameter  $d_c$ ) of 3D-printed biocomposite active layer including channels. These results are presented as mean  $\pm$  standard deviation for 5 replicates ( $n = 5$ ).

Variable parameters	$V_c$ 0%	$V_c$ 2.6%	$V_c$ 5.3%	$V_c$ 7.5%	$d_c$ 3mm	$d_c$ 1mm	$d_c$ 0.5mm
$V_c$ (%)	0	$2.6 \pm 0.3$	$5.3 \pm 0.1$	$7.5 \pm 0.2$	$9.5 \pm 0.5$	$9.9 \pm 0.3$	$9.7 \pm 0.6$
$V_p$ (%)	$0.5 \pm 0.1$	$0.5 \pm 0.1$	$0.5 \pm 0.1$	$0.5 \pm 0.1$	$0.4 \pm 0.1$	$0.4 \pm 0.1$	$0.4 \pm 0.1$
$d_c$ (mm)	-	$1.0 \pm 0.1$	$1.0 \pm 0.1$	$1.0 \pm 0.1$	$3.0 \pm 0.2$	$1.0 \pm 0.1$	$0.5 \pm 0.1$

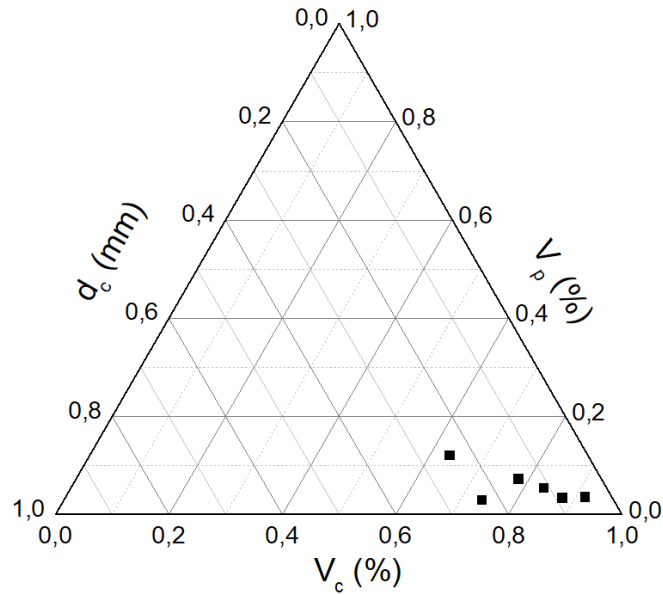


Figure 103: Triangle diagram of the mesostructural parameters (channel content  $V_c$ , porosity content  $V_p$  and channel diameter  $d_c$ ) of 3D-printed biocomposite active layer including channels. These results are presented as mean  $\pm$  standard deviation for 5 replicates ( $n = 5$ ).

### II.2.b. Water sorption and transport during immersion

3D-printed biocomposites (the active layer of HBCs) with variable mesostructures were immersed in water. Figure 104 exhibits their water sorption behavior when varying their channel content (from 0% to 7.5%) and channel distribution (with diameter from 0.5 to 3 mm). The presence of channels (having similar diameter) inside biocomposites yields to a rise in equilibrium water content (+ 34% in mass) between  $V_c = 0\%$  and  $V_c = 7.5\%$  (Figure 104a), as channels act as free tanks for water molecules.

Porosities generated by the manufacturing process as well as wood internal voids (lumen) may also contribute to water uptake but their amount (not measured here) is negligible compared to the amounts contributed by the channels (Figure 101).

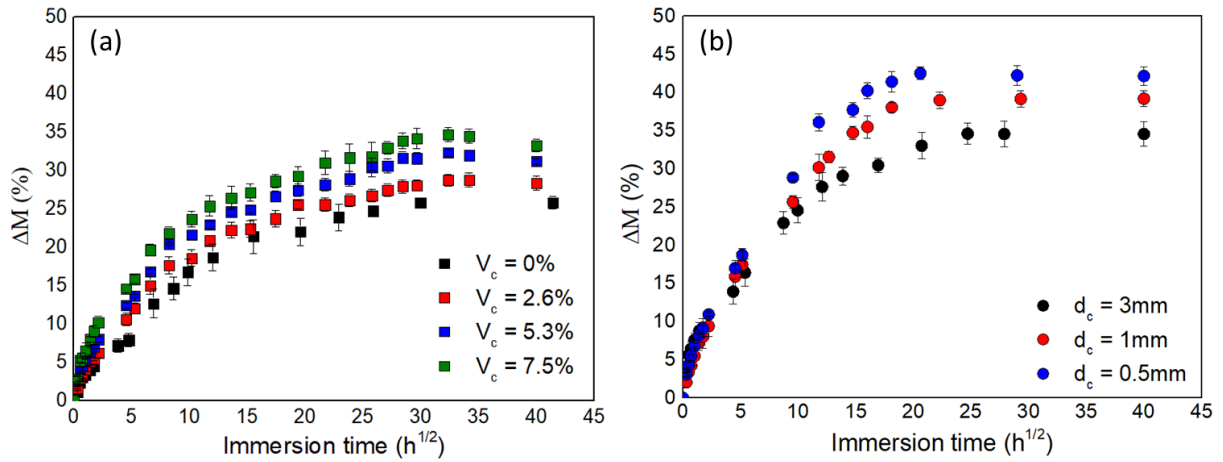


Figure 104: Sorption behavior of 3DP biocomposite samples including channel features as a function of immersion time when varying a) porosity content and b) porosity distribution. Mean  $\pm$  SD, n = 5.

Table 14 demonstrates that increasing channels contents from 0% to 7.5% doubles the kinetic of sorption evaluated as the slope of the curve  $\Delta M = f(\text{immersion time})$ , i.e. from  $4.9$  to  $10.4 \cdot 10^{-6} \text{ s}^{-1}$ . This indicates that increasing the channel content of the active layer leads to an increase in the exchange surface, which in turn triggers the transport of water by a capillary mechanism. These values should be taken with caution as it is well established that when the trapped water mechanism occurs, Fick's assumptions are misleading. Accordingly, specific modelling like Langmuir may be more suitable to predict the evolution of moisture content. Changing the channel distributions and channel sizes (Figure 102) while keeping similar channel volume contents hardly affects the kinetic of sorption. This confirms the prevailing role of the channel content on the kinetic of moisture transport.

Table 14: Sorption parameters of 3DP biocomposites with variable channel content and channel diameter. Mean  $\pm$  SD, n = 5.

	$V_c$ (%)				$d_c$ (mm)		
	0	2.6	5.3	7.5	0.5	1	3
$\Delta M$ (%)	$25.8 \pm 0.8$	$28.4 \pm 0.9$	$31.2 \pm 0.3$	$33.2 \pm 0.8$	$42.2 \pm 1.3$	$39.1 \pm 1.1$	$34.6 \pm 1.6$
$dM/dt$ ( $10^{-6} \text{ s}^{-1}$ )	$4.9 \pm 0.7$	$6.4 \pm 1.3$	$8.3 \pm 1.8$	$10.4 \pm 2.1$	$10.6 \pm 2.0$	$9.1 \pm 1.5$	$11.2 \pm 2.5$
$D$ ( $10^{-8} \text{ m}^2 \cdot \text{s}^{-1}$ )	$2.2 \pm 0.4$	$2.7 \pm 0.1$	$2.5 \pm 0.1$	$3.0 \pm 0.1$	$3.3 \pm 0.1$	$3.1 \pm 0.1$	$2.3 \pm 0.1$

### II.2.c. Hydroscopic expansion

Figure 105a and b represents the hydroscopic expansion of biocomposites, i.e. transverse ( $\epsilon_{\text{hyd},y}$ ), and out-of-plane ( $\epsilon_{\text{hyd},z}$ ) directions, as a function of immersion time for the two investigated cases (channel content and distribution). The investigation of  $\epsilon_{\text{hyd},y}$  is of high importance for the design of HBCs as it will contribute to the mismatch of hygroscopic expansion between active and passive layers. Basically, the expansion in  $x$ -direction which represents the passive layer of HBCs made with 100% biocomposite can be negligible due to anisotropic properties of natural fibers. However, depending on natural fiber type and microstructure (microfibrillar angle, for instance), the swelling anisotropy of biocomposites may be reduced which also reduces the swelling mismatch and thus the actuation potential. Here, in the case of imperfect alignment of the short wood fibers with the direction of extrusion, longitudinal swelling between 1.0 % and 1.3% is observed. Thus, the strategy that will be used in the proof of concept should adopt a passive layer with a lower hygroexpansion. Resulting amplitude and kinetic of hydroexpansion are displayed in Table 15.

The channel content slightly affects  $\epsilon_{\text{hyd},y}$ , + 0.6% from  $V_c = 0\%$  to  $V_c = 7.5\%$ , and  $\epsilon_{\text{hyd},z}$  of the active layer, equal to 4.0% for both  $V_c = 0\%$  and  $V_c = 7.5\%$ . This result shows that intentional mesostructures (channels) make it possible to combine moisture uptake without degrading the expansion potential. However, when randomly distributed, porosities induce a reduction of hydroexpansion [299]. A first proof of concept of a similar approach to designing channels in 4D-printed bilayer structures can be found in previous work by Correa [300], although no material characterization or detailed kinematic analysis was carried out as part of his study.

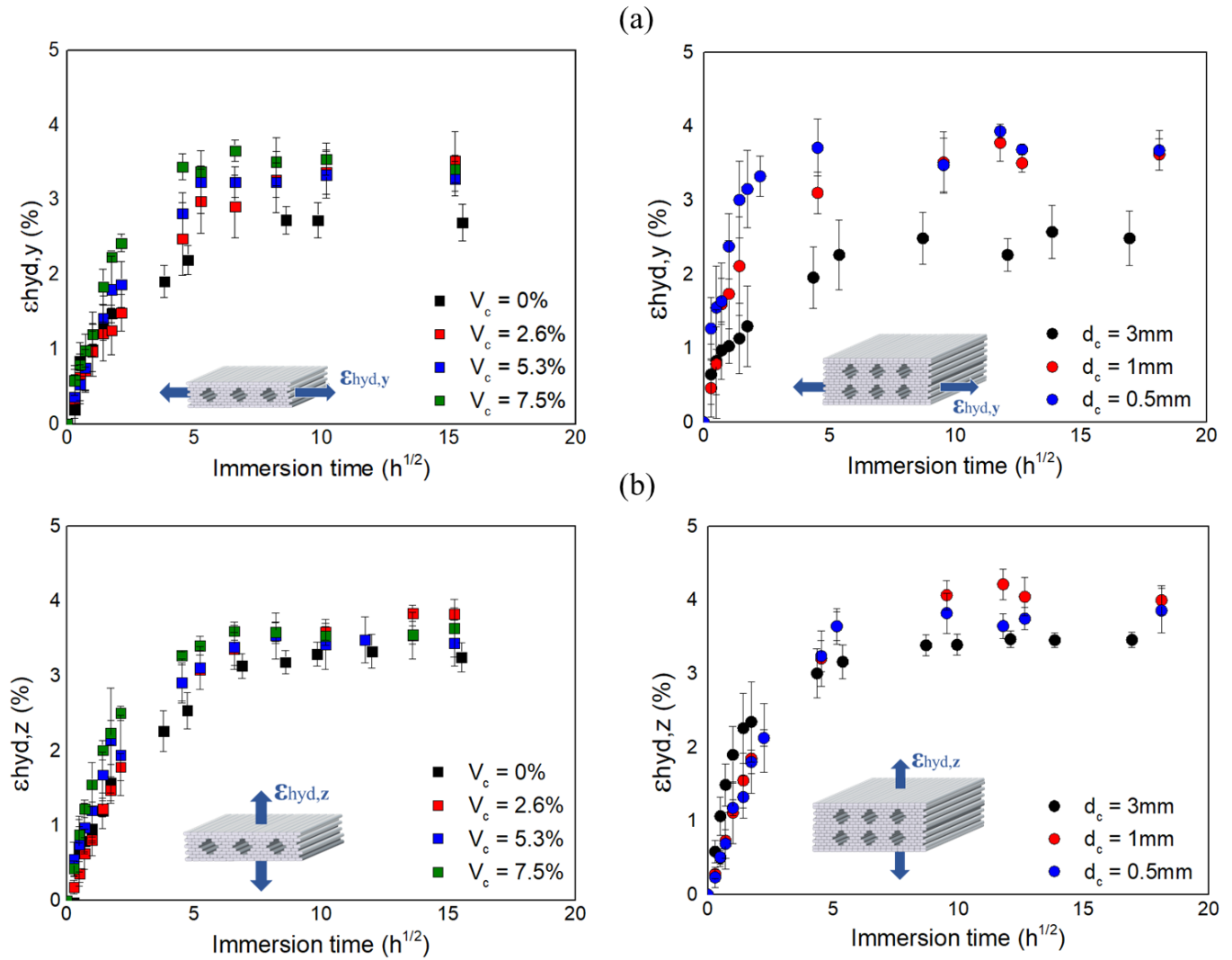


Figure 105: Hydroexpansion of 3D-printed biocomposites including channel features as a function of immersion time in a) transverse and b) out-of-plane directions by varying channel content and distribution. Mean  $\pm$  SD,  $n = 5$ .

The kinetic of expansion (quantified by the initial slope of  $\epsilon_{\text{hyd}} = f(\text{immersion time})$ ) is a first order parameter for HBC design as it represents the motor of actuation. The kinetic of expansion increases by 70% between 3D-printed biocomposites without channels ( $V_c = 0\%$ ) and those containing channels ( $V_c = 7.5\%$ ), both in transversal and out-of-plane directions. Indeed, by accelerating the diffusion of water through the structure, the presence of channels will trigger a quicker expansion of the wood fibers. When no channels are printed, the water only has access to the outer surfaces of the samples (through the edges), making the expansion process longer to reach its equilibrium shape.

Table 15: Maximal hydroexpansion and kinetic of expansion of 3DP biocomposites inducing channel features with (left) various channel content from 0 to 7.5% and (right) various channel distribution, i.e. diameter from 0.5 to 3mm. Mean  $\pm$  SD, n = 5.

	<b>V<sub>c</sub> (mm)</b>				<b>d<sub>c</sub> (mm)</b>		
	<b>0</b>	<b>2.6</b>	<b>5.3</b>	<b>7.5</b>	<b>0.5</b>	<b>1</b>	<b>3</b>
$\epsilon_{hyd,x}$	1.1 $\pm$ 0.2	1.0 $\pm$ 0.2	1.0 $\pm$ 0.0	1.2 $\pm$ 0.1	1.3 $\pm$ 0.1	1.2 $\pm$ 0.2	1.2 $\pm$ 0.2
$d_{\epsilon_{hyd,x}}/dt$ (10 <sup>-6</sup> .s <sup>-1</sup> )	0.3 $\pm$ 0.1	0.1 $\pm$ 0.1	0.2 $\pm$ 0.1	0.5 $\pm$ 0.1	0.7 $\pm$ 0.1	0.5 $\pm$ 0.1	0.5 $\pm$ 0.1
$\beta_{hyd,x}$	0.06 $\pm$ 0.01	0.02 $\pm$ 0.01	0.04 $\pm$ 0.01	0.05 $\pm$ 0.01	0.18 $\pm$ 0.01	0.03 $\pm$ 0.01	0.05 $\pm$ 0.01
$\epsilon_{hyd,y}$	3.1 $\pm$ 0.3	3.4 $\pm$ 0.3	3.3 $\pm$ 0.3	3.7 $\pm$ 0.1	3.9 $\pm$ 0.1	3.8 $\pm$ 0.2	2.6 $\pm$ 0.4
$d_{\epsilon_{hyd,y}}/dt$ (10 <sup>-6</sup> .s <sup>-1</sup> )	1.4 $\pm$ 0.2	1.7 $\pm$ 0.3	1.9 $\pm$ 0.2	2.4 $\pm$ 0.2	5.1 $\pm$ 1.0	3.7 $\pm$ 0.7	1.5 $\pm$ 0.4
$\beta_{hyd,y}$	0.22 $\pm$ 0.02	0.23 $\pm$ 0.01	0.23 $\pm$ 0.01	0.22 $\pm$ 0.01	0.34 $\pm$ 0.01	0.30 $\pm$ 0.02	0.14 $\pm$ 0.01
$\epsilon_{hyd,z}$	4.0 $\pm$ 0.1	4.3 $\pm$ 0.1	3.9 $\pm$ 0.3	4.0 $\pm$ 0.2	3.8 $\pm$ 0.6	4.2 $\pm$ 0.2	3.5 $\pm$ 0.1
$d_{\epsilon_{hyd,z}}/dt$ (10 <sup>-6</sup> .s <sup>-1</sup> )	2.0 $\pm$ 0.2	1.9 $\pm$ 0.2	2.4 $\pm$ 0.4	3.4 $\pm$ 0.6	2.3 $\pm$ 0.4	2.5 $\pm$ 0.3	3.0 $\pm$ 0.5
$\beta_{hyd,z}$	0.30 $\pm$ 0.03	0.24 $\pm$ 0.01	0.25 $\pm$ 0.01	0.24 $\pm$ 0.01	0.17 $\pm$ 0.01	0.21 $\pm$ 0.01	0.25 $\pm$ 0.01

The identification of the hygroscopic expansion coefficient in the y-direction ( $\beta_{hyd,y}$ ) from the slope of  $\epsilon_{hyd} = f(\Delta M)$  allows to better understand the physical role of water and the influence of the mesostructure in the active layer. As the presence of channels enhances the sorption and expansion kinetics in a similar manner,  $\beta_{hyd,y}$  appears to be similar regardless of channel content.  $\beta_{hyd,y}$  also decreases as channel diameter increases confirming the potential of the channel to provide moisture uptake without compromising the hygro-expansion. A 60%-decrease of  $\beta_{hyd,y}$  between a sample with a channel diameter of 0.5 mm and one with a diameter of 3.0 mm highlights the considerable influence of channel size and distribution on the transverse hygroscopic coefficient.

#### II.2.d. Hydromechanical properties

Figure 106a and b illustrate the longitudinal  $E_{11}$  and transverse  $E_{22}$  elastic modulus of the 3D-printed biocomposites active layer in the wet and dry states, as a function of the content, size and distribution of the channels. The dry longitudinal elastic properties are hardly influenced ( $\pm 5\%$ ) by the change of mesostructure regardless of the varying parameter (Table 16). Indeed, the slender geometry of channels along the sample lengths implies that the reduction of the elastic properties of the biocomposite follows an additive law (similarly to a rule of mixture).

Channels are stated to have zero stiffness and undergo similar strain than the biocomposite material. The channels therefore correspond to a lack of load bearing materials rather than to a defect.

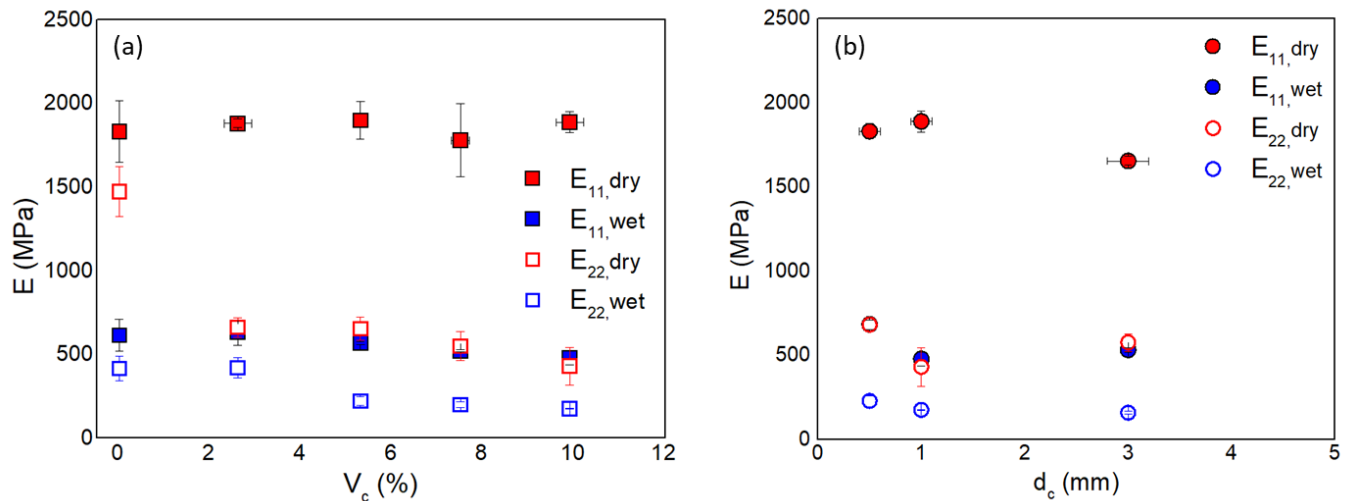


Figure 106: Longitudinal and transverse modulus as a function of a) channel content and b) channel diameter at dry and wet state. Linear regression of transverse modulus by Ashby's law [180] related to variations of c) channel content and d) channel diameter at dry and wet state. Mean  $\pm$  SD, n = 5.

The transverse properties  $E_{22}$  are divided by almost a factor three when channels are introduced and remain almost constant with an increase of  $V_c$  or  $d_c$  (Figure 106a and b). Here the slender channels with assumed zero stiffness are loaded in serial compared to the bulk composite. It highlights their contribution to the overall anisotropy of the printed material. Anisotropic ratio is a key parameter for subsequent morphing on 4D-printed HBCs. Under wet conditions, a dramatic reduction in mechanical properties is observed which is well-known for biocomposite materials and discussed elsewhere [149]. However, increasing the content, size and distribution of the channels does not have a negative effect on the evolution of  $E_{11}$  with moisture. The evolution of  $E_{22}$  with moisture is clearly affected by the channels. The higher the channel content, the lower the transverse stiffness.

Table 16: Tensile properties in wet and dry conditions of the 3D-printed active layer made with biocomposites regarding the influence of (a) channel content and (b) channel diameter (n = 5).

	$V_c$ (%)				$d_c$ (mm)		
	0	2.6	5.3	7.5	0.5	1	3
$E_{11,dry}$	1795 ± 85	1881 ± 26	1843 ± 15	1780 ± 217	1831 ± 47	1889 ± 62	1655 ± 25
$E_{11,wet}$	614 ± 96	635 ± 82	567 ± 10	522 ± 6	683 ± 28	478 ± 42	531 ± 13
$E_{22,dry}$	1474 ± 149	661 ± 57	653 ± 68	550 ± 85	682 ± 42	430 ± 113	576 ± 52
$E_{22,wet}$	424 ± 61	419 ± 60	221 ± 26	199 ± 16	228 ± 33	176 ± 2	158 ± 9

### III. Discussion

#### III.1. 4D-printed HBCs with improved performance

The modification of the active layer by a dedicated mesostructure with channels drastically changes its hydroscopic and hydro-elastic properties. Using the following Timoshenko's equation [60] (previously mentioned Equation 1, **Chapter 1, Section I.4.a**) allows to estimate the effect of the active layer customization on the responsiveness :

$$\Delta K = \frac{\Delta\beta\Delta Mf(m,n)}{t} \quad (\text{Equation 1})$$

$$\text{with } f(m,n) = \frac{6(1+m)^2}{3(1+m)^2 + (1+mn)(m^2 + \frac{1}{mn})}$$

Reactivity and responsiveness are evaluated to evidence the influence of the mesostructure on its morphing ability (Figure 107 and Table 17).

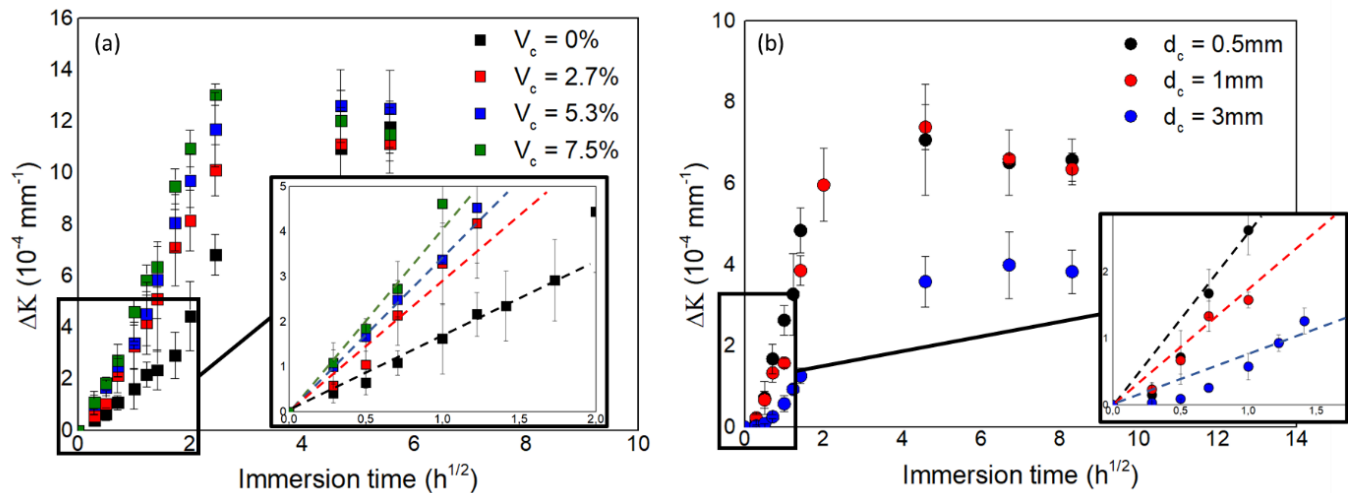


Figure 107: Evolution of curvature of response as a function of a) channel content and b) channel distribution as a function of immersion time. Mean ± SD, n = 5.



No change of responsiveness is observed for ccHBC due to the weak effect of channel content over transverse  $\beta_{\text{hyd},y}$ . However, the reactivity almost triples from 5.0 to 13.7  $10^{-5}\text{mm}^{-1}\text{s}^{-1}$  when the active layer contains channels (Table 17). Then, decreasing the channel diameter from 3 mm to 0.5 mm, the reactivity is multiplied by 5 (from 1.5 to 8.5  $10^{-5}\text{mm}^{-1}\text{s}^{-1}$ ) and the responsiveness by almost 2 (from 4.0 to 7.8  $10^{-4}\text{mm}^{-1}$ ). This is due to the positive effect of channel content, size and distribution on moisture transport and swelling kinetic of the active phase.

Table 17: Actuation properties of 4DP biocomposites including channel features depending on (a) channel content and (b) channel diameter. Mean  $\pm$  SD, n = 5.

	<b>V<sub>c</sub> (%)</b>				<b>d<sub>c</sub> (mm)</b>		
	<b>0</b>	<b>2.6</b>	<b>5.3</b>	<b>7.5</b>	<b>0.5</b>	<b>1</b>	<b>3</b>
<i>Responsiveness</i> ( $10^{-4}\text{mm}^{-1}$ )	11.8 $\pm$ 1.0	11.5 $\pm$ 1.3	12.6 $\pm$ 1.4	13.0 $\pm$ 0.4	7.8 $\pm$ 0.8	7.4 $\pm$ 0.5	4.0 $\pm$ 0.8
<i>Reactivity</i> ( $10^{-5}\text{mm}^{-1}\cdot\text{s}^{-1}$ )	5.0 $\pm$ 0.5	7.8 $\pm$ 0.5	10.8 $\pm$ 1.5	13.7 $\pm$ 1.2	8.5 $\pm$ 0.6	5.1 $\pm$ 0.7	1.5 $\pm$ 0.7

Calculations based on the experimental results on the curvature actuation of 4D-printed HBC, elastic and hydroexpansion properties of 3D-printed biocomposite, and internal hydroscopic stresses can be estimated following Equation 3 [232]:

$$\sigma_{22} = \sigma_{\text{radial}} = \frac{E_{11} \cdot E_{22}}{E_{11} + E_{22}} \frac{t}{\Delta\rho} \left( \frac{1}{2} + \frac{1}{24} \left( 2 + \frac{E_{11}}{G_{12}} + \frac{E_{22}}{G_{12}} \right) \right) \quad \text{Equation 3}$$

with the bilayer thickness (t), E<sub>11</sub> and E<sub>22</sub> the respective elastic moduli of the active and passive layers, G<sub>12</sub> the shear modulus, and Δρ the relative variation of curvature between the dry and wet (after saturation) bilayer.

A reduction of internal hydroscopic stresses by a factor 10 is observed when the channel content increases. Then, it might be assumed that designing channels inside biocomposites reduces the internal stress due to the lower constraint between printed filaments. Thus, implementing channels within the HBC may be favorable to hygromorphing as observed in biological structures such as pine cone scales [151].

### III.2. 4D-printed HBCs with tailored performance

From the previous section, it is possible to imagine a wide range of biomimetic actuators exhibiting complex sequential responses arising from a discrete distribution of channels and actuation response. Inspired by the pine cone scale mesostructure, a 4D-printed proof of concept showing a gradual distribution of channels from its center to the ends in the lengthwise direction was produced (Figure 108). Thus, a greater reactivity occurs in the HBC edge where  $V_c = 7.5\%$  while the most filled section with  $V_c = 2.5\%$  took longer to generate the sorption-induced curvature.

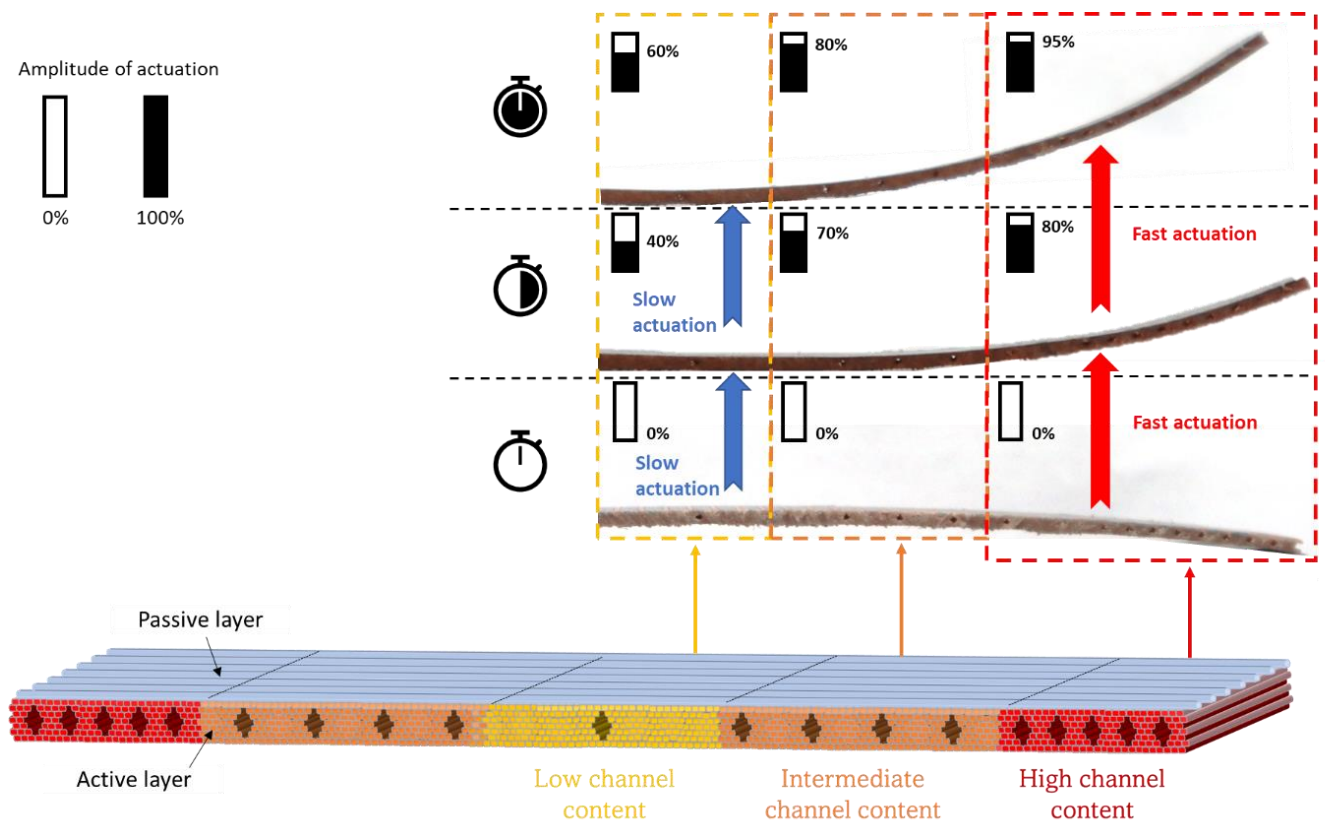


Figure 108: A 4D-printed HBC with sequential responses. The evolution of curvature at three different areas (low, medium and high channel content) of the specimen is assessed. Bars represent the degree of actuation reached by an area at a specific time compared to its final responsiveness at saturation.

## IV. Conclusion

Hydromorph Biocomposites (HBCs) represent a novel generation of bio-based materials able to “sense” their environment and to mimic water-induced shape changing mechanisms of a wide range of passive-hydraulic natural actuators. However, their reactivity, i.e., kinetic of actuation, is currently relatively slow and limited by the moisture transport within the natural fiber-reinforced composites. The 3D-printing process generates composite materials with defects such as porosity. However, plant tissues in nature have demonstrated a range of functional applications for porous structures, here named channel elements.

A biomimetic approach was applied to propose Hydromorph Biocomposites with a bioinspired mesostructure to tailor moisture transport and, consequently, actuation kinetics. Slender porosities were intentionally designed and built using 3D-printing, mimicking the channels and general mesostructure found in the pine cone scale.

As a first step, 3D-printed wood fiber biocomposites representing the active layer of subsequent 4D-printed HBCs has been designed with various percentages of channel content (from 0% to 7.5%) ranging in size (from 0.5 mm to 3 mm) with variable distribution. The channel content influenced the kinetic of water transport but also the amount of water uptake. The kinetic of expansion was improved while the hygroexpansion at saturation was kept almost constant.

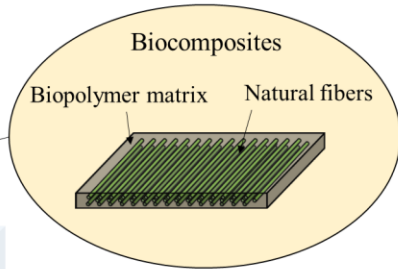
The channel size and distribution within the biocomposites allowed to influence the speed of moisture transport and the hygroscopic expansion. This confirmed that the intentional design of the mesostructure via the biologically inspired channel design allows the combination of moisture uptake without degrading the expansion potential. In perspective, the orientation of channels represents an interesting architectural feature to investigate since it might promote water supply through the specific area of the structure and tune its actuation in the most optimal way.

The implementation of these results into 4D-printing HBC bilayers confirms that the reactivity and responsiveness of HBCs can be tuned by introducing channels into the mesostructure. Finally, the full potential of 4D-printing was used to create heterogeneously distributed bioinspired channels to create complex sequential actuation.

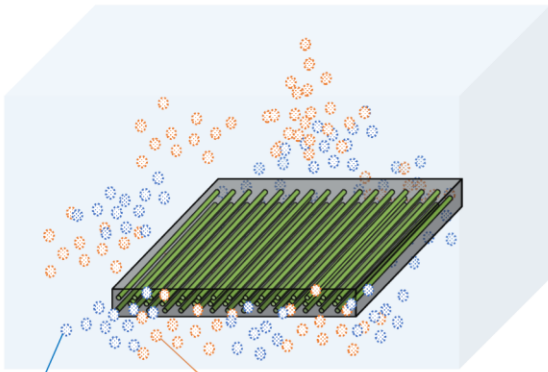


# Chapter 7 : Biocomposites, towards greener artificial reefs ?

What is the potential of biocomposites in the development of artificial reefs ?

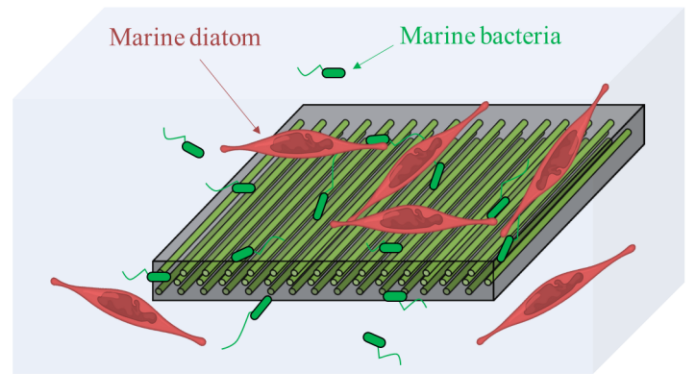


Impact of released products

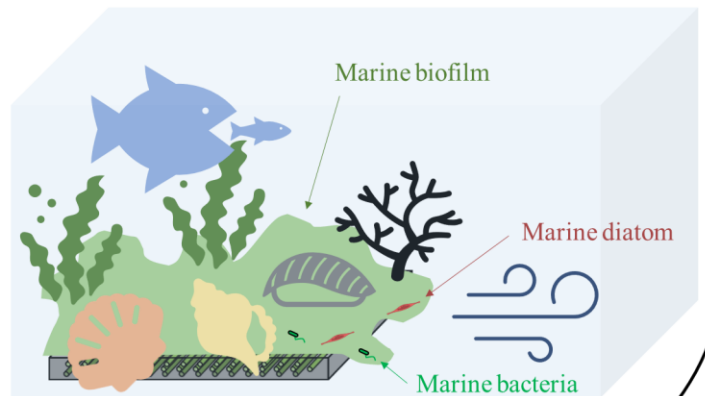


Biofouling potential

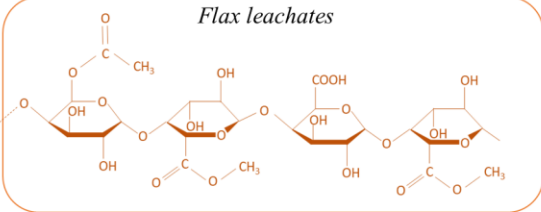
Microfouling



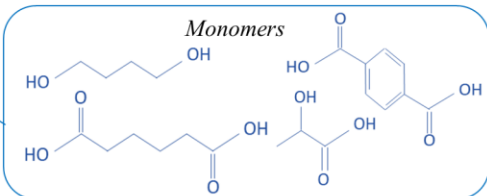
Macrofouling



Flax leachates



Monomers



## I. Introduction

As a direct consequence of anthropogenic activities, the excess of carbon dioxide gas on Earth has induced a dramatic modification of global ecosystems leading to irreversible changes for all its residents. In Oceans, the over-presence of CO<sub>2</sub> molecules generates an acidification of the environment that disrupts the metabolism of marine organisms. For example, the biodiversity of coralline algal has shown an important decrease due to marine acidification [301]. The calcification of polyps is also affected and illustrated by a decline of their growth and so coral reefs [302]. To prevent this apocalyptic depletion, several solutions are developed to rebuild the ecosystems that have been destroyed ([185], [303]). Among them, active restoration consists in implanting artificial structures to create new areas of development for marine organisms. Then, passive restoration aims to treat the external factors that affect the well-being of marine life (pollution removal, control of temperature and acidity, rejecting invasive species). Coral reefs, seagrass (e.g. *Laminaria*), and eelgrass meadows are at the root of marine life, providing both feeding areas for fishes and complex habitats fostering biodiversity and the marine food chain ([304], [305]).

Nowadays a wide range of artificial reefs exhibiting various architecture and formulation are being immersed in seawater ([198], [209], [220], [306]). The development of artificial reefs follows several objectives. For environmental reasons, it might help to recreate sustainable marine ecosystems and fight against the collapse of biodiversity. By promoting fish proliferation, it is also useful for limiting the significant delocalization and/or depletion of biotic resources caused by human activities (overfishing, marine hunting, scuba diving). In the 1980s, a dramatic number of industrial wastes (such as tires, scrap vehicle parts, rail coaches or construction rubbles) immersed in different oceans has shown a totally counterproductive effect on the restoration of biomass. Though being quickly recovered by bacterial biofilm and macro organisms, these petrochemical or heavy materials release harmful and polluting

products that destroy the growing ecosystem ([194], [195]). For a long time, wrecks have been considered suitable surfaces for living benthic organisms. However, these living organisms do not grow similarly in comparison with natural reefs. Walker and Schlacher [196] underscored the fouling variations in coverage rate and species richness between artificial reefs and natural reefs. After 3 years of immersion, only 25 species recovered the wreck surface in comparison with 48 species for natural reefs.

Learning from past mistakes, a number of features must be considered to attribute a specific functionalization and recruitment ability to an artificial habitat. In terms of formulation, the choice of the material is a crucial factor for attracting marine organisms and providing sustainable resettlement of aquatic fauna and flora. Spieler [307] reviewed the wide range of impacting features that fosters/impedes marine organisms to colonize. Among them, physicochemical properties such as composition, texture, color, leachates, surface chemistry must be mentioned. Then, environmental factors (temperature, light, pH, depth, surrounding marine ecosystem) also represent influential parameters.

For decades, concrete block has asserted its position as the most adapted material for designing artificial reefs thanks to its toughness, surface roughness, affordability and processibility ([198], [199]). Though resistant to waves as exhibited by the Atlantic Wall vestiges, concrete ends up into irremediable fragments and/or sediment landfills where metals and additives products are released over structural degradation [195]. Unfortunately, concrete blocks are non-biodegradable materials that do not disappear after their immersion in seawater. Moreover, overcoming successive colonizing stages over the years, the efficiency of the artificial habitat is abated. Renewing the immersed structure is essential to maintain significant interactions with marine organisms and reenergize reef restoration. This long-term inefficiency of immersed reefs has been leading scientists to reconsider their strategies. Since the use of permanent reef



does not bring general agreements, thoughts are given to the use of biobased and/or biodegradable artificial reefs with a controlled lifetime.

Because of the brutal impact of global warming on nature and human society, interests generated by biobased and biodegradable materials is steadily growing. Among them, the potential of bioplastics and biocomposites is already approved. Bioplastics also called biopolymers are defined as polymers that are biobased and/or biodegradable in industrial compost [308]. Biobased polymers usually come from plant polysaccharides (e.g. starch, wood, straw) or can also be synthesized by green chemistry (e.g. polyhydroxyalcanoates PHA, PHB or PHBV) or by conventional synthesis (e.g. polylactic acid PLA). Then, biodegradable polymers such as aliphatic co-polyester (e.g. polybutylene succinate PBS) or aromatic co-polyester (e.g. polybutylene adipate terephthalate PBAT) also have an ongoing development towards a more and more biobased structure. The potential of plastics in the development of innovative artificial reefs have already been reported ([209], [309]). For example, Kennedy et al. [309] discovered that polyvinyl chloride (PVC) gives a more satisfying covering of coralline algae and diversity in the community of colonizing species than ceramics and glass tiles. Using bioplastics as future artificial reefs seems provocative when thinking about current dramatic ocean pollution and marine life extinction caused by the microplastics. However, the use of bioplastics must not be dropped as only few bioplastics have been aged into seawater to assess their ecotoxicity ([207], [310]). Besides, non-toxic biodegradable plastics have already been displayed [311] and their number is expected to increase in the upcoming years.

Biocomposites associate bioplastics with natural fibers (e.g. flax, hemp, wood, bamboo) in order to exacerbate their properties (e.g. density, rigidity, degradability, chemical and thermal resistance). They proposed valuable assets as weight reduction, renewable materials and good mechanical properties comparable to those of synthetic composites ([79], [312]). Using biocomposites as recruitment surface for life restoration could be valuable for several reasons.

At first, immersing natural fiber based materials will generate a release of polysaccharide chains that could impact positively the adhesion mechanism of marine organisms. To our knowledge, this information has not been reported yet in the scientific community. Then, natural fibers are water sensitive components that swell upon water uptake. This swelling behavior has been used inside biocomposites to develop smart shape-changing structures called Hygromorph/Hydromorph BioComposites (HBC) ([62], [159], [225]). Manufactured by 3D-printing, this concept might open the door to the deployment of smart and biobased reconfigurable artificial reefs. Besides, biocomposite substrates have already proved to be a relevant support to the growth of marine organisms. Contardi et al. [205] followed the marine biofouling of starch/silicon and biodegradable lecithin-based structures over 6 months of immersion in the Maldives. Recruiting regular marine species (e.g. bryozoans, coralline algae or sponges), first coral recruits were identified at the surface of lecithin/wax/polyurethane material. Thanks to their results, conceiving biodegradable composites facing water degradation for coral larvae development is conceivable. This is a huge step in the elaboration of artificial reef with controlled lifetime.

Following this dynamic, **Chapter 7** aims to better understand the potential use of biocomposites, made of bioplastic (PBAT, PLA) and locally cultivated flax fibers, as compliant artificial reefs. For that, the influence of flax leachates on microorganism growth was evaluated on two ubiquitous marine microorganisms: *Pseudoalteromonas* sp. 3J6 marine bacterium and *Cylindrotheca closterium* (*C. closterium*) marine diatom. In parallel, an in-depth examination of the biofouling mechanism was carried out, with on the adhesion of micro- and macro-organisms (*in situ*). Comparisons with conventional plastic plates (Polyglass) and concrete blocks (CD, CE, LF, X) are emphasized.

## II. Results and Interpretations

### II.1. Influence of flax leachates on the growth of microorganisms

#### II.1.a. *Pseudoalteromonas* sp. 3J6

Figure 109a shows the evolution of the optical density of bacterial solutions (*Pseudoalteromonas* sp. 3J6 + growing medium MB + flax leachates) as a function of the leachate concentration. For every tested concentration, the absorbance increases testifying a development of bacterial community compared to the reference medium (*Pseudoalteromonas* sp. 3J6 + MB). This slight exponential increase evidences a potential revitalizing influence of flax leachates on the bacterial growth of *Pseudoalteromonas* sp. 3J6. Indeed, high concentration ( $C = 2.5 \text{ mg/mL}$ ) gives a rise of 27% compared to a 20%-drop of bacterial community for low concentration ( $C = 0.08 \text{ mg/mL}$ ). The slight negative effect at low concentrations is not statistically significant compared to the reference medium.

#### II.1.b. *Cylindrotheca closterium*

Figure 109b describes the relative fluorescence of several solutions containing *C. closterium* diatoms, growing medium (ASW) and flax leachates for different concentrations of flax leachates. It shows a parabolic trend with maximal fluorescence exceeding that of the control sample (ASW + *C. closterium*) only at extreme concentrations ( $C = \{0.08, 2.50\} \text{ mg.mL}^{-1}$ ). However, other intermediate concentrations do not give such a pro-active effect on the diatom growth. Hence, the role of flax leachates on *C. closterium* development appears cleaved.

During fiber leaching, internal compound are extracted by water flow such as uronic acid and sugar. The loss of these functional polysaccharides from the pectin region is shown to highly impact the fiber stiffness since it is responsible for the transfer of stress between the microfibrils [211]. While having no impact on the development of certain marine species (e.g. *C. closterium* diatoms), this release of sugar may represent a potential feed intake for marine microorganisms

and contribute to the development of their community (e.g. *Pseudoalteromonas* sp. 3J6). Besides, it could accelerate the degradation process of the artificial reef and be a key for controlling their lifespan.

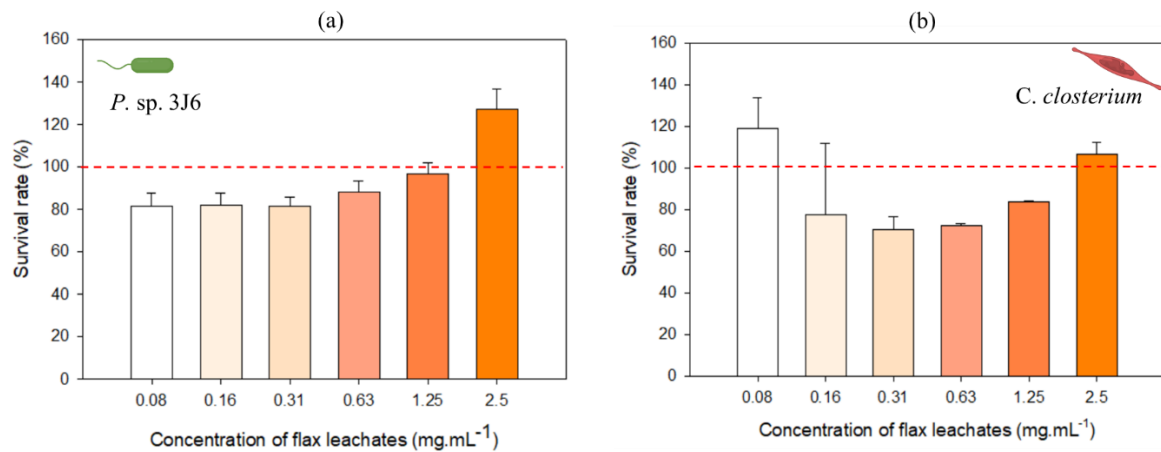


Figure 109: Impact of flax leachates on the growth of marine microorganisms. Survival rates of (a) *Pseudoalteromonas* sp. 3J6 after 24 hours by measure of optical density (600 nm) and (b) *C. closterium* diatoms after 96 hours by measure of relative fluorescence for various flax leachate concentrations ranging from 0.04 to 2.5 mg/mL (n = 6). The control solutions represented by the red dotted lines corresponds to the inherent development of microorganisms in culture medium without the presence of flax leachates. The gradient of colorations illustrates the increase of concentration of flax leachates.

## II.2. Influence of monomers on microorganism growth

### II.2.a. *Pseudoalteromonas* sp. 3J6

As illustrated in Figure 110a, the four tested monomers exert different dynamic on the bacterial growth of *Pseudoalteromonas* sp. 3J6. At the lowest tested concentration (C = 0.08 mg.mL<sup>-1</sup>), lactic acid displays a 50% decrease in absorbance, i.e. testifying a 50% inhibition rate of the bacteria. At the bioplastic scale, PLA has already exhibited a strong toxicity on marine organisms, comparable to conventional plastics [313]. Although partially metabolized by humans and biodegraded by anaerobic bacteria over 30 days [314], adipic acid exhibits a comparable drop of the survival rate. Therefore, its presence negatively impacts the growth of *Pseudoalteromonas* sp. 3J6 for a concentration higher than 0.16 mg.mL<sup>-1</sup>. Finally, increasing the concentration of terephthalic acid and butane-1,4-diol from 0.08 to 2.5 mg.mL<sup>-1</sup> did not modify the bacterial growth. As components of PBAT bioplastic, 1,4-butanediol and

terephthalic acid are both biobased products and do not represent a theoretical threat for marine organisms [310]. For example, terephthalic acid showed a low toxicity on *Allivibrio fischeri* for higher concentrations, i.e. going from 10 mg.mL<sup>-1</sup> to 1000 mg.mL<sup>-1</sup> [315].

### II.2.b. *Cylindrotheca closterium*

Considering the growth of *C. closterium* in presence of monomers (Figure 110b), the interactions with monomers are negative. An increase of the local concentration of monomers to 2.5 mg.mL<sup>-1</sup> generates an inhibition rate, i.e. loss of community compared to the reference medium, of 34% for butane-1,4-diol, 64% for terephthalic acid and almost 100% for adipic acid and acid lactic.

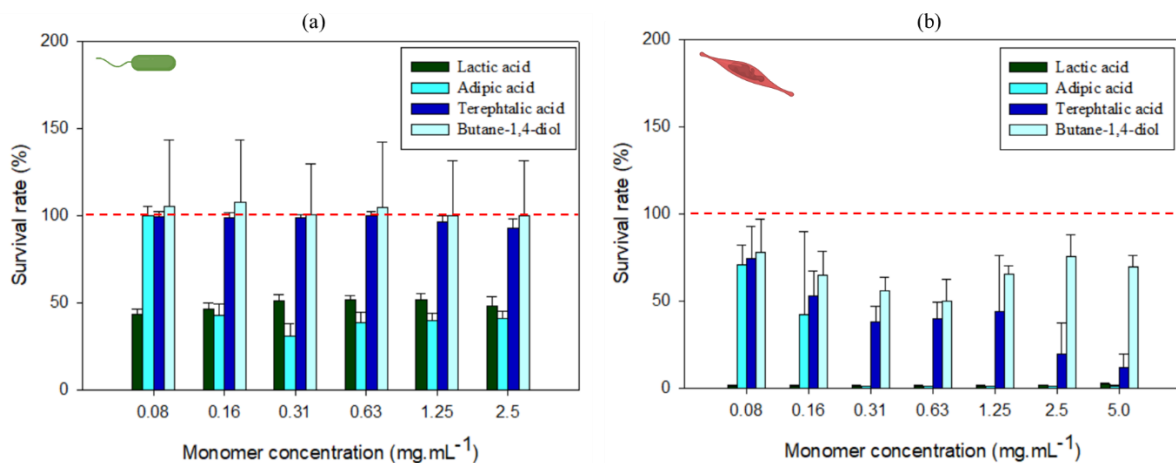


Figure 110: Impact of monomer concentration on the growth marine microorganisms. Survival rates of (a) *Pseudoalteromonas* sp. 3J6 after 24 hours by measure of optical density (600nm) and (b) *C. closterium* diatoms after 96 hours by measure of relative fluorescence for various monomer concentrations ranging from 0.01 to 5.0 mg.mL<sup>-1</sup> (n = 6). The control solutions represented by the red dotted lines corresponds to the inherent development of microorganisms in culture medium without the presence of monomers.

These results highlight the influence of monomers on the development of marine organisms.

Depending on the considered biological models, the presence of monomers might impact the growth rate. Regarding *Pseudoalteromonas* sp. 3J6, butane-1,4-diol and terephthalic acid do not alter its development, unlike lactic acid and adipic acid that generate an inhibition rate of 50% at low concentration (C = 0.16 mg.mL<sup>-1</sup>). For microalgae, this impact is exacerbated since an inhibition rate beyond 50% is obtained for both monomers. However, generalizing this conclusion to the behavior of immersed reefs is delicate since the concentration of released

products is difficult to estimate. Moreover, more tests must be carried on the impact of oligomer chains since the monomer element is rarely reached at the end of the seawater ageing of plastics. In parallel, an *in situ* survey on the impact of released products on the local ecosystem must be conducted to validate or not the use of biopolymers as future artificial reefs.

## II.3. Biofouling potential

### II.3.a. Microorganism adhesion

#### II.3.a.i. *Pseudoalteromonas* sp. 3J6

Figure 111 illustrates the colonization process of *Pseudoalteromonas* sp. 3J6 bacteria on several substrates. The covering rate shows a significant difference between the five tested formulations. At first, the biofouling potential of Polyglass used as control sample highlights an amplitude of  $4.2 \pm 2.7$  %. Both bioplastic substrates reach higher covering rates with  $4.6 \pm 2.5$  % for PLA and  $5.8 \pm 4.4$  % for PBAT. The significant standard deviation obtained for PBAT could be due to its softness that randomizes the bacterial deposition.

When adding flax fibers to the formulation, an analogous trend is given, i.e. it reduces the covering rate of *Pseudoalteromonas* sp. 3J6. This reduction reaches 65% and 60% for Flax/PLA and Flax/PBAT samples. Affecting significantly the biofouling process, the introduction of flax fibers inside the formulation causes structural and biochemical modifications. While structural features (e.g. roughness, porosity) give more opportunities for bacteria to colonize and hide (Figure 112a), biochemical features (e.g. polysaccharide release) might modify the bacterial colonization by interacting with them and providing nutrients in the surrounding growing medium.

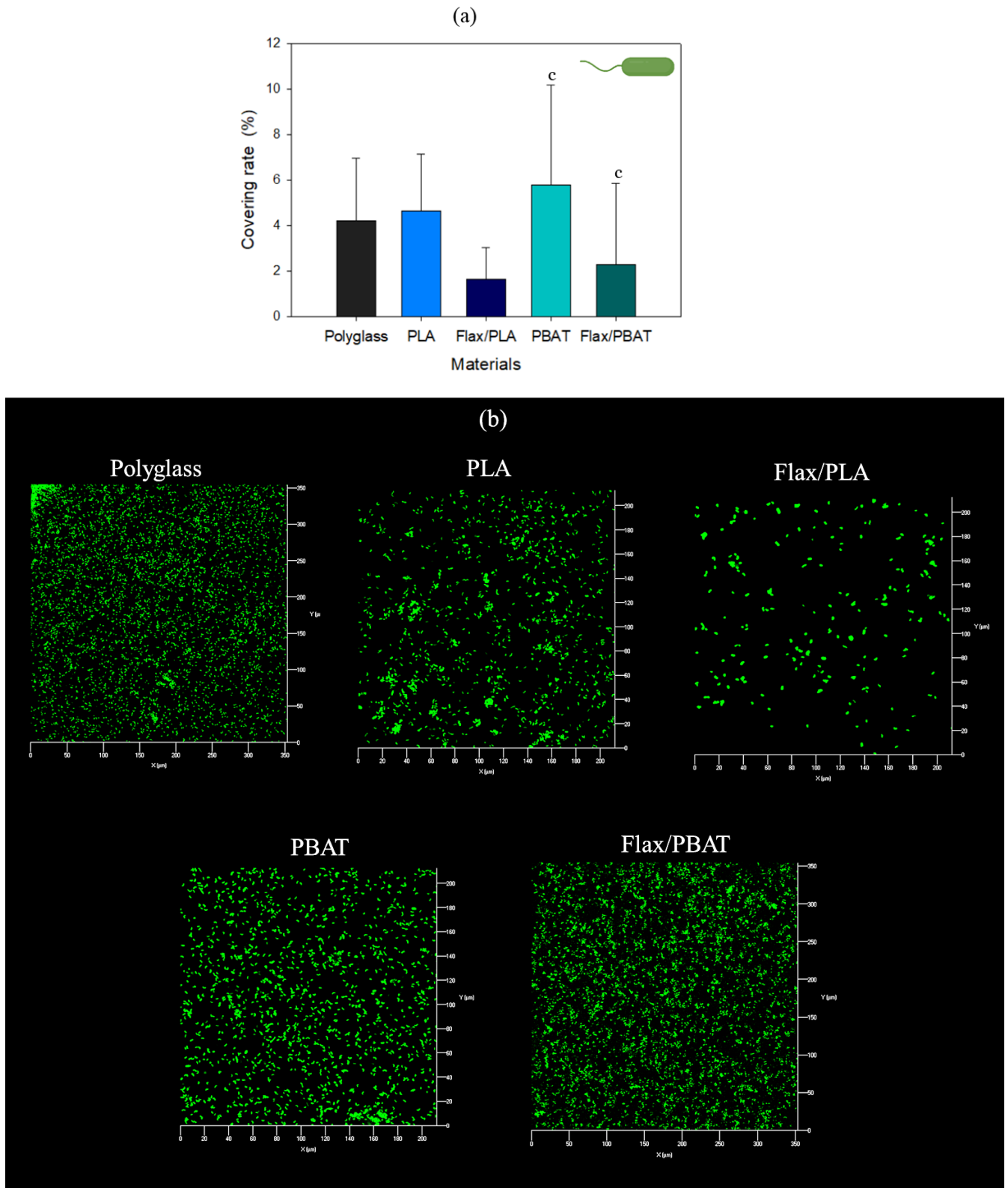


Figure 111: Investigation of the surface colonization of *Pseudoalteromonas* sp. 3J6 on Polyglass, PLA, Flax/PLA, PBAT and Flax/PBAT substrates. (a) Evolution of the covering rate after ImageJ analysis of confocal laser microscopy observation. Data represents mean  $\pm$  the standard deviation (n = 6). The **index a** emphasizes the significant difference ( $\alpha < 0.05$ ) between Polyglass control sample and the other substrates. The **index b** emphasizes the significant difference ( $\alpha < 0.05$ ) between PLA and Flax/PLA. The **index c** emphasizes the significant difference ( $\alpha < 0.05$ ) between PBAT and Flax/PBAT. (b) Confocal laser microscopy observation of a 3h bacterial colonization formed on the different tested substrates.

### II.3.a.ii. *Cylindrotheca closterium*

The results obtained for the colonization of *C. closterium* follow a comparable trend (Figure 113). While PLA and PBAT samples exhibit a covering rate of  $6.7 \pm 4.0\%$  and  $7.2 \pm 5.1\%$ , adding 30% of flax fiber in these bioplastic formulations decrease their covering rate to  $3.1 \pm 1.9\%$  (-54 %) and  $3.8 \pm 2.4\%$  (-53 %). Once again, this difference could be attributed to the loss of structural integrity generates by flax fiber swelling and lixiviation ([53], [211]). Besides, the higher surface roughness of biocomposites (Table 7) might give to microorganisms access to narrowed areas less assessable by microscopic analysis (Figure 112b).

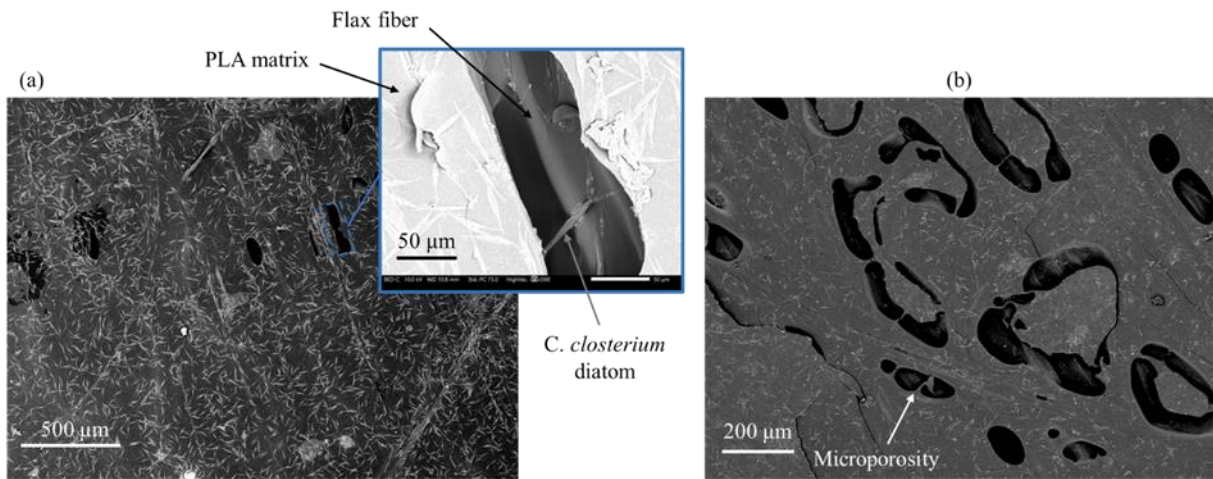
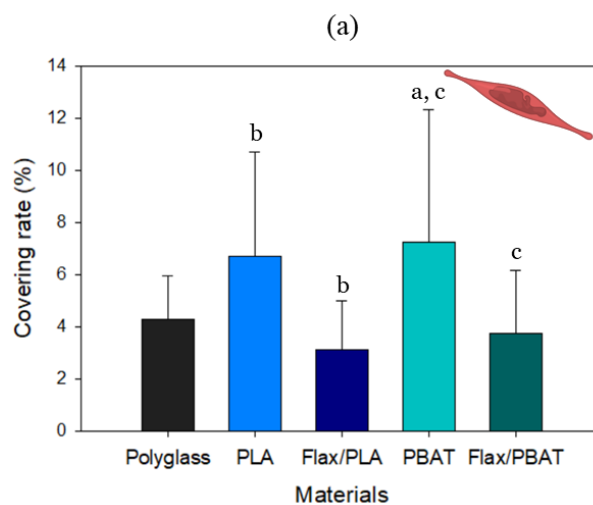


Figure 112: Marine biofouling of *C. closterium* on (a) cFF/PLA and (b) cFF/PBAT biocomposites exhibiting surfacial microporosities by SEM treatment. Inset notifies the diatom adhesion on flax fiber within the biocomposite substrate.





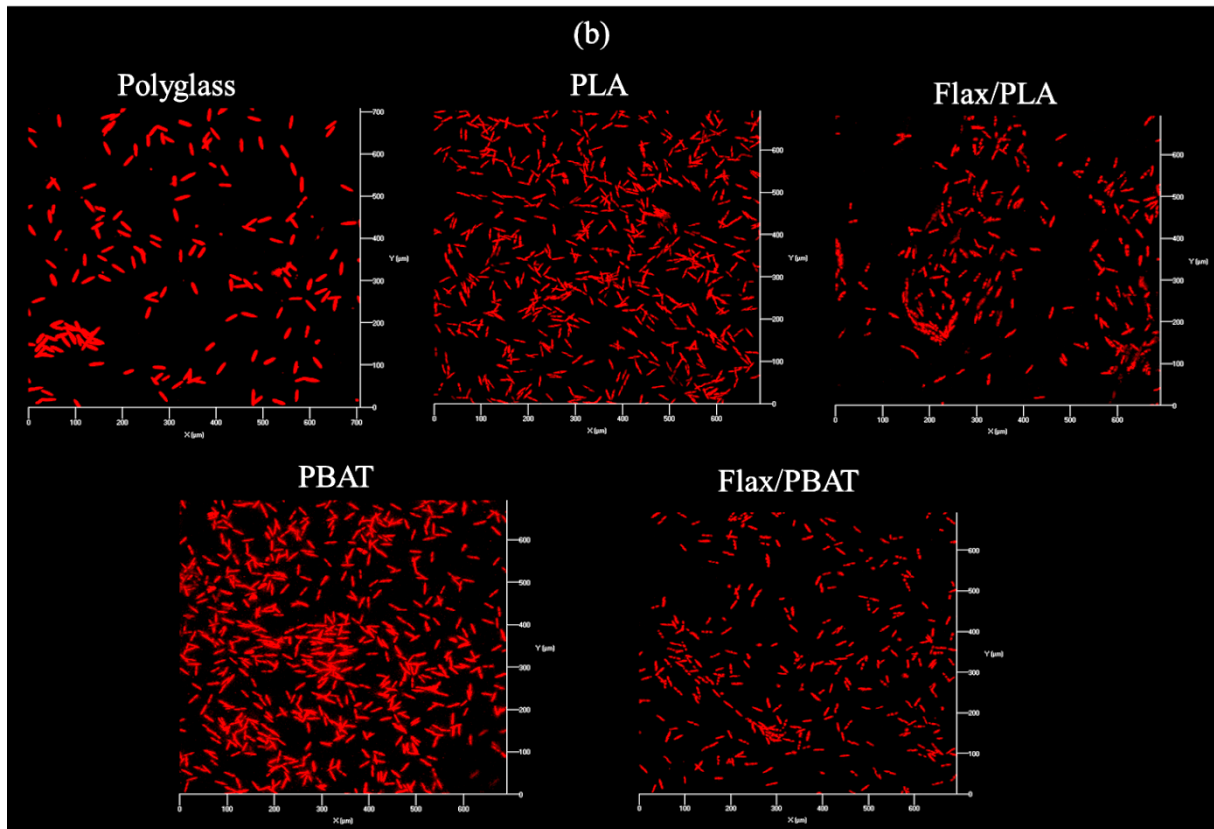


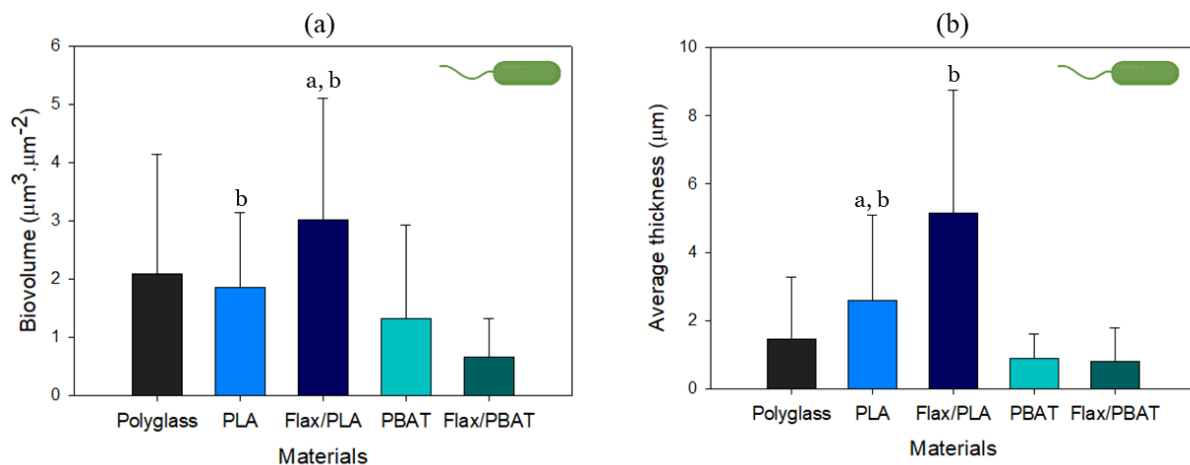
Figure 113: Investigation of the surface colonization of *Cylindrotheca closterium* on Polyglass, PLA, Flax/PLA, PBAT and Flax/PBAT substrates. (a) Evolution of the percentage of surface colonized after ImageJ analysis of confocal laser microscopy observation. Data represents mean  $\pm$  the standard deviation (n = 6). The **index a** emphasizes the significant difference ( $\alpha < 0.05$ ) between Polyglass control sample and the other substrates. The **index b** emphasizes the significant difference ( $\alpha < 0.05$ ) between PLA and Flax/PLA. The **index c** emphasizes the significant difference ( $\alpha < 0.05$ ) between PBAT and Flax/PBAT. (b) Confocal laser microscopy observation of a 72h diatom colonization formed on the different tested substrates.

### II.3.b. Biofilm formation

#### II.3.b.i. *Pseudoalteromonas* sp. 3J6

Figure 114 reveals the biovolume and average thickness of *Pseudoalteromonas* sp. 3J6 biofilm after 72 hours of maturation on Polyglass (control), PLA, PBAT, Flax/PLA and Flax/PBAT substrates. At first, an analogy between biovolume (Figure 114a) and average thickness (Figure 114b) can be discussed. Indeed, for bioplastic (essentially PBAT) and control plastic (Polyglass), the biofilm biovolume reaches much higher standards than those of the average biofilm thickness. On the contrary, biocomposites show fitting bars. It suggests that the biofilm on pure plastics is dense and thin while being wide and thick on biocomposites, certainly due to their specific surface roughness brought by the distribution of flax fibers (Table 7, p. 126).

Moreover, the difference between microorganism adhesion (**Section III.1.a.i**) and biofilm formation must be mentioned. While microorganism adhesion is weakened by the presence of flax fibers, their biofilm formation is promoted for Flax/PLA samples with a biovolume ( $3.0 \pm 2.1 \mu\text{m}^3 \cdot \mu\text{m}^{-2}$ ) and average biofilm thickness ( $5.1 \pm 3.6 \mu\text{m}$ ) 40%- and 49%-higher than biovolume ( $1.8 \pm 1.3 \mu\text{m}^3 \cdot \mu\text{m}^{-2}$ ) and average biofilm thickness ( $2.6 \pm 2.5 \mu\text{m}$ ) of PLA samples (Figure 114c). Indeed, the higher surface roughness and toughness brought by flax fibers enhance the number of crevices and heterogenous surfaces profitable to biofilm growth. However, Flax/PBAT proposes an opposite effect since it decreases the biovolume and average biofilm thickness compared to PBAT samples. This point must be normalized by the physico-chemical properties of the bioplastic such as hydromechanical properties, degradation kinetic in seawater and structural integrity when facing fiber swelling.



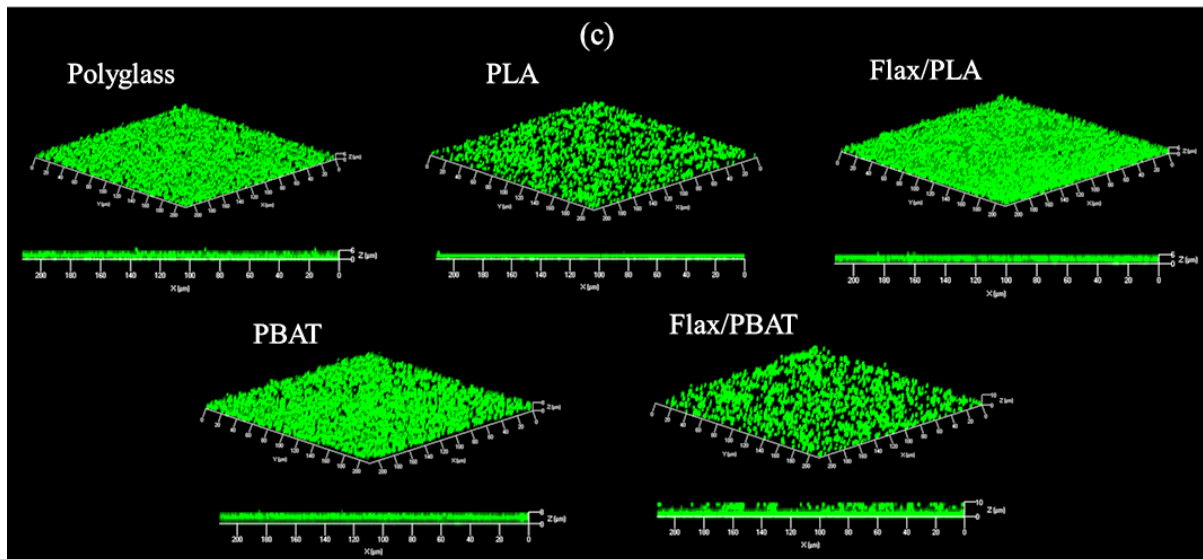


Figure 114: Investigation of the biofilm formation of *Pseudoalteromonas* sp. 3J6 after 72h at 20°C on Polyglass, PLA, Flax/PLA, PBAT and Flax/PBAT substrates. (a) Evolution of the biovolume and (b) average thickness of the generated biofilm after COMSTAT analysis of confocal laser microscopy observation. Data represents the mean  $\pm$  standard deviation ( $n = 6$ ). The **index a** emphasizes the significant difference ( $\alpha < 0.05$ ) between Polyglass control sample and the other substrates. The **index b** emphasizes the significant difference ( $\alpha < 0.05$ ) between PLA and Flax/PLA. The **index c** emphasizes the significant difference ( $\alpha < 0.05$ ) between PBAT and Flax/PBAT. (c) Confocal laser microscopy observation of the bacterial biofilm formed on the different tested substrates.

### II.2.a.ii. *Cylindrotheca closterium*

Focusing on *C. closterium* diatoms, the resulting biofilm emphasizes a strong connection with Polyglass substrates that outmatches the biovolume and average thickness of bioplastic and biocomposites (Figure 115). The high hydrophilicity of Polyglass promotes chemical interactions with diatoms. Even if biocomposite materials do not exhibit such a biofilm potential, there is here again a positive impact of the presence of flax fibers on the biofilm growth. In this situation, the surface roughness of biocomposites can create a better link with diatoms promoting the exopolysaccharide secretion and biofilm growth. Unlike observed for *Pseudoalteromonas* sp. 3J6 biofilm, no significant difference are observed between Flax/PLA and Flax/PBAT substrates.

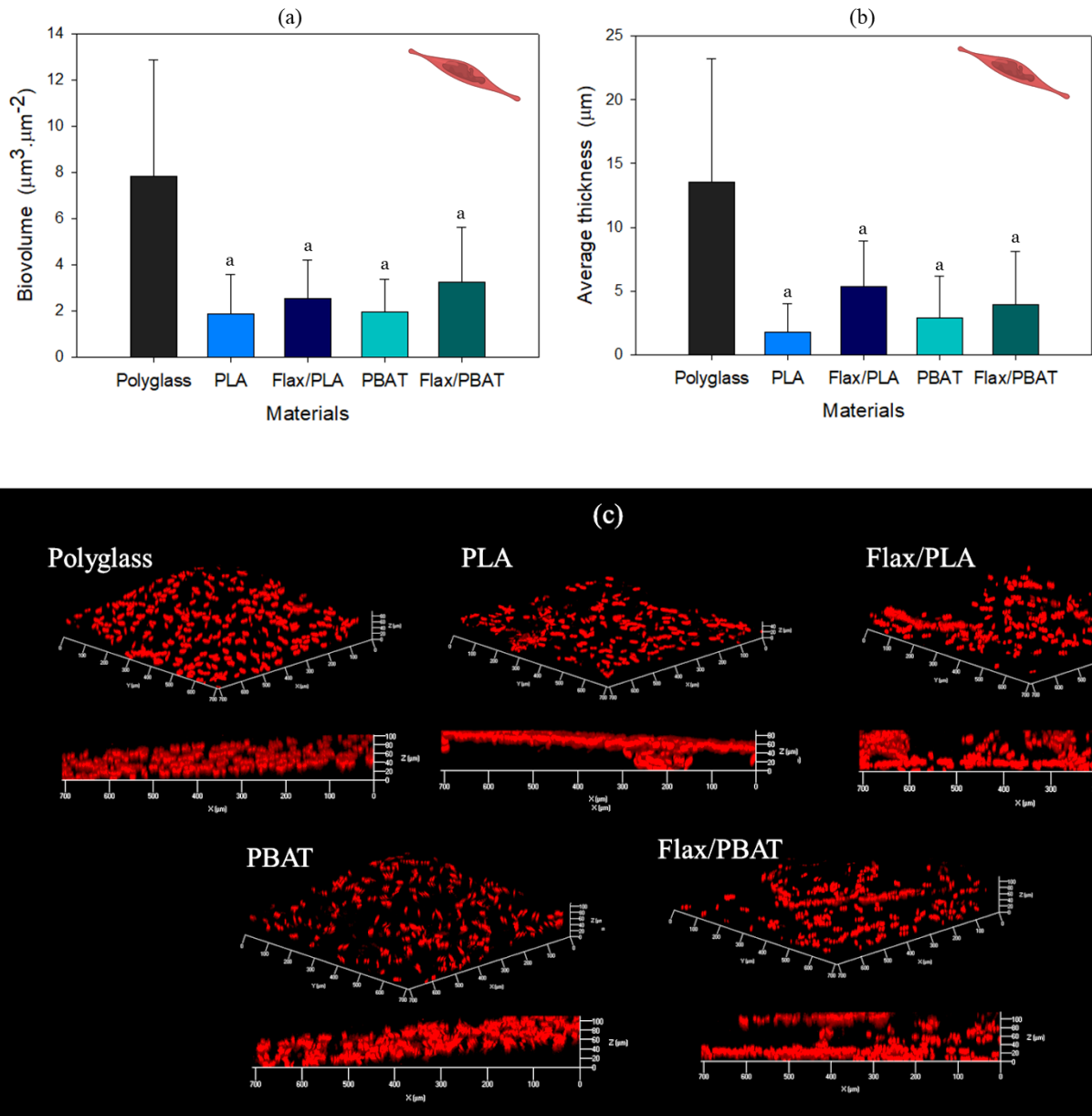


Figure 115: Investigation of the biofilm formation of *Cylindrotheca closterium* on several substrates after 72h at 18°C. (a) Evolution of the biovolume and (b) average thickness of the generated biofilm after COMSTAT analysis of confocal laser microscopy observation. Data represents the mean  $\pm$  standard deviation ( $n = 6$ ). The **index a** emphasizes the significant difference ( $\alpha < 0.05$ ) between Polyglass control sample and the other substrates. The **index b** emphasizes the significant difference ( $\alpha < 0.05$ ) between PLA and Flax/PLA. The **index c** emphasizes the significant difference ( $\alpha < 0.05$ ) between PBAT and Flax/PBAT. (c) Confocal laser microscopy observation of the diatom biofilm formed on the different tested substrates (Polyglass, PLA, Flax/PLA, PBAT and Flax/PBAT).

## II.2.c. Macroorganism adhesion (*in situ* study)

### II.2.c.i. Impact of the material

At the macrofouling scale, important variations of recovery rate are recorded between bioplastics, biocomposites and concrete substrates (Figure 116a). Concrete materials exhibit a constant rate higher than 95% from March to September. In the other hand, biocomposites and

bioplastics samples do not obtain a full recovery. Besides, an evolution of the recovery rate along the immersion time is noticed for each formulations. Flax/PLA and PLA slabs have an increasing recovery rate from March to July and decrease from July to September. These results agree with the seasonal effect on marine colonization which is promoted during the spring and summer and stabilizes or reduces during fall and winter [316]. However, the colonization rate of PBAT and Flax/PBAT decreases from March to September and the final measured covering rate after 1 year of immersion, i.e. in September 2022, shows a significant variation between pure PBAT ( $82.6 \pm 0.2\%$ ) and Flax/PBAT biocomposites whose  $V_f = 30\%$  ( $75.0 \pm 2.0\%$ ). Hence, increasing the volume content of flax fibers could exacerbate the surface degradation (Figure 117) of the substrate due to a greater expansion of the fiber in a soft biopolymer matrix (**Chapter 3**). This might negatively impact the process of biofouling by releasing slab parts and losing the present marine colonizers.

After one year of immersion, PBAT slabs displays the highest specific richness where 16 macro-colonizers were assessed (Figure 116b). This observation is in opposition with the low covering ratio recorded on PBAT slabs induced by a higher surface degradation. On the opposite, Flax/PLA ( $V_f = 15\%$ ) shows the lowest specific richness of 11 while those of concrete blocks range from 12 to 15. Moreover, most of the main colonizing species are present on biocomposites while bioplastics and concrete slabs are mainly in a lack of porifera and/or chlorophyta species. These variations give opportunity for the development of functional reefs.

An important parameter to biofouling and marine restoration is the lifetime of the reef. When using a soft matrix as PBAT, the lifetime of biocomposites reefs is expected to be shorter and the spreading of flax leachates faster compared to those made of a rigid PLA matrix, i.e. more sustainable in seawater. Regarding the natural reinforcement, the selected flax fiber also impact the recruitment process and the structural integrity of biocomposites along immersion. This point was emphasized by Haramina et al. while testing hemp/epoxy and flax/epoxy

biocomposites in seawater conditions [317]. This makes the lifetime of the reef tunable by the selected biopolymer and natural fibers, i.e. compatible with short-term (e.g. halieutic purposes) and long-term (environmental protection) applications.

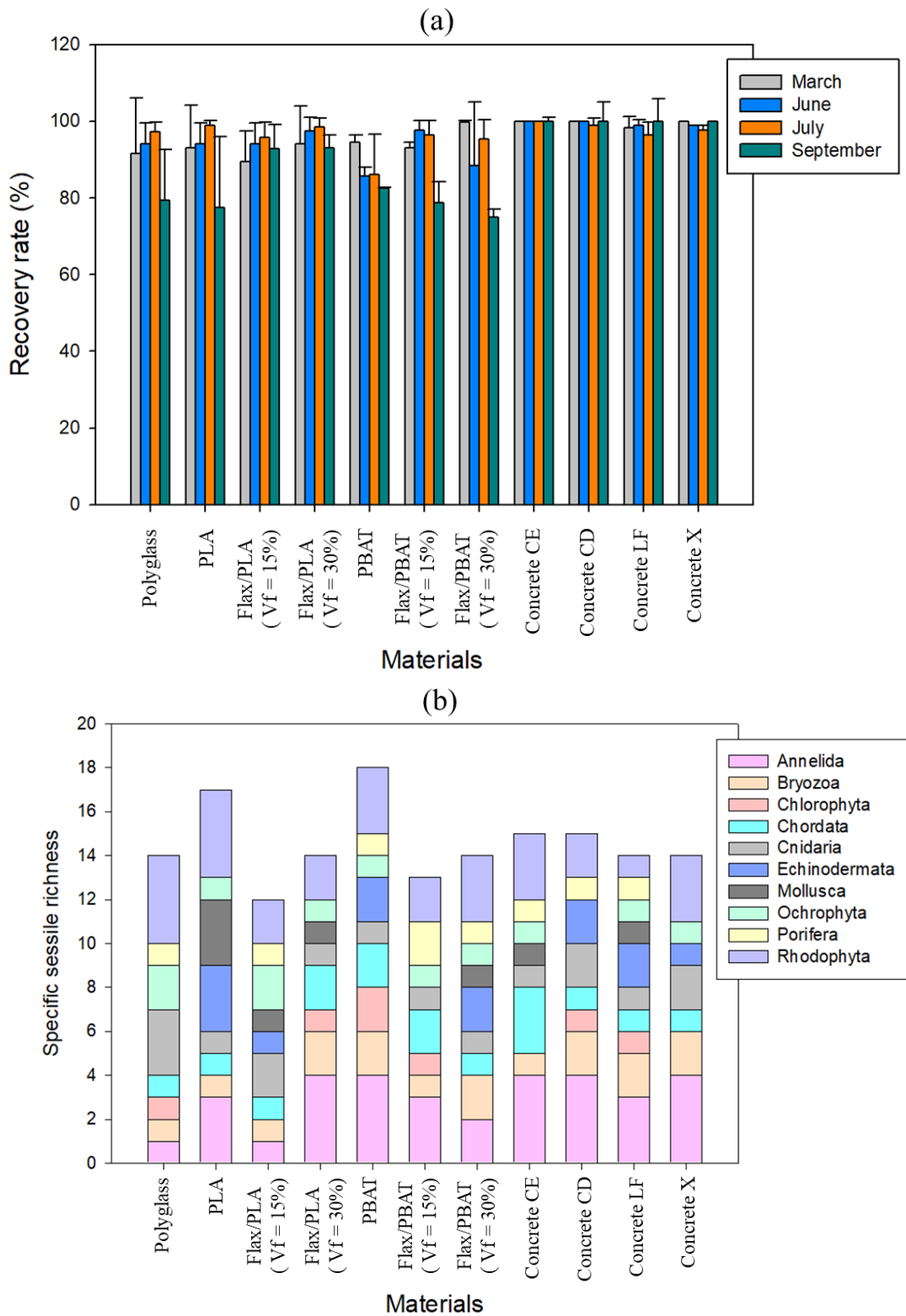


Figure 116: (a) Covering rate of marine organisms on various substrates assessed in March, June, July and September 2022. (b) Specific sessile richness on various substrates after 1 year of immersion. Samples were immersed from October 2021 to September 2022.

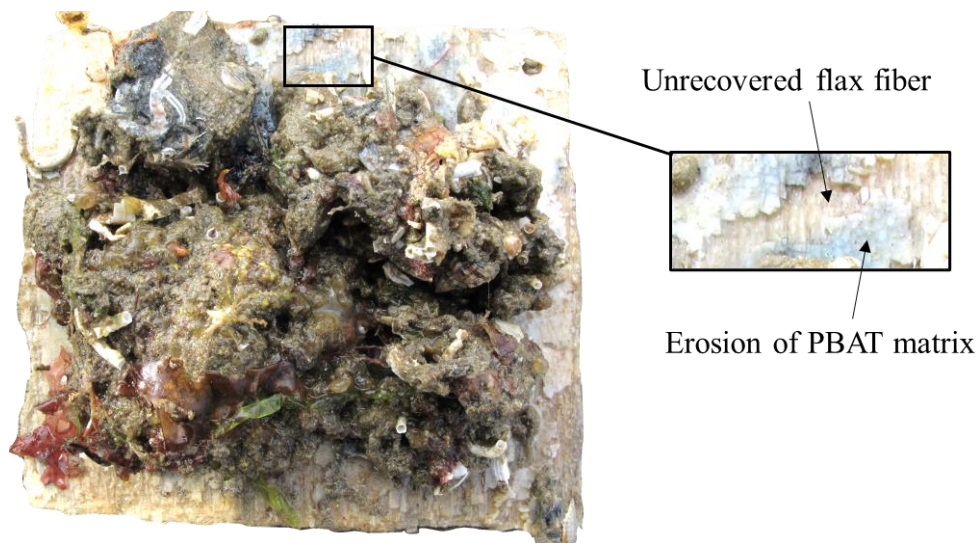


Figure 117: Surface degradation of Flax/PBAT ( $V_f = 30\%$ ) slab in seawater after 1 year of immersion.

### III. Conclusion

Artificial reefs have proved to be very useful in repopulating marine ecosystems. Although the used of heavy concrete materials is widespread, it is necessary to find solutions for more natural and biocompatible materials. Biocomposite materials made of natural fibers are now increasingly popular in load-bearing structures and shipbuilding fields, thanks to their environmental, economic and performing benefits. **Chapter 7** evaluated the impact of a locally cultivated flax fiber as component of biocomposites materials for recreating marine habitats. From the initial colonization and biofilm formation of marine microorganisms, i.e. *Pseudoalteromonas* sp. 3J6 and *Cylindrotheca closterium*, to the macrofouling stage, several variations are recorded when changing the flax fiber content or the surrounding biopolymer. Main insights are related to the biopolymer selection for controlling the release of flax leachates, the material degradation and promote or not a long-term colonization of marine organisms. Although less colonized, the specific sessile richness of biocomposites can compete with concrete formulation.

However, material selection is not the only aspect to consider when elaborating a compliant artificial reef. On the design side, the structural complexity is also linked to species diversity



and survival [219]. The optimal living environment differs for microbial, shellfish and fish communities. Roughness, colors, generated shadows or accessibility to predators are also important structural features of which impact on biofouling potential has already been clarified [318], [319]. In perspective, controlling the architectural complexity with 3D-printing represent a relevant insight to examine in the deployment of biocompatible biocomposite reefs. Besides, the emergence of 4D-printing widens the range of architected metamaterials. Hence, it encourages further thoughts on the design of water-induced shape-changing materials, e.g. Hygromorph/Hydromorph Biocomposites, to go from easily designed and immersible materials to complex final marine habitats (e.g. dome, scaffold, cone).



# General Conclusion and Perspectives

## I. Context

In today's world, humans are searching for sustainable solutions to preserve the Earth. One of the current problems relates to the loss of the biodiversity caused by climatic disruption. A prime example is the depletion of biotic resources in the Oceans representing the root of marine biodiversity and carbon reservoirs. To help revitalize the marine ecosystems, artificial reefs are immersed by humans to recreate compliant habitats for the local micro- and macroorganisms. Mainly composed of heavy materials, there is still a limited development of biobased reefs in the field of sustainable development.

Hygromorph Biocomposites are a new range of shape-changing materials actuated by a gradient of water. Inspired from biological structures such as the pine cone scale, they propose an adaptative behavior to climatic factors. It gives them an interesting potential for functional applications, e.g. morphing systems and deployable structures for soft robotics or sun shading. Therefore, HBC have known a considerable expansion in the last decades explained by their great hygroscopic properties and significant mechanical properties. However, their development is today facing several challenges, preventing them to target a wider range of applications.

At this moment, HBC represents an area which is flourishing with the development of modern manufacturing techniques, such as 4D-printing, allowing a specific distribution of matter to control the anisotropy and thus morphing behavior. A deeper look still needs to be carried out to exacerbate their use in load-bearing applications. Connecting with aforementioned environmental challenges, HBC might play a role in the revitalization mechanism of marine ecosystems by creating complex biobased structures favorable to the colonization of organisms (e.g. sustainable artificial reefs).

## II. Achievements

The formulation of flax-fiber biocomposites has been the first tackled feature. Creating an artificial reef with HBC requires an amplified shape-changing behavior to maximize the exchange surface with marine life. For this reason, strategies for enhancing the hydroexpansion of HBC was followed. Generated by the inherent swelling of the selected natural fiber, this hydroexpansion is also influenced by the biopolymer matrix employed. **Using soft biopolymer matrix (PBAT), i.e. with low mechanical properties, opens the door to greater expansion of the flax fiber and a greater actuation of HBC (Chapter 3).**

On the structural side, many parameters can influence the morphing pattern and thus predefine the final shape and architecture of the reef. Among them, thickness ratio, stiffness ratio and aspect ratio represent architectural features sliceable by 4D-printing. By optimizing these features, the complex dual stage shape-changing mechanism of the pine cone scale is mimicked. **Chapter 4 gives insights on the relation between mesostructured and actuation of HBC favorable to build tunable artificial reefs.**

Going along with the reef conception, **more complex HBC structures are today unreachable by 3D-printing when reinforced with continuous natural fibers. Chapter 5 displayed the geometrical limitations that exist when designing out-of-plane structures with continuous flax fiber/PLA filament.** This lock remains problematic for closing the structural gap with natural reef ecosystems.

Although not controlling the anisotropy within HBC, the use of short flax fiber reinforced filament brings advantages in the design of complex bioinspired structures compared to continuous flax fiber reinforced filament. **Inspired from plant metabolism, introducing channel elements inside HBC accelerates their response and leads to the development of HBC with sequential response (Chapter 6).** This new concept might promote the shape-changing behavior of the reef as well as the colonization of microorganisms.

Finally, the interactions between HBC and marine organisms are decisive to validate the concept. As this reef is intended to be biocompatible and with a controlled lifespan, a comparison with regular concrete formulations has been conducted. **The selection of biocomposite formulation (biopolymer, natural fiber, fiber content) has an influence on the biofouling mechanism (covering rate, specific sessile richness) (Chapter 7).** Although not as efficient as concrete reefs when dealing with biofouling potential, they bring a temporary aspect by vanishing along the immersion, freeing space for a fully natural rehabilitation.

### III. Perspectives

- Ecotoxicity of raw materials

One main aspect to explore is the ecotoxicity of released flax leachates and polymer products along the immersion. Investigated on two local microorganisms, many other biological marine models should be tested to get a deeper look on the biocompatibility of the proposed reef.

- Developing scaffold structures

Another interesting shape-changing pattern to reproduce in marine life is the scaffold expansion. As observed in foams, the multiple channels with interconnected pores could represent a favorable support for colonizers. Besides, the harmonization of conducts could upgrade the material expansion and increase the exchange surface with living species.

- Seawater ageing

Some investigations have already targeted the ageing behavior of biocomposites in seawater. However, since multiple formulations are tested in this project, a larger study must be envisioned.

- Toward a full-scale prototype

Then, when the surveys carried on ecotoxicity and seawater ageing of HBC will be done, the final exclamation mark would be to upscale the 4D-printed prototypes to the marine ecosystem.



## References

- [1] R. M. Kozłowski et M. Mackiewicz-Talarczyk, « 1A - Introduction to natural textile fibres », in *Handbook of Natural Fibres (Second Edition)*, R. M. Kozłowski et M. Mackiewicz-Talarczyk, Éd., in Woodhead Publishing Series in Textiles. Woodhead Publishing, 2020, p. 1-13. doi: 10.1016/B978-0-12-818398-4.00001-3.
- [2] A. Kulma, K. Skorkowska-Telichowska, K. Kostyn, M. Szatkowski, et J. Szopa, « New flax producing bioplastic fibers for medical purposes - ScienceDirect », 2015, Consulté le: 20 mars 2023. [En ligne]. Disponible sur: <https://www.sciencedirect.com/science/article/abs/pii/S0926669014005585>
- [3] H. Godwin, « Pollen-analytic evidence for the cultivation of Cannabis in England », *Rev. Palaeobot. Palynol.*, vol. 4, n° 1, p. 71-80, oct. 1967, doi: 10.1016/0034-6667(67)90173-X.
- [4] A. Gomez-Campos, C. Vialle, A. Rouilly, C. Sablayrolles, et L. Hamelin, « Flax fiber for technical textile: A life cycle inventory », *J. Clean. Prod.*, vol. 281, p. 125177, janv. 2021, doi: 10.1016/j.jclepro.2020.125177.
- [5] A. Bourmaud, J. Beaugrand, D. U. Shah, V. Placet, et C. Baley, « Towards the design of high-performance plant fibre composites », *Prog. Mater. Sci.*, vol. 97, p. 347-408, août 2018, doi: 10.1016/j.pmatsci.2018.05.005.
- [6] A. Fitzgerald *et al.*, « A Life Cycle Engineering Perspective on Biocomposites as a Solution for a Sustainable Recovery », *Sustainability*, vol. 13, n° 3, p. 1160, janv. 2021, doi: 10.3390/su13031160.
- [7] S. Begum, S. Fawzia, et M. S. J. Hashmi, « Polymer matrix composite with natural and synthetic fibres », *Adv. Mater. Process. Technol.*, vol. 6, n° 3, p. 547-564, juill. 2020, doi: 10.1080/2374068X.2020.1728645.
- [8] M. Jawaid et H. P. S. Abdul Khalil, « Cellulosic/synthetic fibre reinforced polymer hybrid composites: A review », *Carbohydr. Polym.*, vol. 86, n° 1, p. 1-18, août 2011, doi: 10.1016/j.carbpol.2011.04.043.
- [9] N. Martin, N. Mouret, P. Davies, et C. Baley, « Influence of the degree of retting of flax fibers on the tensile properties of single fibers and short fiber/polypropylene composites », *Ind. Crops Prod.*, vol. 49, p. 755-767, août 2013, doi: 10.1016/j.indcrop.2013.06.012.
- [10] K. Haag *et al.*, « Influence of flax fibre variety and year-to-year variability on composite properties », *Ind. Crops Prod.*, vol. 98, p. 1-9, avr. 2017, doi: 10.1016/j.indcrop.2016.12.028.
- [11] M. Z. Rong, M. Q. Zhang, Y. Liu, G. C. Yang, et H. M. Zeng, « The effect of fiber treatment on the mechanical properties of unidirectional sisal-reinforced epoxy composites », *Compos. Sci. Technol.*, vol. 61, n° 10, p. 1437-1447, août 2001, doi: 10.1016/S0266-3538(01)00046-X.
- [12] S. Kalia et L. Avérous, Éd., *Biodegradable and Biobased Polymers for Environmental and Biomedical Applications: Kalia/Biodegradable*. Hoboken, NJ, USA: John Wiley & Sons, Inc., 2016. doi: 10.1002/9781119117360.
- [13] H. Kawaguchi, C. Ogino, et A. Kondo, « Microbial conversion of biomass into bio-based polymers », *Bioresour. Technol.*, vol. 245, p. 1664-1673, déc. 2017, doi: 10.1016/j.biortech.2017.06.135.
- [14] S. Laurichesse et L. Avérous, « Chemical modification of lignins: Towards biobased polymers », *Prog. Polym. Sci.*, vol. 39, n° 7, p. 1266-1290, juill. 2014, doi: 10.1016/j.progpolymsci.2013.11.004.
- [15] K.-K. Tremblay-Parrado, C. García-Astrain, et L. Avérous, « Click chemistry for the synthesis of biobased polymers and networks derived from vegetable oils », *Green Chem.*, vol. 23, n° 12, p. 4296-4327, 2021, doi: 10.1039/D1GC00445J.
- [16] B. Aaliya, K. V. Sunooj, et M. Lackner, « Biopolymer composites: a review », *Int. J. Biobased Plast.*, vol. 3, n° 1, p. 40-84, janv. 2021, doi: 10.1080/24759651.2021.1881214.

- [17] S. RameshKumar, P. Shaiju, K. E. O'Connor, et R. B. P, « Bio-based and biodegradable polymers - State-of-the-art, challenges and emerging trends », *Curr. Opin. Green Sustain. Chem.*, vol. 21, p. 75-81, févr. 2020, doi: 10.1016/j.cogsc.2019.12.005.
- [18] S. Youssefian et N. Rahbar, « Molecular Origin of Strength and Stiffness in Bamboo Fibrils », *Sci. Rep.*, vol. 5, n° 1, p. 11116, juin 2015, doi: 10.1038/srep11116.
- [19] A. Bourmaud, C. Morvan, A. Bouali, V. Placet, P. Perré, et C. Baley, « Relationships between micro-fibrillar angle, mechanical properties and biochemical composition of flax fibers », *Ind. Crops Prod.*, vol. 44, p. 343-351, janv. 2013, doi: 10.1016/j.indcrop.2012.11.031.
- [20] M. Tanguy, A. Bourmaud, J. Beaugrand, T. Gaudry, et C. Baley, « Polypropylene reinforcement with flax or jute fibre; Influence of microstructure and constituents properties on the performance of composite », *Compos. Part B Eng.*, vol. 139, p. 64-74, avr. 2018, doi: 10.1016/j.compositesb.2017.11.061.
- [21] M. Eder, O. Arnould, J. W. C. Dunlop, J. Hornatowska, et L. Salmén, « Experimental micromechanical characterisation of wood cell walls », *Wood Sci. Technol.*, vol. 47, n° 1, p. 163-182, janv. 2013, doi: 10.1007/s00226-012-0515-6.
- [22] S. J. Eichhorn et R. J. Young, « The Young's modulus of a microcrystalline cellulose ».
- [23] C. Badouard, F. Traon, C. Denoual, C. Mayer-Laigle, G. Paës, et A. Bourmaud, « Exploring mechanical properties of fully compostable flax reinforced composite filaments for 3D printing applications », *Ind. Crops Prod.*, vol. 135, p. 246-250, sept. 2019, doi: 10.1016/j.indcrop.2019.04.049.
- [24] A. Le Duigou et M. Castro, « Moisture-induced self-shaping flax-reinforced polypropylene biocomposite actuator », *Ind. Crops Prod.*, vol. 71, p. 1-6, sept. 2015, doi: 10.1016/j.indcrop.2015.03.077.
- [25] G. Samorini, « The oldest archeological data evidencing the relationship of Homo sapiens with psychoactive plants: A worldwide overview », *J. Psychedelic Stud.*, vol. 3, n° 2, p. 63-80, mars 2019, doi: 10.1556/2054.2019.008.
- [26] A. Céline, S. Fréour, F. Jacquemin, et P. Casari, « The hygroscopic behavior of plant fibers: a review », *Front. Chem.*, vol. 1, 2014, doi: 10.3389/fchem.2013.00043.
- [27] J. A. Howsmon, « Water Sorption and the Poly-Phase Structure of Cellulose Fibers », *Text. Res. J.*, 1949.
- [28] K. Nakamura, T. Hatakeyama, et H. Hatakeyama, « Studies on Bound Water of Cellulose by Differential Scanning Calorimetry », *Text. Res. J.*, vol. 51, n° 9, p. 607-613, sept. 1981, doi: 10.1177/004051758105100909.
- [29] M. M. Lu, C. A. Fuentes, et A. W. Van Vuure, « Moisture sorption and swelling of flax fibre and flax fibre composites », *Compos. Part B Eng.*, vol. 231, p. 109538, févr. 2022, doi: 10.1016/j.compositesb.2021.109538.
- [30] P. H. Hermans, « Physics and chemistry of cellulose fibers », *Elsevier Pub Co*, 1949.
- [31] S. Okubayashi, U. Griesser, et T. Bechtold, « A kinetic study of moisture sorption and desorption on lyocell fibers », *Carbohydr. Polym.*, vol. 58, n° 3, p. 293-299, nov. 2004, doi: 10.1016/j.carbpol.2004.07.004.
- [32] W. Wang, M. Sain, et P. Cooper, « Study of moisture absorption in natural fiber plastic composites », *Compos. Sci. Technol.*, vol. 66, n° 3-4, p. 379-386, mars 2006, doi: 10.1016/j.compscitech.2005.07.027.
- [33] V. K. S. Shante et S. Kirkpatrick, « An introduction to percolation theory », *Adv. Phys.*, vol. 20, n° 85, p. 325-357, mai 1971, doi: 10.1080/00018737100101261.
- [34] B. Djellouli, « Analysis of the hygroscopic and hygroelastic behaviours of water aged flax-epoxy composite », *Compos. Struct.*, p. 14, 2021.
- [35] W. Garat, N. Le Moigne, S. Corn, J. Beaugrand, et A. Bergeret, « Swelling of natural fibre bundles under hydro- and hydrothermal conditions: Determination of hydric expansion coefficients by automated laser scanning », *Compos. Part Appl. Sci. Manuf.*, vol. 131, p. 105803, avr. 2020, doi: 10.1016/j.compositesa.2020.105803.



- [36] I. Burgert et P. Fratzl, « Actuation systems in plants as prototypes for bioinspired devices », *Philos. Trans. R. Soc. Math. Phys. Eng. Sci.*, vol. 367, n° 1893, p. 1541-1557, avr. 2009, doi: 10.1098/rsta.2009.0003.
- [37] E. K. Gamstedt, « Moisture induced softening and swelling of natural cellulose fibres in composite applications », *IOP Conf. Ser. Mater. Sci. Eng.*, vol. 139, p. 012003, juill. 2016, doi: 10.1088/1757-899X/139/1/012003.
- [38] M. Lindner, « Factors affecting the hygroexpansion of paper », *J. Mater. Sci.*, vol. 53, n° 1, p. 1-26, 2018, doi: 10.1007/s10853-017-1358-1.
- [39] B. Pejic, M. Kostic, P. Skundric, et J. Praskalo, « The effects of hemicelluloses and lignin removal on water uptake behavior of hemp fibers », *Bioresour. Technol.*, vol. 99, p. 8, 2007, doi: 10.1016/j.biortech.2007.12.073.
- [40] A. Le Duigou, S. Requile, J. Beaugrand, F. Scarpa, et M. Castro, « Natural fibres actuators for smart bio-inspired hygromorph biocomposites », *Smart Mater. Struct.*, vol. 26, n° 12, p. 125009, déc. 2017, doi: 10.1088/1361-665X/aa9410.
- [41] R. C. Neagu et E. K. Gamstedt, « Modelling of effects of ultrastructural morphology on the hygroelastic properties of wood fibres », *J. Mater. Sci.*, vol. 42, n° 24, p. 10254-10274, déc. 2007, doi: 10.1007/s10853-006-1199-9.
- [42] A. Rafsanjani, M. Stiefel, K. Jefimovs, R. Mokso, D. Derome, et J. Carmeliet, « Hygroscopic swelling and shrinkage of latewood cell wall micropillars reveal ultrastructured anisotropy », 2015.
- [43] E. Marklund et J. Varna, « Modeling the hygroexpansion of aligned wood fiber composites », *Compos. Sci. Technol.*, vol. 69, n° 7-8, p. 1108-1114, juin 2009, doi: 10.1016/j.compscitech.2009.02.006.
- [44] N. Wang, W. Liu, et J. Lai, « An attempt to model the influence of gradual transition between cell wall layers on cell wall hygroelastic properties », *J. Mater. Sci.*, vol. 49, n° 5, p. 1984-1993, mars 2014, doi: 10.1007/s10853-013-7885-5.
- [45] A. le Duigou, J. Merotte, A. Bourmaud, P. Davies, K. Belhouli, et C. Baley, « Hygroscopic expansion: A key point to describe natural fibre/polymer matrix interface bond strength », *Compos. Sci. Technol.*, vol. 151, p. 228-233, oct. 2017, doi: 10.1016/j.compscitech.2017.08.028.
- [46] M. Abida, F. Gehring, J. Mars, A. Vivet, F. Dammak, et M. Haddar, « Hygro-mechanical coupling and multiscale swelling coefficients assessment of flax yarns and flax / epoxy composites », *Compos. Part Appl. Sci. Manuf.*, vol. 136, p. 105914, sept. 2020, doi: 10.1016/j.compositesa.2020.105914.
- [47] T. Joffre, E. L. G. Wernersson, A. Miettinen, C. L. Luengo Hendriks, et E. K. Gamstedt, « Swelling of cellulose fibres in composite materials: Constraint effects of the surrounding matrix », *Compos. Sci. Technol.*, vol. 74, p. 52-59, janv. 2013, doi: 10.1016/j.compscitech.2012.10.006.
- [48] K. M. Almgren, E. K. Gamstedt, et J. Varna, « Contribution of wood fiber hygroexpansion to moisture induced thickness swelling of composite plates », *Polym. Compos.*, p. NA-NA, 2009, doi: 10.1002/pc.20858.
- [49] K. M. Almgren, E. K. Gamstedt, F. Berthold, et M. Lindström, « HYGROEXPANSION OF WOOD-FIBRE COMPOSITE MATERIALS: EFFECTS OF CELL-WALL CROSS-LINKING AND COMPOSITION OF THERMOPLASTIC MATRIX », p. 10.
- [50] C. Humeau, P. Davies, et F. Jacquemin, « An experimental study of water diffusion in carbon/epoxy composites under static tensile stress », *Compos. Part Appl. Sci. Manuf.*, vol. 107, p. 94-104, avr. 2018, doi: 10.1016/j.compositesa.2017.12.016.
- [51] M. Arhant, P.-Y. Le Gac, M. Le Gall, C. Burtin, C. Briançon, et P. Davies, « Effect of sea water and humidity on the tensile and compressive properties of carbon-polyamide 6 laminates », *Compos. Part Appl. Sci. Manuf.*, vol. 91, p. 250-261, déc. 2016, doi: 10.1016/j.compositesa.2016.10.012.

- [52] A. Le Duigou, P. Davies, et C. Baley, « Seawater ageing of flax/poly(lactic acid) biocomposites », *Polym. Degrad. Stab.*, vol. 94, n° 7, p. 1151-1162, juill. 2009, doi: 10.1016/j.polymdegradstab.2009.03.025.
- [53] H. Dhakal, Z. Zhang, N. Bennett, A. Lopez-Arraiza, et F. Vallejo, « Effects of water immersion ageing on the mechanical properties of flax and jute fibre biocomposites evaluated by nanoindentation and flexural testing », *J. Compos. Mater.*, vol. 48, n° 11, p. 1399-1406, mai 2014, doi: 10.1177/0021998313487238.
- [54] H. Chen, M. Miao, et X. Ding, « Influence of moisture absorption on the interfacial strength of bamboo/vinyl ester composites », *Compos. Part Appl. Sci. Manuf.*, vol. 40, n° 12, p. 2013-2019, déc. 2009, doi: 10.1016/j.compositesa.2009.09.003.
- [55] S. Réquillé, A. Le Duigou, A. Bourmaud, et C. Baley, « Interfacial properties of hemp fiber/epoxy system measured by microdroplet test: Effect of relative humidity », *Compos. Sci. Technol.*, vol. 181, p. 107694, sept. 2019, doi: 10.1016/j.compscitech.2019.107694.
- [56] S. Réquillé, A. Le Duigou, A. Bourmaud, et C. Baley, « Deeper insights into the moisture-induced hygroscopic and mechanical properties of hemp reinforced biocomposites », *Compos. Part Appl. Sci. Manuf.*, vol. 123, p. 278-285, août 2019, doi: 10.1016/j.compositesa.2019.05.006.
- [57] J. César dos Santos *et al.*, « Ageing of autoclaved epoxy/flax composites: Effects on water absorption, porosity and flexural behaviour », *Compos. Part B Eng.*, vol. 202, p. 108380, déc. 2020, doi: 10.1016/j.compositesb.2020.108380.
- [58] C. Baley, C. Morvan, et Y. Grohens, « Influence of the Absorbed Water on the Tensile Strength of Flax Fibers », *Macromol. Symp.*, vol. 222, n° 1, p. 195-202, mars 2005, doi: 10.1002/masy.200550425.
- [59] A. Le Duigou, V. Keryvin, J. Beaugrand, M. Pernes, F. Scarpa, et M. Castro, « Humidity responsive actuation of bioinspired hygromorph biocomposites (HBC) for adaptive structures », *Compos. Part Appl. Sci. Manuf.*, vol. 116, p. 36-45, janv. 2019, doi: 10.1016/j.compositesa.2018.10.018.
- [60] S. Timoshenko, « Analysis of Bi-Metal Thermostats », *J. Opt. Soc. Am.*, vol. 11, n° 3, p. 233, sept. 1925, doi: 10.1364/JOSA.11.000233.
- [61] A. Holstov, B. Bridgens, et G. Farmer, « Hygromorphic materials for sustainable responsive architecture », *Constr. Build. Mater.*, vol. 98, p. 570-582, nov. 2015, doi: 10.1016/j.conbuildmat.2015.08.136.
- [62] E. Reyssat et L. Mahadevan, « Hygromorphs: from pine cones to biomimetic bilayers », *J. R. Soc. Interface*, vol. 6, n° 39, p. 951-957, oct. 2009, doi: 10.1098/rsif.2009.0184.
- [63] M. Langhansl, J. Dörrstein, P. Hornberger, et C. Zollfrank, « Fabrication of 3D-printed hygromorphs based on different cellulosic fillers », *Funct. Compos. Mater.*, vol. 2, n° 1, p. 4, déc. 2021, doi: 10.1186/s42252-020-00014-w.
- [64] A. Le Duigou et M. Castro, « Hygromorph BioComposites: Effect of fibre content and interfacial strength on the actuation performances », *Ind. Crops Prod.*, vol. 99, p. 142-149, mai 2017, doi: 10.1016/j.indcrop.2017.02.004.
- [65] V. Popineau, A. Céline, M. Péron, C. Baley, et A. Le Duigou, « Understanding the effect of hygroscopic cycling on the internal stress and stiffness of natural fibre biocomposites », *Compos. Part Appl. Sci. Manuf.*, vol. 158, p. 106995, juill. 2022, doi: 10.1016/j.compositesa.2022.106995.
- [66] M. Péron, A. Céline, F. Jacquemin, et A. Le Duigou, « Hygroscopic stresses in asymmetric biocomposite laminates submitted to various relative humidity conditions », *Compos. Part Appl. Sci. Manuf.*, vol. 134, p. 105896, juill. 2020, doi: 10.1016/j.compositesa.2020.105896.
- [67] J. M. B. Fernandes Diniz, M. H. Gil, et J. A. A. M. Castro, « Hornification?its origin and interpretation in wood pulps », *Wood Sci. Technol.*, vol. 37, n° 6, p. 489-494, avr. 2004, doi: 10.1007/s00226-003-0216-2.

- [68] S. Reichert, A. Menges, et D. Correa, « Meteorosensitive architecture: Biomimetic building skins based on materially embedded and hygroscopically enabled responsiveness », *Comput.-Aided Des.*, vol. 60, p. 50-69, mars 2015, doi: 10.1016/j.cad.2014.02.010.
- [69] M. Rüggeberg et I. Burgert, « Bio-Inspired Wooden Actuators for Large Scale Applications », *PLOS ONE*, vol. 10, n° 4, p. e0120718, avr. 2015, doi: 10.1371/journal.pone.0120718.
- [70] A. Le Duigou et M. Castro, « Evaluation of force generation mechanisms in natural, passive hydraulic actuators », *Sci. Rep.*, vol. 6, n° 1, p. 18105, mai 2016, doi: 10.1038/srep18105.
- [71] T. N. Tran *et al.*, « Cocoa Shell Waste Biofilaments for 3D Printing Applications », *Macromol. Mater. Eng.*, vol. 302, n° 11, p. 1700219, nov. 2017, doi: 10.1002/mame.201700219.
- [72] Y. A. El-Shekeil, S. M. Sapuan, K. Abdan, et E. S. Zainudin, « Influence of fiber content on the mechanical and thermal properties of Kenaf fiber reinforced thermoplastic polyurethane composites », *Mater. Des.*, vol. 40, p. 299-303, sept. 2012, doi: 10.1016/j.matdes.2012.04.003.
- [73] D. Pollard, C. Ward, G. Herrmann, et J. Etches, « The manufacture of honeycomb cores using Fused Deposition Modeling », *Adv. Manuf. Polym. Compos. Sci.*, vol. 3, n° 1, p. 21-31, janv. 2017, doi: 10.1080/20550340.2017.1306337.
- [74] M. V. Candal *et al.*, « Thermo-rheological effects on successful 3D printing of biodegradable polyesters », *Addit. Manuf.*, vol. 36, p. 101408, déc. 2020, doi: 10.1016/j.addma.2020.101408.
- [75] L. G. Blok, M. L. Longana, H. Yu, et B. K. S. Woods, « An investigation into 3D printing of fibre reinforced thermoplastic composites », *Addit. Manuf.*, vol. 22, p. 176-186, août 2018, doi: 10.1016/j.addma.2018.04.039.
- [76] K. Sugiyama, R. Matsuzaki, M. Ueda, A. Todoroki, et Y. Hirano, « 3D printing of composite sandwich structures using continuous carbon fiber and fiber tension », *Compos. Part Appl. Sci. Manuf.*, vol. 113, p. 114-121, oct. 2018, doi: 10.1016/j.compositesa.2018.07.029.
- [77] A. Kanyilmaz, F. Berto, I. Paoletti, R. J. Caringal, et S. Mora, « Nature-inspired optimization of tubular joints for metal 3D printing », *Struct. Multidiscip. Optim.*, vol. 63, n° 2, p. 767-787, févr. 2021, doi: 10.1007/s00158-020-02729-7.
- [78] F. Ribeiro, « 3D printing with metals », *Comput. Control Eng. J.*, 1998.
- [79] A. Le Duigou, A. Barbé, E. Guillou, et M. Castro, « 3D printing of continuous flax fibre reinforced biocomposites for structural applications », *Mater. Des.*, vol. 180, p. 107884, oct. 2019, doi: 10.1016/j.matdes.2019.107884.
- [80] B. Akhoundi, A. H. Behraves, et A. Bagheri Saed, « Improving mechanical properties of continuous fiber-reinforced thermoplastic composites produced by FDM 3D printer », *J. Reinf. Plast. Compos.*, vol. 38, n° 3, p. 99-116, févr. 2019, doi: 10.1177/0731684418807300.
- [81] J. Justo, L. Távara, L. García-Guzmán, et F. París, « Characterization of 3D printed long fibre reinforced composites », *Compos. Struct.*, vol. 185, p. 537-548, févr. 2018, doi: 10.1016/j.compstruct.2017.11.052.
- [82] H. Zhang *et al.*, « Materials selection of 3D-printed continuous carbon fiber reinforced composites considering multiple criteria », *Mater. Des.*, vol. 196, p. 109140, nov. 2020, doi: 10.1016/j.matdes.2020.109140.
- [83] H. Zhao, X. Liu, W. Zhao, G. Wang, et B. Liu, « An Overview of Research on FDM 3D Printing Process of Continuous Fiber Reinforced Composites », *J. Phys. Conf. Ser.*, vol. 1213, p. 052037, juin 2019, doi: 10.1088/1742-6596/1213/5/052037.
- [84] A. S. M. Bashir et Y. Manusamy, « Recent Developments in Biocomposites Reinforced with Natural Biofillers from Food Waste », *Polym.-Plast. Technol. Eng.*, vol. 54, n° 1, p. 87-99, janv. 2015, doi: 10.1080/03602559.2014.935419.
- [85] O. Faruk, A. K. Bledzki, H.-P. Fink, et M. Sain, « Biocomposites reinforced with natural fibers: 2000–2010 », *Prog. Polym. Sci.*, vol. 37, n° 11, p. 1552-1596, 2012.
- [86] O. Faruk, A. K. Bledzki, H.-P. Fink, et M. Sain, « Progress Report on Natural Fiber Reinforced Composites: Progress Report on Natural Fiber Composites », *Macromol. Mater. Eng.*, vol. 299, n° 1, p. 9-26, janv. 2014, doi: 10.1002/mame.201300008.

- [87] A. Le Duigou, D. Correa, M. Ueda, R. Matsuzaki, et M. Castro, « A review of 3D and 4D printing of natural fibre biocomposites », *Mater. Des.*, vol. 194, p. 108911, 2020, doi: 10.1016/j.matdes.2020.108911.
- [88] A. Le Duigou, G. Chabaud, R. Matsuzaki, et M. Castro, « Tailoring the mechanical properties of 3D-printed continuous flax/PLA biocomposites by controlling the slicing parameters », *Compos. Part B Eng.*, vol. 203, p. 108474, déc. 2020, doi: 10.1016/j.compositesb.2020.108474.
- [89] M. Kurihara, T. Fruleux, A. Le Duigou, U. Masahito, et R. Matsuzaki, « Bridging in 4D printing using continuous natural-fiber composites », 2023.
- [90] R. Matsuzaki *et al.*, « Three-dimensional printing of continuous-fiber composites by in-nozzle impregnation », *Sci. Rep.*, vol. 6, n° 1, p. 23058, 2016, doi: 10.1038/srep23058.
- [91] H. Zhang, D. Liu, T. Huang, Q. Hu, et H. Lammer, « Three-Dimensional Printing of Continuous Flax Fiber-Reinforced Thermoplastic Composites by Five-Axis Machine », *Materials*, vol. 13, n° 7, p. 1678, 2020, doi: 10.3390/ma13071678.
- [92] A. Lanzotti, M. Martorelli, et G. Staiano, « Understanding Process Parameter Effects of RepRap Open-Source Three-Dimensional Printers Through a Design of Experiments Approach », *J. Manuf. Sci. Eng.*, vol. 137, n° 1, p. 011017, févr. 2015, doi: 10.1115/1.4029045.
- [93] P. Ficzer et N. L. Lukács, « Influence of 3D printing parameters », *IOP Conf. Ser. Mater. Sci. Eng.*, vol. 903, p. 012008, août 2020, doi: 10.1088/1757-899X/903/1/012008.
- [94] Y. Long, « Microstructural and mechanical characterisation of continuous flax fibre/poly(lactic acid) composites by 3D printing », p. 32.
- [95] K. Chen, L. Yu, Y. Cui, M. Jia, et K. Pan, « Optimization of printing parameters of 3D-printed continuous glass fiber reinforced polylactic acid composites », *Thin-Walled Struct.*, vol. 164, p. 107717, juill. 2021, doi: 10.1016/j.tws.2021.107717.
- [96] C. De Kergariou, H. Saidani-Scott, A. Perriman, F. Scarpa, et A. Le Duigou, « The influence of the humidity on the mechanical properties of 3D printed continuous flax fibre reinforced poly(lactic acid) composites », *Compos. Part Appl. Sci. Manuf.*, vol. 155, p. 106805, avr. 2022, doi: 10.1016/j.compositesa.2022.106805.
- [97] I. Fudos *et al.*, « A Characterization of 3D Printability », *ArXiv201012930 Cs*, oct. 2020, Consulté le: 24 décembre 2020. [En ligne]. Disponible sur: <http://arxiv.org/abs/2010.12930>
- [98] D. U. Shah, « Damage in biocomposites: Stiffness evolution of aligned plant fibre composites during monotonic and cyclic fatigue loading », *Compos. Part Appl. Sci. Manuf.*, vol. 83, p. 160-168, avr. 2016, doi: 10.1016/j.compositesa.2015.09.008.
- [99] A. Mitchell, U. Lafont, M. Holyńska, et C. Semprimoschnig, « Additive manufacturing — A review of 4D printing and future applications », *Addit. Manuf.*, vol. 24, p. 606-626, déc. 2018, doi: 10.1016/j.addma.2018.10.038.
- [100] F. Momeni, S. M. Mehdi Hassani, N. X. Liu, et J. Ni, « A review of 4D printing », *Mater. Des.*, vol. 122, p. 42-79, mai 2017, doi: 10.1016/j.matdes.2017.02.068.
- [101] P. Rastogi et B. Kandasubramanian, « Breakthrough in the printing tactics for stimuli-responsive materials: 4D printing », *Chem. Eng. J.*, vol. 366, p. 264-304, juin 2019, doi: 10.1016/j.cej.2019.02.085.
- [102] F. Momeni et J. Ni, « Laws of 4D Printing », *Engineering*, vol. 6, n° 9, p. 1035-1055, sept. 2020, doi: 10.1016/j.eng.2020.01.015.
- [103] S. Tibbits, « 4D Printing: Multi-Material Shape Change », *Archit. Des.*, vol. 84, n° 1, p. 116-121, janv. 2014, doi: 10.1002/ad.1710.
- [104] S. V. Hoa et D. I. Rosca, « Formation of letters in the alphabet using 4D printing of composites », *Mater. Today Commun.*, vol. 25, p. 101115, déc. 2020, doi: 10.1016/j.mtcomm.2020.101115.
- [105] Y. Dong *et al.*, « 4D Printed Hydrogels: Fabrication, Materials, and Applications », *Adv. Mater. Technol.*, vol. 5, n° 6, p. 2000034, juin 2020, doi: 10.1002/admt.202000034.

- [106] Y. Li, F. Zhang, Y. Liu, et J. Leng, « 4D printed shape memory polymers and their structures for biomedical applications », *Sci. China Technol. Sci.*, vol. 63, n° 4, p. 545-560, avr. 2020, doi: 10.1007/s11431-019-1494-0.
- [107] W. Zhang *et al.*, « Shape memory behavior and recovery force of 4D printed textile functional composites », *Compos. Sci. Technol.*, vol. 160, p. 224-230, mai 2018, doi: 10.1016/j.compscitech.2018.03.037.
- [108] J. Ma *et al.*, « Spatial Control of Functional Response in 4D-Printed Active Metallic Structures », *Sci. Rep.*, vol. 7, n° 1, p. 46707, avr. 2017, doi: 10.1038/srep46707.
- [109] A. R. Rajkumar et K. Shanmugam, « Additive manufacturing-enabled shape transformations via FFF 4D printing », *J. Mater. Res.*, vol. 33, n° 24, p. 4362-4376, déc. 2018, doi: 10.1557/jmr.2018.397.
- [110] B. An *et al.*, « Thermorph: Democratizing 4D Printing of Self-Folding Materials and Interfaces », in *Proceedings of the 2018 CHI Conference on Human Factors in Computing Systems*, Montreal QC Canada: ACM, avr. 2018, p. 1-12. doi: 10.1145/3173574.3173834.
- [111] G. Wang, Y. Tao, O. B. Capunaman, H. Yang, et L. Yao, « A-line: 4D Printing Morphing Linear Composite Structures », in *Proceedings of the 2019 CHI Conference on Human Factors in Computing Systems - CHI '19*, Glasgow, Scotland Uk: ACM Press, 2019, p. 1-12. doi: 10.1145/3290605.3300656.
- [112] M. Ueda, Y. Watanabe, Y. Mukai, et N. Katsumata, « Three-dimensional printing of locally bendable short carbon fiber reinforced polymer composites », *Adv. Ind. Eng. Polym. Res.*, p. S2542504821000129, févr. 2021, doi: 10.1016/j.aiepr.2021.02.004.
- [113] S. Yamamura et E. Iwase, « Hybrid hinge structure with elastic hinge on self-folding of 4D printing using a fused deposition modeling 3D printer », *Mater. Des.*, vol. 203, p. 109605, mai 2021, doi: 10.1016/j.matdes.2021.109605.
- [114] A. Zolfagharian, A. Kaynak, S. Y. Khoo, et A. Kouzani, « Pattern-driven 4D printing », *Sens. Actuators Phys.*, vol. 274, p. 231-243, mai 2018, doi: 10.1016/j.sna.2018.03.034.
- [115] Q. Wang, X. Tian, L. Huang, D. Li, A. V. Malakhov, et A. N. Polilov, « Programmable morphing composites with embedded continuous fibers by 4D printing », *Mater. Des.*, vol. 155, p. 404-413, oct. 2018, doi: 10.1016/j.matdes.2018.06.027.
- [116] K. Dong, H. Ke, M. Panahi-Sarmad, T. Yang, X. Huang, et X. Xiao, « Mechanical properties and shape memory effect of 4D printed cellular structure composite with a novel continuous fiber-reinforced printing path », *Mater. Des.*, vol. 198, p. 109303, janv. 2021, doi: 10.1016/j.matdes.2020.109303.
- [117] Z. Ding, C. Yuan, X. Peng, T. Wang, H. J. Qi, et M. L. Dunn, « Direct 4D printing via active composite materials », *Sci. Adv.*, vol. 3, n° 4, p. e1602890, avr. 2017, doi: 10.1126/sciadv.1602890.
- [118] M. Saint-Jean, « Cellular structures for shape morphing ».
- [119] T. van Manen, S. Janbaz, et A. A. Zadpoor, « Programming 2D/3D shape-shifting with hobbyist 3D printers », *Mater. Horiz.*, vol. 4, n° 6, p. 1064-1069, 2017, doi: 10.1039/C7MH00269F.
- [120] S. Poppinga, D. Correa, B. Bruchmann, A. Menges, et T. Speck, « Plant Movements as Concept Generators for the Development of Biomimetic Compliant Mechanisms », *Integr. Comp. Biol.*, vol. 60, n° 4, p. 886-895, oct. 2020, doi: 10.1093/icb/icaa028.
- [121] T. Speck et O. Speck, « Process sequences in biomimetic research », in *Design and Nature IV*, Algarve, Portugal: WIT Press, juin 2008, p. 3-11. doi: 10.2495/DN080011.
- [122] A. J. Mc Elrone, B. Choat, et G. Gambetta, « Water Uptaker and Transport in Vascular Plants », 2013.
- [123] M. J. Canny, « Flow and Transport in Plants », *Annu. Rev. Fluid Mech.*, vol. 9, n° 1, p. 275-296, janv. 1977, doi: 10.1146/annurev.fl.09.010177.001423.
- [124] M. J. Canny, « A New Theory for the Ascent of Sap—Cohesion Supported by Tissue Pressure », *Ann. Bot.*, vol. 75, n° 4, p. 343-357, avr. 1995, doi: 10.1006/anbo.1995.1032.
- [125] W. F. Pickard, « THE ASCENT OF SAP IN PLANTS », p. 49.

- [126] K. A. McCulloh, J. S. Sperry, et F. R. Adler, « Water transport in plants obeys Murray's law », vol. 421, p. 4, 2003.
- [127] Zimmerman, « Mechanisms of long-distance water transport in plants: a re-examination of some paradigms in the light of new evidence », *Philos. Trans. R. Soc. Lond. B. Biol. Sci.*, vol. 341, n° 1295, p. 19-31, juill. 1993, doi: 10.1098/rstb.1993.0087.
- [128] J. Dumais et Y. Forterre, « "Vegetable Dynamics": The Role of Water in Plant Movements », *Annu. Rev. Fluid Mech.*, vol. 44, n° 1, p. 453-478, janv. 2012, doi: 10.1146/annurev-fluid-120710-101200.
- [129] T. Ohyama *et al.*, « Amino Acid Metabolism and Transport in Soybean Plants », in *Amino Acid - New Insights and Roles in Plant and Animal*, T. Asao et Md. Asaduzzaman, Éd., InTech, 2017. doi: 10.5772/intechopen.68992.
- [130] C. M. Willmer et L. N. Beattie, « Cellular osmotic phenomena during stomatal movements of *Commelina communis*: I. Limitations of the incipient plasmolysis technique for determining osmotic pressures », *Protoplasma*, vol. 95, n° 4, p. 321-332, déc. 1978, doi: 10.1007/BF01291408.
- [131] P. J. Franks et G. D. Farquhar, « The Mechanical Diversity of Stomata and Its Significance in Gas-Exchange Control », *Plant Physiol.*, vol. 143, n° 1, p. 78-87, janv. 2007, doi: 10.1104/pp.106.089367.
- [132] J. M. Skotheim, « Physical Limits and Design Principles for Plant and Fungal Movements », *Science*, vol. 308, n° 5726, p. 1308-1310, mai 2005, doi: 10.1126/science.1107976.
- [133] S. Poppinga, T. Masselter, et T. Speck, « Faster than their prey: New insights into the rapid movements of active carnivorous plants traps: Review essay », *BioEssays*, vol. 35, n° 7, p. 649-657, juill. 2013, doi: 10.1002/bies.201200175.
- [134] Y. Forterre, J. M. Skotheim, J. Dumais, et L. Mahadevan, « How the Venus flytrap snaps », *Nature*, vol. 433, n° 7024, p. 421-425, janv. 2005, doi: 10.1038/nature03185.
- [135] G. Durak, R. Thierer, R. Sachse, B. Manfred, S. Thomas, et P. Simon, « Smooth or with a Snap Biomechanics of Trap Reopening in the Venus Flytrap », *Adv. Sci.*, p. 8, 2022.
- [136] F. Esser *et al.*, « Adaptive Biomimetic Actuator Systems Reacting to Various Stimuli by and Combining Two Biological Snap-Trap Mechanics », in *Biomimetic and Biohybrid Systems*, U. Martinez-Hernandez, V. Vouloutsis, A. Mura, M. Mangan, M. Asada, T. J. Prescott, et P. F. M. J. Verschure, Éd., in *Lecture Notes in Computer Science*, vol. 11556. Cham: Springer International Publishing, 2019, p. 114-121. doi: 10.1007/978-3-030-24741-6\_10.
- [137] X. Noblin, N. O. Rojas, J. Westbrook, C. Llorens, M. Argentina, et J. Dumais, « The Fern Sporangium: A Unique Catapult », *Science*, vol. 335, n° 6074, p. 1322-1322, mars 2012, doi: 10.1126/science.1215985.
- [138] J. Edwards, D. Whitaker, S. Klionsky, et M. J. Laskowski, « A record-breaking pollen catapult », *Nature*, vol. 435, n° 7039, p. 164-164, mai 2005, doi: 10.1038/435164a.
- [139] C. Pandolfi et D. Izzo, « Biomimetics on seed dispersal: survey and insights for space exploration », *Bioinspir. Biomim.*, vol. 8, n° 2, p. 025003, mai 2013, doi: 10.1088/1748-3182/8/2/025003.
- [140] Y. Abraham et R. Elbaum, « Hygroscopic movements in Geraniaceae: the structural variations that are responsible for coiling or bending », *New Phytol.*, vol. 199, n° 2, p. 584-594, juill. 2013, doi: 10.1111/nph.12254.
- [141] D. Evangelista, S. Hotton, et J. Dumais, « The mechanics of explosive dispersal and self-burial in the seeds of the filaree, *Erodium cicutarium* (Geraniaceae) », *J. Exp. Biol.*, vol. 214, n° 4, p. 521-529, févr. 2011, doi: 10.1242/jeb.050567.
- [142] W. Jung, W. Kim, et H.-Y. Kim, « Self-burial Mechanics of Hygroscopically Responsive Awns », *Integr. Comp. Biol.*, vol. 54, n° 6, p. 1034-1042, déc. 2014, doi: 10.1093/icb/icu026.
- [143] C. Llorens, M. Argentina, N. Rojas, J. Westbrook, J. Dumais, et X. Noblin, « The fern cavitation catapult: mechanism and design principles », *J. R. Soc. Interface*, vol. 13, n° 114, p. 20150930, janv. 2016, doi: 10.1098/rsif.2015.0930.

- [144] H. Bae et J. Kim, « Functional Principles of Morphological and Anatomical Structures in Pinecones », *Plants*, vol. 9, n° 10, p. 1343, oct. 2020, doi: 10.3390/plants9101343.
- [145] C. Dawson, J. F. V. Vincent, et A.-M. Rocca, « How pine cones open », *Nature*, vol. 390, n° 6661, p. 668-668, déc. 1997, doi: 10.1038/37745.
- [146] C. J. Eger *et al.*, « The Structural and Mechanical Basis for Passive-Hydraulic Pine Cone Actuation », *Adv. Sci.*, vol. 9, n° 20, p. 2200458, 2022, doi: 10.1002/advs.202200458.
- [147] W. M. Harlow, W. A. Côté, et A. C. Day, « The Opening Mechanism of Pine Cone Scales », *J. For.*, vol. 62, n° 8, p. 538-540, août 1964, doi: 10.1093/jof/62.8.538.
- [148] F. Zhang *et al.*, « Unperceivable motion mimicking hygroscopic geometric reshaping of pine cones », *Nat. Mater.*, nov. 2022, doi: 10.1038/s41563-022-01391-2.
- [149] V. Gager, A. Le Duigou, A. Bourmaud, F. Pierre, K. Behlouli, et C. Baley, « Understanding the effect of moisture variation on the hygromechanical properties of porosity-controlled nonwoven biocomposites », *Polym. Test.*, vol. 78, p. 105944, sept. 2019, doi: 10.1016/j.polymertesting.2019.105944.
- [150] « Voids in fiber-reinforced polymer composites: A review on their formation, characteristics, and effects on mechanical performance ». <https://journals.sagepub.com/doi/epub/10.1177/0021998318772152> (consulté le 12 octobre 2022).
- [151] H. Quan, A. Piroso, W. Yang, R. O. Ritchie, et M. A. Meyers, « Hydration-induced reversible deformation of the pine cone », *Acta Biomater.*, vol. 128, p. 370-383, juill. 2021, doi: 10.1016/j.actbio.2021.04.049.
- [152] A. L. Duigou, J. Beaugrand, et M. Castro, « Compréhension des mécanismes d'actionneur des pommes de pin pour améliorer les performances des biocomposites hygromorphes », p. 11, 2017.
- [153] S. Lin, Y. M. Xie, Q. Li, X. Huang, et S. Zhou, « On the shape transformation of cone scales », *Soft Matter*, vol. 12, n° 48, p. 9797-9802, 2016, doi: 10.1039/C6SM01805J.
- [154] D. Correa *et al.*, « 4D pine scale: biomimetic 4D printed autonomous scale and flap structures capable of multi-phase movement », *Philos. Trans. R. Soc. Math. Phys. Eng. Sci.*, vol. 378, n° 2167, p. 20190445, mars 2020, doi: 10.1098/rsta.2019.0445.
- [155] T. Cheng, Y. Tahouni, D. Wood, B. Stolz, R. Mülhaupt, et A. Menges, « Multifunctional Mesostructures: Design and Material Programming for 4D-printing », in *Symposium on Computational Fabrication*, Virtual Event USA: ACM, nov. 2020, p. 1-10. doi: 10.1145/3424630.3425418.
- [156] Y. Tahouni *et al.*, « Self-shaping Curved Folding:: A 4D-printing method for fabrication of self-folding curved crease structures », in *Symposium on Computational Fabrication*, Virtual Event USA: ACM, nov. 2020, p. 1-11. doi: 10.1145/3424630.3425416.
- [157] E. Vazquez et B. Gursoy, « 3D Printed Responsive Wood Interfaces: Shape-Changing Origami-Inspired Prototypes », in *Blucher Design Proceedings*, Medellín, Colombia: Editora Blucher, déc. 2020, p. 600-607. doi: 10.5151/sigradi2020-83.
- [158] E. Vazquez, B. Gürsoy, et J. P. Duarte, « Formalizing shape-change: Three-dimensional printed shapes and hygroscopic material transformations », *Int. J. Archit. Comput.*, vol. 18, n° 1, p. 67-83, mars 2020, doi: 10.1177/1478077119895216.
- [159] C. de Kergariou, F. Demoly, A. Perriman, A. L. Duigou, et F. Scarpa, « The design of 4D printed hygromorphs: state-of-the-art and future challenges. », p. 114.
- [160] W. Y. Liao, W. D. Z. Li, et Y. Zhang, « Sulfur and oxygen dual vacancies manipulation on 2D NiS<sub>2</sub>/CeO<sub>2</sub> hybrid heterostructure to boost overall water splitting activity », *Mater. Today Chem.*, vol. 24, p. 100791, juin 2022, doi: 10.1016/j.mtchem.2022.100791.
- [161] D. You *et al.*, « 4D Printing of Multi-Responsive Membrane for Accelerated In Vivo Bone Healing Via Remote Regulation of Stem Cell Fate », *Adv. Funct. Mater.*, vol. 31, n° 40, p. 2103920, oct. 2021, doi: 10.1002/adfm.202103920.

- [162] R. Guseinov, C. McMahan, J. Pérez, C. Daraio, et B. Bickel, « Programming temporal morphing of self-actuated shells », *Nat. Commun.*, vol. 11, n° 1, p. 237, déc. 2020, doi: 10.1038/s41467-019-14015-2.
- [163] G. Stoychev, S. Turcaud, J. W. C. Dunlop, et L. Ionov, « Hierarchical Multi-Step Folding of Polymer Bilayers », *Adv. Funct. Mater.*, vol. 23, n° 18, p. 2295-2300, mai 2013, doi: 10.1002/adfm.201203245.
- [164] Y. Tahouni *et al.*, « Programming sequential motion steps in 4D-printed hygromorphs by architected mesostructure and differential hygro-responsiveness », *Bioinspir. Biomim.*, vol. 16, n° 5, p. 055002, sept. 2021, doi: 10.1088/1748-3190/ac0c8e.
- [165] L. Ren *et al.*, « 4D Printing Dual Stimuli-Responsive Bilayer Structure Toward Multiple Shape-Shifting », *Front. Mater.*, vol. 8, p. 655160, mai 2021, doi: 10.3389/fmats.2021.655160.
- [166] C. Yuan, F. Wang, et Q. Ge, « Multimaterial direct 4D printing of high stiffness structures with large bending curvature », *Extreme Mech. Lett.*, vol. 42, p. 101122, janv. 2021, doi: 10.1016/j.eml.2020.101122.
- [167] A. K. Bastola, N. Rodriguez, M. Behl, P. Soffiatti, N. P. Rowe, et A. Lendlein, « Cactus-inspired design principles for soft robotics based on 3D printed hydrogel-elastomer systems », *Mater. Des.*, vol. 202, p. 109515, avr. 2021, doi: 10.1016/j.matdes.2021.109515.
- [168] L. Born *et al.*, « Fiber-Reinforced Plastics with Locally Adapted Stiffness for Bio-Inspired Hingeless, Deployable Architectural Systems », *Key Eng. Mater.*, vol. 742, p. 689-696, juill. 2017, doi: 10.4028/www.scientific.net/KEM.742.689.
- [169] A. Körner *et al.*, « Flectofold—a biomimetic compliant shading device for complex free form facades », *Smart Mater. Struct.*, vol. 27, n° 1, p. 017001, janv. 2018, doi: 10.1088/1361-665X/aa9c2f.
- [170] Z. Xin, Y. Duan, W. Xu, T. Zhang, et B. Wang, « Review of the mechanical performance of variable stiffness design fiber-reinforced composites », *Sci. Eng. Compos. Mater.*, vol. 25, n° 3, p. 425-437, avr. 2018, doi: 10.1515/secm-2016-0093.
- [171] T. van Manen et A. A. Zadpoor, « Theoretical stiffness limits of 4D printed self-folding metamaterials », p. 24.
- [172] J. W. Boley *et al.*, « Shape-shifting structured lattices via multimaterial 4D printing », *Proc. Natl. Acad. Sci.*, vol. 116, n° 42, p. 20856-20862, oct. 2019, doi: 10.1073/pnas.1908806116.
- [173] M. Keshavarzan, M. Kadkhodaei, et F. Forooghi, « An investigation into compressive responses of shape memory polymeric cellular lattice structures fabricated by vat polymerization additive manufacturing », *Polym. Test.*, vol. 91, p. 106832, nov. 2020, doi: 10.1016/j.polymertesting.2020.106832.
- [174] L. Guiducci *et al.*, « Honeycomb Actuators Inspired by the Unfolding of Ice Plant Seed Capsules », *PLOS ONE*, vol. 11, n° 11, p. e0163506, nov. 2016, doi: 10.1371/journal.pone.0163506.
- [175] P. Grönquist, P. Panchadcharam, D. Wood, A. Menges, M. Rüggeberg, et F. K. Wittel, « Computational analysis of hygromorphic self-shaping wood gridshell structures », *R. Soc. Open Sci.*, vol. 7, n° 7, p. 192210, juill. 2020, doi: 10.1098/rsos.192210.
- [176] Y. Wang *et al.*, « Stimuli-responsive composite biopolymer actuators with selective spatial deformation behavior », *Proc. Natl. Acad. Sci.*, vol. 117, n° 25, p. 14602-14608, juin 2020, doi: 10.1073/pnas.2002996117.
- [177] H. Jiang, Z. Zhang, et Y. Chen, « 3D printed tubular lattice metamaterials with engineered mechanical performance », *Appl. Phys. Lett.*, vol. 117, n° 1, p. 011906, juill. 2020, doi: 10.1063/5.0014932.
- [178] A. Armillotta et R. Pelzer, « Modeling of porous structures for rapid prototyping of tissue engineering scaffolds », *Int. J. Adv. Manuf. Technol.*, vol. 39, n° 5-6, p. 501-511, nov. 2008, doi: 10.1007/s00170-007-1247-x.
- [179] V. Vouloutsi, A. Mura, F. Tauber, T. Speck, T. J. Prescott, et P. F. M. J. Verschure, Éd., *Biomimetic and Biohybrid Systems: 9th International Conference, Living Machines 2020*,



- Freiburg, Germany, July 28–30, 2020, *Proceedings*, vol. 12413. in Lecture Notes in Computer Science, vol. 12413. Cham: Springer International Publishing, 2020. doi: 10.1007/978-3-030-64313-3.
- [180] M. F. Ashby et R. F. M. Medalist, « The mechanical properties of cellular solids », *Metall. Trans. A*, vol. 14, n° 9, p. 1755-1769, sept. 1983, doi: 10.1007/BF02645546.
- [181] A. Li, « 4D Printing of Recyclable Lightweight Architectures Using High Recovery Stress Shape Memory Polymer », p. 13.
- [182] O. Elnagar, « Gridshell structures in laminated bamboo », 2017, doi: 10.13140/RG.2.2.14388.55688.
- [183] F. Tayeb, B. Lefevre, O. Baverel, J.-F. Caron, et L. D. Peloux, « Design and Realisation of Composite Gridshell Structures », p. 11.
- [184] GIEC 2020, « The Importance of the Ocean and Cryosphere for People ».
- [185] L. Boström-Einarsson *et al.*, « Coral restoration – A systematic review of current methods, successes, failures and future directions », *PLOS ONE*, vol. 15, n° 1, p. e0226631, janv. 2020, doi: 10.1371/journal.pone.0226631.
- [186] J.-M. Thierry, « Artificial reefs in Japan - A general outline », in *Aquacultur engineering*, 1988.
- [187] J. S. Lima, I. R. Zalmon, et M. Love, « Overview and trends of ecological and socioeconomic research on artificial reefs », *Mar. Environ. Res.*, vol. 145, p. 81-96, mars 2019, doi: 10.1016/j.marenvres.2019.01.010.
- [188] S. Abarzua et S. Jakubowski, « Biotechnological investigation for the prevention of biofouling. I. Biological and biochemical principles for the prevention of biofouling », *Mar. Ecol. Prog. Ser.*, vol. 123, p. 301-312, 1995, doi: 10.3354/meps123301.
- [189] R. D. Monds et G. A. O'Toole, « The developmental model of microbial biofilms: ten years of a paradigm up for review », *Trends Microbiol.*, vol. 17, n° 2, p. 73-87, févr. 2009, doi: 10.1016/j.tim.2008.11.001.
- [190] P.-Y. Qian, S. C. K. Lau, H.-U. Dahms, S. Dobretsov, et T. Harder, « Marine Biofilms as Mediators of Colonization by Marine Macroorganisms: Implications for Antifouling and Aquaculture », *Mar. Biotechnol.*, vol. 9, n° 4, p. 399-410, sept. 2007, doi: 10.1007/s10126-007-9001-9.
- [191] H. Dang et C. R. Lovell, « Bacterial Primary Colonization and Early Succession on Surfaces in Marine Waters as Determined by Amplified rRNA Gene Restriction Analysis and Sequence Analysis of 16S rRNA Genes », *Appl. Environ. Microbiol.*, vol. 66, n° 2, p. 467-475, févr. 2000, doi: 10.1128/AEM.66.2.467-475.2000.
- [192] Q. Xie, J. Pan, C. Ma, et G. Zhang, « Dynamic surface antifouling: mechanism and systems », *Soft Matter*, vol. 15, n° 6, p. 1087-1107, févr. 2019, doi: 10.1039/C8SM01853G.
- [193] J. Nauta *et al.*, « Biodegradable artificial reefs enhance food web complexity and biodiversity in an intertidal soft-sediment ecosystem », *J. Appl. Ecol.*, vol. 60, n° 3, p. 541-552, mars 2023, doi: 10.1111/1365-2664.14348.
- [194] R. L. Sherman et R. E. Spieler, « Tires: unstable materials for artificial reef construction », in *Environmental Problems in Coastal Regions VI*, Rhodes, Greece: WIT Press, mai 2006, p. 215-223. doi: 10.2495/CENV060211.
- [195] K. Collins, « Environmental impact assessment of a scrap tyre artificial reef », *ICES J. Mar. Sci.*, vol. 59, p. S243-S249, oct. 2002, doi: 10.1006/jmsc.2002.1297.
- [196] S. J. Walker et T. A. Schlacher, « Limited habitat and conservation value of a young artificial reef », *Biodivers. Conserv.*, vol. 23, n° 2, p. 433-447, févr. 2014, doi: 10.1007/s10531-013-0611-4.
- [197] A. Abelson, « Comparison of the development of coral and fish communities on rock-aggregated artificial reefs in Eilat, Red Sea », *ICES J. Mar. Sci.*, vol. 59, p. S122-S126, oct. 2002, doi: 10.1006/jmsc.2002.1210.
- [198] O. Ly *et al.*, « Optimisation of 3D printed concrete for artificial reefs: Biofouling and mechanical analysis », *Constr. Build. Mater.*, vol. 272, p. 121649, févr. 2021, doi: 10.1016/j.conbuildmat.2020.121649.

- [199] S. Clark et A. J. Edwards, « Use of Artificial Reef Structures to Rehabilitate Reef Flats Degraded by Coral Mining in the Maldives ».
- [200] L. Carral, J. Tarrío-Saavedra, J. J. Cartelle Barros, C. C. Fabal, A. Ramil, et C. Álvarez-Feal, « Considerations on the programmed functional life (one generation) of a green artificial reef in terms of the sustainability of the modified ecosystem », *Heliyon*, vol. 9, n° 4, p. e14978, avr. 2023, doi: 10.1016/j.heliyon.2023.e14978.
- [201] M. Eriksen *et al.*, « Plastic Pollution in the World's Oceans: More than 5 Trillion Plastic Pieces Weighing over 250,000 Tons Afloat at Sea », *PLoS ONE*, vol. 9, n° 12, p. e111913, déc. 2014, doi: 10.1371/journal.pone.0111913.
- [202] G. G. N. Thushari et J. D. M. Senevirathna, « Plastic pollution in the marine environment », *Heliyon*, vol. 6, n° 8, p. e04709, août 2020, doi: 10.1016/j.heliyon.2020.e04709.
- [203] R. C. P. Monteiro, J. A. Ivar do Sul, et M. F. Costa, « Plastic pollution in islands of the Atlantic Ocean », *Environ. Pollut.*, vol. 238, p. 103-110, juill. 2018, doi: 10.1016/j.envpol.2018.01.096.
- [204] S. Bejgarn, M. MacLeod, C. Bogdal, et M. Breitholtz, « Toxicity of leachate from weathering plastics: An exploratory screening study with *Nitocra spinipes* », *Chemosphere*, vol. 132, p. 114-119, août 2015, doi: 10.1016/j.chemosphere.2015.03.010.
- [205] M. Contardi *et al.*, « Marine Fouling Characteristics of Biocomposites in a Coral Reef Ecosystem », *Adv. Sustain. Syst.*, vol. 5, n° 9, p. 2100089, sept. 2021, doi: 10.1002/adsu.202100089.
- [206] G. Bishop, D. Styles, et P. N. L. Lens, « Environmental performance comparison of bioplastics and petrochemical plastics: A review of life cycle assessment (LCA) methodological decisions », *Resour. Conserv. Recycl.*, vol. 168, p. 105451, mai 2021, doi: 10.1016/j.resconrec.2021.105451.
- [207] C. Venâncio, I. Lopes, et M. Oliveira, « Bioplastics: known effects and potential consequences to marine and estuarine ecosystem services », *Chemosphere*, vol. 309, p. 136810, déc. 2022, doi: 10.1016/j.chemosphere.2022.136810.
- [208] T. Uribe-Echeverria, « Toxicity trend of biodegradable and non-biodegradable plastic leachates during microbial exposure in seawater », 2020.
- [209] C. Leonard *et al.*, « Performance of innovative materials as recruitment substrates for coral restoration », *Restor. Ecol.*, déc. 2021, doi: 10.1111/rec.13625.
- [210] V. Popineau, A. Céline, M. Le Gall, L. Martineau, C. Baley, et A. Le Duigou, « Vacuum-Bag-Only (VBO) Molding of Flax Fiber-reinforced Thermoplastic Composites for Naval Shipyards », *Appl. Compos. Mater.*, vol. 28, n° 3, p. 791-808, juin 2021, doi: 10.1007/s10443-021-09890-2.
- [211] A. Le Duigou, A. Bourmaud, et C. Baley, « In-situ evaluation of flax fibre degradation during water ageing », *Ind. Crops Prod.*, vol. 70, p. 204-210, août 2015, doi: 10.1016/j.indcrop.2015.03.049.
- [212] P. Mehta et H. Haynes, « Durability of Concrete in Seawater », 1975, doi: <https://doi.org/10.1061/JSDEAG.0004131>.
- [213] A. Nakayama, N. Yamano, et N. Kawasaki, « Biodegradation in seawater of aliphatic polyesters », *Polym. Degrad. Stab.*, vol. 166, p. 290-299, août 2019, doi: 10.1016/j.polymdegradstab.2019.06.006.
- [214] M. Deroïn *et al.*, « Accelerated ageing of polylactide in aqueous environments: Comparative study between distilled water and seawater », *Polym. Degrad. Stab.*, vol. 108, p. 319-329, oct. 2014, doi: 10.1016/j.polymdegradstab.2014.01.020.
- [215] G. Wang, D. Huang, J. Ji, C. Völker, et F. R. Wurm, « Seawater-Degradable Polymers—Fighting the Marine Plastic Pollution », *Adv. Sci.*, vol. 8, n° 1, p. 2001121, janv. 2021, doi: 10.1002/advs.202001121.
- [216] V. Popineau, « Biocomposites renforcés par des fibres végétales : hautes performances mécaniques et durabilité en environnement maritime », 2021.
- [217] C. Morvan, C. Andème-Onzighi, R. Girault, D. S. Himmelsbach, A. Driouich, et D. E. Akin, « Building flax fibres: more than one brick in the walls », *Plant Physiol. Biochem.*, vol. 41, n° 11-12, p. 935-944, nov. 2003, doi: 10.1016/j.plaphy.2003.07.001.

- [218] J. Ramos *et al.*, « An artificial reef at the edge of the deep: An interdisciplinary case study », *Ocean Coast. Manag.*, vol. 210, p. 105729, sept. 2021, doi: 10.1016/j.ocecoaman.2021.105729.
- [219] G. Suzuki, « Narrower grid structure of artificial reef enhances initial survival of in situ settled coral », *Mar. Pollut. Bull.*, p. 10, 2011.
- [220] E. J. Ruhl et D. L. Dixon, « 3D printed objects do not impact the behavior of a coral-associated damselfish or survival of a settling stony coral », *PLOS ONE*, vol. 14, n° 8, p. e0221157, août 2019, doi: 10.1371/journal.pone.0221157.
- [221] A. I. Yoris-Nobile *et al.*, « Artificial reefs built by 3D printing: Systematisation in the design, material selection and fabrication », *Constr. Build. Mater.*, vol. 362, p. 129766, janv. 2023, doi: 10.1016/j.conbuildmat.2022.129766.
- [222] O. Berman *et al.*, « Design and application of a novel 3D printing method for bio-inspired artificial reefs », *Ecol. Eng.*, vol. 188, p. 106892, mars 2023, doi: 10.1016/j.ecoleng.2023.106892.
- [223] J. S. Mohammed, « Applications of 3D printing technologies in oceanography », *Methods Oceanogr.*, vol. 17, p. 97-117, déc. 2016, doi: 10.1016/j.mio.2016.08.001.
- [224] A. Gleadall, « FullControl GCode Designer: Open-source software for unconstrained design in additive manufacturing », *Addit. Manuf.*, vol. 46, p. 102109, oct. 2021, doi: 10.1016/j.addma.2021.102109.
- [225] A. Le Duigou, T. Fruleux, R. Matsuzaki, G. Chabaud, M. Ueda, et M. Castro, « 4D printing of continuous flax-fibre based shape-changing hygromorph biocomposites: Towards sustainable metamaterials », *Mater. Des.*, vol. 211, p. 110158, déc. 2021, doi: 10.1016/j.matdes.2021.110158.
- [226] A. Célineo, S. Fréour, F. Jacquemin, et P. Casari, « Characterization and modeling of the moisture diffusion behavior of natural fibers », *J. Appl. Polym. Sci.*, vol. 130, n° 1, p. 297-306, oct. 2013, doi: 10.1002/app.39148.
- [227] A. Kaboorani, « Characterizing water sorption and diffusion properties of wood/plastic composites as a function of formulation design », *Constr. Build. Mater.*, vol. 136, p. 164-172, avr. 2017, doi: 10.1016/j.conbuildmat.2016.12.120.
- [228] D. U. Shah, « Damage in biocomposites: Stiffness evolution of aligned plant fibre composites during monotonic and cyclic fatigue loading », *Compos. Part Appl. Sci. Manuf.*, vol. 83, p. 160-168, avr. 2016, doi: 10.1016/j.compositesa.2015.09.008.
- [229] N. Sweygers *et al.*, « Prediction of the equilibrium moisture content based on the chemical composition and crystallinity of natural fibres », *Ind. Crops Prod.*, vol. 186, p. 115187, oct. 2022, doi: 10.1016/j.indcrop.2022.115187.
- [230] I. A. Reis, P. I. Cunha Claro, A. L. Marcomini, L. H. Capparelli Mattoso, S. P. Silva, et A. R. Sena Neto, « Annealing and crystallization kinetics of poly(lactic acid) pieces obtained by additive manufacturing », *Polym. Eng. Sci.*, vol. 61, n° 7, p. 2097-2104, juill. 2021, doi: 10.1002/pen.25737.
- [231] S. Krishnan, C. J. Weinman, et C. K. Ober, « Advances in polymers for anti-biofouling surfaces », *J. Mater. Chem.*, vol. 18, n° 29, p. 3405, 2008, doi: 10.1039/b801491d.
- [232] P. P. Parlevliet, H. E. N. Bersee, et A. Beukers, « Residual stresses in thermoplastic composites—A study of the literature—Part II: Experimental techniques », *Compos. Part Appl. Sci. Manuf.*, vol. 38, n° 3, p. 651-665, mars 2007, doi: 10.1016/j.compositesa.2006.07.002.
- [233] D. Pantaloni, D. Shah, C. Baley, et A. Bourmaud, « Monitoring of mechanical performances of flax non-woven biocomposites during a home compost degradation », *Polym. Degrad. Stab.*, vol. 177, p. 109166, juill. 2020, doi: 10.1016/j.polymdegradstab.2020.109166.
- [234] B. Grasland *et al.*, « Bacterial Biofilm in Seawater: Cell Surface Properties of Early-attached Marine Bacteria », *Biofouling*, vol. 19, n° 5, p. 307-313, oct. 2003, doi: 10.1080/0892701031000121041.

- [235] A. Dheilly *et al.*, « Antibiofilm Activity of the Marine Bacterium *Pseudoalteromonas* sp. Strain 3J6 », *Appl. Environ. Microbiol.*, vol. 76, n° 11, p. 3452-3461, juin 2010, doi: 10.1128/AEM.02632-09.
- [236] F. Traon, K. Réhel, I. Linossier, et F. Faÿ, « Potential antifouling properties of copper loaded zeolites on fouling diatoms », *Microporous Mesoporous Mater.*, 2021, doi: <https://doi.org/10.1016/j.micromeso.2020.110734>.
- [237] J. L. Levy, J. L. Stauber, et D. F. Jolley, « Sensitivity of marine microalgae to copper: The effect of biotic factors on copper adsorption and toxicity », *Sci. Total Environ.*, vol. 387, n° 1-3, p. 141-154, nov. 2007, doi: 10.1016/j.scitotenv.2007.07.016.
- [238] C. Sivapathasekaran, P. Das, S. Mukherjee, J. Saravanakumar, M. Mandal, et R. Sen, « Marine Bacterium Derived Lipopeptides: Characterization and Cytotoxic Activity Against Cancer Cell Lines », *Int. J. Pept. Res. Ther.*, vol. 16, n° 4, p. 215-222, déc. 2010, doi: 10.1007/s10989-010-9212-1.
- [239] I. Ezzaraa, N. Ayrilmis, M. K. Kuzman, S. Belhouideg, et J. Bengourram, « Study of the effects of microstructure on the mechanical properties of 3D printed wood/PLA composite materials by a micromechanical approach », in *2020 IEEE 2nd International Conference on Electronics, Control, Optimization and Computer Science (ICECOCS)*, Kenitra, Morocco: IEEE, 2020, p. 1-5. doi: 10.1109/ICECOCS50124.2020.9314564.
- [240] A. Céline, O. Gonçalves, F. Jacquemin, et S. Fréour, « Qualitative and quantitative assessment of water sorption in natural fibres using ATR-FTIR spectroscopy », *Carbohydr. Polym.*, vol. 101, p. 163-170, janv. 2014, doi: 10.1016/j.carbpol.2013.09.023.
- [241] C. J. Kennedy, A. Šturcová, M. C. Jarvis, et T. J. Wess, « Hydration effects on spacing of primary-wall cellulose microfibrils: a small angle X-ray scattering study », *Cellulose*, vol. 14, n° 5, p. 401-408, août 2007, doi: 10.1007/s10570-007-9129-9.
- [242] B. Madsen, P. Hoffmeyer, et H. Lilholt, « Hemp yarn reinforced composites – III. Moisture content and dimensional changes », *Compos. Part Appl. Sci. Manuf.*, vol. 43, n° 11, p. 2151-2160, nov. 2012, doi: 10.1016/j.compositesa.2012.07.010.
- [243] M. Péron, A. Céline, M. Castro, F. Jacquemin, et A. Le Duigou, « Study of hygroscopic stresses in asymmetric biocomposite laminates », *Compos. Sci. Technol.*, vol. 169, p. 7-15, janv. 2019, doi: 10.1016/j.compscitech.2018.10.027.
- [244] C. de Kergariou *et al.*, « Measure of porosity in flax fibres reinforced polylactic acid biocomposites », *Compos. Part Appl. Sci. Manuf.*, vol. 141, p. 106183, févr. 2021, doi: 10.1016/j.compositesa.2020.106183.
- [245] C. A. S. Hill, A. Norton, et G. Newman, « The water vapor sorption behavior of natural fibers », *J. Appl. Polym. Sci.*, vol. 112, n° 3, p. 1524-1537, mai 2009, doi: 10.1002/app.29725.
- [246] S. Alix, L. Lebrun, C. Morvan, et S. Marais, « Study of water behaviour of chemically treated flax fibres-based composites: A way to approach the hydric interface », *Compos. Sci. Technol.*, vol. 71, n° 6, p. 893-899, avr. 2011, doi: 10.1016/j.compscitech.2011.02.004.
- [247] M. Péron, F. Jacquemin, P. Casari, G. Orange, J.-L. Bailleul, et N. Boyard, « Thermo-mechanical characterization of a thermoplastic composite and prediction of the residual stresses and lamina curvature during cooling », présenté à PROCEEDINGS OF THE INTERNATIONAL CONFERENCE OF GLOBAL NETWORK FOR INNOVATIVE TECHNOLOGY AND AWAM INTERNATIONAL CONFERENCE IN CIVIL ENGINEERING (IGNITE-AICCE'17): Sustainable Technology And Practice For Infrastructure and Community Resilience, Penang, Malaysia, 2017, p. 030015. doi: 10.1063/1.5008002.
- [248] M. F. Pucci, P.-J. Liotier, D. Seveno, C. Fuentes, A. Van Vuure, et S. Drapier, « Wetting and swelling property modifications of elementary flax fibres and their effects on the Liquid Composite Molding process », *Compos. Part Appl. Sci. Manuf.*, vol. 97, p. 31-40, juin 2017, doi: 10.1016/j.compositesa.2017.02.028.

- [249] A. Rafsanjani, M. Stiefel, K. Jefimovs, R. Mokso, D. Derome, et J. Carmeliet, « Hygroscopic swelling and shrinkage of latewood cell wall micropillars reveal ultrastructural anisotropy », p. 10.
- [250] G. Chabaud, M. Castro, C. Denoual, et A. Le Duigou, « Hygromechanical properties of 3D printed continuous carbon and glass fibre reinforced polyamide composite for outdoor structural applications », *Addit. Manuf.*, vol. 26, p. 94-105, mars 2019, doi: 10.1016/j.addma.2019.01.005.
- [251] PP. Parlevliet, HEN. Bersee, et A. Beukers, « Residual stresses in thermoplastic composites—A study of the literature—Part II: Experimental techniques », *Comp Part Appl. Sci. Manuf.*, vol. 38, n° 3, p. 651-655, 2007.
- [252] I. Straumit, D. Vandepitte, M. Wevers, et S. V. Lomov, « Identification of the flax fibre modulus based on an impregnated quasi-unidirectional fibre bundle test and X-ray computed tomography », *Compos. Sci. Technol.*, vol. 151, p. 124-130, oct. 2017, doi: 10.1016/j.compscitech.2017.07.029.
- [253] C. Baley, « Analysis of the flax fibres tensile behaviour and analysis of the tensile stiffness increase », *Compos. Part Appl. Sci. Manuf.*, vol. 33, n° 7, p. 939-948, juill. 2002, doi: 10.1016/S1359-835X(02)00040-4.
- [254] S. Lin, YM. Xie, Q. Lib, X. Huang, et SH. Zhoua, « On the shape transformation of cone scales », *Soft Matter*, vol. 12, p. 9797-9802, 2016.
- [255] D. Correa *et al.*, « 4D Pine Scale: Biomimetic 4D Printed Autonomous Scale and Flap Structures Capable of Multi-Phase Movement », *Philos. Transact. A Math. Phys. Eng. Sci.*, vol. 378, n° 2167, p. 20190445, 2020, doi: 10.1098/rsta.2019.0445.
- [256] D. Lunni, M. Cianchetti, C. Filippeschi, E. Sinibaldi, et B. Mazzolai, « Plant-Inspired Soft Bistable Structures Based on Hygroscopic Electrospun Nanofibers », *Adv. Mater. Interfaces*, vol. 7, n° 4, p. 1901310, févr. 2020, doi: 10.1002/admi.201901310.
- [257] N. D. K. Tran et D.-A. Wang, « Design of a crab-like bistable mechanism for nearly equal switching forces in forward and backward directions », *Mech. Mach. Theory*, vol. 115, p. 114-129, sept. 2017, doi: 10.1016/j.mechmachtheory.2017.05.005.
- [258] S. Poppinga *et al.*, « Hygroscopic motions of fossil conifer cones », *Sci. Rep.*, vol. 7, n° 1, p. 40302, févr. 2017, doi: 10.1038/srep40302.
- [259] A. Sydney Gladman, E. A. Matsumoto, R. G. Nuzzo, L. Mahadevan, et J. A. Lewis, « Biomimetic 4D printing », *Nat. Mater.*, vol. 15, n° 4, p. 413-418, avr. 2016, doi: 10.1038/nmat4544.
- [260] M. Gigliotti, M. R. Wisnom, et K. D. Potter, « Loss of bifurcation and multiple shapes of thin [0/90] unsymmetric composite plates subject to thermal stress », *Compos. Sci. Technol.*, vol. 64, n° 1, p. 109-128, janv. 2004, doi: 10.1016/S0266-3538(03)00213-6.
- [261] T. Chen, O. R. Bilal, K. Shea, et C. Daraio, « Harnessing bistability for directional propulsion of soft, untethered robots », *Proc. Natl. Acad. Sci.*, vol. 115, n° 22, p. 5698-5702, mai 2018, doi: 10.1073/pnas.1800386115.
- [262] Y. Huang, J. Zhao, et S. Liu, « Design optimization of segment-reinforced bistable mechanisms exhibiting adjustable snapping behavior », *Sens. Actuators Phys.*, vol. 252, p. 7-15, déc. 2016, doi: 10.1016/j.sna.2016.10.014.
- [263] J. Etches, K. Potter, P. Weaver, et I. Bond, « Environmental effects on thermally induced multistability in unsymmetric composite laminates », *Compos. Part Appl. Sci. Manuf.*, vol. 40, n° 8, p. 1240-1247, août 2009, doi: 10.1016/j.compositesa.2009.05.018.
- [264] T. U. Rehman, Z. Qaiser, et S. Johnson, « Tuning bifurcation loads in bistable composites with tunable stiffness mechanisms », *Mech. Mach. Theory*, vol. 142, p. 103585, déc. 2019, doi: 10.1016/j.mechmachtheory.2019.103585.
- [265] M.-L. Dano et M. W. Hyer, « Snap-through of unsymmetric fiber-reinforced composite laminates », *Int. J. Solids Struct.*, p. 24, 2022.
- [266] M. Schlecht, K. Schulte, et M. W. Hyer, « A comparative study for the calculation of the temperature dependent shapes of unsymmetric laminates based on finite element analysis

- and extended classical lamination theory », *Mech. Compos. Mater.*, vol. 31, n° 3, p. 247-254, 1995, doi: 10.1007/BF00615638.
- [267] M. A. Cantera, J. M. Romera, I. Adarraga, et F. Mujika, « Modelling and testing of the snap-through process of bi-stable cross-ply composites », *Compos. Struct.*, vol. 120, p. 41-52, févr. 2015, doi: 10.1016/j.compstruct.2014.09.064.
- [268] M.-L. Dano et J.-P. Bourque, « Deformation behaviour of paper and board subjected to moisture diffusion », *Int. J. Solids Struct.*, vol. 46, n° 6, p. 1305-1316, mars 2009, doi: 10.1016/j.ijsolstr.2008.10.035.
- [269] J. Qiu, J. H. Lang, et A. H. Slocum, « A Curved-Beam Bistable Mechanism », *J. Microelectromechanical Syst.*, vol. 13, n° 2, p. 137-146, avr. 2004, doi: 10.1109/JMEMS.2004.825308.
- [270] A. Pirrera, D. Avitabile, et P. M. Weaver, « Bistable plates for morphing structures: A refined analytical approach with high-order polynomials », *Int. J. Solids Struct.*, vol. 47, n° 25-26, p. 3412-3425, déc. 2010, doi: 10.1016/j.ijsolstr.2010.08.019.
- [271] Z. Yuan *et al.*, « A model on the curved shapes of unsymmetric laminates including tool-part interaction », *Sci. Eng. Compos. Mater.*, vol. 25, n° 1, p. 1-8, janv. 2018, doi: 10.1515/secm-2015-0215.
- [272] D. Borowska-Wykre, R. Wrzalik, et D. Kwiatkowska, « Gradient of structural traits drives hygroscopic movements of scarious bracts surrounding *Helichrysum bracteatum capitulum* », p. 19.
- [273] A. Le Duigou, J. Beaugrand, et M. Castro, « Compréhension des mécanismes d'actionnement des pommes de pin pour améliorer les performances des biocomposites hygromorphes », *Comptes Rendus JNC 20*, 2017.
- [274] S. K. Gülsoy, H. Hafizoğlu, A. Kılıç Pekgözlü, İ. Tümen, İ. E. Dönmez, et H. Sivrikaya, « Fiber properties of axis and scale of eleven different coniferous cones », *Ind. Crops Prod.*, vol. 109, p. 45-52, déc. 2017, doi: 10.1016/j.indcrop.2017.07.044.
- [275] Q. Li, A. Le Duigou, V. Kumar Thakur, L. Liu, J. Leng, et F. Scarpa, « Three-dimensional water diffusion and modelling of flax/shape memory epoxy composites », *Compos. Part Appl. Sci. Manuf.*, vol. 171, p. 107574, août 2023, doi: 10.1016/j.compositesa.2023.107574.
- [276] C. A. S. Hill, A. Norton, et G. Newman, « The water vapor sorption behavior of natural fibers », *J. Appl. Polym. Sci.*, vol. 112, n° 3, p. 1524-1537, mai 2009, doi: 10.1002/app.29725.
- [277] K. Strømdahl, « Water Sorption in Wood and Plant Fibres », p. 153.
- [278] W. M. van Rees, E. A. Matsumoto, A. S. Gladman, J. A. Lewis, et L. Mahadevan, « Mechanics of biomimetic 4D printed structures », *Soft Matter*, vol. 14, n° 43, p. 8771-8779, 2018, doi: 10.1039/C8SM00990B.
- [279] T. Fruleux, M. Castro, P. Sauleau, R. Matsuzaki, et A. Le Duigou, « Matrix stiffness: a key parameter to control hydro-elasticity and morphing of 3D printed biocomposite », *Compos. Part Appl. Sci. Manuf.*, p. 106882, févr. 2022, doi: 10.1016/j.compositesa.2022.106882.
- [280] S. Wolff, T. Lee, E. Faierson, K. Ehmann, et J. Cao, « Anisotropic properties of directed energy deposition (DED)-processed Ti-6Al-4V », *J. Manuf. Process.*, vol. 24, p. 397-405, oct. 2016, doi: 10.1016/j.jmapro.2016.06.020.
- [281] A. K. Sood, R. K. Ohdar, et S. S. Mahapatra, « Parametric appraisal of mechanical property of fused deposition modelling processed parts », *Mater. Des.*, vol. 31, n° 1, p. 287-295, janv. 2010, doi: 10.1016/j.matdes.2009.06.016.
- [282] S. Ahn, M. Montero, D. Odell, S. Roundy, et P. K. Wright, « Anisotropic material properties of fused deposition modeling ABS », *Rapid Prototyp. J.*, vol. 8, n° 4, p. 248-257, oct. 2002, doi: 10.1108/13552540210441166.
- [283] S. Poppinga *et al.*, « Toward a New Generation of Smart Biomimetic Actuators for Architecture », *Adv. Mater.*, vol. 30, n° 19, p. 1703653, mai 2018, doi: 10.1002/adma.201703653.

- [284] A. Mader, M. Langer, J. Knippers, et O. Speck, « Learning from plant movements triggered by bulliform cells: the biomimetic cellular actuator », *J. R. Soc. Interface*, vol. 17, n° 169, p. 20200358, août 2020, doi: 10.1098/rsif.2020.0358.
- [285] B. I. Oladapo, S. O. Ismail, A. V. Adebisi, F. T. Omigbodun, M. A. Olawumi, et D. B. Olawade, « Nanostructural interface and strength of polymer composite scaffolds applied to intervertebral bone », *Colloids Surf. Physicochem. Eng. Asp.*, vol. 627, p. 127190, oct. 2021, doi: 10.1016/j.colsurfa.2021.127190.
- [286] U. Morales, A. Esnaola, M. Iragi, L. Aretxabaleta, et J. Aurrekoetxea, « The effect of cross-section geometry on crushing behaviour of 3D printed continuous carbon fibre reinforced polyamide profiles », *Compos. Struct.*, vol. 274, p. 114337, oct. 2021, doi: 10.1016/j.compstruct.2021.114337.
- [287] M. Yamawaki et Y. Kouno, « Fabrication and mechanical characterization of continuous carbon fiber-reinforced thermoplastic using a preform by three-dimensional printing and via hot-press molding », *Adv. Compos. Mater.*, vol. 27, n° 2, p. 209-219, mars 2018, doi: 10.1080/09243046.2017.1368840.
- [288] R. Matsuzaki *et al.*, « Effects of Set Curvature and Fiber Bundle Size on the Printed Radius of Curvature by a Continuous Carbon Fiber Composite 3D Printer », *Addit. Manuf.*, vol. 24, p. 93-102, déc. 2018, doi: 10.1016/j.addma.2018.09.019.
- [289] H. L. Bos, « Tensile and compressive properties of flax fibres for natural fibre reinforced composites », p. 10.
- [290] H. Shiratori, A. Todoroki, M. Ueda, R. Matsuzaki, et Y. Hirano, « Mechanism of folding a fiber bundle in the curved section of 3D printed carbon fiber reinforced plastics », *Adv. Compos. Mater.*, vol. 29, n° 3, p. 247-257, mai 2020, doi: 10.1080/09243046.2019.1682794.
- [291] K. Hofstetter, B. Hinterstoisser, et L. Salmén, « Moisture uptake in native cellulose – the roles of different hydrogen bonds: a dynamic FT-IR study using Deuterium exchange », *Cellulose*, vol. 13, n° 2, p. 131-145, avr. 2006, doi: 10.1007/s10570-006-9055-2.
- [292] W. Simpson, « Sorption Theories Applied To Wood », *Wood Fiber Sci.*, p. 183-195, 1980.
- [293] Wang, Zhao, Fuh, et Lee, « Effect of Porosity on Mechanical Properties of 3D Printed Polymers: Experiments and Micromechanical Modeling Based on X-Ray Computed Tomography Analysis », *Polymers*, vol. 11, n° 7, p. 1154, juill. 2019, doi: 10.3390/polym11071154.
- [294] H. L. Tekinalp *et al.*, « Highly oriented carbon fiber–polymer composites via additive manufacturing », *Compos. Sci. Technol.*, vol. 105, p. 144-150, déc. 2014, doi: 10.1016/j.compscitech.2014.10.009.
- [295] U. Zimmermann, H. Schneider, L. H. Wegner, et A. Haase, « Water ascent in tall trees: does evolution of land plants rely on a highly metastable state? », *New Phytol.*, vol. 162, n° 3, p. 575-615, juin 2004, doi: 10.1111/j.1469-8137.2004.01083.x.
- [296] G. Bramhall, « The validity of Darcy's law in the axial penetration of wood », p. 14, 1971.
- [297] K. Krabbenhoft et L. Damkilde, « Double porosity models for the description of water infiltration in wood », *Wood Sci. Technol.*, vol. 38, n° 8, p. 641-659, déc. 2004, doi: 10.1007/s00226-004-0253-5.
- [298] J. Jurin, « II. An account of some experiments shown before the Royal Society; with an enquiry into the cause of the ascent and suspension of water in capillary tubes. », *Philos. Trans. R. Soc. Lond.*, vol. 30, n° 355, p. 739-747, avr. 1718, doi: 10.1098/rstl.1717.0026.
- [299] A. Le Duigou, M. Castro, R. Bevan, et N. Martin, « 3D printing of wood fibre biocomposites: From mechanical to actuation functionality », *Mater. Des.*, vol. 96, p. 106-114, avr. 2016, doi: 10.1016/j.matdes.2016.02.018.
- [300] D. Correa, « 4D-printed hygroscopic programmable material architectures », Institute for Computational Design and Construction, 2022.
- [301] V. Peña *et al.*, « Major loss of coralline algal diversity in response to ocean acidification », *Glob. Change Biol.*, vol. 27, n° 19, p. 4785-4798, oct. 2021, doi: 10.1111/gcb.15757.

- [302] S. Hohn et A. Merico, « Modelling coral polyp calcification in relation to ocean acidification », *Biogeosciences*, vol. 9, n° 11, p. 4441-4454, nov. 2012, doi: 10.5194/bg-9-4441-2012.
- [303] C. Jacob, A. Buffard, S. Pioch, et S. Thorin, « Marine ecosystem restoration and biodiversity offset », *Ecol. Eng.*, vol. 120, p. 585-594, sept. 2018, doi: 10.1016/j.ecoleng.2017.09.007.
- [304] A. J. Cole, M. S. Pratchett, et G. P. Jones, « Diversity and functional importance of coral-feeding fishes on tropical coral reefs », *Fish Fish.*, vol. 9, n° 3, p. 286-307, sept. 2008, doi: 10.1111/j.1467-2979.2008.00290.x.
- [305] V. Komyakova, P. L. Munday, et G. P. Jones, « Relative Importance of Coral Cover, Habitat Complexity and Diversity in Determining the Structure of Reef Fish Communities », *PLoS ONE*, vol. 8, n° 12, p. e83178, déc. 2013, doi: 10.1371/journal.pone.0083178.
- [306] C. S. L. Ng, T. C. Toh, et L. M. Chou, « Artificial reefs as a reef restoration strategy in sediment-affected environments: Insights from long-term monitoring », *Aquat. Conserv. Mar. Freshw. Ecosyst.*, vol. 27, n° 5, p. 976-985, oct. 2017, doi: 10.1002/aqc.2755.
- [307] R. E. Spieler, D. S. Gilliam, et R. L. Sherman, « Artificial substrate and coral reef restoration: What do we need to know to know what we need », *Bull. Mar. Sci.*, vol. 69, n° 2, 2001.
- [308] L. Avérous, « Les polymères biodégradables et biosourcés », p. 8.
- [309] E. Kennedy, A. Ordoñez, B. Lewis, et G. Diaz-Pulido, « Comparison of recruitment tile materials for monitoring coralline algae responses to a changing climate », *Mar. Ecol. Prog. Ser.*, vol. 569, p. 129-144, avr. 2017, doi: 10.3354/meps12076.
- [310] M. Kedzierski *et al.*, « Threat of plastic ageing in marine environment. Adsorption/desorption of micropollutants », *Mar. Pollut. Bull.*, vol. 127, p. 684-694, févr. 2018, doi: 10.1016/j.marpolbul.2017.12.059.
- [311] Z. Yang et G. Wu, « Effects of soft segment characteristics on the properties of biodegradable amphiphilic waterborne polyurethane prepared by a green process », *J. Mater. Sci.*, vol. 55, n° 7, p. 3139-3156, mars 2020, doi: 10.1007/s10853-019-04237-6.
- [312] L. Avérous et F. Le Digabel, « Properties of biocomposites based on lignocellulosic fillers », *Carbohydr. Polym.*, vol. 66, n° 4, p. 480-493, nov. 2006, doi: 10.1016/j.carbpol.2006.04.004.
- [313] C. Venancio, I. Lopez, et M. Oliveira, « Bioplastics: known effects and potential consequences to marine and estuarine ecosystem services | Elsevier Enhanced Reader », *Chemosphere*, 2022. doi: 10.1016/j.chemosphere.2022.136810.
- [314] G. L. Kennedy, « TOXICITY OF ADIPIC ACID », *Drug Chem. Toxicol.*, vol. 25, n° 2, p. 191-202, janv. 2002, doi: 10.1081/DCT-120003259.
- [315] M. Djapovic *et al.*, « Synthesis and characterization of polyethylene terephthalate (PET) precursors and potential degradation products: Toxicity study and application in discovery of novel PETases », *Chemosphere*, vol. 275, p. 130005, juill. 2021, doi: 10.1016/j.chemosphere.2021.130005.
- [316] F. Kerckhof, B. Rumes, A. Norro, T. G. Jacques, et S. Degraer, « Chapter 5. Seasonal variation and vertical zonation of the marine biofouling on a concrete offshore windmill foundation on the Thornton Bank (southern North Sea) ».
- [317] T. Haramina, N. Hadžić, et Z. Keran, « Epoxy Resin Biocomposites Reinforced with Flax and Hemp Fibers for Marine Applications », *J. Mar. Sci. Eng.*, vol. 11, n° 2, p. 382, févr. 2023, doi: 10.3390/jmse11020382.
- [318] S. Pioch, K. Kilfoyle, H. Levrel, et R. Spieler, « Green Marine Construction », *J. Coast. Res.*, vol. 61, p. 257-268, déc. 2011, doi: 10.2112/SI61-001.24.
- [319] R. Sherman, « Artificial reef design: void space, complexity, and attractants », *ICES J. Mar. Sci.*, vol. 59, p. S196-S200, oct. 2002, doi: 10.1006/jmsc.2001.1163.





**Titre :** Contribution au développement de Biocomposites Hydromorphes (HBC) par impression 4D pour applications marines

**Mots clés :** Biomimétisme – Biocomposites Hydromorphes - Impression 4D – Récif artificiel

**Résumé :** La problématique de déplétion des ressources biotiques dans les zones côtière et littorale est désormais admise par la communauté scientifique. Pour y remédier, des récifs artificiels censés favoriser la dynamique de repeuplement ont été développés ces dernières décennies comme par exemple en France ou au Japon. Néanmoins, ces derniers sont souvent composés de blocs de bétons, parpaings, coques de navires ou pneus usagés, ne représentant pas des solutions soutenables et durables pour l'océan.

L'objectif de ce projet de thèse est de développer un nouveau concept de récif artificiel bioinspiré, biocompatible avec les organismes marins, déployable et à durée de vie contrôlée.

Inspirés de la microstructure asymétrique présente chez certaines structures biologiques (pomme de pin, épi de blé...), ces nouveaux éléments de récifs, appelés Biocomposites Hydromorphes, proposent des changements de forme lors de leur immersion. Composés de ressources naturelles locales (fibres de lin), la formulation et la structure spécifique obtenue par impression 4D permettra au récif d'interagir positivement avec les espèces colonisatrices présentes; afin de redynamiser les écosystèmes marins.

**Title :** Contribution to the development of 4D-printed Hydromorph Biocomposites for marine restoration

**Keywords :** Bioinspiration – Hydromorph Biocomposites – 4D-printing – Artificial reefs

**Abstract :** The depletion of biotic resources in coastal areas is now recognized by the scientific community. To face this problem, artificial reefs are being developed to save the marine ecosystems as for example in France or Japan. However, they are often made of concrete blocks, building blocks, boat hulls or tires which do not represent sustainable solutions for the Oceans.

This project aims to develop a new concept of artificial reefs being bioinspired, biocompatible with marine organisms, deployable and with a controlled lifespan.

Inspired from asymmetrical architecture observable in nature (e.g. pine cone scale, wheat awns...), these new materials, called Hydromorph Biocomposites, are able to modify their shape when immersed in water. Made of natural and local resources (i.e. flax fibers), their formulation and their specific architecture generated by 4D-printing would allow the reef to interact positively with local marine organisms in order to restore their marine habitats.